3D Printing of Electrically Conductive Soft Multi-Material Composites for Strain and Pressure Sensors

Meshari Mubarak Awadh Alsharari

Submitted for the degree of Doctor of Philosophy

Heriot-Watt University

School of Engineering and Physical Sciences

May 2021

Abstract

3D printing on flexible microelectronics design and manufacturing is an emerging and burgeoning field. However, the existing platforms cannot meet the requirements for processing complex 3D flexible electronic circuit models. This project aims to establish a full-scale framework for 3D printing and its applications.

The combination of stretchable polymers with conductive carbon-based fillers has attracted attention in the multifunctional sensing materials field. Upon dynamic loading, these polymer composites exhibit piezoresistive behaviour that can be utilised for strain and tactile pressure-sensing applications. This project investigates the piezoresistive behaviour of stretchable thermoplastic conductive polymers and their strain and pressure-sensing capabilities.

Modification of the conductive composites has led to the development of fully 3D printed strain sensors. A 3D printer with a dual material extrusion system was employed to fabricate the conductive composites embedded in a stretchable elastomer substrate to create highly sensitive and linear strain sensors. Pre-straining of the 3D printed strain sensors caused crack formations; higher pre-straining values resulted in higher sensitivity. The sensors' sensitivity reached a gauge factor (GF) value of 163. Highly sensitive and tuneable pressure sensors were also realised by utilising multi-material 3D printing techniques. Combining conductive flexible polymers and scaffold materials allowed the fabrication of novel pressure sensors with enhanced compressibility and a wide sensing range. The physical properties of the materials were tested, and the electromechanical properties of the 3D printed sensors were investigated. Characterisation through scanning electron microscopy (SEM) and optical microscopic imaging was conducted throughout this research. The 3D printed strain and pressure sensors demonstrated cyclic behaviour with linear, repeatable, and reproducible responses suggesting great potential for many applications.

Dedication

To my parents and my grandparents!

Acknowledgements

First and foremost, all Praise to ALLAH the Almighty, for giving me the blessing, the strength, the chance and endurance to complete this study.

The Prophet (ﷺ) said: He who does not thank the people is not thankful to Allah.

I am grateful to have such amazing parents and grandparents who helped me with their continued encouragement and prayers to pursue my dreams. I feel blessed to have continuous support from my beautiful wife. So many thanks to my family (specially my brothers and sisters) and friends in Saudi Arabia who have kept in touch and made sure that I am doing ok.

My sincere thanks and appreciation to my supervisor Prof. Will Shu, who has always supported me through hard, good and fun times. He has helped me a lot during this exciting and challenging journey. A special thanks to Dr. Baixin Chen for his great help and continuous support. I also would like to thank Dr. Wei Wang for his mentoring. Special thanks to Dr. Sun and Nicholas for their help in SEM imaging, Dr. Kong for giving space in his lab, Nathan for his guidance in the 3D printing lab, Cameron for making sure to have our purchases arrive on time (or faster) and Alistair for his help and guidance in the workshop. I would like to thank all my group colleagues including Chris, Dr. Alan, Dr. Ian, Dr. Atabak, and all the others who have been fun, helpful and supportive all the time.

I would like to thank the examiners, Dr. Carmen Torres (external) and Dr. Xianwen Kong (internal), for the great time we had and the many useful recommendations they enlightened me with during my PhD Viva.

Special thanks to all my friends in the UK who have been supportive and made sure that we escape the work and have fun outside university. This includes Dr. Khaled Aliqab, Khaled Alsharari, Dr. Ibrahim Alotaibi, Abdullah Alsharari, Abdullah Bin Girad, Ghazi Alanazy, Saleh Komies, Bandar Alshammari, Marwan Alabiri, Khaled Alrushud, Abdulaziz Alomairi, Yousef Almajid, Dr. Mohammed Algarni, Dr. Abdulrahman Alwadea, Dr. Fahad Alsaleem, Abdulmajeed Alahmadi, Dr. Abdulrahman Alqarafi and so many others.

I am deeply grateful for the countless support and funding of my education from my kingdom, Kingdom of Saudi Arabia, all the way from elementary school, until I have become a doctor.

Research Thesis Submission

Name*:*	Meshari Mubarak A Alsharari		
School:	School of Engineering and Physical Sciences		
Version: *(i.e. First, Resubmission, Final)*	Final	Degree Sought:	PhD, Elect Electronic & Comp Eng.

Declaration

In accordance with the appropriate regulations I hereby submit my thesis and I declare that:

1. The thesis embodies the results of my own work and has been composed by myself
2. Where appropriate, I have made acknowledgement of the work of others
3. The thesis is the correct version for submission and is the same version as any electronic versions submitted*.
4. My thesis for the award referred to, deposited in the Heriot-Watt University Library, should be made available for loan or photocopying and be available via the Institutional Repository, subject to such conditions as the Librarian may require
5. I understand that as a student of the University I am required to abide by the Regulations of the University and to conform to its discipline.
6. I confirm that the thesis has been verified against plagiarism via an approved plagiarism detection application, e.g. Turnitin.

ONLY for submissions including published works

7. Where the thesis contains published outputs under Regulation 6 (9.1.2) or Regulation 43 (9) these are accompanied by a critical review which accurately describes my contribution to the research and, for multi-author outputs, a signed declaration indicating the contribution of each author (complete)
8. Inclusion of published outputs under Regulation 6 (9.1.2) or Regulation 43 (9) shall not constitute plagiarism.

* *Please note that it is the responsibility of the candidate to ensure that the correct version of the thesis is submitted.*

Signature of Candidate*:*	MESHARI	Date:	03 May 2021

Submission

Submitted By *(name in capitals):*	MESHARI ALSHARARI
Signature of Individual Submitting:	MESHARI
Date Submitted:	03 May 2021

For Completion in the Student Service Centre (SSC)

Limited Access	Requested	Yes		No		Approved	Yes		No	
E-thesis Submitted (mandatory for final theses)										
Received in the SSC by *(name in capitals):*						Date:				

Table of Contents

List of Tables

List of Figures

List of Abbreviations and Symbols

Abbreviations

2D	Two-dimensional
2PP	Two-photon polymerisation
3D	Three-dimensional
3DP	Three-dimensional printing
ABS	Acrylonitrile butadiene styrene
Ag	Silver
AM	Additive manufacturing
CAD	Computer-aided design
CB	Carbon black
CBTPU	Carbon black thermoplastic polyurethane
CNC	Computer numerical control
CNT	Carbon nanotube
CNTTPU	Carbon nanotube thermoplastic polyurethane
DC	Direct current
DIW	Direct ink writing
DW	Direct Write
EMB3D	Embedded 3D
FDM	Fused deposition modelling
G-Code	Geometric code
GF	Gauge factor
GPLA	Graphene polylactic acid
GWF	Graphene woven fabric
HIPS	High impact polystyrene
kN	Kilonewton
mm/s	Millimetre per second
MWCNT	Multiwalled carbon nanotube
PC	Personal computer
PDMS	Polydimethylsiloxane
PLA	Polylactic acid
PVA	polyvinyl alcohol

SD	Secure digital
SEM	Scanning electron microscopy
SLA	Stereolithography
SLS	Selective laser sintering
STL	Stereolithography
TPU	Thermoplastic polyurethane
USB	Universal Serial Bus
UV	Ultraviolet
v	Volts
X, Y, Z	Cartesian coordinates

Symbols

Ω	Ohm
Ω.m	Ohm-metre (Electrical resistivity unit)
σ	Electrical conductivity
°C	Degree centigrade
ε	Change in strain
kPa	Kilo Pascal
L	Length
ΔL	Change in length
L_o	Initial length
m	Filler mass
m_c	Percolation threshold
Pa	Pascal
ΔP	Change in pressure
R_o	Initial resistance
R	Electrical resistance

ΔR	Change in electrical resistance
S/m	Siemens per metre (Electrical conductivity unit)
t	Critical resistance exponent
wt.%	Weight in per cent

List of publications

M. Alsharari, B. Chen, and W. Shu, "3D Printing of Highly Stretchable and Sensitive Strain Sensors Using Graphene Based Composites," *Proceedings of EUROSENSORS conference*, 2018, vol. 2, no. 13.

Meshari Alsharari, Baixin Chen, and Wenmiao Shu, "Tuneable Sensitivity by Multi-material 3D Printing of Multi-layered Pressure Sensors ", *Adv. Funct. Mater.*, Feb. 2021, (submitted)

Meshari Alsharari and Wenmiao Shu, "Multi-Material 3D Printing of Highly Sensitive Strain Sensors Based on Crack Formation ", *Adv. Funct. Mater.*, (in preparation)

Chapter 1– Introduction

1.1 Introduction

Additive manufacturing (AM), also known as three-dimensional printing (3DP), has attracted considerable attention over the past few decades. It is recognised as one of the most promising new manufacturing technologies for the revolutionising of conventional fabrication. It is an advanced technology that constructs computer-aided design (CAD) by building the models layer-by-layer. 3DP is based on the process of making a physical object from a 3D digital model, typically by laying down many thin layers until a 3D structure is formed. The resolution of the 3D model is determined by both the vertical resolution (Z-axis), which is the smallest achievable layer thickness and the horizontal resolution, which is the minimum feature size that can be made through the XY plane [1]. Stereolithography (SLA), selective laser sintering (SLS), and fused deposition modelling (FDM) are amongst the first and earliest 3D printing technologies found in the 1980s [2]. Since then, AM has been rapidly evolving and expanding to include a myriad of applications in areas including aerospace, automotive, electronics and medicine. Recent progress in additive manufacturing AM has shown great potential in paving the way towards soft electronics.

In electronics, engineering customised and miniaturised computers, transportation and medical products all rely on advances that have made smaller, faster, and smarter electronic circuits. However, to date, most of these circuits and sensors are mechanically limited as they consist of rigid and brittle components [3], [4]. Recently, the need has arisen for new types of electronic devices that are flexible and stretchable. These devices are inspired by human biology and, at the same time, offer similar if not better electrical and performance characteristics of rigid components. Developments in soft electronics, including stretchable, wearable biosensors, artificial skin, and soft actuators, have proven to be essential for future electronics and biomedical applications. Specifically, strain and pressure sensors play a significant role in advancing the field of human-machine interfaces, wearable electronics, soft robotics, and health monitoring.

The technologies offered by AM enabled the fabrication of hierarchically complex structures that had not been possible otherwise. It offers many advantages such as single-step fabrication, density tuning of models, material waste reduction and simplified operation. Extrusion based 3D printing such as FDM has been gaining popularity in academic research due to availability, affordability, the ability to be modified, simultaneous multi-material fabrication, ease of

material adaption and development [5], [6]. FDM uses thermoplastic materials that are easy to use, widely available. Some have conductive and other functional fillers and are recyclable. Some of the most common thermoplastic materials explored in FDM are polylactic acid (PLA) and acrylonitrile butadiene styrene (ABS). They are rigid materials that offer ease of use, are abundant, have stiffness and strength and are used primarily on prototype models. Other popular thermoplastic materials are elastomer and industrial-grade polymers filled with functional nanomaterials such as carbon fibre filled nylon and carbon nanotube, and graphene filled thermoplastic polyurethane. The nanofillers add more functionality to the materials, such as electrical conductivity, more stiffness and strength. Graphene, carbon nanotube (CNT) and carbon black (CB) have been popular nanofillers for elastomer polymers owing to their outstanding mechanical and electrical properties. These nanocomposite elastomers offer stretchability and compressibility that meet the requirements of several strains and tactile sensing applications [7], [8]. There are also other materials that are 3D printed as scaffold support structures and later removed, such as water-soluble polyvinyl alcohol (PVA) [9].

The development of composite polymers infused with nanofillers promise to improve the electrical and mechanical properties of objects produced by FDM. Recently, thermoplastic polymers infused with nanocomposites have attracted much attention and opened the possibility of enhancing the properties of the addition of host material with a small amount of filler [10]. The FDM technique relies solely on the use of thermoplastic materials that are driven via geared motors to a heated nozzle. FDM process uses thermoplastic polymers where the filament is extruded at a temperature above its glass transition through a nozzle and deposited on a platform layer-by-layer to build a three-dimensional object. The focus of this research was on thermoplastic elastomers for use in stretchable and compressible sensing systems. Thermoplastic elastomers are polymers that consist of hard and soft segments. The hard segments have a melting temperature that acts as physical crosslinks. The FDM 3D printer's heating zone melts the filament's driven spool through the heated nozzle to form arbitrary 3D designs.

Sensors are one of the primary devices that benefit from the evolving development of such technologies. They are used to detect the change of the surrounding environment and could be employed to collect data that are inaccessible otherwise or to register and store data for further analysis and decision making. The development of flexible, skin-mountable and wearable sensors has gained much attention due to their high stretchability, low power consumption, biocompatibility, durability, and lightweight [11]. Flexible sensors have facilitated data

logging and monitoring to an unprecedented number of applications, including biomedical and wearable electronics [10]. Unlike rigid sensors, flexible sensors are more suitable and compliant for mounting onto an object, clothing or attaching directly to human skin, offering higher monitoring efficiency and minimum discomfort. The focus here was on stretchable and compressible sensors that rely on electrical resistance change upon induced mechanical change. Piezoresistive strain and pressure sensors are amongst the most popular due to their inherent flexibility, stretchability, low energy consumption and easy data read-out [8]. These types of sensors hold great promise for the development of health monitoring devices, electronic skin for human machine interaction, robotics, and prosthetics.

Wearable and flexible technologies have been of great interest in the area of electronics and biomedical engineering. Data read from temperature, heartbeat and blood pressure attached to a wearable device can be sent wirelessly to a nearby device via various technologies for continuous monitoring. Also, integrating sensing capabilities in soft robotics has the potential to advance the area of human-machine interfaces [12]. Here, this thesis presents the realisation of 3D printed soft electronics in wearable technology and its potential for innovation in numerous applications in sensors, health monitoring and biomedical devices. A method for employing multi-material FDM 3D printing to fabricate highly sensitive strain and pressure sensors has also been presented.

1.2 Motivation for the thesis

Additive manufacturing using 3D printing is a promising technology with the advantages of rapid and distinct manufacturing processes. Extrusion based 3D printing technologies such as fused deposition modelling (FDM) and direct ink write (DIW) offer rapid prototyping, customisation, and complex model fabrication for soft electronics. The use of flexible elastomer materials can act as substrate elastomers, and conductive polymer composites act as conductive interconnects to be utilised for various applications. Flexible materials with their composition of conductive fillers play a major role in enabling 3D printed soft sensor fabrication. However, it was observed that the addition of more conductive loading to the elastomer matrix to enhance the electrical performance affects the mechanical properties dramatically. Conductive elastomers used in sensing applications offer excellent stretchability and compressibility, suffer nonlinear mechanical and electrical behaviour. This nonlinear hysteresis behaviour prevents their reliability in soft electronics and health monitoring applications. The current 3D printed strain sensors suffered from either poor stretchability [13], [14], low sensitivity determined by the low values of gauge factor [15], [16] or hysteresis and

non-linearity [17], [18]. Poor stretchability means that the strain sensor has a maximum stretchability of up to 5% [13], [14]. Hysteresis and non-linearity were experienced in stretchable strain sensor where the change in electrical resistance does not linearly change with the applied strain [17], [18]. Thus, there is a need for new fabrication techniques as well as a new class of materials modification to overcome the issues faced in stretchable, skin mountable and soft sensing materials. In this matter, 3D printing has proved its potential to facilitate the fabrication of multi-material innovative sensing designs. The purpose of this project was to employ FDM 3D printing techniques to overcome the aforementioned limitations. Therefore, the conductive composite materials were modified to enhance the linearity and improve on the sensitivity of the 3D printed strain sensors. In addition, the use of supporting sacrificial material for the 3D printed pressure sensor influenced its mechanical compressibility and enhanced its sensitivity and sensing range. The ability to fabricate soft conductive materials printed layer-by-layer and embedded within flexible substrate has been utilised. This has allowed for the implementation of these 3D printed sensors in applications including wearable soft electronics, robotics and health monitoring.

1.3 Significance of the study

It was found in the literature that most of the current conventional technologies used to fabricate soft electronics usually suffered from complexity, high cost, multi-step and time-consuming fabrication processes. On the other hand, 3D printing has proved its potential to facilitate the fabrication of multi-material innovative sensing designs. It is an additive manufacturing tool that offers the possibility of rapid prototyping, novel and innovative geometrical freeform 3D designs. One of the key devices to enable wearable and soft electronics is stretchable and compressible sensing devices. Flexible materials with their composition of conductive fillers play a major role in enabling 3D printed soft sensors. One of the challenges of flexible sensors and wearable electronics is integrating a closed-loop system to provide feedback from the controlled machine and ensure the human-machine interaction has been successful. Most previously reported sensors focused on achieving high sensitivity and ignored the importance of simplifying the fabrication and packaging process of such flexible sensory systems. It is therefore essential to utilise a customisable and simple fabrication system to realise the growing interest in wearable soft electronics. As previously discussed, the implementation of high stretchability, linearity, and high sensitivity attributes remains challenging [19]–[23]. Furthermore, the current 3D printed strain and pressure sensors suffered either poor stretchability [13], [14], low sensitivity[15], [16] or hysteresis and non-linearity [17], [18]. This

nonlinear hysteresis behaviour prevents their reliability in soft electronics and health monitoring applications. The need arose for the development of fabrication techniques as well as a new class of materials modification to overcome the issues faced in wearable soft electronics. Therefore, the purpose of this project is to employ FDM 3D printing techniques to overcome these limitations.

1.4 Aims and objectives

1.4.1 Aims

3D printing of flexible conductive composites remains a new area to explore in research. This project presents a methodology to test the 3D printability of these thermoplastic materials. It also delves into analysing and characterising the mechanical and electrical properties of the 3D printed samples. This project presents the development of 3D printed multi-layered resistive strain and pressure sensors. 3D printing using dual extrusion FDM has been employed here to 3D print the prepared conductive composites embedded in a stretchable elastomer substrate to create highly sensitive and linear strain sensors. The emphasis here is on utilising flexible conductive polymer composites for the fabrication of 3D printed soft electronics for wearable and health monitoring applications.

The composites have been characterised using scanning electron microscopy (SEM) and optical microscopic imaging. The mechanical and electrical properties have been tested further. The set of materials and design of the multi-material strain and pressure sensors have also been described. A method of mixing 2 conductive pellets to fabricate highly sensitive strain sensors with linear response has been presented for the sensing material. For the pressure sensor, a novel design that utilises the advantages of multi-material 3D printing has been developed. Simultaneous multi-material printing allowed the fabrication of the sensing flexible thermoplastic polyurethane TPU material with soluble scaffold materials to support the pressure sensor's novel design structure. The 3D printed pressure sensor exhibited improved compressibility in comparison to the solid structure and presented linear, cyclic behaviour to applied pressure with an extensive sensing range. This allows the sensors to be applied in various wearable soft electronic applications.

1.4.2 Objectives

- To investigate 3D printability of thermoplastic materials using a dual extrusion 3D printer and test the strain sensing behaviour of 3D printed conductive elastomers.

- To explore CNT, CB and Graphene filled polymers and their strain and pressure-sensing capabilities
- To modify the conductive polymer composites for the 3D printed strain sensors in order to enhance their stretchability, linearity and sensitivity.
- To introduce the novel design of pressure sensor using conductive elastomer simultaneously 3D printed with PVA as scaffold support material to enhance the sensitivity and sensing range of the 3D printed pressure sensor.
- To demonstrate the feasibility of the novel, 3D printed sensors in terms of performance, reliability and sensitivity and further demonstrate functional applications of the fabricated sensors.

1.5 Thesis outline

Chapter 1 introduces the thesis and the motivation behind the work.

Chapter 2 gives the background focusing on 3D printing technologies. It also delves into the materials employed for stretchable and compressible sensing materials for electronic skin, wearable soft electronics and health monitoring applications.

Chapter 3 demonstrates the methodologies performed throughout the research that enabled the fabrication of the sensors, the electrical and mechanical analysis as well as the characterisation and applications of the fabricated sensors.

Chapter 4 explores the feasibility of fused deposition modelling FDM 3D printing technology. It investigates the multi-material 3D printing of the prepared, flexible filaments challenges of printability of flexible filaments and their strain-sensing behaviour compared to rigid and brittle conductive materials.

Chapter 5 presents a method for mixing 2 conductive pellets to fabricate highly sensitive strain sensors with a linear response. Various ratios of the 2 conductive pellets were mixed to tune their mechanical and electrical properties. The resulting conductive mixtures were extruded to form a 3D printable filament. The purpose was to enhance the sensors' performance to overcome non-linearity and sensitivity issues.

Chapter 6 introduces the development of 3D printed multi-layered resistive pressure sensors and their performance under compressive load. A novel method of fabricating soft compressible multi-layered pressure sensors via FDM 3D Printing was presented. The layer-

by-layer fabrication process and post-processing have been demonstrated throughout the chapter.

Chapter 7 summarises the research and suggests future work and applications of the outcome of this project.

Chapter 2– Literature review

2.1 Introduction

In the last two decades, 3D printing, also known as additive manufacturing (AM), has been widely researched in electronics, automotive aerospace, biomedical and many other fields. Fabrication of various complex designs that would not have been possible otherwise has been successfully realised by 3D printing [1], [4], [24]–[26]. It is claimed that AM holds the promise to revolutionise conventional computerised numerical control (CNC) subtractive methods from prototyping to end-parts by building the structures layer by layer from CAD models instead. Additive Manufacturing (AM) is a distinct rapid prototyping technique first introduced in the 1980s [2]. Various 3D printing technologies have been explored, specifically fused deposition modelling FDM, direct ink writing (DIW), selective laser sintering (SLS), and stereolithography (SLA). These techniques have been investigated widely and thoroughly developed. Consequently, many 3D printers and 3D bioprinters based on these technologies are commercially available [27].

AM eliminates the need for moulding, CNC, lithography, and other conventional methods. Instead, as described in Figure 2.1, the CAD model is designed and saved in the form of a stereolithography (STL) file. It is then sliced into a series of two-dimensional (2D) layers in the form of pattern-generating geometric code (Gcode). After that, these layers are translated through a computer-controlled pattern to build the 3D object [28], [29].

Figure 2.1: Generic vision of 3D printing process. [28]

2.1.1 Stereolithography (SLA)

SLA is the oldest AM process, originating in 1986. An ultraviolet (UV) laser is directed into photo-curable liquid resin to build the layers in this method. As shown in Figure 2.2 below,

once a layer solidifies, a new layer is introduced, and depending on the CAD model, supporting structure in the building process may be required. The directed laser, which causes the resin to polymerise, has a beam diameter resolution, which is as low as 0.025 mm, resulting in an accurate solidification process [30]. The resolution can reach 100 nm in newer techniques like two-photon polymerisation (2PP), which uses the same basic concept [31], [32].

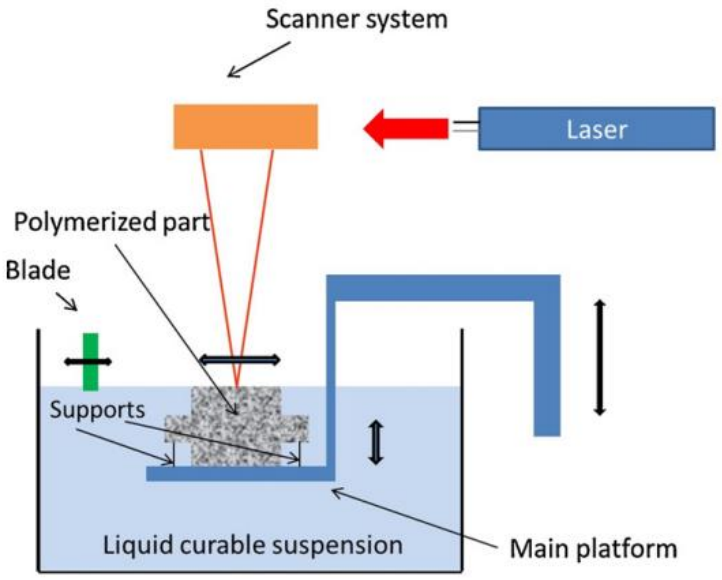

Figure 2.2: Stereolithography 3D printing process. [30]

2.1.2 Selective laser sintering (SLS)

SLS is a laser-based 3D printing process. In SLS, a laser beam is directed to a thin layer of metal powder, which causes it to heat the particles and fuse them selectively. The build platform is then lowered, as illustrated in Figure 2.3, and a new thin layer of powder is spread on the building platform. The minimum accuracy of the SLS method reaches 0.1 mm, which is considered a high resolution. One distinct advantage this process has is that no supporting structure is required during building the 3D model. However, this makes it hard to construct completely hollowed structures with solid surfaces that trap the metal powder inside [33], [34].

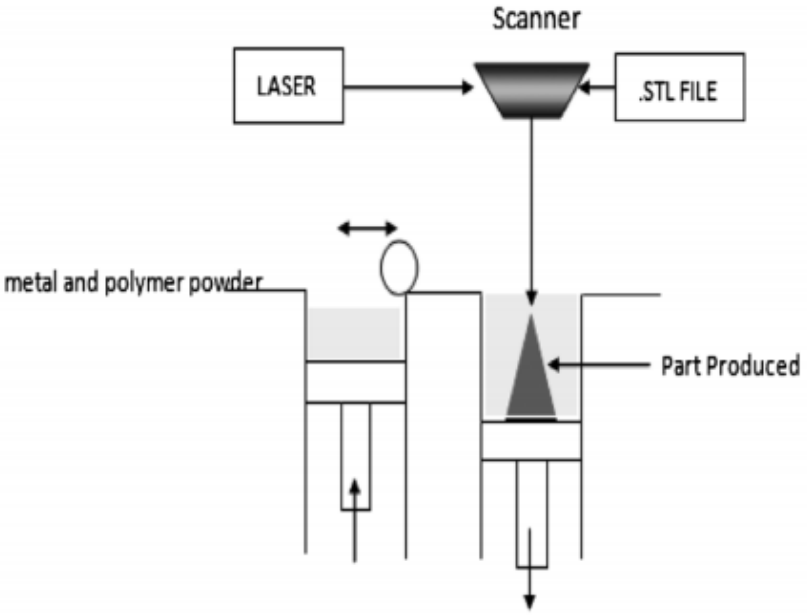

Figure 2.3: Selective laser sintering 3D printing process. [33]

Although SLA and SLS techniques offer high accuracy 3D printing, they are significantly expensive to buy and maintain. Another disadvantage is that they have a limited selection of materials, which restricts the freedom to introduce more flexible, biocompatible, and functional composition materials. In addition, these processes only allow one material to be used for each print. This limitation means that SLS and SLA lack the ability to 3D print multi-material simultaneously in a one-step process. In contrast, the second core AM techniques such as FDM and DIW are extrusion-based 3D printing processes that enable a wide range of rigid and flexible materials. They also allow multi-material fabrication simultaneously in one step. Various processing methods can be utilised by adjusting parameters such as shear yield stress, viscosity, shear loss and elastic moduli of the material composites. To date, the most common 3D printing processes that allow multi-material fabrication are hot-melt extrusion methods known as FDM and liquid deposition modelling known as direct writing [1], [4], [24], [25], [30], [33], [35], [36].

2.1.3 Direct ink writing (DIW)

DIW or otherwise known as direct writing DW, is an extrusion-based 3D printing process. It usually processes at room temperature and does not require an elevated temperature to heat the extruded material. This process exhibits few limitations in the range of materials used, unlike other 3D printing techniques. Consequently, the DIW method has been demonstrated as an alternative process with a broad range of material composites. The composite's viscosity should

be low to facilitate the fabrication via various mechanical techniques described in Figure 2.4, including pneumatic, piston, and screw extrusions. However, one drawback of DIW is that it requires low viscous materials, which adds an additional post-treatment of the deposited material. Therefore, this process requires extensive development and modification in the material to ensure the correct tuning for the extrusion process. It also requires post-processing to ensure optimal solidification of the deposited structure. It is also commonly employed for 3D printing of simple structures but cannot fabricate complex models [15], [37]–[40].

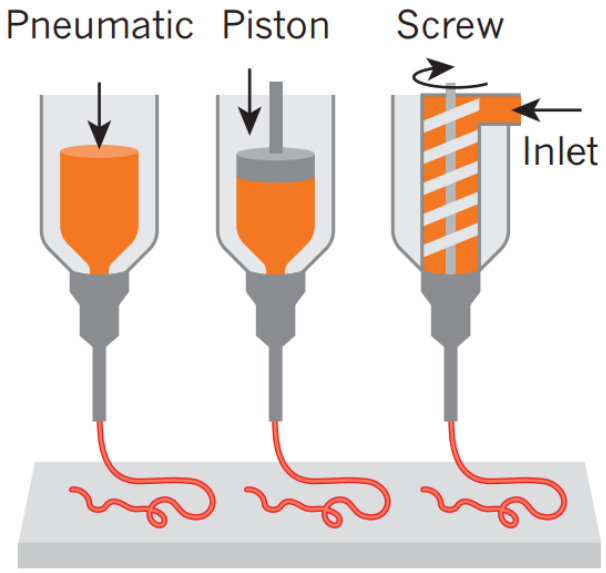

Figure 2.4: Three different methods of direct-write 3D printing. [27]

2.1.4 Fused deposition modelling (FDM)

FDM 3DP technique is achieved by melting thermoplastic materials through a heated nozzle, as shown in Figure 2.5. Rigid, soft and electrically conducting materials can be 3D printed by adjusting the filament and 3D printer's parameters. The filaments used in this technique are strands of thermoplastic polymers driven through a geared motor to the heated nozzle tip and solidify instantly on the printing platform. The heating temperature required depends on the melting point of the deposited material. FDM 3D printing offers many advantages, such as fabrication simplicity and attainable complexity of 3D printed models. The use of thermoplastic materials allows this technique to include various types of rigid and flexible materials. This technique also offers multi-material fabrication capability, and it is cheap to buy and maintain [37], [41]–[43].

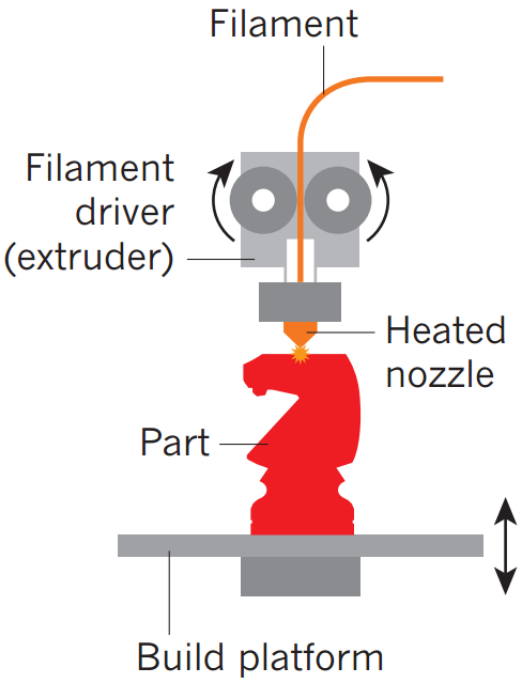

Figure 2.5: Illustrative schematic of FDM 3D printing process. [27]

2.1.5 3D printing method choice

It was found in the literature that although SLS and SLA offer high-resolution 3D printing, they can only fabricate one material at a time, lacking the ability to fabricate multi-materials in one step. Also, they are very expensive to install and maintain [30]–[34]. On the other hand, extrusion-based 3D printing, such as DIW and FDM, offer multi-material fabrication capability. However, it was found that DIW techniques could only fabricate low viscous materials, which require the post-treatment of the fabricated samples. Also, low viscosity 3D printing prevents their ability to fabricate hierarchically complex 3D models [15], [37]–[40]. In contrast, FDM offers a variety of highly viscous thermoplastic materials that can be melted through a heated nozzle with high-resolution ability. It also offers simultaneous multi-material 3D printing with no need for post-treatment of the materials [37], [41]–[43]. Due to its advantages for this research, FDM was employed as our 3D printing method.

2.1.5.1 FDM 3D printing materials

Examples of the most common used thermoplastic materials are polylactic acid (PLA) and acrylonitrile butadiene styrene (ABS). These two materials have various prototyping applications and can be printed in multi-colour. In addition, other forms of materials such as water-soluble polyvinyl alcohol (PVA) and high impact polystyrene (HIPS), which can be, applied as sacrificial (supporting) materials, as illustrated in Figure 2.6. However, these materials are rigid and cannot be employed as elastomers [6], [27], [44]–[46].

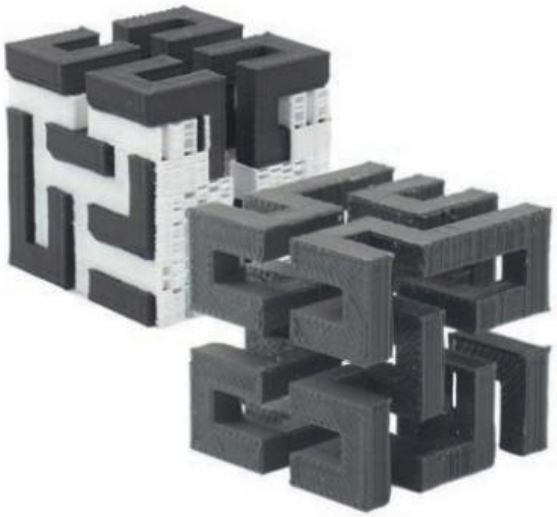

Figure 2.6: FDM printing with white support material (back) and then removed (front) revealing a Hilbert cube. [27]

In other 3D printable thermoplastic polymers have flexible and stretchable properties. An example is Ninja-Flex, a flexible thermoplastic polyurethane (TPU) with soft and elastic properties. Figure 2.7 shows the compressibility of 3D printed honeycomb-shaped NinjaFlex under a compressive load [47]–[50].

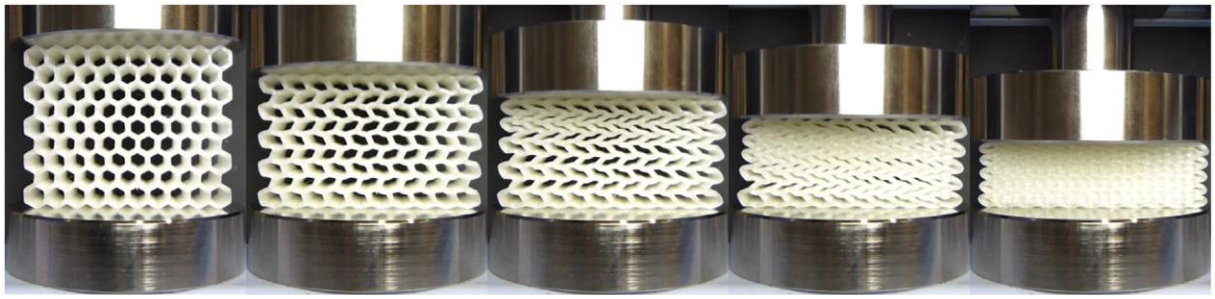

Figure 2.7: Compressibility of 3D printed NinjaFlex TPU filament.[47]

These types of polymers can also use additive fillers to add functionality to the material. For example, adding conductive nanofillers such as carbon nanotubes CNT can create electrical conductivity. Another example of these nanomaterials is electrically conductive TPU, a carbon additive that enables it to act as electrically conductive flexible interconnects for low current applications. Due to its thermoplastic behaviour, TPU with additional conductive filler has proven its compatibility for use in the FDM 3D printing process [18], [42], [51], [52]. Figure 2.8 shows an exemplar neat TPU and an image of TPU substrate with electrically conductive flexible CNT/TPU on top, simultaneously 3D printed to form a flexible circuit board [53]–[55].

It has been observed that FDM has been widely used on industrial and desktop printers, which are commercially available and open-source, permitting modification of the printer and

material at relatively low-price points. FDM also allows the fabrication of multi-materials simultaneously in one process. In addition, the nature of the thermoplastic materials used in FDM technique facilitates the modification of the conductive composite to tune the material as desired before 3D printing. The fabrication of complex models is also possible using FDM by incorporating soluble support materials that can be simultaneously 3D printed as needed. Consequently, the FDM 3D printing technique was chosen in this project for multi-material fabrication due to the ability to modify materials and easy modification of the process [13], [14], [42], [51], [56].

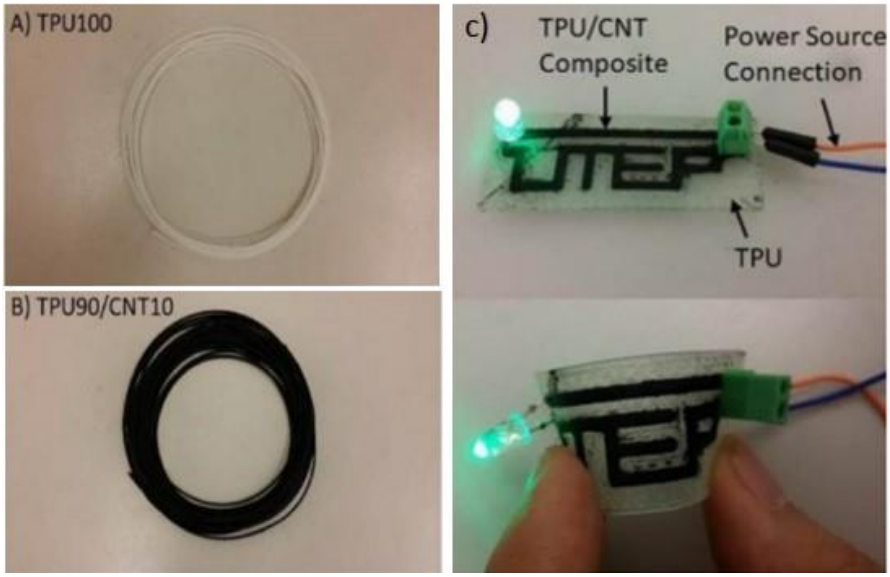

Figure 2.8: a) Pure insulative TPU 3D printable filament, b) Electrically infused TPU/carbon nanotubes 3D printable filament and c) Multi-material 3D printed flexible circuit board. [53]

2.2 Flexible conductive polymer composites

The composition of insulating and electrically conductive materials has led to new applications in soft electronic skin, sensors and biomedical devices. Developments in flexible conductive polymer composites have paved the way to facilitate the fabrication of soft electronics by integrating various methods of extrusion-based 3D printing. In addition, TPU based conductive polymer possesses stretchability of more than 100% tensile strain unlike rigid polymers such as PLA, which exhibited a very low tensile strain of less than 5% when filled with conductive polymers such as graphene PLA strain sensors [57]. TPU can bend to a strain of more than 100% while maintaining electrical conductivity, unlike rigid polymers such as PLA, which is naturally brittle and breaks when stretched to a maximum of 5% [13], [14], [58], [59].

Graphene is an example of an effective carbon-based conductive filler. It is one atom thick and exhibits excellent mechanical and electrical properties [60], [61]. An example of a simple

method of adding graphene to a TPU matrix by mixing them in a solvent is shown in Figure 2.9 below. Adding less than 1 wt% of graphene to an elastomer TPU matrix shows a significant impact on strain sensitivity compared to rigid metal-based sensors. CNT is another carbon-based conductive filler that has drawn much attention due to its high aspect ratio and affinity to flexible materials. This has made it a candidate for stretchable sensing applications [62]. Carbon black is another popular nanofiller due to its abundance, low cost and good electrical conductivity for use in conductive polymer composites [63]–[68].

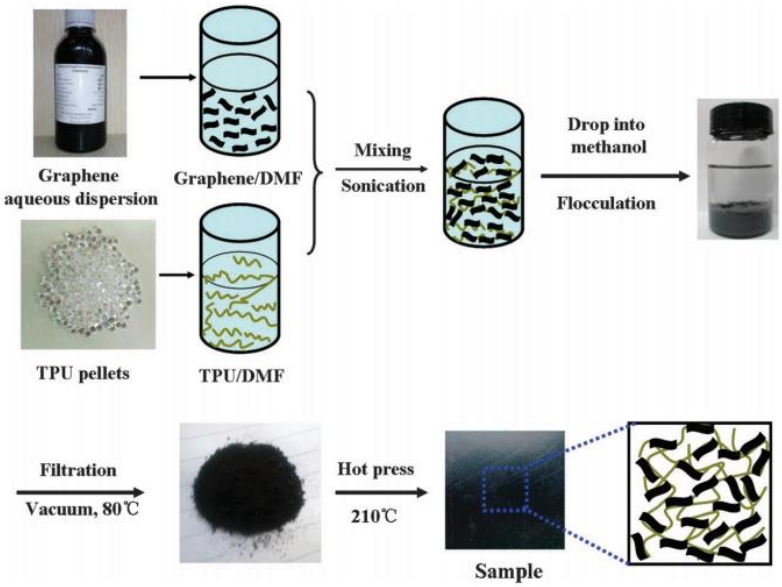

Figure 2.9: Steps for obtaining a homogeneous mixture of graphene-TPU.[69]

The addition of conductive filler to the elastomer matrix is based on the percolation threshold theory. The percolation threshold is described as the critical value reached when the conductive network is formed in the elastomer matrix, as shown in Equation (2.1) below:

$$\sigma = \sigma_0(m - m_c)^t \tag{2.1}$$

Where σ is the conductivity, m represent filler mass, m_c is the percolation threshold and t is the critical resistance exponent. It was observed that the addition of graphene impacts the mechanical properties of the elastomer matrix. Hence**,** Figure 2.10 shows the stress-strain test and the impact of adding 0.1, 0.2, 0.4, 0.6 and 0.8 weight in per cent (wt%) of graphene to the TPU matrix. It was found that due to their high aspect ratio, CNT and graphene require minimal addition to the host polymer of less than 10 wt% to assure electrical conductivity. On the other hand, carbon black usually requires an addition of ~30 wt% to the total weight of the composite to fulfil the percolation threshold and ensure electrical conductivity [69]–[73].

Here, the 3 carbon-based additives, namely, CNT, graphene and CB, were tested in this project due to their affinity to TPU [69]–[73]. In addition, the elastomer used in this research was TPU due to its 3D printability via our chosen FDM 3D printing technique.

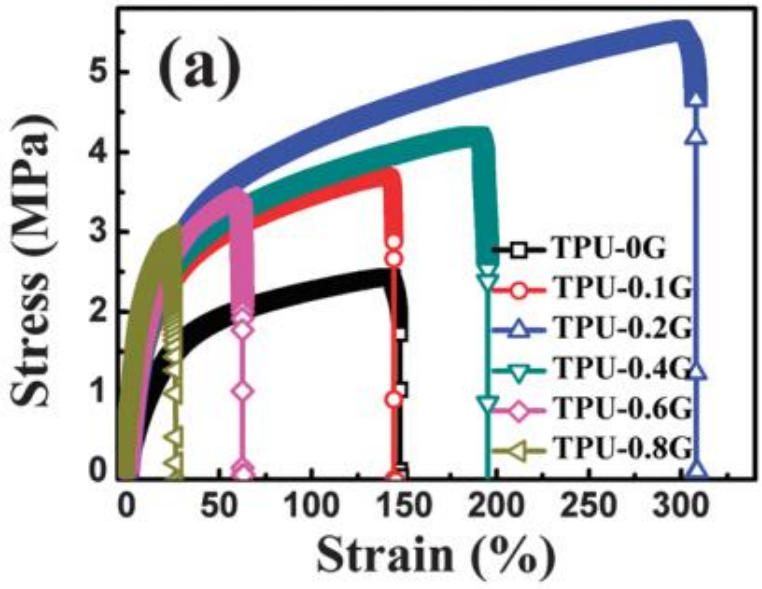

Figure 2.10: Effect of graphene loading on TPU. [69]

2.3 Conductive TPU composites as strain and pressure-sensing materials

Sensors are used to detect changes in the surrounding environment. Strain and pressure sensors are usually used to monitor the mechanical and physical changes of their attached objects. For the sensors to be adequate for wearable and health monitoring applications, they must be flexible, compressible and stretchable [74], [75]. TPU is an engineering thermoplastic polymer that offers the flexibility, compressibility and stretchability that fulfil the requirement for strain and pressure-sensing applications. Carbon-based nanofillers namely, graphene, CNT and carbon black, have been commonly used as conductive fillers within conductive polymer composites. Figure 2.11 shows the piezoresistive behaviour of TPU filled with various carbon-based conductive composites when subject to tensile strain [7], [8], [67], [76]–[79]. Resistive-based strain and pressure sensors have gained much interest in research and applications [80]–[82]. Compared to capacitive sensors, they require low-voltage and simple read-outs without the complication of capacitive sensors arising from electric field interaction, a complex read-out setup or electrochemical reactions [39], [83].

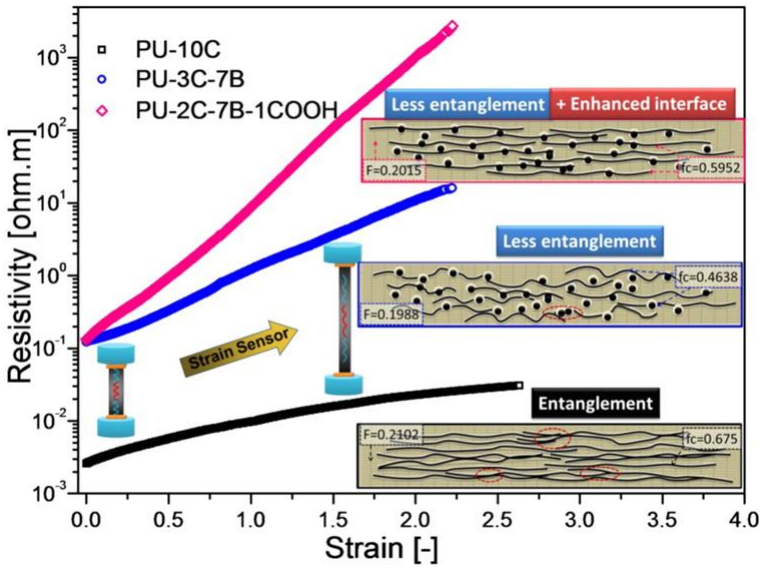

Figure 2.11: Electrical resistance change of conductive TPU strain sensors with mixed carbon fillers. [79]

The combination of TPU as an insulative stretchable matrix with carbon-based conductive nanofillers has shown outstanding electromechanical performance for pressure-sensing applications. The use of TPU as a host matrix has proved its feasibility for use in pressure sensors. When homogenously filled with conductive additives, under dynamic loading, as illustrated in Figure 2.12, they show significant piezoresistive behaviour, leading to high sensitivity. Carbon-based conductive fillers have proven to be a great candidate for conductive polymer composites due to their affinity with TPU and their functional properties in electromechanical pressure sensors. Given their superior properties, the combination of TPU with the carbon-based conductive fillers was investigated here for their feasibility to be used as strain and pressure sensors [8], [67], [84]–[87].

TPU is an engineering thermoplastic polymer that is compatible with our chosen FDM technique and offers flexibility, compressibility, and stretchability, fulfilling the requirements for strain and pressure-sensing applications [58], [59]. Due to its thermoplastic behaviour, TPU with additional conductive filler has proven its compatibility for use in the FDM 3D printing process [88]. TPU and carbon-filled TPU materials can be stretched to strain values of more than 100% while maintaining electrical conductivity, unlike rigid polymers such as PLA, which is naturally brittle and breaks when stretched to a maximum of 5% [13], [14], [58], [59].

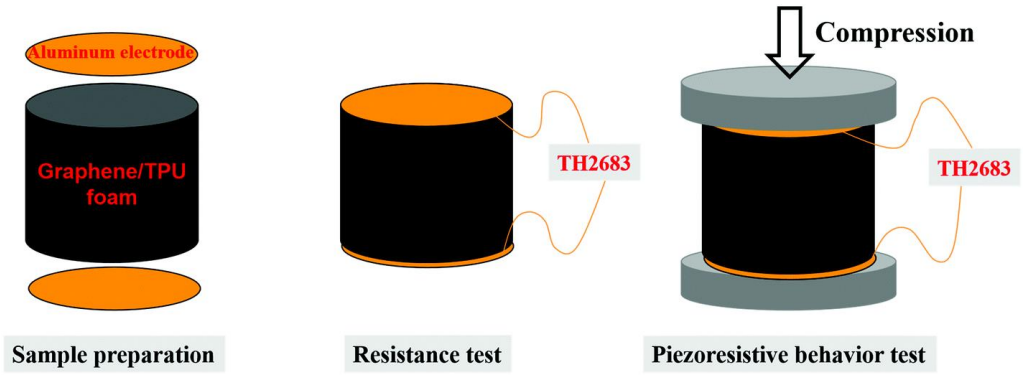

Figure 2.12: Schematic diagram of sample preparation illustrating the mechanism of pressure sensor resistance measurement and piezoresistance behaviour test under compression. [89]

2.3.1 Mechanism of resistive-based strain and pressure sensors

Strain sensing is driven by the piezoresistive effect caused by the conductive network's change upon mechanical loading. Stretching a conductive polymer composite decreases the conductive network's density leading to a decrease in the electrical conductivity and consequently increases the electrical resistance [90]. When a conductive polymer is stretched, it causes changes in the conductive network that can be acquired by calculating the change in electrical resistance. This mechanism is explained schematically in Figure 2.13. Upon loading, the main changes to the conductive nanoparticles within conductive polymers include the breakage of conductive pathways and an increase in the tunnelling distance between conductive nanoparticles, resulting in electrical resistance.

The tunnelling effect is an acceptable scenario where an excited voltage or temperature causes electrons to hop through a thin polymer layer and tunnel a small distance in the nanometre range [91], [92]. In some cases, the reconstruction of new conductive pathways occurs upon stretching, causing a decrease in electrical resistance. Upon strain release, while some broken conductive pathways become irreversible, other conductive pathways return to their original state resulting in fewer changes to the electrical resistance. This electromechanical behaviour governs the working principle of strain sensors. When the material is stretched, the conductive filler network changes, allowing the loss of conductive pathways to be observed. This stretching leads to non-recoverable behaviour in the initial value of the electrical resistance [93]–[95].

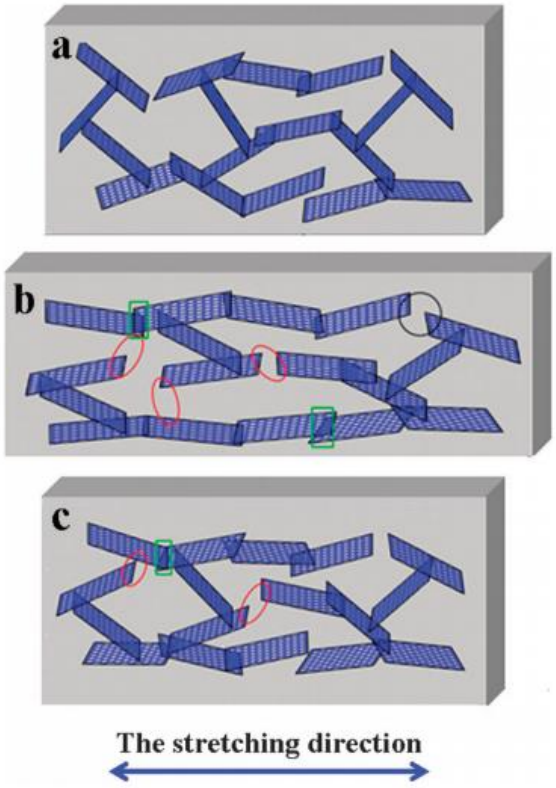

Figure 2.13: Mechanism of strain sensing upon loading/unloading of graphene-TPU elastomer. [69]

At the same time, piezoresistive behaviour can also be experienced in compressive strain loading, which occurs in pressure sensors as described schematically in Figure 2.14 [96]. The represented schematic illustrated the compressive behaviour of piezoresistive pressure sensors upon pressure input. When the pressure force is applied to the flexible sensor, the resulting mechanical compression enhances the sensing material's conductive pathways, leading to a decrease in electrical resistance. The change in electrical resistance is measured by calculating the effect of strain or pressure loading on the value of electrical resistance, as illustrated in Equation (2.2):

$$\frac{\Delta R}{R_o} = \frac{(R - R_o)}{R_o} \tag{2.2}$$

Where R_o represents the initial resistance and ΔR represents the change in resistance. A significant requirement for the evaluation of good strain and pressure sensors is that the change in electrical resistance ΔR to the initial resistance value R_o with respect to change in length $\boldsymbol{L}$ to the initial length $\boldsymbol{l}$ of the sensors should be as large as possible. This change is known as a gauge factor (GF), and the sensitivity of the strain and pressure sensors can be evaluated by the measurement of GF illustrated by Equation (2.3) below**,** which is expressed as:

$$Gauge\ Factor\ (GF) = \frac{\frac{\Delta R}{R_o}}{\varepsilon} \quad (2.3)$$

where ΔR represents the change resistance during strain loading, $R_o$represents the value of the initial sensor's resistance, ε denotes the strain, $\varepsilon = \frac{\Delta L}{L_o}$ where ΔL is the change in length and L_o is the initial length. In pressure sensors, sensitivity can also be evaluated by dividing the theoretical change in resistance by the pressure applied in kPa, as demonstrated in Equation (2.4), which is expressed as:

$$\frac{\Delta R/R_o}{\Delta P} \quad (2.4)$$

Where $\frac{\Delta R}{R_o}$ represents the change in electrical resistance divided by initial resistance R_o and ΔP represents the varied applied pressure measured in Pascal. [97]

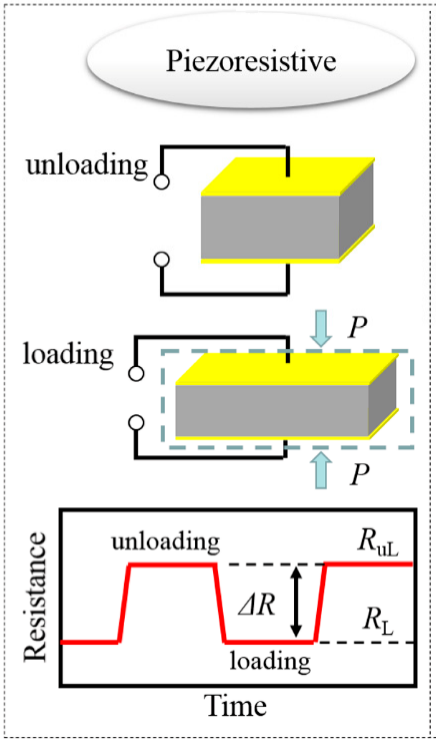

Figure 2.14: Sensing mechanism of piezoresistive pressure sensor. [41]

2.3.2 Linearity, hysteresis and negative strain effect of stretchable conductive polymers

The stretchable conductive polymers' strain and pressure-sensing mechanism is mainly influenced by the activity of the conductive network within the polymer matrix during the stretching and releasing process. The negative strain effect is when the change in electrical resistance is not linearly proportional to the applied strain, as shown in Figure 2.15 below. Previous research has found an inherent negative strain effect in the electrical piezoresistivity

change to applied strain [8], [98], [99]. The electrical resistance is expected to increase to the increase in applied tensile strain, but the negative strain effect occurs when electrical resistance decreases to strain increase, as illustrated in Figure 2.15b. One of the main factors that causes this effect is the competition between the destruction of the conductive network and the newly introduced conductive pathways. Other factors that influence this negative effect include the type of conductive fillers and a negative Poisson's ratio. When the material is stretched, the Poisson's ratio compresses the material perpendicular to the strain direction. In pressure sensors, the negative effect can be seen in terms of applied compressive pressure as opposed to applied strain [98], [100].

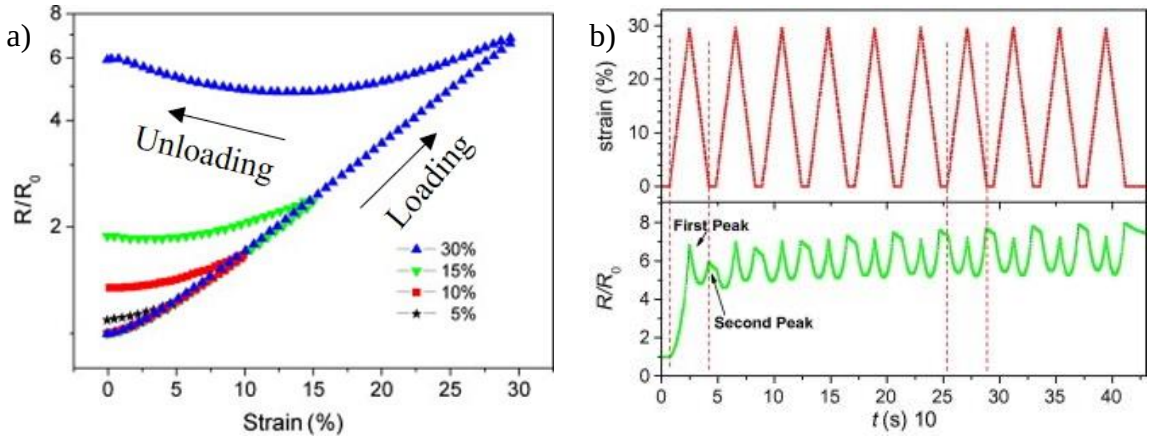

Figure 2.15: a) First cycle of relative change in resistance to various tensile strain values, and b) The change in resistance to applied strain with apparent negative strain effect after the 1st cycle. [100]

Under a dynamic load, strain sensors can experience a hysteresis effect in the electromechanical curve. Large hysteresis impacts the reliability of the sensor, causing irreversible sensing behaviour. The viscoelastic nature of stretchable polymers is thought to be the primary factor causing hysteresis behaviour in stretchable strain sensors. Avoiding hysteresis is essential for the sensor's feasibility for use in wearable and health monitoring applications. Hysteresis in elastomers and conductive elastomers can be seen in their mechanical stress-strain curve in which the stress (measured in Pascal) does not increase linearly to applied strain (%). This inversely occurs upon strain release, and it can consequently influence the electrical resistance behaviour of the conductive elastomer [7], [101], [102].

Elastomers also experience a softening effect referred to as the "Mullins' effect". In a conductive elastomer, the combination of soft domains due to the nature of the host elastomer and hard domain is because of the addition of a stiffer conductive filler such as graphene. When the material is stretched, more significant deformation occurs to the soft domain to accommodate the applied stress and the conductive filler experience low strain. Mullins and

Tobin (1957) suggested that the softening in filled elastomers is due to decreased volume fraction of the hard domains, resulting in an irreversible rearrangement of the microstructure network during dynamic load [103].

2.3.3 Pre-straining impact on stretchable and compressible resistive sensors

Pre-straining is a process that is employed to regulate the conductive pathways within stretchable conductive polymers. It is essential to acquire regular electrical resistance behaviour to applied strain loading and unloading. This behaviour ensures the reliability and reproducibility of the sensors [104], which is critical as the first few strain cycles ensure monotonic behaviour in the fabricated sensor's electromechanical behaviour for use in strain and pressure-sensing applications. After the first 3-4 cycles, the electromechanical behaviour follows a regular electrical resistance curve to applied strain loading and unloading, as illustrated in Figure 2.16.

Pre-straining was performed to regulate the conductive network embedded in the stretchable material, especially under large strain amplitudes. Upon strain application, the competition between lost and newly constructed conductive pathways could induce double peaks in the electrical resistance curve. It was also suggested that pre-straining resolves double peak issues, as shown in Figure 2.16 and consequently obtain a better single peak response pattern in the electrical resistance curve. The single peak pattern is preferable as it demonstrates a linear electromechanical relationship with the electrical resistance curve upon mechanical strain loading and unloading.

As can be seen, cyclic pre-straining between 5-20% stabilised the electrical resistance change when the same sample was tested at cyclic strain between 0-15% after 24h, see Figure 2.16b. The observed significant difference in the change in electrical resistance before and after the pre-straining is attributed to the non-recoverable electrical resistance caused by the initial loading/unloading, which is apparent in the first cycle in Figure 2.16a. It can be said that pre-straining can modify the electrical resistance to ensure predictable electromechanical behaviour for reliance in use for strain and pressure- sensing applications [99], [105]–[108].

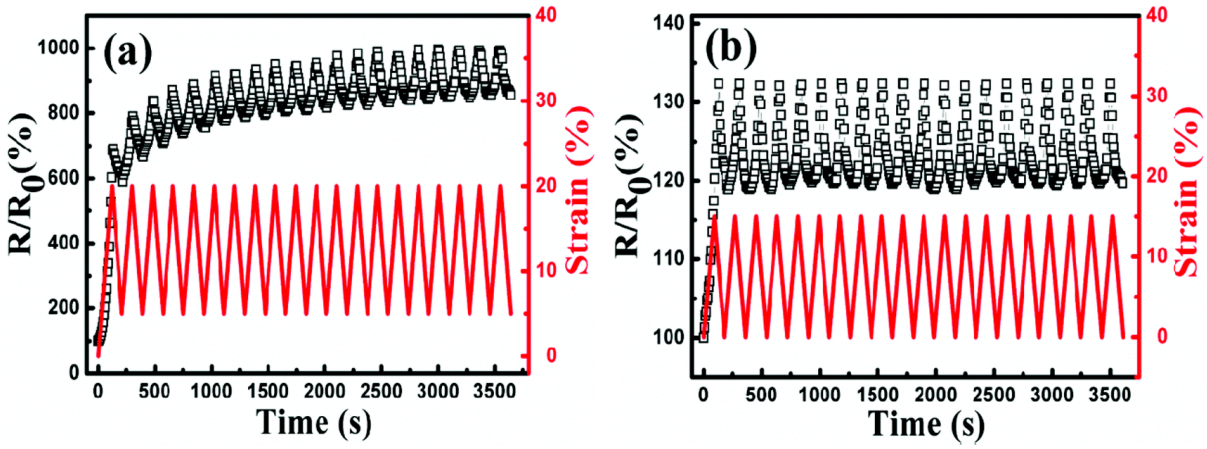

Figure 2.16: Effect of pre-straining showing strain sensing behaviour of conductive-TPU at (a) Initial strains between 5-20%, and (b) Cyclic strain between 0-15% after the initial pre-straining. [104]

2.3.4 Crack-based sensing mechanism

Upon stretching, fabricated strain sensors are prone to cracks in the sensing material, either controlled or unintentionally. The incident of cracks can lead to a positive effect on the sensitivity of the sensors. For example, when carbon nanotubes (CNT) are embedded in stretchable polydimethylsiloxane (PDMS), the PDMS accommodates the tensile strain as shown in Figure 2.17, whereas the embedded CNT has a crack formation due to its high stiffness in comparison to PDMS [109]. The cracks in the conductive material cause a loss in electrical connection, leading to a high electrical resistance increase. Cracks that occur on stretched strain sensors add advantageous properties because of their sensitivity, and they can detect unprecedented low strain levels like monitoring heart rate pulses. The cracks usually occur to the sensing material embedded or adhered on top of a stretchable substrate. Previous research has presented highly sensitive crack-based strain sensors; the sensors suffered a low strain range of up to 20% [110]–[116]. The crack formation is caused when the strain or pressure sensor is subjected to stretching or compression. While the stretchable substrate by nature responds elastically to applied strain, crack formation occurs in various levels to the sensing material due to its higher stiffness or brittleness [117]–[120]. Other previously reported crack assisted strain and pressure sensors involved scattering conductive fillers such as thin gold films[121], silver (Ag) nanowire [122], carbon nanotubes [109], [123]–[125] and graphene [126] meshes wrapped within a stretchable substrate, required multiple steps and lacked the freedom of customising the sensors for a broader range of applications [109], [123]. The incident of cracks causes a substantial increase in electrical resistance, which results in high sensitivity strain and pressure sensors. The steep increase in electrical resistance caused by fractures is rarely reversible, and stretchable encapsulate materials play a significant role in

assuring reversibility. Therefore, linearity between the applied strain and electrical resistance under cyclic test is an essential property to be satisfied for the application of strain sensing [121], [127]–[131].

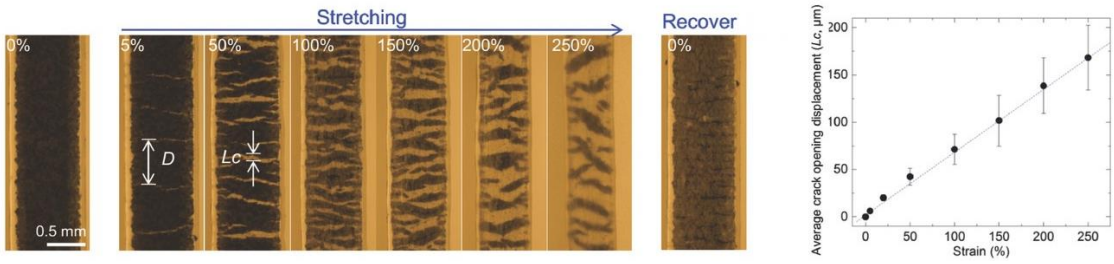

Figure 2.17: Opening of cracks of CNT embedded within TPU elastomer under tensile strain from 0-250% and inset showing the average crack displacement to applied strain. [109]

Previously reported crack-based sensors focused on high sensitivity for low tensile strain ranges of up to 20%. Besides, the highest sensitivity that can be achieved is inversely proportional to the stretchability, with the highest sensitivity values reported were for strain limited to 2%. On the other hand, crack induced strain sensors that offered high stretchability commonly suffered low sensitivity with a measured gauge factor of up to 30. Upon the crack formation on stretchable sensors, electrical conduction can be preserved to an extent as illustrated schematically for graphene woven fabric (GWF) in Figure 2.18 [110]. The requirements of linearity and high sensitivity can be satisfied by ensuring reversibility and considerable variation in electrical resistance, respectively. Innovative geometrical designs achieved substantial changes under slight strain, such as woven fabrics, crack-assisted overlap, spider's slit inspired sensory system and thickness gradient films usually suffered from complexity, high costs and time-consuming fabrication processes. Although research has been dedicated to crack-based sensors, fulfilling the combination of high sensitivity, high stretchability and linearity with a simple and customisable fabrication process remains a challenge.

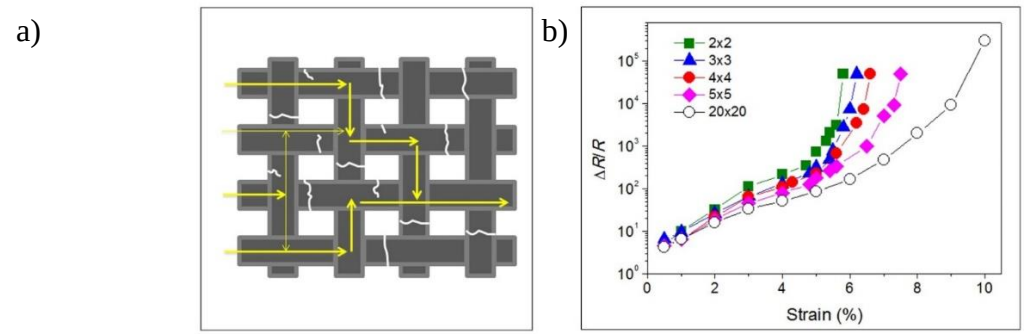

Figure 2.18: a) Schematic illustration of electrical current path of graphene woven fabric undergoing crack formation, and b) Change in electrical resistance of GWFs with various sizes. [110]

2.4 3D printed strain sensors

Additive manufacturing employing 3D printing has been explored for the fabrication of strain sensors. AM has proven to be an effective technique to fabricate strain sensors and is a viable tool that can be utilised to fabricate customisable strain sensors. Previously 3D printed strain sensors either suffered a negative strain effect or presented low sensitivity, as illustrated in Table 2.1 [132]–[136]. Various 3D printing techniques have been employed to fabricate stretchable strain sensors. For example, a DIW method named embedded 3D printing (EMB3D) printing was developed to fabricate highly conformable and stretchable strain sensors [137]. This method involves extruding conductive elastomer into an elastomeric reservoir in which, afterwards, the materials are thermally cured to form the strain sensor [15]. The EMB3D printing technique has also been employed to fabricate multi-material, multi resistive-based sensory for a closed-loop feedback system for robotic and human machine interaction applications [15], [38], [39], [138]. Although the strain sensors showed high stretchability, the sensitivity was limited by a gauge factor of 3.8 [15]. In addition, the 3D printing technique requires the use of a reservoir or a moulded elastomeric matrix, which limits the freedom of design and customisation. Another technique involves modifying an FDM 3D printer by replacing the extruder with a syringe pump. Then, using the syringe pump, the multiwalled carbon nanotube MWCNT/PDMS mixture is 3D printed on a pre-cured PDMS to create a strain sensor [139]. The 3D printed sensor performed with a linear piezoresistive response of up to 30% of maximum strain and had moderate sensitivity with a gauge factor value of 4.3 [139]. Another strain sensor, fabricated using the FDM 3D printing technique, has shown high stretchability and sensitivity (illustrated in Figure 2.19) [18]. Although they achieved a gauge factor of 176, the sensors suffered from nonlinear behaviour in the electrical resistance curve upon dynamic loading, which prevented their reliability and feasibility for use in strain sensing applications [16], [18], [42], [140]–[144][145].

Table 2.1: Stretchability, linearity and sensitivity of previous work on 3D printed strain sensors.

Tensile strain (%) (stretchability)	Linearity	Sensitivity (Gauge Factor)	Reference
1.5	Linear	n/a	[13]
100	Linear	3.8	[15]
50	Non-linear	3	[17]
100	Non-linear	176	[18]
30	Linear	4.3	[139]

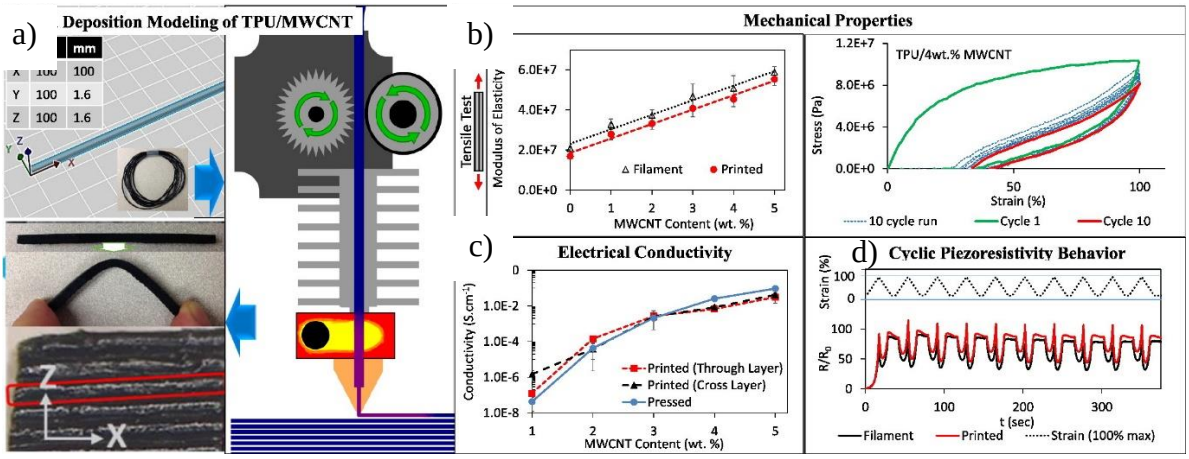

Figure 2.19: a) Schematic of FDM 3D printing process, b) Mechanical properties, c) Electrical conductivity measurement and d) Cyclic piezoresistive behaviour of 3D printed strain sensors. [18]

2.5 3D printed pressure sensors

Pressure sensors play a leading role in advancing human machine interaction, wearable electronics, soft robotics, and health monitoring. Piezoresistive pressure sensors specifically are amongst the most popular due to their inherent flexibility, stretchability, low energy consumption and easy read-out [146]–[149]. High sensitivity and a wide sensing range are 2 crucial properties that mark a good pressure sensor. Various 3D printing techniques were adapted to fabricate pressure sensors, owing to their flexibility, simplicity, and cost-effectiveness, as illustrated in Table 2.2. To date, many additive manufacturing technologies have been employed for pressure- sensing applications, including FDM multi-material and direct-write 3D printing techniques [51], [150]–[155]. The latest advances also include the use of 3D printed moulds to create microstructures that enhance the sensitivity of tactile pressure sensors [150]. In this type, 3D printing is employed to fabricate novel mould designs that tailor the surface structure of the sensing element of a pressure sensor. A dual-material FDM 3D printer was used to fabricate a 3D multiaxial force sensor that contains MWCNT/TPU filament as the sensing material and a neat TPU as the structural support body [51]. As illustrated in Figure 2.20, the two materials were 3D printed simultaneously in a one-step fabrication process. The 3D printed sensor could measure the forces along 3 axes (x, y and z) with moderate sensing capability apparent in the theoretical change of electrical resistance [19], [51], [152].

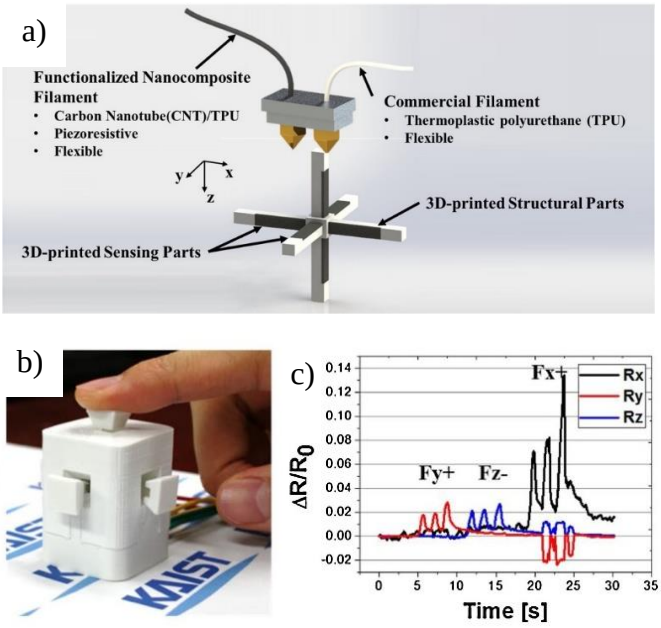

Figure 2.20: a) Schematic illustration of FDM 3D printing process of multiaxial force/pressure sensors, b) Image of the 3D printed multiaxial force sensor, and c) Real time electrical resistance measurements of the sensor under simultaneous multiaxial mechanical forces. [51]

Table 2.2: Sensing range and sensitivity of previous work on 3D printed pressure sensors.

3D printing technique	Sensing range (kPa)	Sensitivity	Reference
FDM	n/a	$\frac{\Delta R}{R_o}$ = (0.14)	[51]
DIW	20	GF (180)	[151]
FDM of moulds	2	3.5 kPa^{-1}	[150]

Innovation using a direct writing technique showed promise for the fabrication of multi-material, multifunctional 3D pressure sensors. The process involves 4 independently controlled nozzles to fabricate nanocomposites with varied conductive contents and a sacrificial supporting material in a one-step 3D printing process [151]. The tactile sensors were 3D printed under ambient conditions conformally onto a freeform surface. The sensitivity was evaluated using a gauge factor with the highest value reaching 180. Although the tactile sensor exhibited high stretchability and compressibility, the practical sensing range presented went up to 20kPa. Microstructure templates of pyramid, semi-sphere and semi-cylinder shapes were firstly fabricated via FDM 3D printing. After printing, uncured PDMS was poured into these templates [150]. The PDMS was then cured, peeled off the templates and spray-coated with a thin layer of carbon nanotubes to create highly sensitive pressure sensors. The use of 3D printed

mould replaced the multistep photolithography process with a single 3D printing step. These sensors exhibited high sensitivity reaching -3.6 kPa^{-1} but the maximum sensing range presented was up to 2kPa [150].

2.6 Applications of flexible sensors

Flexible sensors have great potential in many applications, including biomedical devices for health monitoring, wearables for sports, virtual reality and entertainment. They also hold great promise in the development of human-machine interaction, soft robotics, prosthetics, smart skin and textiles. Tactile sensors that mimic human touch perceptions have been explored to translate mechanical signals such as pressure, strain and force into electrical signals for use in wearable electronic applications [156]. Various types of strain and pressure sensors have been developed for health monitoring, prosthetics, robotics and wearable electronics embedded in textiles or attached directly to the human body. For example, it has been possible to control a robot remotely using strain sensors attached to a glove controlled by human bending fingers. Figure 2.21 shows an example of a robotic hand mimicking human fingers' motion via the strain sensors mounted on a human hand. In biomedical applications, such sensors would be useful for controlling and monitoring medical devices used in surgery and injury rehabilitation [157]–[159].

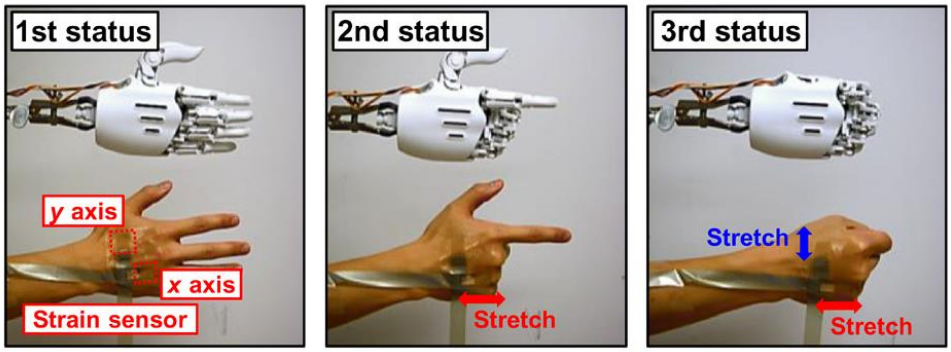

Figure 2.21: Representative images for strain sensors application in human motion mimicking for human machine interaction. [160]

With the rise of wireless communication and the internet of things, the potential of such personalised wearable devices can allow remote health monitoring and reduce the pressure on medical systems [161]. It also plays a significant role in the early diagnosis of viral diseases and enhances health quality for elderly and vulnerable people. Wearable health stretchable and skin mountable sensors can monitor heart pulses, blood pressure, oxygen levels and breathing

rates. For example, a pressure sensor attached to the artery of a wrist was able to capture real-time physical pulses of heartbeats, as shown in Figure 2.22 [90], [162]–[165]. In addition, strain sensors that offer high stretchability can be employed to monitor human body movements. Regarding human motion detection, usually up to 50% strain can fulfil most of a human body's joint movement. For example, a strain sensor attached to a glove was able to detect fingers movement. Another strain sensor woven into trousers was able to detect various knee movements such as extending, flexing, squatting, and jumping. Stretchable sensors can also be utilised for human-machine interaction for controlling robots and robotic arms. Controlling robotics from afar is crucial in areas unreachable by people or for safety purposes such as dangerous, harsh environments [88], [147], [166]–[170].

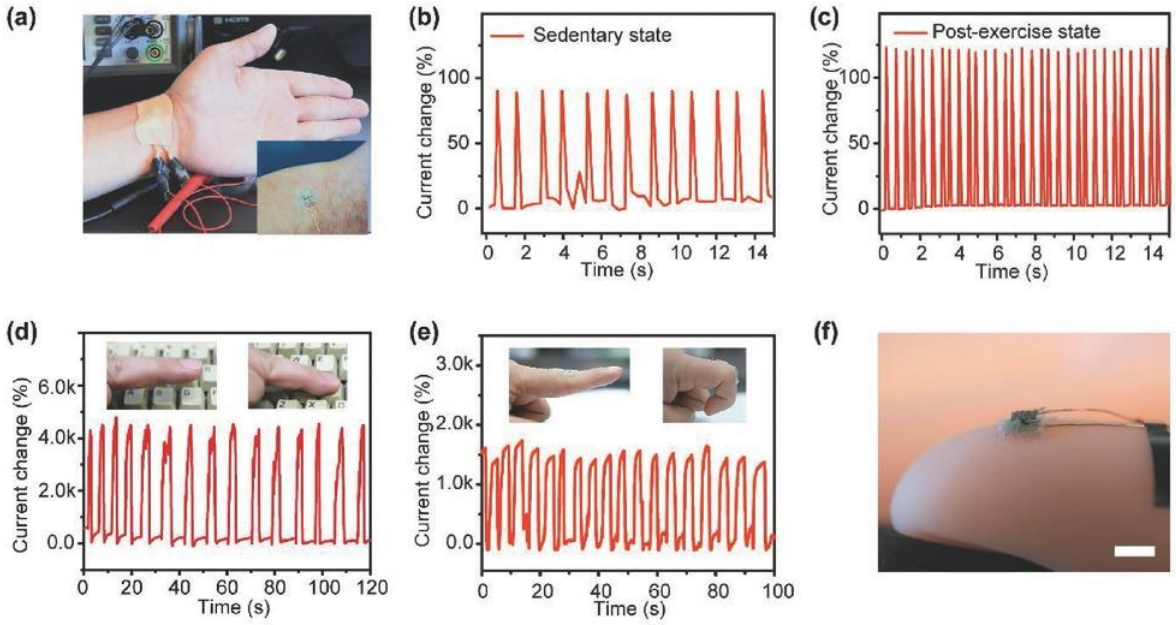

Figure 2.22: Applications of 3D printed tactile sensor showing a) Image of the sensor attached directly on hand wrist for heart pulse detection, b) Heart pulse measurement in resting state, c) Pulses post-exercise state, d) Signal of a sensor attached to finger-tip, e) Signal corresponding to sensor attached on top of an index for finger bending and f) Optical image showing the conformally 3D printed tactile sensor on a fingertip. [151]

2.7 Contribution to knowledge

It was found in the literature that previously 3D printed strain and pressure sensors have had apparent limitations. In the 3D printed strain sensors, the sensors that achieved GF values of up to 176 suffered non-linear behaviour in their change in electrical resistance to applied strain [17], [18], whereas achieving high stretchability of >50% with linear response was associated with low sensitivity [13], [15], [139]. For the 3D printed pressure sensors, it was found that that previous works presented high sensitivity, but the maximum sensing range presented was up to 20kPa [51], [150], [151]. Therefore, in order to overcome the issues mentioned above, a

method of 3D printed conductive composites simultaneously embedded within a stretchable substrate was presented. The crack formation caused by the pre-straining of the 3D printed strain sensors was investigated to explore its influence on the measured sensitivity. In addition, the use of a removable supporting scaffold via simultaneous multi-material 3D printing was implemented to explore its influence on the mechanical compressibility of the multi-layered pressure sensor. It was further investigated to explore its influence on the change in electrical resistance in comparison to a solid sample of the same material. The purpose was to overcome the limitations and enhance the sensitivity and the sensing range of the 3D printed multi-layered pressure sensor.

Chapter 3– Materials and methods

3.1 Introduction

This chapter presents the materials used in this research and explains the properties and purposes of each material. This chapter also summarises the experimental methodologies and techniques. The methodology, which explains how to combine, mix and produce 3D printable materials, is also introduced here. This chapter describes the 3D printing technology employed to fabricate samples with various materials. For the analysis of the samples, data acquisition techniques were used to collect electrical and mechanical data to assist in completing the thesis. Different imaging instruments were also introduced here for the characterisation of the 3D printed materials.

3.2 Materials

This research involved the use of thermoplastic materials which are compatible with the fused deposition modelling (FDM) 3D printing technique. Thermoplastic polyurethane (TPU) was used as the insulating stretchable substrate. In addition, 3 types of carbon-filled conductive polymers were utilised. Two of the conductive materials were TPU based stretchable materials, and one was polylactic acid (PLA) based rigid material. Polyvinyl alcohol (PVA) water-soluble material was also used.

3.2.1 Insulating stretchable substrate

Thermoplastic polyurethane (TPU), namely NinjaFlex, (Ninjatek Ltd, USA), has been used for the 3D printing of insulating substrates. It is a highly elastic and stretchable material with a shore hardness of 85A and elongation of up to 660% strain at break [171]. It was received in the form of 3D printing filament spool, as shown in Figure 3.1 and was used as received. The material was purchased and used in various colours, including white, clear, red and blue. It was employed as the encapsulating 3D printed substrate material in Chapters 4 and 5.

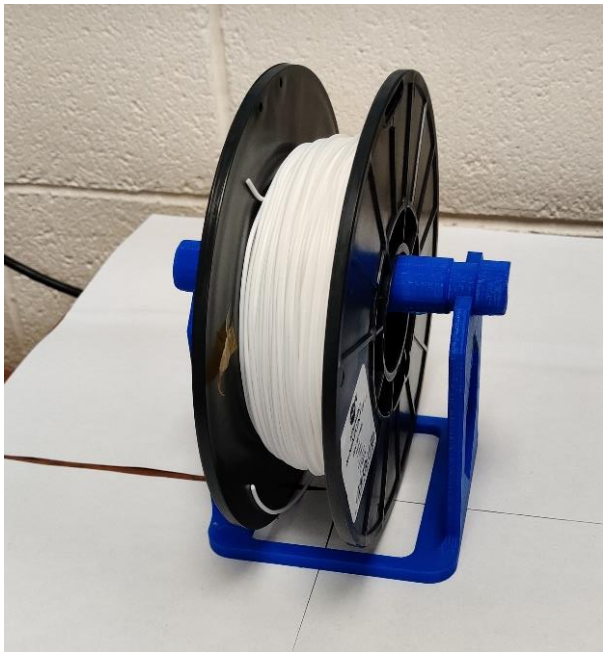

Figure 3.1: NinjaFlex thermoplastic polyurethane TPU.

3.2.2 Conductive materials

3.2.2.1 Carbon black thermoplastic polyurethane (CBTPU)

Carbon black thermoplastic polyurethane (CBTPU), with a shore hardness of 70A, was purchased from Hexpol TPE (see Figure 3.2a, below). According to the manufacturer, this CBTPU has a carbon black content of 30 % and electrical volume resistivity < 104 Ω.cm, [172]. CBTPU has a pellet diameter of 2 mm, and it was used as a sensing material in 3D printed strain and pressure sensors in Chapters 4-6.

3.2.2.2 PLASTYCYL™ TPU1001

PLASTYCYL™ TPU1001, multi-walled carbon nanotube thermoplastic polyurethane (CNTTPU) provided by Nanocyl SA (Sambreville, Belgium), was used. CNTTPU, shown in Figure 3.2b, has a shore hardness of 93A, carbon nanotubes content of 10% and electrical volume resistivity of 3.61 x 102 Ω. cm [173]. It has a pellet diameter ranging between 1 – 2 mm, and it was employed as a sensing material in 3D printed strain sensors in Chapter 4.

3.2.2.3 Graphene polylactic acid (GPLA)

The third conductive material used in this work was graphene polylactic acid (GPLA), and it was purchased from Graphene Lab Ltd (USA). Due to the host polylactic acid polymer, GPLA is a rigid material with a graphene content of 16% and an electrical volume resistivity of 1 Ω.cm [174]. GPLA, shown in Figure 3.2c, has a pellet diameter between 1.5 – 2 mm, and it

was employed as an addition sensing composite material in 3D printed strain sensors in Chapter 5.

All 3 conducting polymers were employed to evaluate the strain and pressure behaviour of thermoplastic materials and to test their viability as strain and pressure sensors. They are compatible with our chosen FDM technique and were received in the form of pellets, as illustrated in Figure 3.2.

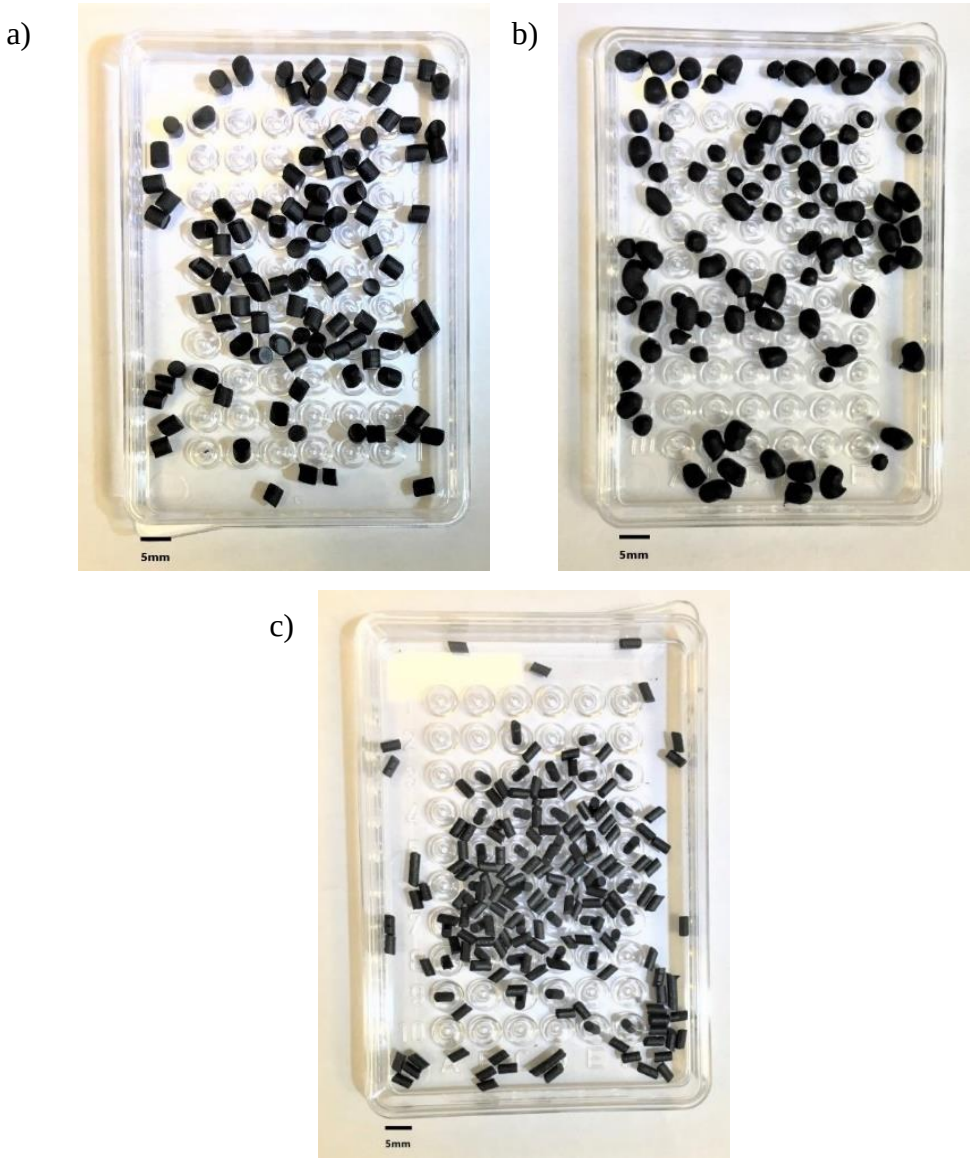

Figure 3.2: Examples of conductive pellets: a) Carbon black thermoplastic polyurethane (CBTPU), b) Carbon nanotubes thermoplastic polyurethane (CNTTPU), and c) Graphene polylactic acid (GPLA).

3.2.3 Water-soluble material

Polyvinyl alcohol (PVA), shown in Figure 3.3, is a dissolvable material purchased from eSun (China). It was utilised as the supporting structure for the 3D printed samples that included

overhangs structures, detailed in Chapter 6. It is a water-soluble material in the form of a 3D printing filament spool and was used as received [175].

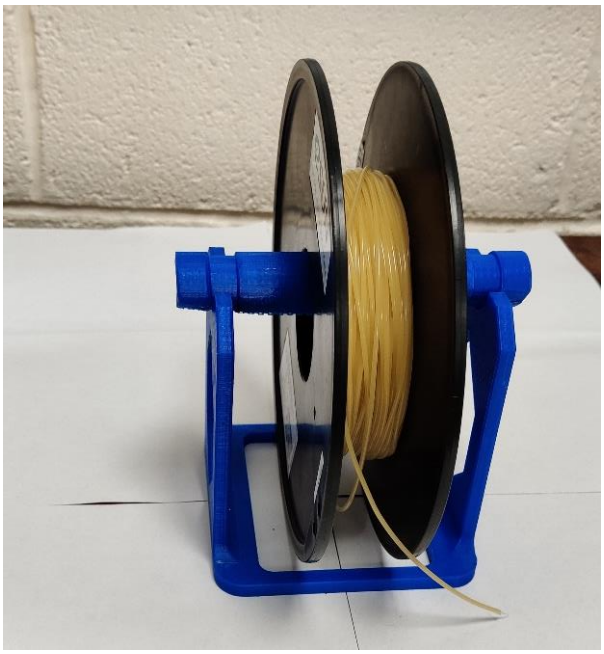

Figure 3.3: Polyvinyl alcohol PVA, a water-soluble material.

3.3 Composites filament preparation

3.3.1 Filament extruder

Noztek Pro is a desktop filament extruder purchased from (Noztek, UK) [176]. It can be loaded with various thermoplastic polymer pellets such as ABS, PLA and TPU. The filament extruded can then be used with the 3D printer. It can extrude a single type or combination of polymer composites. The extruder, pictured in Figure 3.4a, consists of a hopper to load the pellets. The extruder temperature is adjustable and can heat up to 300 °C. It includes 2 swappable nozzles of 1.75 mm and 3 mm diameters which can extrude strand of filament with (±0.04 mm tolerance) to use with the 3D printer. The pellets are driven to the heated nozzle through a single screw, driven by a direct current (DC) motor. It has an extrusion speed of up to 2.5 metres per minute with an attached fan to cool the material as it is extruded through the nozzle. It also has a 45-degree bracket to ease the process of filament extrusion [176].

a)

b)

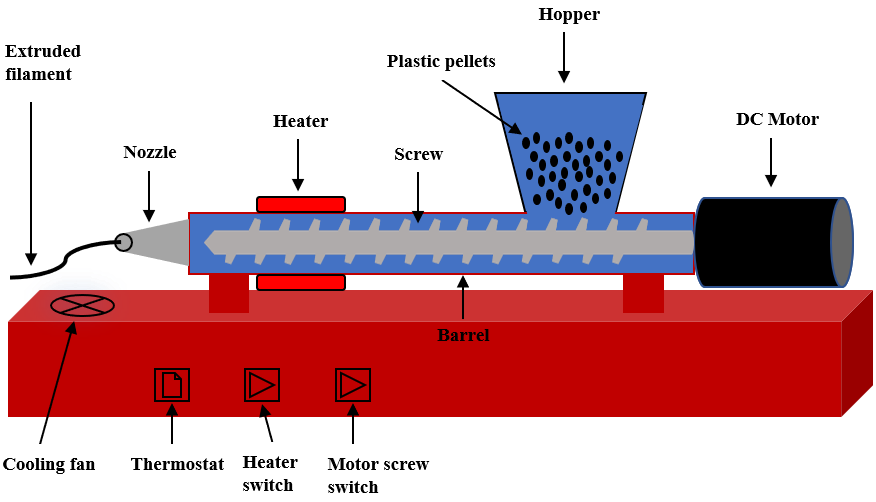

Figure 3.4: a) Image of Noztek Pro filament extruder and b) schematic explanation of the composite preparation via filament extruder

3.3.2 Composites preparation

The conductive pellets used throughout this research were dried at 70 °C overnight before any melt processing using material dryer Figure 3.5b The pelletized materials were dry mixed, melt-processed and extruded at 170 °C, using the single-screw filament extruder (Noztek), and described in a schematic in Figure 3.4b, above. The digital scale, shown in Figure 3.5c, was used to control the weight of conductive pellets loaded. In addition to the 3 types of conductive materials, CNTTPU, CBTPU and GPLA, a mixture of CBTPU and GPLA were achieved by dry mixing CBTPU-30GPLA, CBTPU-40GPLA and CBTPU-50GPLA prior to filament

extruding. The mass loading (wt.%) of GPLA to CBTPU is denoted as CBTPU-χGPLA, where χ denotes the mass loading wt.% of GPLA to CBTPU. The mixed pellets were first extruded through Noztek Pro using the 3 mm nozzle diameter. They were then manually cut to form pellets and were dry mixed one more time to ensure a homogenous mix. The extruder formed a consistent strand of 3D printable filament with a diameter of 1.75 mm (±0.04 mm tolerance).

a) b)

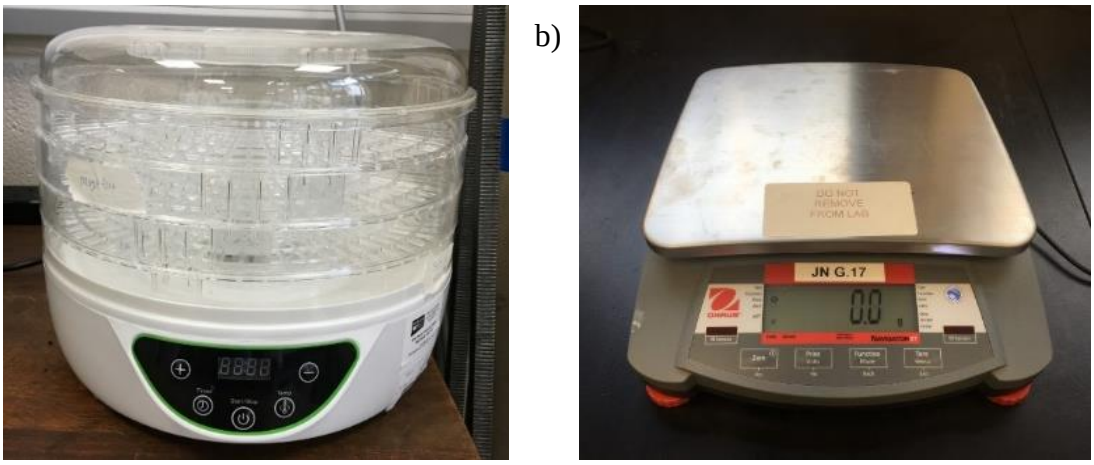

Figure 3.5: a) Materials dryer, and b) Digital scale.

3.4 Fused deposition modelling (FDM)

3.4.1 3D printer

The fabrication of the samples utilised a FlashForge Creator Pro FDM printer, pictured in Figure 3.6 below, which was purchased from (FlashForge Corporation, China) [177]. It has a build volume of 227 mm length X 148 mm width X 150 mm height and a maximum speed of up to 100 mm/s. The layer resolution is between 100–500 µm; the positioning accuracy is 11 µm in XY and 2.5 µm on the Z-axis. The printer uses a dual extrusion system that allows a simultaneous fabrication of 2 materials, which in this research were the insulating substrate and the conductive filaments in one single step. The dual extrusion system in the 3D printer also allows for the simultaneous fabrication of the conductive filament and sacrificial water-soluble filament.

Figure 3.6: FlashForge Creator Pro 3D Printer.

3.4.2 Flexion extruder

The extrusion system in the purchased FlashForge Creator Pro FDM 3D printer was originally designed to 3D print rigid materials such as PLA and ABS. Therefore, the printer was modified by fitting a flexion extruder purchased from (Diabase Engineering, USA) and shown in Figure 3.7a below [178]. This extruder allows for the printing of flexible filaments like TPU elastomers, used in this work. As shown in Figure 3.7b and further explained schematically in Figure 3.7c, the extruder uses a Cam dial that adjusts the pressure on the driven filament through the motor gear to the hot end nozzle. Figure 3.7b shows a closed up image of the fitted extruder with the left extruder's filament fan dismantled to illustrate the extruder's features [178].

3.4.3 3D CAD design PTC Creo

PTC Creo is a piece of Computer-aided design (CAD) software that has been used in this work. It has been primarily employed to create 3D digital models for 3D printing. The 3D model designs are then converted into stereolithography (STL) formats, which is the 3D modelling format compatible with additive manufacturing AM and 3D printing [179].

a)

b)

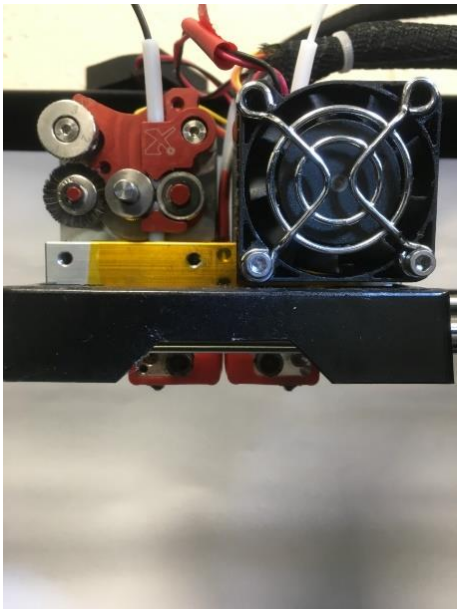

c)

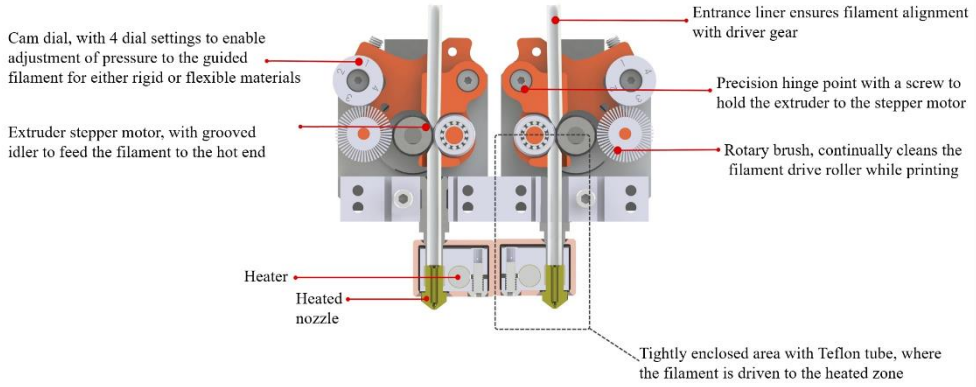

Figure 3.7: a) Image of the flexion dual extruder, b) Closed up image of the extruder fitted to the 3D printer, and c) Schematic explanation of the flexion dual extruder's features (image was modified from the source [178]*).*

3.4.4 MakerBot software

MakerBot software was used to combine and slice the 3D models of STL format. This slicer software allows for the 3D models to be transformed into a sequence of two-dimensional layer-by-layer deposition of the material via 3D printing. It controls the values of the 3D printing parameters, such as the extruder nozzle's temperature, printing speed and layer height which is detailed in the 4th chapter. Table 3.1 summarises the values of parameters used in this work which were then sliced and exported to a secure digital (SD) card as geometric code (Gcode) files which the 3D printer can read. As shown in Table 3.1, a slightly larger nozzle was used to print the conductive filaments composites to avoid clogging during printing.

Table 3.1: 3D printing parameters used in the dual extrusion process.

Parameters	Conductive filaments	Insulating filament	Water-soluble filament
Print Temperature (°C)	230	230	200
Platform Temperature (°C)	60	60	60
Nozzle Diameter (mm)	0.8	0.5	0.5
Layer Height (mm)	0.2	0.2	0.2
Print infill (%)	100	100	100
Print Speed (mm/s)	15	15	15

3.4.5 Multi-material 3D printing process

Multi-material 3D printing was employed here using 2 independent extruders which can function simultaneously in the 3D printer. Each extruder can load a different material, and the 3D printer alternately dispenses materials one at a time, as illustrated in Figure 3.8 below. The 3D printer consists of an automated XYZ plane, where the extruders move on the printer's XY axis. At the start of the print, the platform that translates the printer's Z-axis rises until it almost hits the tip of the extruders' nozzles. After that, it lowers layer by layer during the 3D printing process. The process follows a pattern given by a CAD file and materials exiting the heated nozzle welds to the printing platform and solidifies layer by layer.

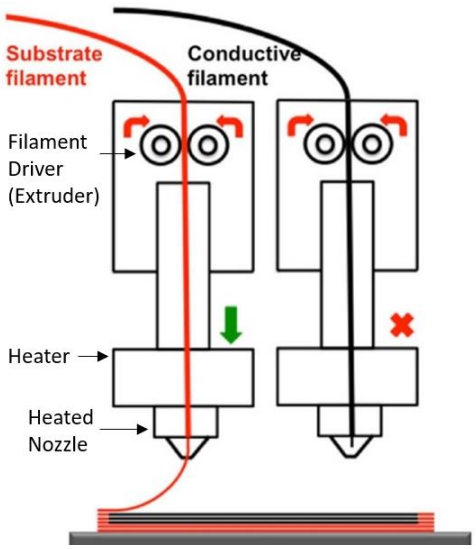

Figure 3.8: Schematic of the process of 3D FDM dual printing.

3.5 Electrical conductivity testing

The electrical conductivity test was performed using Agilent TTi 1604, 4000 count digital multi-metre shown in Figure 3.9. Strands of the extruded conductive filaments were measured; each had a length of 40 mm and a diameter of 1.75 mm (±0.04 mm). The samples were coated in a silver paste at the 2 ends of the strands before measuring to ensure electrical connection to the digital multi-metre.

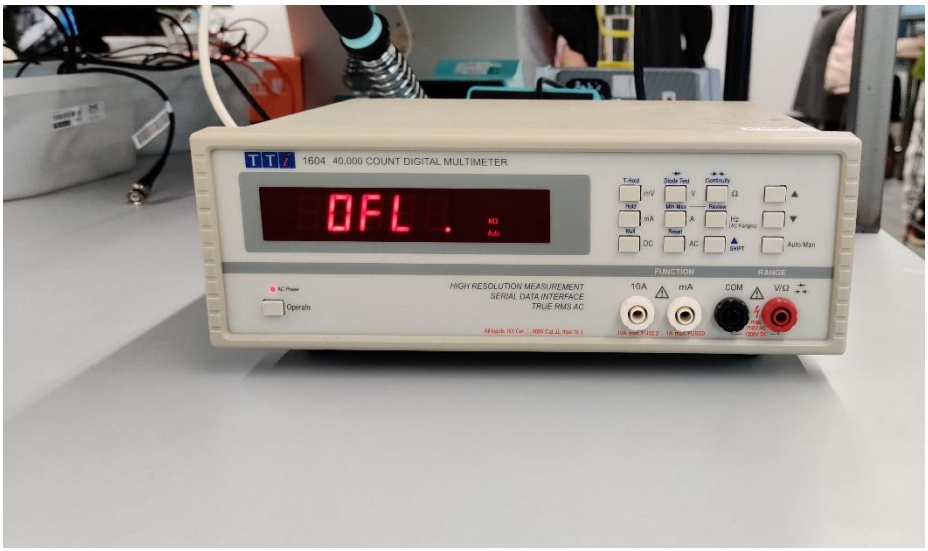

Figure 3.9: Agilent TTi digital multi-metre.

3.6 Mechanical testing

The Instron 3367 machine shown in Figure 3.10 was used to test the mechanical behaviour of the materials. It was utilised to evaluate the elasticity of the materials, tensile strength, compression and examine the fracture properties at which tensile strain the materials break. Specimens used were of the extruded filaments with lengths of 40 mm and diameter of 1.75 mm and the 3D printed samples throughout this work. The 3D printed samples' gauge length was 20mm; the width was 5mm and thickness 1mm.

Figure 3.10: Instron (tensile and pressure) machine.

3.7 Data acquisition

3.7.1 PicoLog 1000 series

PicoLog 1000 series is a portable universal serial bus (USB) multichannel data acquisition device which was purchased from (Pico Technology, UK) [180]. As shown in Figure 3.11a, it has 12 input channels and up to 4 output channels. The 12 input channels can be used for the data logging to acquire the data and register the values to a computer through the PicoLog software. The output channels can be used to supply a voltage of up to 2.5 Volts. It has a 10-bit resolution which means the data logger can detect a change in voltage as low as 2.4 mV from the supplied 2.5 V. It can acquire data at a sampling rate of up to 1 million samples per second. Furthermore, as shown in Figure 3.11b, an external terminal board was attached to the data logger. The external terminal board has screw terminals to allow the connection of wires without the need for soldering.

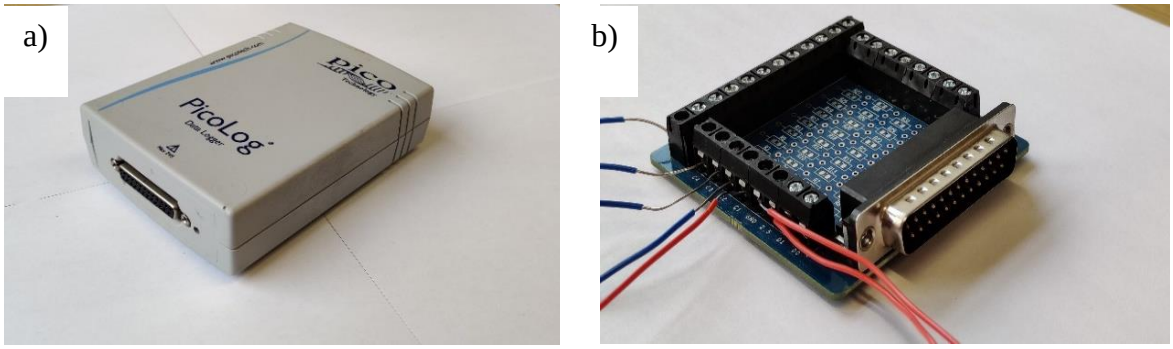

Figure 3.11: a) Image of PicoLogger 1000 series and b) Image of the external terminal board.

3.7.2 Breadboard

As shown in Figure 3.12a, a breadboard is a constructed rectangular base with a grid of holes that can build and connect electronic circuits. It was used to connect the data logger and the 3D printed samples by pushing electrical wires and other electronic components into the grid holes. The breadboard offers a solderless connection which eliminates the need to solder for easy adjustment of the wires.

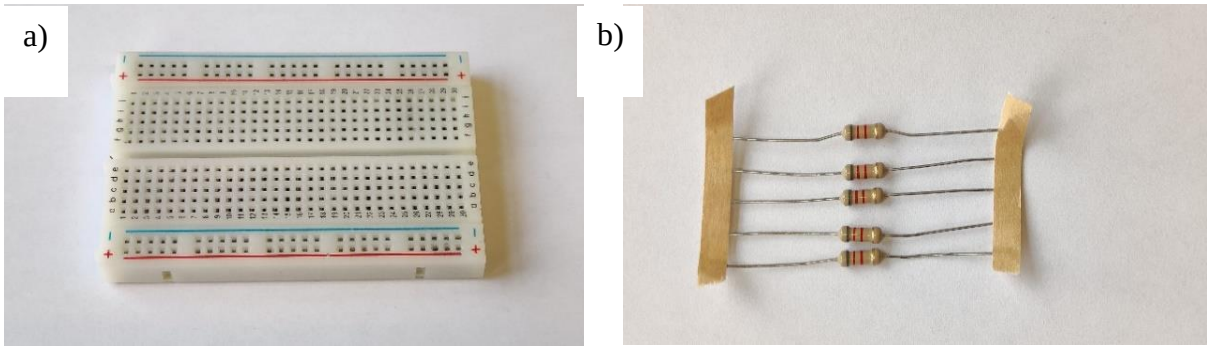

Figure 3.12: a) Image of the breadboard and b) Examples of the electrical resistors.

3.7.3 Electrical resistors

The electrical resistor is a passive two-terminal component illustrated in Figure 3.12b above. It controls the flow of the electrical current depending on the resistor's value, which is measured in ohms (Ω). Electrical resistance describes how much the material resists electrons' flow and can be measured using a digital multi-metre. It was used here as a constant element to construct the electrical circuits used in this research.

3.8 Electromechanical testing

In order to evaluate the electromechanical response of the 3D printed samples, the samples were first wired, and silver coated at the 2 ends to reduce the contact resistance to the probes. The samples were then connected to a PicoLog Data Logger with a supply of constant input

voltage of 2.5 V. A voltage divider circuit was designed as shown in Figure 3.13 below, and with corresponding Equation (3.1) expressed as:

$$V_{out} = V_{in} \times \frac{R_2}{R_2+R_1} \tag{3.1}$$

Where V_{in} is the constant voltage of 2.5V supplied from the data logger, R_1 is a constant resistor, R_2 is the 3D printed strain sensor.

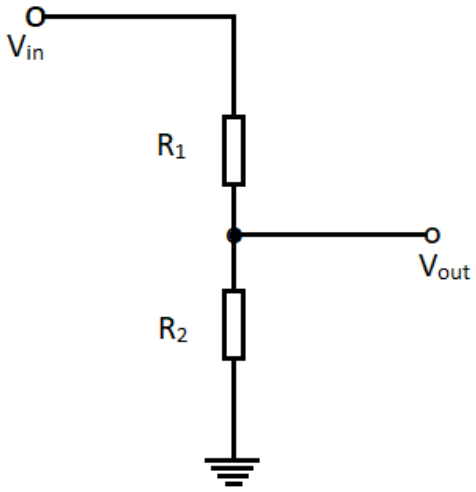

Figure 3.13: Voltage divider circuit.

Using a breadboard as shown in the schematic in Figure 3.14a, a resistor R_1 of 8 kΩ was connected in series with the 3D printed samples to form the voltage divider circuit. The node between the constant resistor and 3D printed sensor was connected to Channel 1 in the data logger to register the data of the output voltage V_{out}, illustrated in schematic form in Figure 3.14a. They were simultaneously attached to an Instron 3367 (Instron Ltd., Norwood, MA, USA) machine to perform the tensile test at a strain rate of 1 millimetre per second (mm/s), shown in Figure 3.14b. The voltage divider circuit was rearranged for R_2 (as the 3D printed sensor) to obtain the value of the 3D printed sensor and is expressed in Equation (3.2) as:

$$R_2 = R_1 \times \frac{V_{in}}{V_{out}-1} \tag{3.2}$$

Where R_2 represents 3D printed sensors, R_1 represents constant 8kΩ resistor, V_{in} is the input voltage, and V_{out} is the output voltage. The gauge factor which is defined as the ratio of the electrical resistance to the mechanical strain applied was utilised to evaluate the sensitivity of the sensors expressed in Equation (2.3).

a)

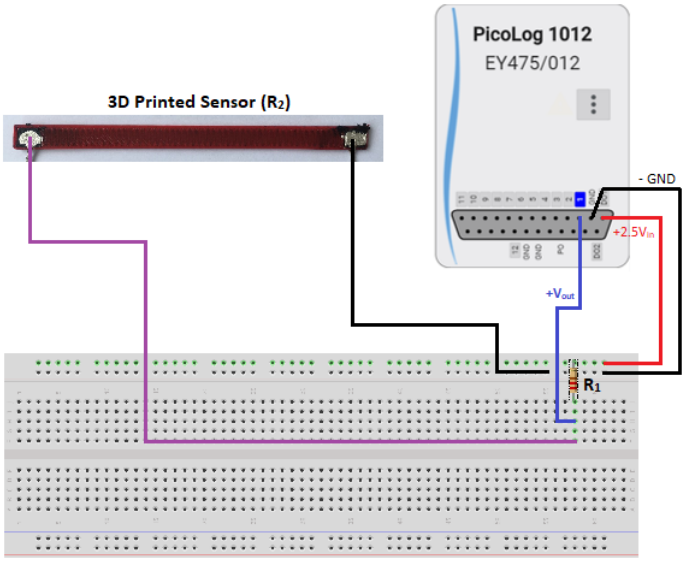

b)

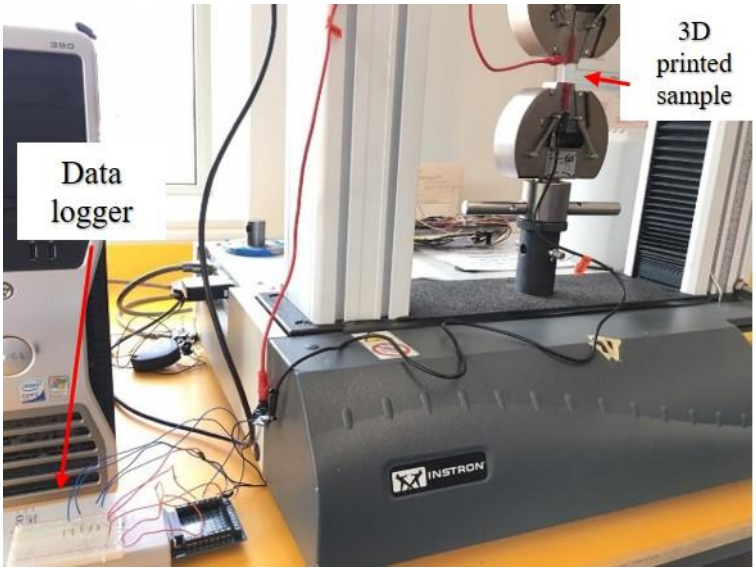

Figure 3.14: a) Schematic of data logging setup and b) Image of the calibration of the data logging setup to the Instron machine.

3.9 Arduino and servo motors

Servo motors were employed to provide finger movements of the 3D printed robotic hand. An Arduino Uno was used to power and programme the servo motors to perform coded movements.

Figure 3.15(a-b) shows an image of the Arduino Uno and a servo motor, respectively.

Figure 3.15c illustrates schematically an exemplar electrical wiring connection of a servo motor to the Arduino Uno to provide power from the 5V source and control of the servo motor from the Arduino Uno Digital pin [181].

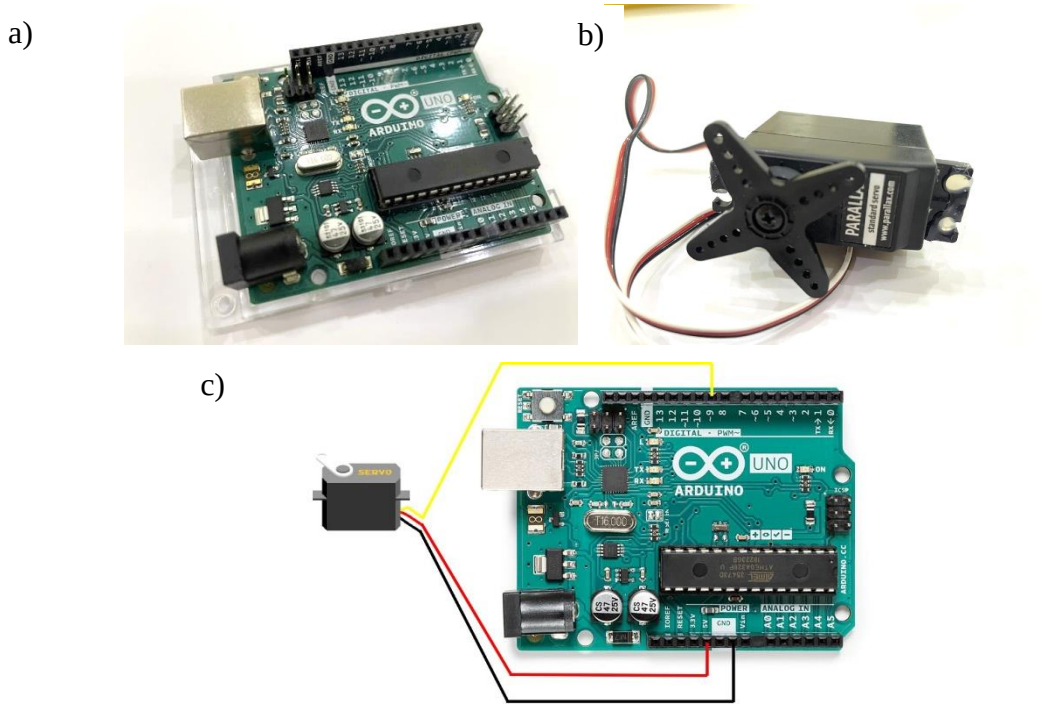

Figure 3.15: a) image of the Arduino Uno, b) Servo motor, and c) Schematic illustration of the wiring of the servo motor to the Arduino Uno to provide power and control.

3.10 Scanning electron microscopy (SEM)

SEM (SEM, FEI Quanta 3D FEG), shown in Figure 3.16 below, was used to characterise the surface morphology of the conductive materials and their composition. Samples were pre-dried without coating, and images were acquired at voltage operation of 5 kV, in high vacuum mode with a magnification of 60x, 67x, 2500x and 5000x. This procedure allowed us to examine the mixture of the conductive polymers by evaluating the surface profile of the composite materials.

Figure 3.16: Image of the scanning electron microscopy (SEM) instrument.

3.11 Optical microscopy

Optical microscopic images were taken using a Dino-Lite AD4113ZTL digital microscope, purchased from (Dino-Lite, UK) and shown in Figure 3.17a below [182]. It has a magnification capability of 20x-90x, long working distance ability and a resolution of 1.3 megapixels (1280x1024 pixels) with an adjustable polarizer to avoid glare on the surface of the samples. It was attached to a personal computer (PC) using a dedicated Dino Capture software to acquire the images with the setup shown in Figure 3.17b. Throughout this work, it was used to characterise the structure of the 3D printed samples and the behaviour of the conductive material during compression and tensile testing.

a) b)

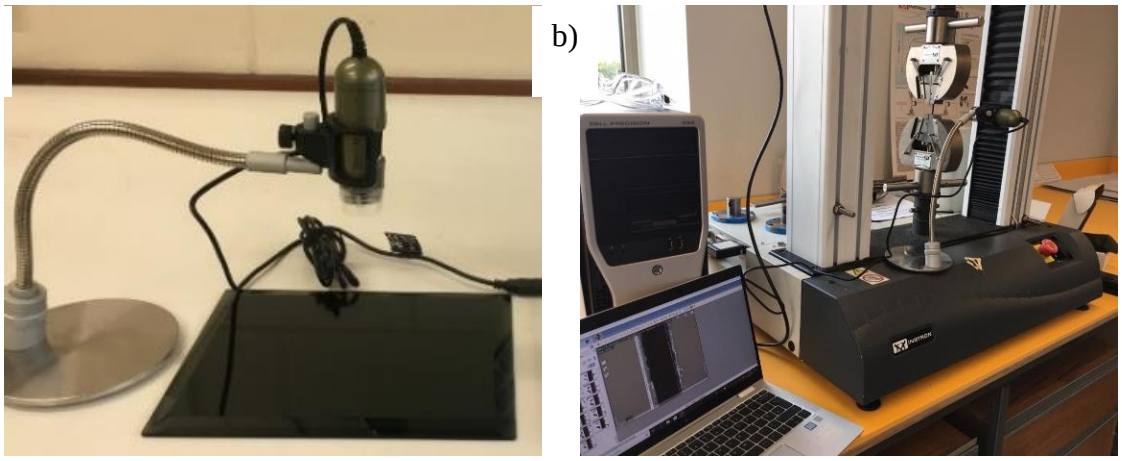

Figure 3.17: a) Image of the optical microscope and b) Image of the optical microscope setup with the Instron machine.

Chapter 4– 3D Printing of multi-material composite filaments

4.1 Introduction

This chapter aims to establish the digital platform and materials necessary for the multi-material fabrication of wearable soft electronics. It introduces an experimental method of multi-material FDM 3D printing technology. Prior to 3D printing, pellets of conductive polymers were first prepared for the sensing materials via a filament maker extruder. To investigate the 3D printability of prepared materials, a combination of conductive filaments with an encapsulate substrate were simultaneously 3D printed using a dual extrusion 3D printer. The electrical and mechanical properties of the 3D printed samples were further explored throughout. The focus of this chapter is to explore the compliance of these flexible conductive materials and their viability in 3D printing, specifically here in FDM. We further investigated the feasibility of these conductive polymer composites for their potential in sensing small and large strain deformations.

4.2 Filament preparation

Pellets of CNTTPU, CBTPU and GPLA were firstly prepared for use as conductive element materials using filament maker extruder. Before using the filament extrusion, the pellets were dried at 70 °C overnight before any melt processing using a material dryer. The materials were weighed using the digital scale where 25 grams of each of the conductive materials, CNTTPU, CBTPU and GPLA were prepared. It was essential to measure the weight of each material to compare it with the final batches of the extruded filament. After that, each material was melt-processed and extruded at 170 °C, using the single-screw filament extruder (Noztek) with a 1.75 mm nozzle, as shown in Figure 4.1a. A 1.75 mm nozzle was used since it was the compatible size of filament diameter for the 3D printer used in this research. Between the filament extrusions of each material, the filament maker's nozzle was unscrewed, and the inner side of the barrel was cleaned using isopropyl alcohol to ensure there was no residue from the previous material. The resulting filament measured 1.75mm (±0.04 mm) in diameter, and batches of the filaments extruded were wound manually to filament spools, as shown in Figure 4.1b. A pure thermoplastic polyurethane elastomers TPU namely NinjaFlex^{TM} was used as the encapsulating substrate without any modification.

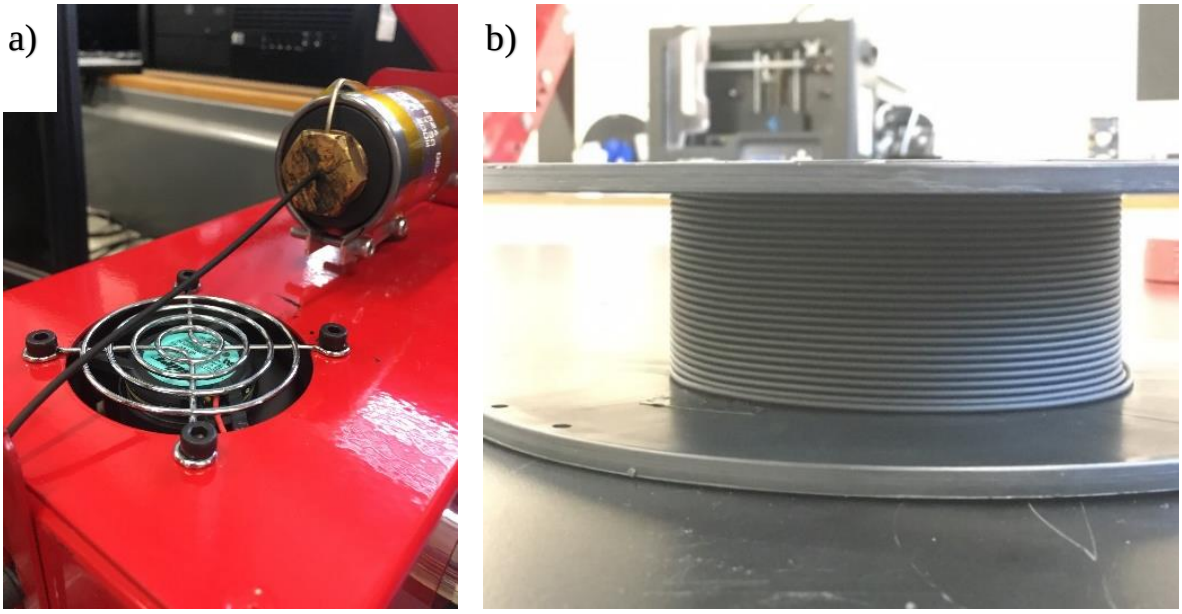

Figure 4.1: Image of a) Filament maker extrusion process and b) Extruded 3D printing filament wound in a spool.

4.3 Physical properties of the filaments

4.3.1 Electrical conductivity

Strands of the extruded CNTTPU, CBTPU and GPLA conductive filaments were prepared. Five samples from each of the filaments were measured and cut to a length of 40 mm. The samples were coated in the silver paste at the 2 ends of the strands before measuring the electrical conductivity to ensure an electrical connection to the digital multi-metre. An Agilent TTi 1604, a 4000-count digital multi-metre was used to measure the electrical conductivity samples.

As shown in Figure 4.2, the samples' conductivity differs due to the type of carbon material and content of the polymer matrix. Although the CBTPU has carbon black content as high as 30 wt.%, it was well established in the literature that the spherical dimensionality structure of carbon black reduces electrical conductivity. This is why the percolation threshold of carbon black was higher than that of the carbon nanotubes and graphene. Graphene polylactic acid had the highest conductivity due to the high aspect ratio of graphene. In addition, GPLA had graphene nanomaterial content of 16 wt.%, which was higher than the carbon nanotube content in CNTTPU of 10 wt.% according to the materials' datasheets.

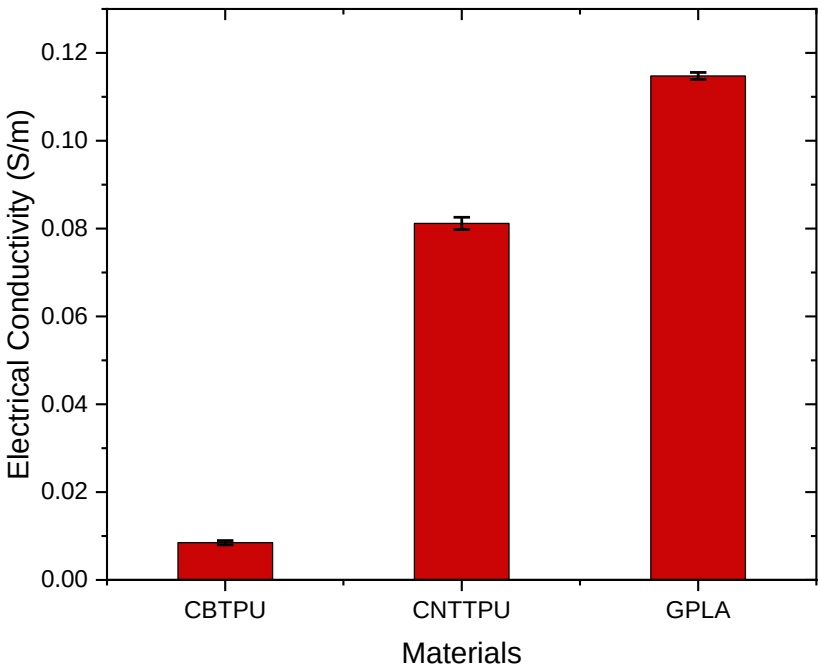

Figure 4.2: Electrical conductivity of extruded 3D printing conductive filaments.

4.3.2 Strain at break

Strands of the CNTTPU, CBTPU and GPLA filaments were subjected to mechanical testing to explore their mechanical behaviour using the Instron machine. Five samples of each of the filaments were measured and cut to lengths of 40 mm with a diameter of 1.75 mm each. The 3 conductive materials were also compared with 5 samples with the same dimensions of the encapsulate pure TPU, namely NinjaFlex.

A tensile strain was performed on all the materials, and the strain at break for each was obtained, see Figure 4.3a. TPU based materials showed a significant strain capability, breaking at strains above 300%. On the other hand, GPLA showed a brittle behaviour breaking at strains as low as 2%. This fragility was mainly due to the rigid polylactic acid PLA based polymer. Figure 4.3b shows the average strain at break values, demonstrating a relatively small standard deviation error.

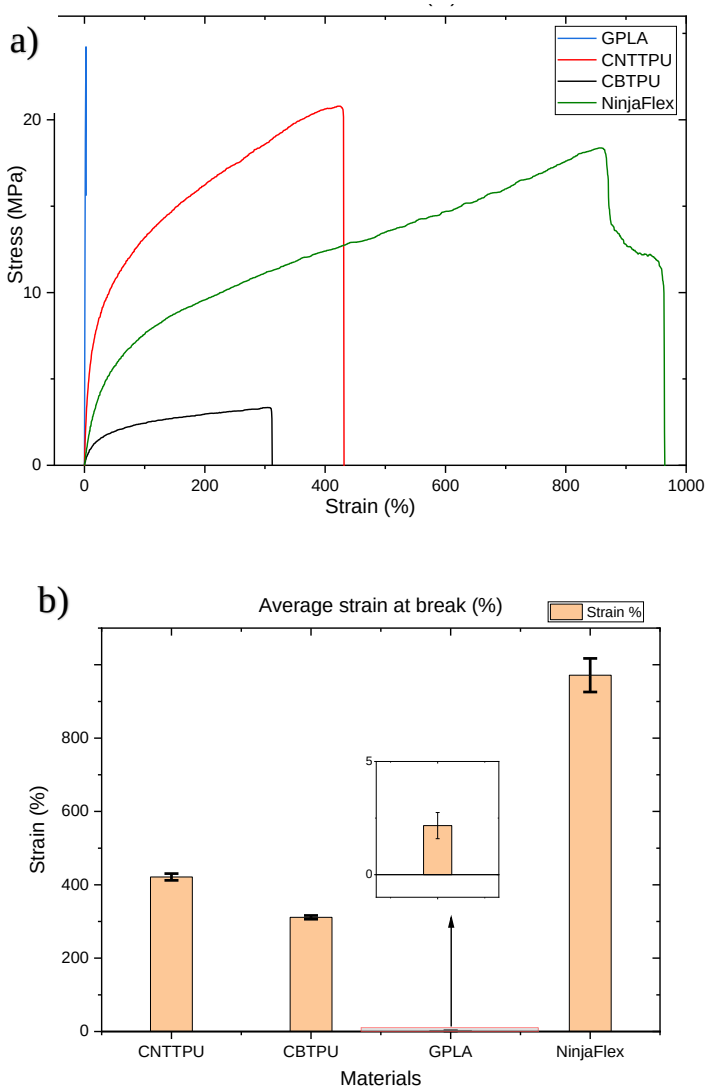

Figure 4.3: a) Stress-strain curve showing maximum values of strain at break. b) Comparison of average values of strain at break (inset magnifies GPLA bar).

4.3.3 Tensile strength

The tensile strength measures the maximum stress materials can withstand when elongated. It can be acquired from the tensile stress-strain curve. It has been observed that stretchable materials often with tensile strain larger than 100%, which here were TPU filaments, deform elastically until breaking and do not exhibit yield point. The stretchable materials' elasticity was further explored by obtaining the tensile stress at 50% and 100% of the stress-strain curves shown in Figure 4.4. The tensile strength values were summarised in Table 4.1. GPLA had the highest tensile strength value due to the rigidity inherited from the PLA's base material compared to elastomers TPU based materials. CNTPU had the highest tensile strength of the TPU based materials due to the high aspect ratio of the carbon nanotube filler. CBTPU had the

lowest tensile strength noticeably due to the spherical dimensionality of carbon black and the use of a base TPU with higher soft segment content.

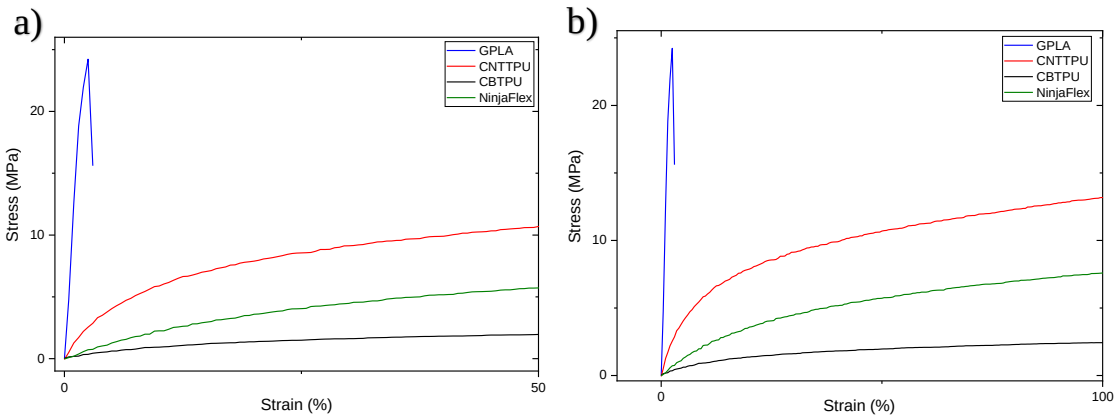

Figure 4.4: Stress-strain behaviour of the materials at a) 50% strain and b) 100% strain.

4.3.4 Young's modulus

Young's modulus measures the stiffness of materials in the stress-strain curve's linear state at low deformation. The higher the Young's modulus value, the stiffer and less elastic the material becomes. Young's modulus was calculated by taking a secant value between strain levels of 0.05%-0.25% based on the International Organization for Standardization (ISO), ISO 527 standard and the measured values were summarised in Table 4.1 and Figure 4.5 [102]. CBTPU exhibited high elasticity with a Young's modulus value as low as 13 MPa. NinjaFlex was also highly elastic with a value of 29 MPa. However, CNTPU was shown to be the least elastic TPU based material reaching a Young's modulus value of just over 100 MPa. On the other hand, GPLA was highly stiff compared to the TPU based materials reaching a Young's modulus close to 1 GPa.

Table 4.1: Average tensile strength, stress and Young's modulus values of 3D printing filaments.

	Tensile Strength (MPa)	Tensile Stress at 50% (MPa)	Tensile Stress at 100% (MPa)	Young's Modulus (MPa)
CNTTPU	21	11.2	13.6	104
CBTPU	3.3	1.96	2.45	14.3
GPLA	24	-	-	1024
NinjaFlex	20.4	5.7	7.6	25.6

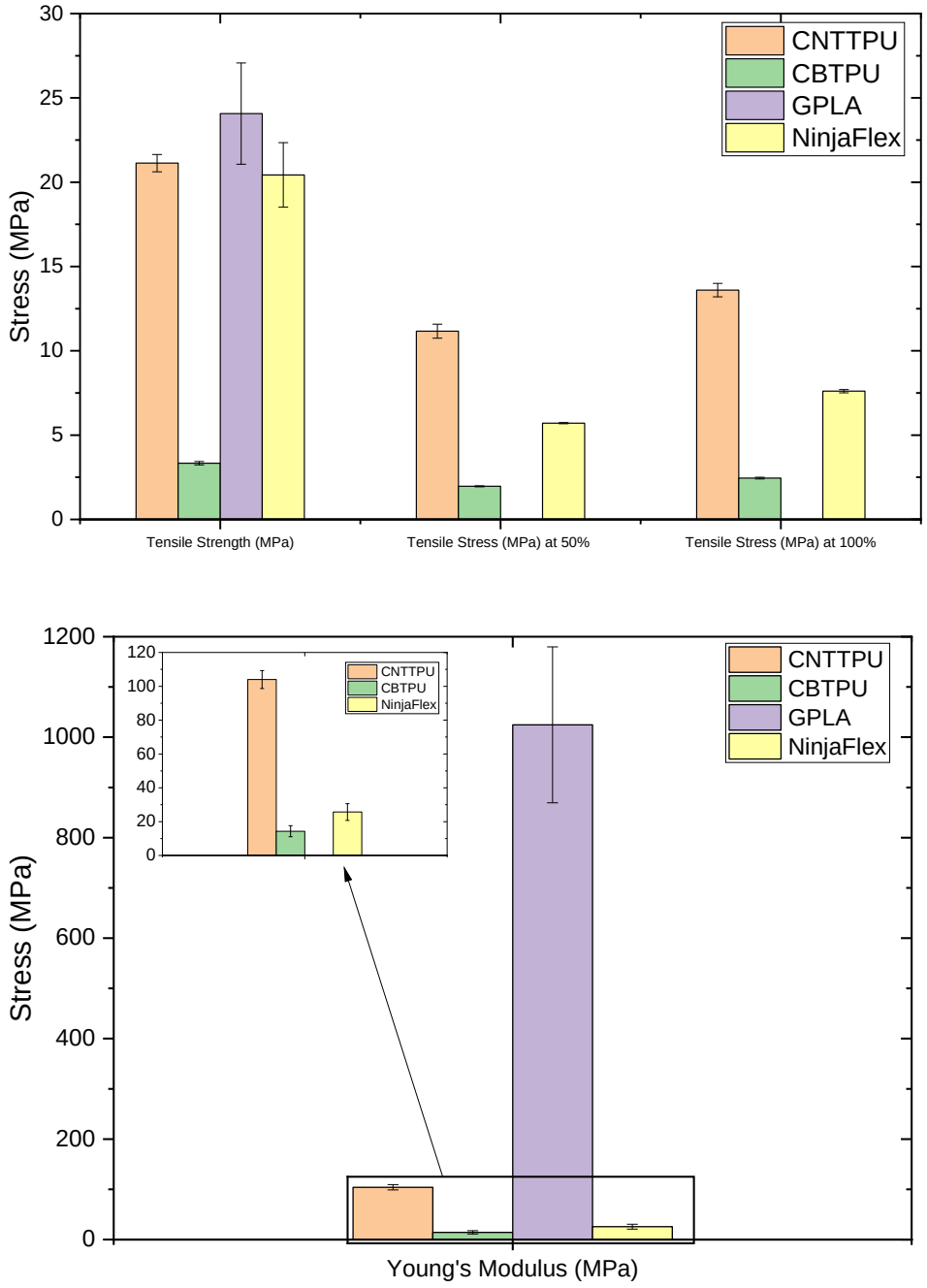

Figure 4.5: a) Average theoretical tensile strength and tensile stress at 50&100% strain, and b) Average theoretical Young's modulus (inset magnifies samples with low Young's modulus values).

4.4 3D printability of the materials

4.4.1 Flexible filament printing

It was observed that during the preparation process of 3D printing, the 3D printer's extruder was designed for rigid materials (i.e. PLA and ABS). Since most of the materials in this research were flexible materials, it was noticed that soft materials block between the drive gears of the extruder and the heated nozzle. The reason for this was a gap between the filament drive

gears and the hot end. This gap caused the soft materials to find the least resistant area, which caused the filament to clog, as illustrated in Figure 4.6a.

In an attempt to overcome the problem, the extruder was replaced with a flexion extruder system as this ensures an enclosed area between the drive gear and the hot end and is suitable for rigid and flexible materials. It has a dial from 1-4 to specify the desired pressure depending on the material deposited. This dial controls the amount of pressure that the gear's roller compresses on the guided filament. Figure 4.6b below shows the fitted extruder, which has an enclosed path for the 3D printable filaments to travel from the drive gear to the hot end.

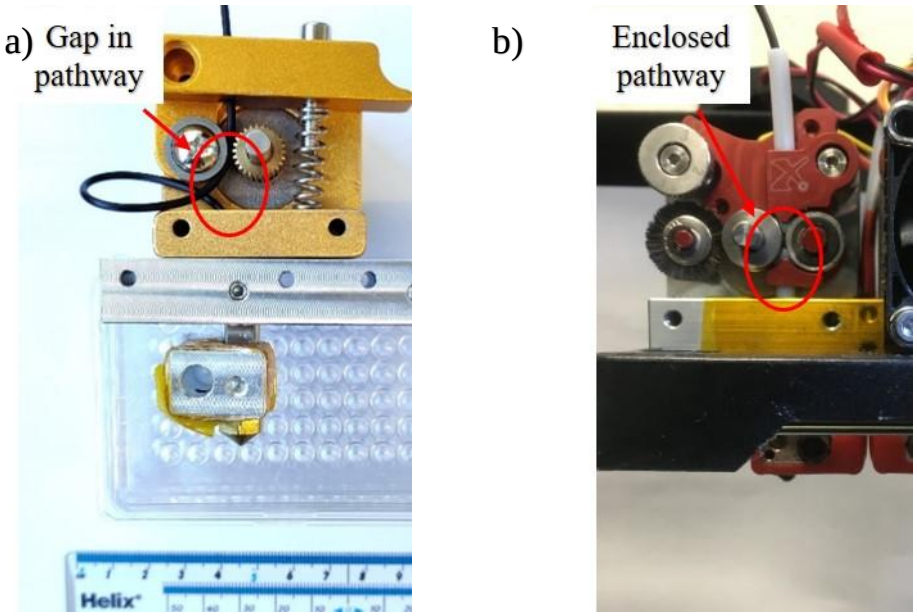

Figure 4.6: a) Default extruder designed for rigid materials with the apparent gap between drive gear and hot end. b) Replacement of Flexion extruder with enclosed path to the hot end fitted to the printer.

4.4.2 Filament loading

Before the 3D printing process, each filament must be loaded to the extruder to test its viability for 3D printing. The loading process shows if the materials can be driven through the printer's motor drive gear and subsequently can exit the hot end via the hot nozzles. The hot end temperature was set to the recommended 230 °C for the 4 materials demonstrated in Table 4.2 below and experimented with 3 nozzle sizes. The 3 nozzles were tested for the 3 conductive and the NinjaFlex filaments, and Table 4.2 below shows if tested materials were able to load through the nozzles or not. Due to its highest elasticity, CBTPU was loaded only via the largest 0.8 mm nozzle tip.

Table 4.2: Filament loading test through various nozzle sizes.

Nozzle Diameter / Filament Type	0.5 mm	0.6 mm	0.8 mm
CNTTPU	No	Yes	Yes
CBTPU	No	No	Yes
GPLA	Yes	Yes	Yes
NinjaFlex	Yes	Yes	Yes

Figure 4.7 shows the conductive filaments while loading through a 0.8 mm nozzle and the NinjaFlex loading through the second extruder with a 0.6 mm nozzle. It was possible to load GPLA in all the nozzles due to its rigidity which allowed the filament to be easily driven to the hot nozzle. NinjaFlex could also be loaded through all the nozzles because of its pure TPU elastomer, which has no carbon filler content. However, CNTTPU is relatively stiff, which suggests that the morphology of the carbon nanotubes prevented the filament from being loaded through the small 0.5 mm nozzle tip. It was also found that CBTPU was only extruded through a 0.8 mm in diameter nozzle tip due to its high elasticity and high carbon black content, indicating that even with the Flexion extruder, the high content of carbon black might only allow the load through a nozzle with a large diameter.

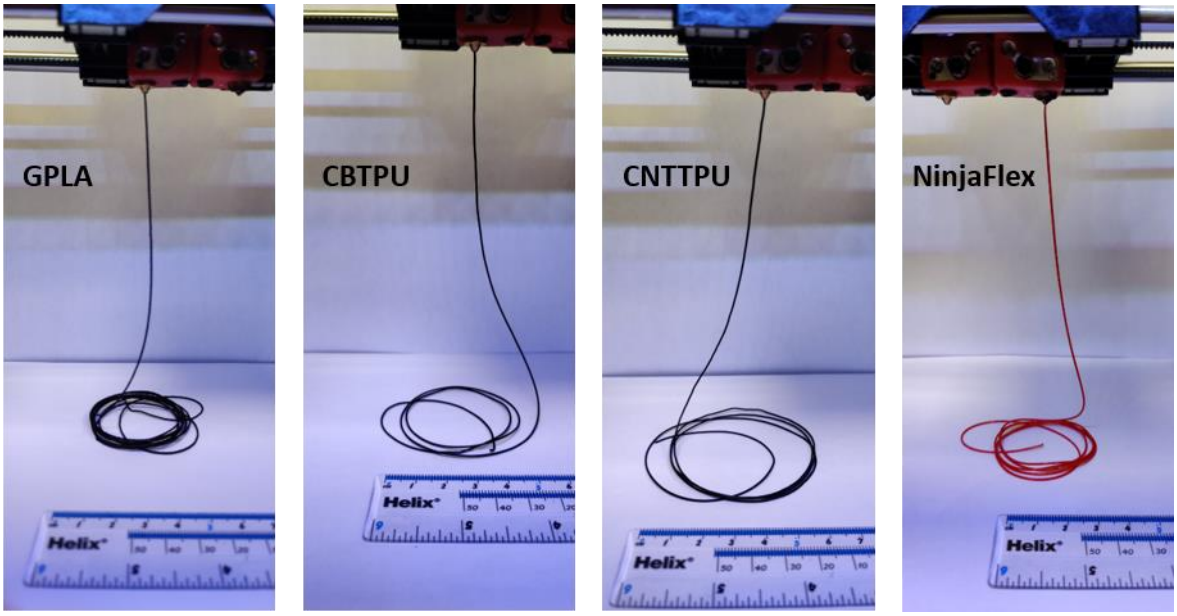

Figure 4.7: Images of the loading process of filaments through the 3D printer's hot nozzles.

4.4.3 Flow rate

The flow rate defines the filament amount that the motor extruder drives to the hot end during 3D printing. This rate is determined by the number of steps per millimetre that the motor extruder pushes the filament through the heated nozzle. Under and over, extrusions were controlled by the value of the extrusion multiplier to be below or over 1, respectively. In the software, setting the extrusion multiplier below 1 makes the 3D printed lines thinner whereas, setting it higher than 1 causes the lines to thicken, as illustrated schematically in Figure 4.8.

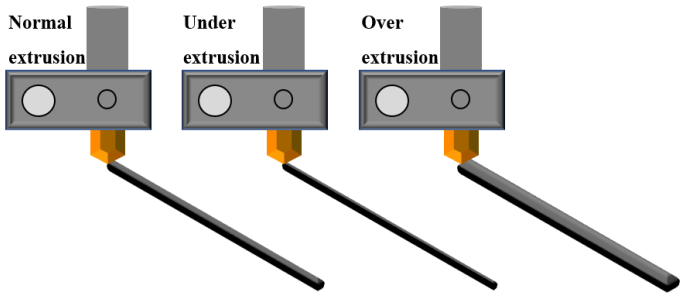

Figure 4.8: Schematic representation of normal, under and over extrusions of filament through the hot nozzle.

Examples were 3D printed to illustrate the result of various extrusion multiplier values. Using a 0.5 mm nozzle and setting the multiplier value to 0.8, 1, and 1.2 resulted in the line width variants of a 3D printed GPLA filament shown in Figure 4.9a-c, respectively.

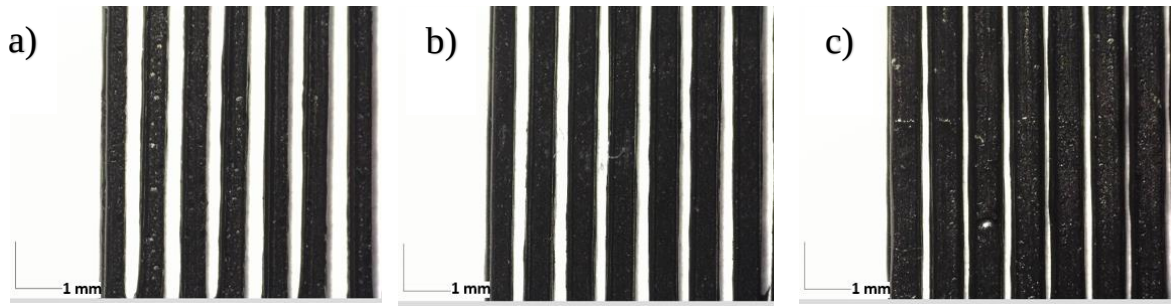

Figure 4.9: Optical microscopic images of extrusion multiplier values of a) 0.8, b) 1, and c) 1.2.

4.5 3D printing of multi-material samples

4.5.1 CAD designs

The designs were prepared using CAD software called PTC Creo Parametric 3.0. Each 3D printed sample was composed of electrically conductive sensing filament encapsulated within an elastomer substrate (i.e. embedded within an insulative TPU). Two designs were prepared for the conductive models; one was the straight lines used for the TPU based stretchable conductive filaments shown in Figure 4.10a with associated measurements. The second design was a meander structure, which had 90° of orientation as illustrated in Figure 4.10b and was

used for the rigid GPLA conductive filament. The substrate shown in Figure 4.10c had a total length of 40 mm, a width of 5 mm, and 1 mm thickness. It was designed for the conductive material to be embedded inside the encapsulate substrate. As further illustrated in Figure 4.10d, the substrate had a cavity inside that allowed the conductive model to be merged in the substrate during the 3D printing process.

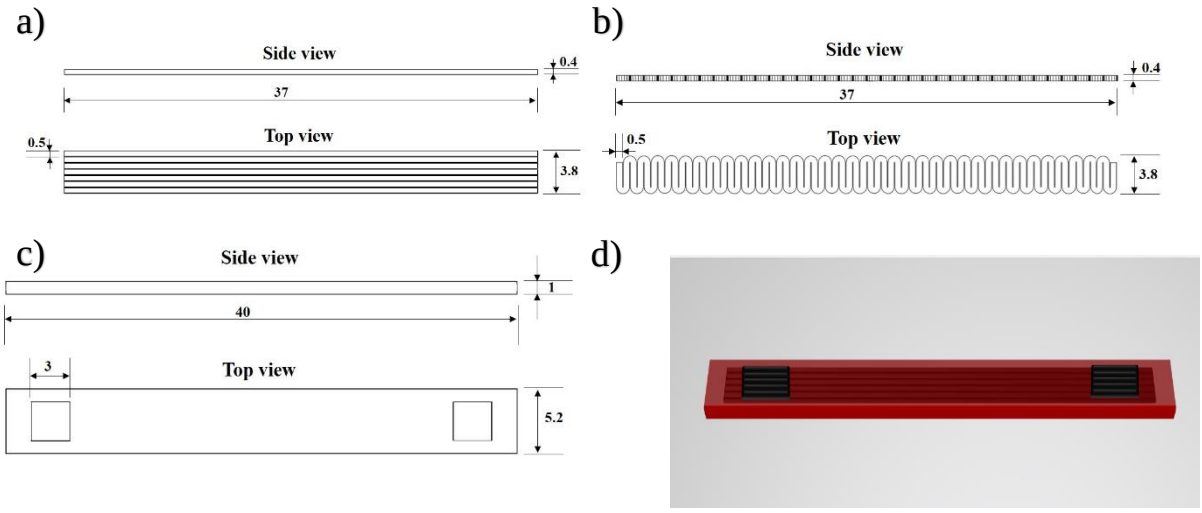

Figure 4.10: 3D models of a) Strain lines of conductive traces. b) meander lines with 90˚ of orientation, c) Substrate model with cavity inside that allows the conductive model to be merged, and d) Schematic example of straight lines (black) embedded inside insulative substrate (red)

4.5.2 Dual extrusion 3D printing process results

The fabrication of the samples was based on simultaneous fused deposition modelling FDM 3D printing process. Firstly, stereolithography STL files of 3D models were exported to slicer software. The STL files of the substrate and the conductive filament models were merged, and each of the materials was assigned to an extruder. The values of 3D printing parameters used in this work were summarised in Table 3.1.

The multi-material platform enabled the fabrication of the samples using the 3D printer. The right extruder was assigned for 3D printing the conductive filaments, and the left one was for the encapsulate insulative substrate. The process illustrated schematically in Figure 4.11 follows the Gcode pattern generated in the software alternating between the 2 materials to construct the 3D samples of the models.

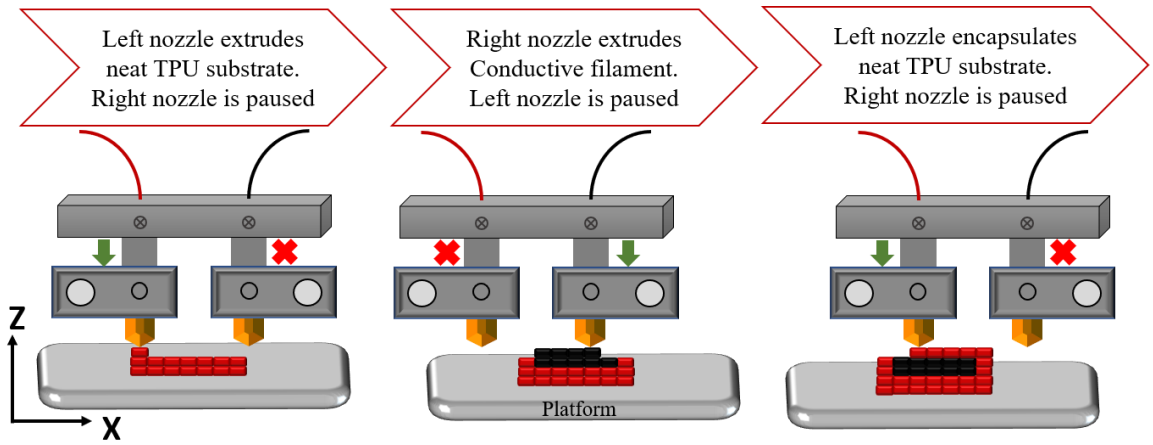

Figure 4.11: Schematic illustration of the dual extrusion 3D printing process, which deposit materials by alternating between 2 independent extruders.

Using the 3D slicing software, Figure 4.12a shows the merged CAD models of conductive material (grey) and substrate material (red) converted into a series of discrete coordinate positions sliced layer by layer. These settings were then exported to an SD card as Gcode files in which the 3D printer can read. Figure 4.12b shows an image of dual materials 3D printing in progress. An exemplar sample shown in Figure 4.12c was wired with electrical wires and silver coated using a silver paste at the 2 ends, as shown in Figure 4.12d, to reduce the contact resistance to the probes for electrical testing.

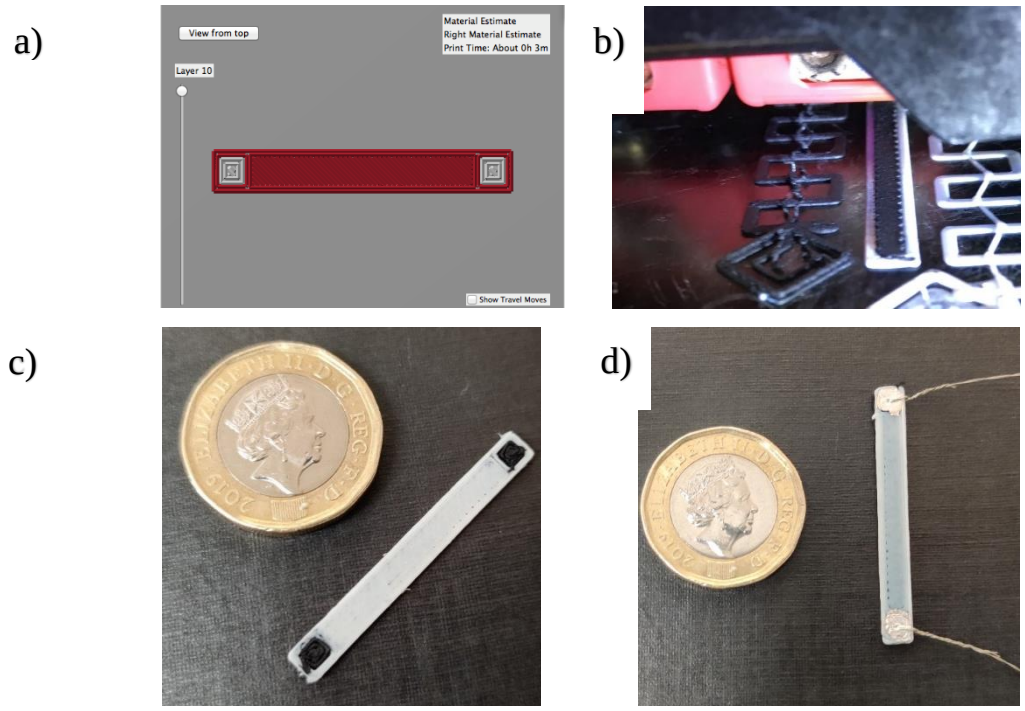

Figure 4.12: a) Image of the 3D merged model converted into layers for 3D printing process, b) Image of the dual extrusion 3D printing process in action, c) Image of 3D printed sample as off the printer and d) 3D printed sample wired and silver coated.

4.6 Mechanical testing of 3D printed samples

4.6.1 Stress-strain behaviour

The 3D multi-material printed samples were subject to initial uniaxial tensile tests. The 3D printed samples' gauge length was 20mm; the width was 5mm and thickness 1mm. The tensile strength was acquired, and the stress-strain curves of 18 samples were obtained.

Figure 4.13 and Figure 4.14 show the stress-strain behaviour of the CBTPU and CNTTPU over the initial 10 cycles at 50% and 100% of tensile strain, respectively. Both strain amplitudes were acquired from fresh samples for each strain to investigate the effect of higher strain magnitude on the stress-strain curve of the samples. The loading curve in the first cycle of both CBTPU and CNTTPU showed stiffer behaviour than the following cycles.

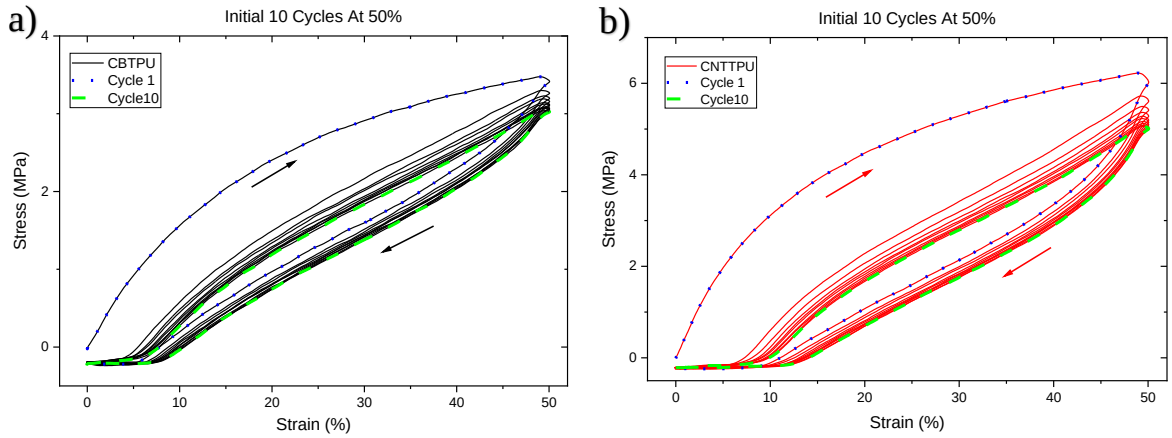

Figure 4.13: Stress-strain curve of 10 Cycles stretched at 50% of a) CBTPU and b) CNTTPU.

TPU based materials composed of hard and soft segments, which under tensile strain exhibit noticeable softening. Stress from the applied strain causes strain softening, which is attributed to the rearrangement and breakage of the elastomer polymer hard and soft segment. This was proportional to the value of strain, as a higher strain caused more breakages to the polymer chains and hence caused more strain softening, as shown in Figure 4.14b at 100% strain. It can be noticed that strain softening appeared mainly in the first few cycles before reaching a state of equilibrium.

The applied strain caused rearrangement and breakage of elastomer molecular chains known as strain softening. This phenomenon occurring in the elastomer is referred to as the “Mullins’ effect”, named after Mullins due to his comprehensive study on filled and unfilled elastomers [8]. The Mullin’s effect explains that elastomer softening was due to the irreversible rearrangement of the molecular network during tensile strains deformation. From the 1st-10th

cycle, a downward shift of the stress-strain curve was observed. After the first few cycles (4 cycles), the Mullin's effect saturated the stress-strain curve, and the samples reached an equilibrium that indicated the cyclic pre straining's viability to minimise the softening and Mullin's effect.

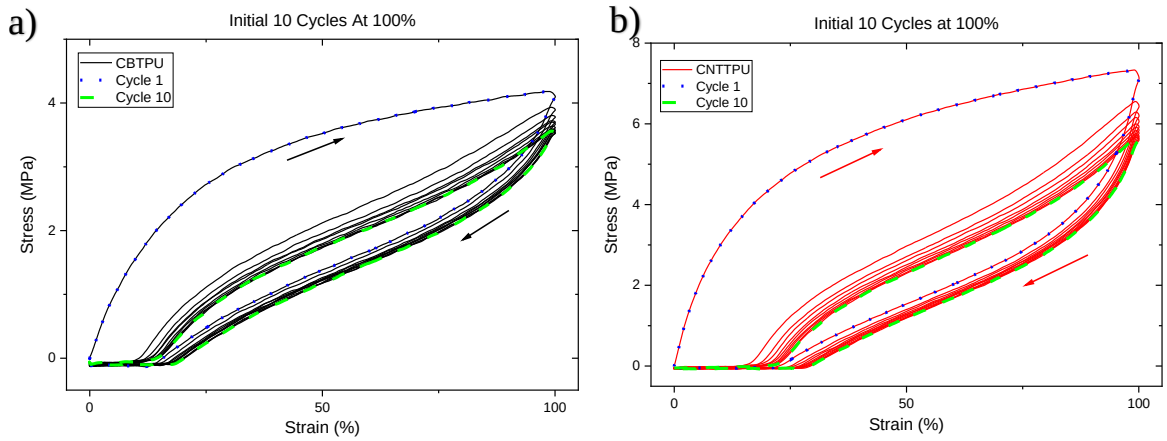

Figure 4.14: Stress-strain curve of 10 cycles stretched at 100% of a) CBTPU and b) CNTTPU.

4.6.2 Effect of carbon nanofillers on the stress-strain behaviour

As shown in Figure 4.15, there was a noticeable difference between the first cycles of CNTTPU and CBTPU. The existence of stiff carbon-based fillers magnifies the amplitude of strain on the host elastomer's soft segment. In this case, greater deformation occurred on the soft segment of the TPU to accommodate the applied strain, which had little effect on deforming carbon-based nano contents. The influence of the stiffer CNTTPU on the mechanical behaviour in comparison with CBTPU can be seen in the 1st and 10th cycles of strain amplitude of 50% and 100%, as shown in Figure 4.15(a-b) respectively. The higher stiffness in the CNTTPU stress curve was influenced by its higher Young's modulus and tensile strength.

Furthermore, all the samples showed the softening effect in the 10th cycles; however, greater stiffness in the CNTTPU samples could still be observed. It can be noticed that the unloading paths showed significant hysteresis behaviour with noticeable residual strain. The higher level of stiffness in the CNTTPU loading resulted in a higher value of residual strain than in the CBTPU, as shown in the stress curve upon unloading in Figure 4.15.

It can be observed that the stress-strain behaviour normalised to steady cyclic stress to subjected strain in the 10th cycle, as demonstrated in Figure 4.13 and Figure 4.14 above. It was noticed that the loading and unloading behaviour tended to stabilise as most of the softening effect occurred in the 1st cycle. This stabilisation highlights the importance of pre-straining the

samples to ensure the stress-strain curve is stabilised, which is confirmed by the literature [104].

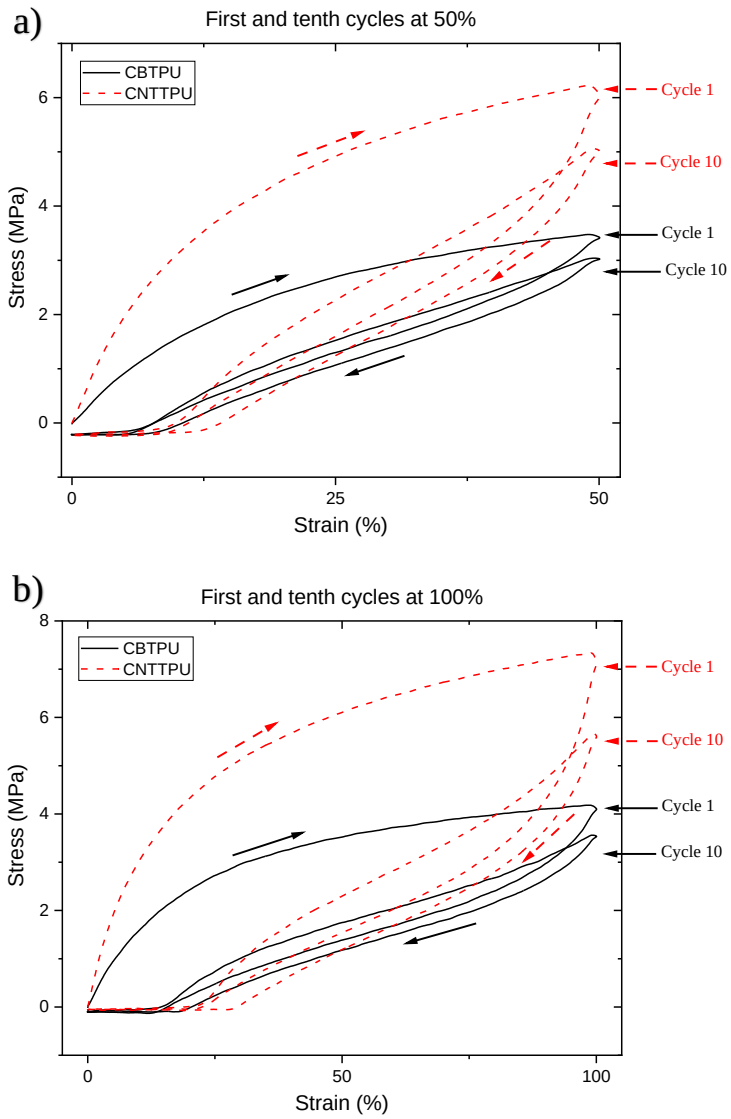

Figure 4.15: Comparative stress-strain curves of 1st and 10th cycles of both CBTPU and CNTTPU stretched at a) 50% strain and b) 100% strain.

4.7 Electrical testing

4.7.1 Electrical response of initial strain cycle

Carbon-filled elastomers exhibit piezoresistive behaviour upon mechanical strain deformation. This deformation increases or decreases the gaps and contacts of the carbon nanofillers in the elastomer matrix leading to an overall increase or decrease in the electrical resistance. This dynamic change in electrical resistance upon applied strain was studied for the 3D printed samples to evaluate their potential as strain sensors. The PicoLog data logger was used here for

recording the electrical resistance change and was coupled synchronously with the mechanical stress-strain cyclic loading.

The change in electrical resistance was simultaneously measured during the initial strain of CBTPU and CNTTPU samples at 50% and 100% strain amplitudes, as illustrated in Figure 4.16(a-b), respectively. The corresponding initial change in electrical resistance increased linearly with increasing the strain for all samples, which agrees with previous reports [18], [67], [79], [98]. This increase was mainly caused by the breakdown in the carbon nanotube and carbon black network structures in the CNTTPU and CBTPU samples.

The change in electrical resistance in CNTTPU samples in the initial strain loading was noticeably higher than in the CBTPU of both 50% and 100% strain amplitudes. One reason could be that the CBTPU had a carbon black content of 30wt.% (as purchased), which was higher than the carbon nanotube content of 10 wt.% in the CNTTPU samples. The higher content of the conductive filler in CBTPU meant a more stable conductive network in which the initial increase in electrical resistance was less than the change in CNTTPU. Thus, the conductive network in the CNTTPU was more straightforward to destruct than in the CBTPU, which resulted in a more significant change in electrical resistance. Whereas in CBTPU samples, the competition between destruction and reconstruction of the high content of conductive networks inside the polymer matrix caused a moderate change in electrical resistance in both strain amplitudes.

In addition, at 100% strain, as shown in Figure 4.16b, CNTTPU had a sharper change in electrical resistance than the lower strain value of 50%. This difference could be attributed to the increase in distance between the percolation network of the carbon nanotubes. Furthermore, with less CNT, the percolation network that governed the conductive network was upon a large deformation of 100% tensile strain [67], [100].

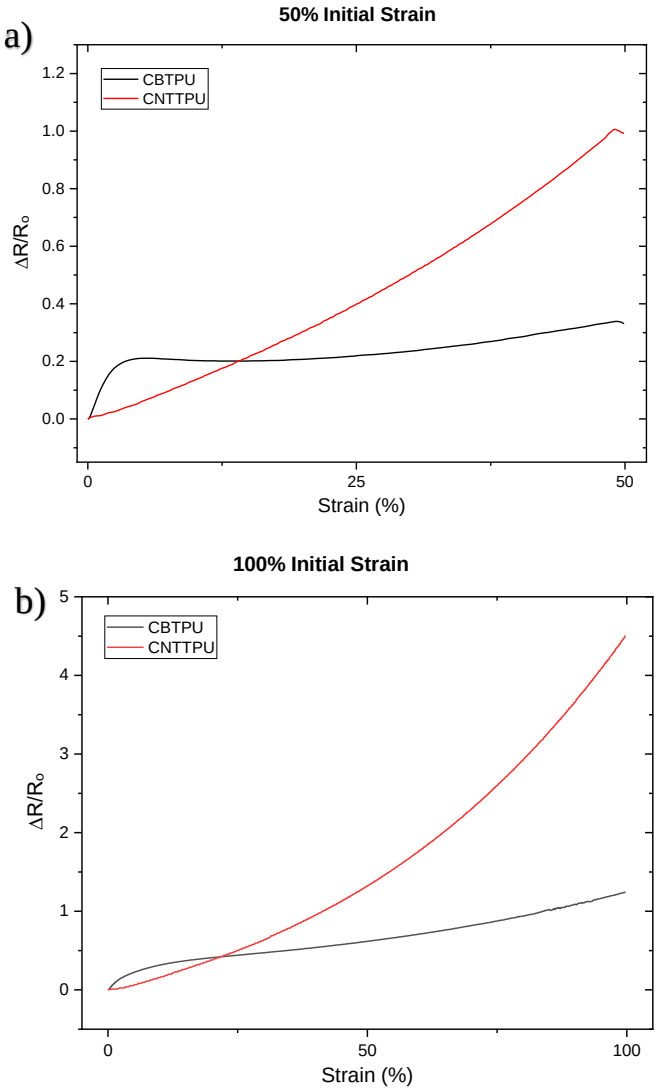

Figure 4.16: Change in electrical resistance of CBTPU and CNTTPU initially stretched at a) 50% of strain and b) 100% of strain.

Figure 4.17 shows the complete cycle of loading and unloading of the first cycle for CBTPU and CNTTPU at 50% and 100% strain amplitudes, respectively. Upon unloading, the electrical resistance values that the samples returned to were significantly higher than the values before strain. Permanent destruction of conductive paths caused non-recoverable residual of high electrical resistance. During the unloading process, a permanent increase in electrical resistance was observed in both samples. At 50% strain, the increase in electrical resistance upon unloading was relatively similar in CNTTPU and CBTPU. However, at 100% strain, the increase in CNTTPU was noticeably larger than in CBTPU. This increase was caused by the morphology of the carbon nanotubes that caused a non-recoverable aggregate upon unloading, which led to a higher increase in electrical resistance. At 100%, the higher value of tensile strain caused high destruction and a non-recoverable conductive network in CNTTPU.

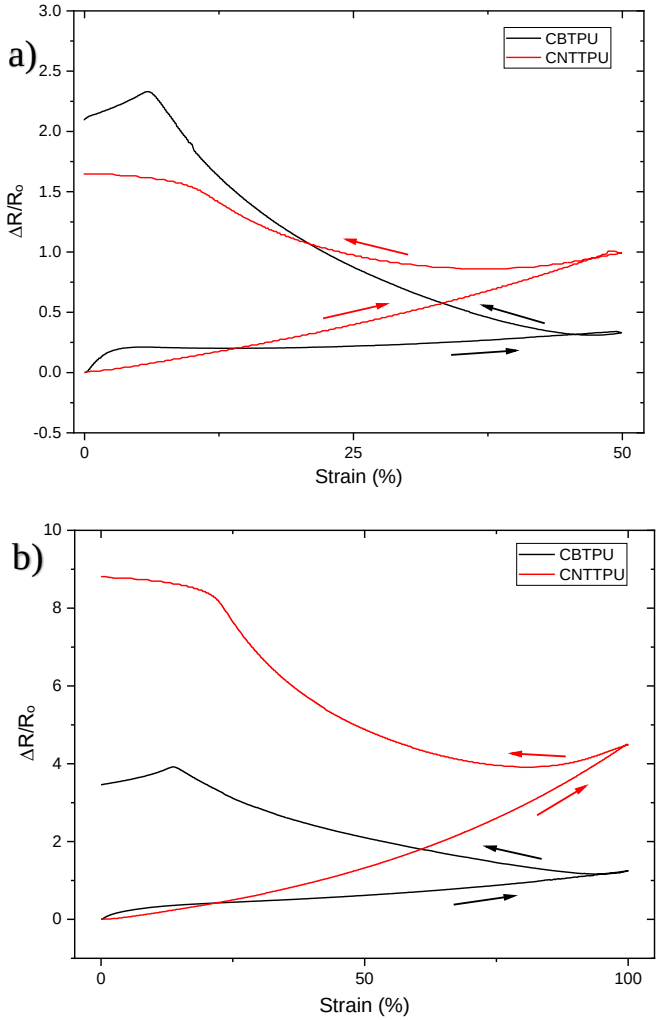

Figure 4.17: Change in electrical resistance of CBTPU and CNTTPU initial cycles stretched at a) 50% of strain and b) 100% of strain.

Another reason for the hysteresis behaviour was the apparent mechanical residual strain noticed in the mechanical unloading of the samples. The residual strain of the first cycle, experienced on the stress-strain curve, caused the non-recoverable initial value of electrical resistance in both CBTPU and CNTTPU samples. The CNTTPU had a higher residual strain which led to an increase in electrical resistance upon unloading. The microstructure of the carbon nanotubes in CNTTPU had a significantly greater aspect ratio of the spherical structure of the carbon black in CBTPU. This ratio resulted in further excluded areas in the CNTTPU due to less CNT content meaning there were fewer conductive paths within the elastomer matrix than in the CBTPU. The reduction in conductive paths could be one of the reasons for the large change in electrical resistance in the first loading in CNTTPU, according to the literature [8], [101]. Further indicating that the conductive networks within the elastomers reorganise during the

first loading-unloading cycle result from the mechanical strain and release of residual stresses [98].

Furthermore, the mechanical deformation of the samples also induced compressive strain perpendicular to the strain direction. As illustrated in Figure 4.18a, elastic polymers experience a negative compressive strain (lateral strain) in the transverse direction to axial strain (longitudinal strain), and this is referred to as Poisson's ratio [101], [183]. As demonstrated in Figure 4.18(b-e), when the CBTPU sample was stretched from 0-100% in the axial direction, the Poisson effect caused a compressive strain in the normal direction of the tensile strain axis apparent in the decrease in width in the CBTPU sample from 5.6 mm at 0% to 4.55 mm at 100%. Hence, the compressive strain in CNTTPU and CBTPU introduce new conductive paths, which in turn causes competition between destructed and newly constructed conductive pathways.

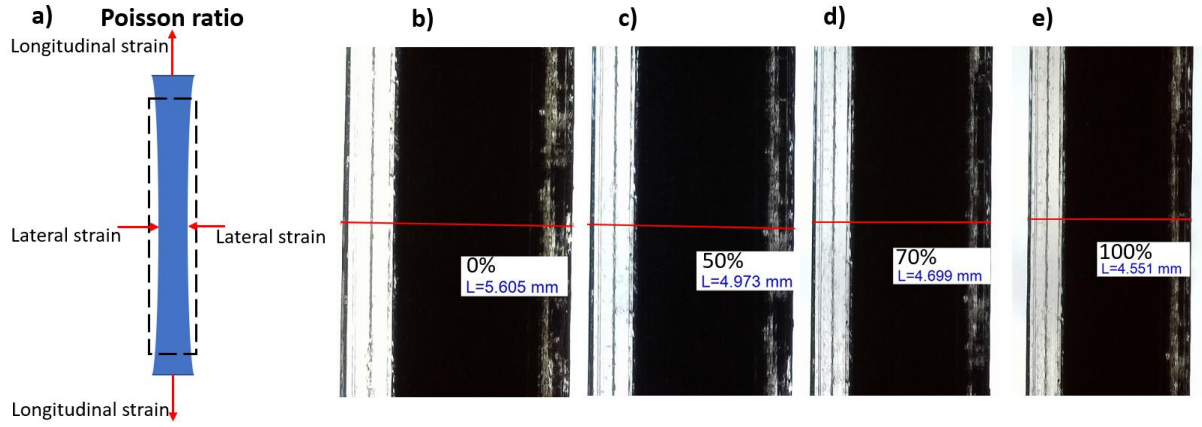

Figure 4.18: a) Schematic of Poisson's ratio effect and (b-e) illustration of the Poisson effect on the CBTPU sample upon tensile strain from 0-100%.

The deformation upon stretching also caused an increase in the distance between the carbon nanofillers inside the elastomer, which is referred to as the tunnelling effect [42], [69], [184]. This effect appears in carbon-filled elastomers where electrons move between neighbouring conductive particles separated by a very thin insulative polymer in the nanoscale. Upon stretching, the change in distance between neighbouring conductive particles causes an increase or decrease in electrical resistance. The destruction and increase in distance between conductive nanofillers led to hysteresis behaviour in the change of electrical resistance in both CNTTPU and CBTPU samples. The hysteresis effect of the polymer caused the non-recoverability of the initial electrical resistance value.

4.7.2 Electrical response of cyclic strain

The change in electrical resistance behaviour was further measured simultaneously as the samples were subject to cyclic strain. As explained previously, it was observed that the significant change in the mechanical and electrical behaviour during the first cycle was associated with the permanent rearrangement and breakage of polymer chains. The change in electrical resistance of 10 cyclic loading and unloading of the CBTPU and CNTTPU samples at 50% and 100% strain amplitudes is demonstrated in Figure 4.19(a-b), respectively. After the first cycle, the change in electrical resistance showed a repeatable trend in both strain amplitudes. The cyclic mechanical deformation of the samples resulted in a repeatable piezoresistive response.

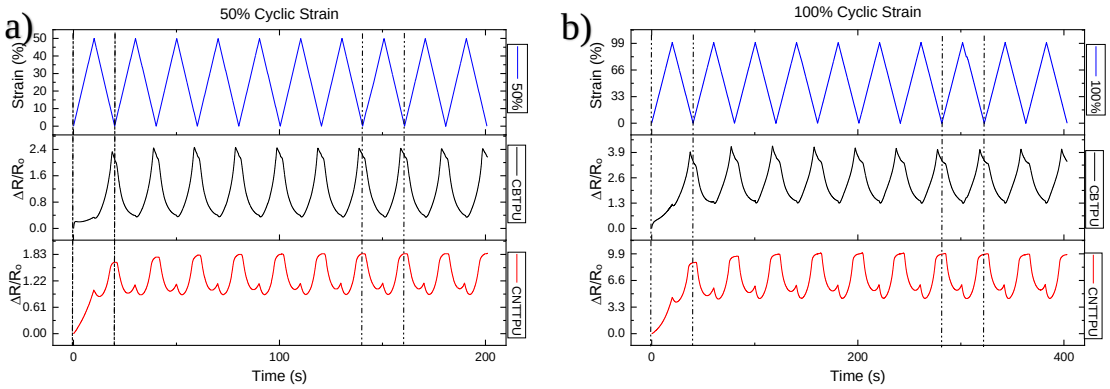

Figure 4.19: Change in electrical resistance under 10 cycles of CBTPU, and CNTTPU stretched at a) 50% of strain and b) 100% of strain.

It was noticed that after the first cycle, CBTPU showed a linear electrical resistance behaviour during cyclic loading and unloading. In contrast, CNTTPU tended to linearly decrease and then fluctuate to a slight increase in electrical resistance during loading when reaching maximum strain value. In the releasing process, CNTTPU showed fluctuation again in electrical resistance during the unloading at both strain amplitudes of 50% and 100%. This fluctuation is illustrated in Figure 4.20(a-b), which showed the 10^{th} cycles of the CBTPU and CNTTPU samples at 50% and 100% strain amplitudes. At 50% strain, in the 10^{th} cycle, both samples showed similar amplitude in the electrical resistance. However, CBTPU showed linear behaviour with an increased change in resistance, whereas CNTTPU showed fluctuation in electrical resistance during loading and unloading. At 100% strain, it was observed that most of the higher change from initial resistance in CNTTPU was not recovered. Also, CBTPU showed linear behaviour in comparison to apparent fluctuation behaviour in CNTTPU upon loading and unloading. This fluctuation is referred to as double peak and was well established stretchable conductive composites in the literature [67], [100], [104].

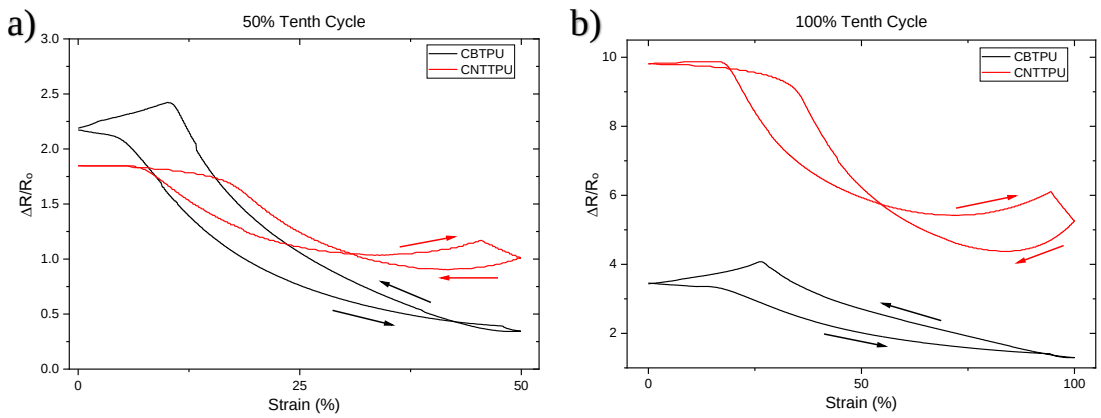

Figure 4.20: Change in electrical resistance of 10th cycles of CBTPU and CNTTPU stretched at a) 50% of strain and b) 100% of strain.

4.7.3 Negative strain effect

The negative strain effect was experienced in the first cycle in which the electrical resistance increased in both the loading and unloading, creating new permanent higher value of electrical resistance. After that, the change in electrical resistance became transverse to the applied strain, meaning a decrease upon increasing the strain loading and increase when unloading. The phenomenon was further illustrated in Figure 4.21(a-b), which shows the magnification of 3 cycles where the change in electrical resistance was inversely proportional to applied strain values of 50% and 100%, respectively. This is known as the negative strain effect, which occurs in stretchable conductive filled elastomers. The negative change in resistance upon loading was trending down from the newly created resistance value and then reverse linearly back up upon unloading.

The mechanical hysteresis behaviour, Poisson's ratio and residual strain influenced the cyclic electrical resistance response. Conductive paths within carbon-filled CBTPU and CNTTPU elastomers were disconnected and lost due to the residual strain, and new conductive paths were potentially created due to the Poisson's ratio compressive effect. Although an inverse response was obtained, it was observed that stabilisation of cyclic loading after the first cycle led to repeatable resistance variation. Linear behaviour was noticed in CBTPU whereas, a slight fluctuation of double peaks at the maximum strain in the CNTTPU curve was noticeably present in both strain amplitudes; 50% and 100%.

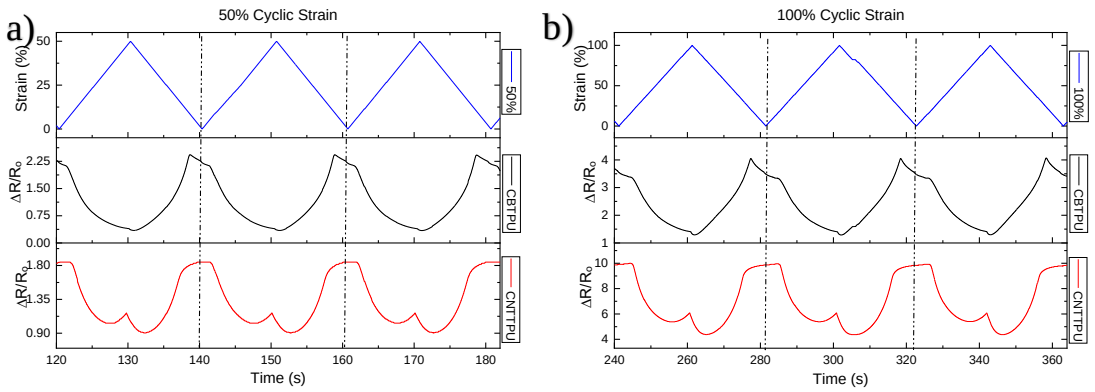

Figure 4.21: magnified 7th, 8th, and 9th cycles of CBTPU and CNTTPU illustrating negative change in electrical resistance under a) 50% of cyclic strain and b) 100% of cyclic strain.

4.7.4 Cyclic electrical response at low strain amplitudes

The behaviour of the 3D printed samples was further monitored under cyclic loading at relatively lower strain amplitudes after the initial tensile strain cycles were achieved. The change in electrical resistance was measured by calculating the change in electrical resistance divided by the initial resistance as illustrated in Equation (2.2). Therefore, the change in electrical resistance was measured for 10 cycles of 10%, 30% of tensile strains, shown in Figure 4.22 after both initial strain amplitudes of 50% (in Figure 4.22a-b) and 100% (in Figure 4.22c-d). The equilibrium state reached in the initial pre straining cycles demonstrated earlier resulted in a continuous and reproducible change in electrical resistance of the samples' following response. Cyclic variation in strain loading and unloading return to the original value in a repeatable manner.

Interestingly, CBTPU showed a continuous and repeatable change in electrical resistance in samples pre-stretched to 50% and 100% with no apparent drifting (Figure 4.22a-d). On the other hand, CNTTPU samples pre-stretched to 50% only showed a steady change in electrical resistance during cyclic strain at 10%. However, CNTTPU samples pre-stretched to 100% showed a steep reduction in electrical resistance magnitude during cyclic strain from the 1st – 10th cycles, as shown in Figure 4.22c-d with apparent fluctuation, which is referred to as double-peak [98], [100], [104]. This double-peak was mainly attributed to the significant non-recoverable electrical resistance experienced in CNTTPU in its initial strain of 100% in Figure 4.20b. It was suggested that cyclic strain allowed a slight recoverability of the change in electrical resistance during cyclic strain from the 1st – 10th cycles in CNTTPU, which had undergone considerable destruction during the 100% initial strain. In addition, it was noted that behaviour slightly fluctuated in the CBTPU samples only at 10% strain after 100% initial straining; however, a steady performance was also observed, as can be seen in Figure 4.22c.

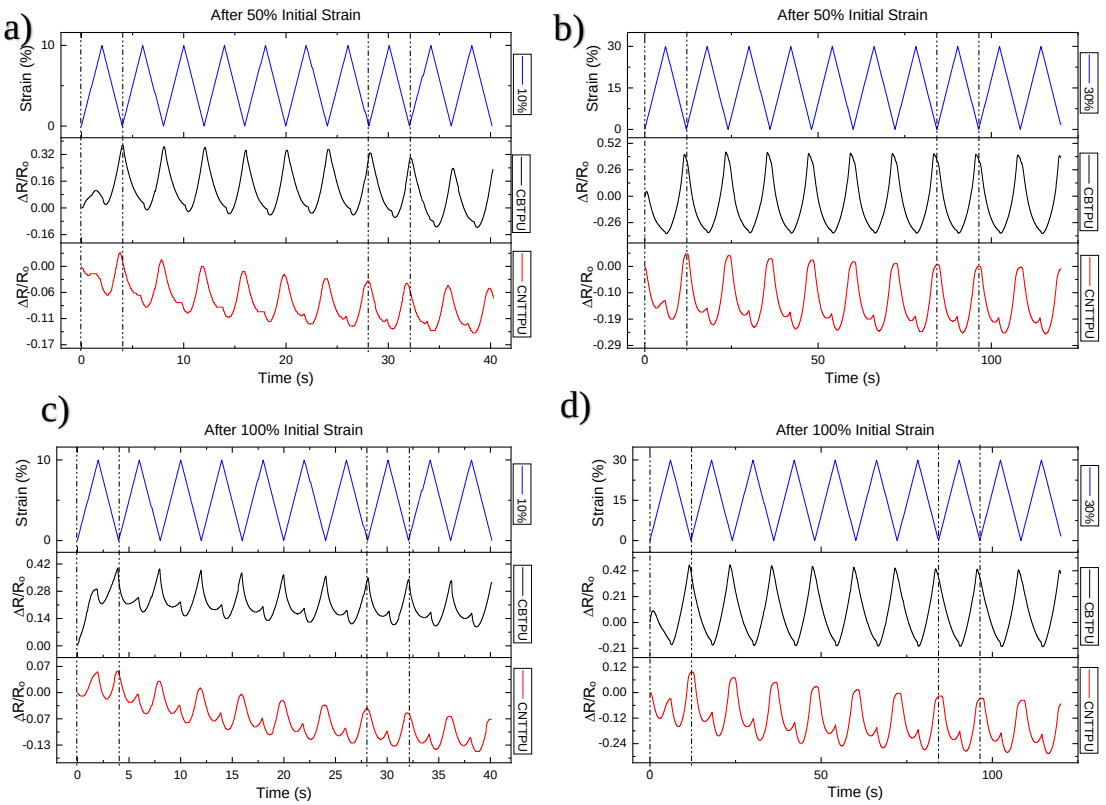

Figure 4.22: Change in electrical resistance under 10 cycles of CBTPU, and CNTTPU stretched at a) 10% of samples pre-stretched at 50%, b) 30% of samples pre-stretched at 50%, c) 10% of samples pre-stretched at 100% and d) 30% of samples pre-stretched at 100%.

4.8 Discussion

It was found that the results acquired were in good agreement with previous studies [17], [18], [98], [100]. Generally, although high stretchability of >50% and good reproducibility of the results, the sensors suffered negative strain effect in their mechanical and electrical tests. The non-linear mechanical stress-strain curve of TPU based conductive polymers led to a non-linear electrical response apparent in the decrease in the change in electrical resistance to applied strain. CNTTPU presented fluctuation in the change of electrical resistance, which is referred to as the double-peak effect [98], [100], [104]. On the other hand, the CBTPU strain sensor presented a steady response in its change in electrical resistance upon cyclic loading between 10-100% with moderate fluctuation only at 10% cyclic strain. The TPU substrate proved its ability to withstand great stretchability along with the embedded conductive polymer and showed the major advantage of simultaneous multi-material 3D printing. It was essential to test rigid conductive polymer and evaluate its strain sensing capabilities to overcome the negative strain effect found in the embedded stretchable conductive polymers. However, it was found in the literature that the rigid conductive polymer could only withstand minimal strain (<5%) [13], [46], [56], [185]. This fragility was evident in the strain at break test here of GPLA,

which showed significantly lower stretchability of <5% compared to TPU based composites with a stretchability of well over 100%. One of the major advantages that AM offers is the ability to 3D print any given design regardless of its complexity. In this case, it allows us to design conductive traces and structure the rigid conductive composite in a way that it can withstand the great stretchability of its host substrate. The purpose was to design the GPLA in a way that it could withstand high stretchability and obtain the strain sensing response under dynamic loading. The design of conductive GPLA should consider its rigidity when embedded in stretchable TPU substrate and be able to withstand high stretchability of up to 100% for strain sensors. Straight-line rigid conductive traces would break if stretched to higher than 5% due to the brittleness nature of rigid 3D printable materials such as PLA. Therefore, in the remainder of this chapter, there is a discussion of the testing of 3D printing conductive rigid polymers embedded in a stretchable substrate in meander structure. We further tested their electromechanical behaviour for use as strain sensors. [166], [186], [187].

4.9 Graphene polylactic acid (GPLA) samples

4.9.1 Meander traces of GPLA

By analysing the results in TPU based conductive composites, it was found that they offer superior stretchability beyond the stretching range required for wearable and skin mountable applications. In contrast, it was observed in the literature that rigid conductive composites and cracked based strain sensing materials offer high sensitivity with positive strain response but lack stretchability. Therefore, to evaluate the feasibility of these rigid and brittle conductive materials, we utilised the advantages of freeform design and fabrication offered by the FDM technique. The advantage of multi-material FDM allowed us to 3D print GPLA as sensing material embedded within a stretchable elastomer. The idea is to design the brittle GPLA in a way that it could withstand high stretchability and obtain the strain sensing response under dynamic loading. PLA demonstrated bonding with Graphene and ease of 3D printability; For strain sensing applications, however, its rigidity limits the stretchability [4].

On the other hand, elastomers such as thermoplastic polyurethane TPU showed stretchability and 3D printability but commonly had an inherent mechanical and electrical negative strain effect, which limited the linearity and sensitivity of these stretchable materials. The purpose of this test is to see further the possibility of combining the advantages of the stretchable conductive elastomers and sensitivity of the crack and brittle conductive composites. The intention was to combine the advantages of both conductive materials to create highly sensitive,

linear, and stretchable 3D printed sensing materials. The electromechanical behaviour of GPLA samples was evaluated separately from the TPU based conductive materials due to the brittleness nature of the PLA. The use of 3D printing multi-material capability allowed for the construction of traces that would not affect the brittleness of the conductive materials. In order to overcome the low stretchability, 3D printing offers freedom of design that allowed us to fabricate rigid conductive traces embedded in stretchable elastomer that can withstand extreme stretchability. The brittleness of the material allowed us only to test the samples with the meander shaped trace of the conductive GPLA. As illustrated in Figure 4.23(a-b), it was found that the meander structure of the rigid GPLA conductive traces had a spring-like behaviour when subject to tensile strain up to 100%. Following the same process illustrated previously in this chapter, Figure 4.23c shows an image of the simultaneous dual-material 3D printing process of meander-shaped GPLA filament embedded in TPU filament. Meander structure was chosen for rigid conductive GPLA embedded within the stretchable substrate to accommodate the intended high values of applied strain.

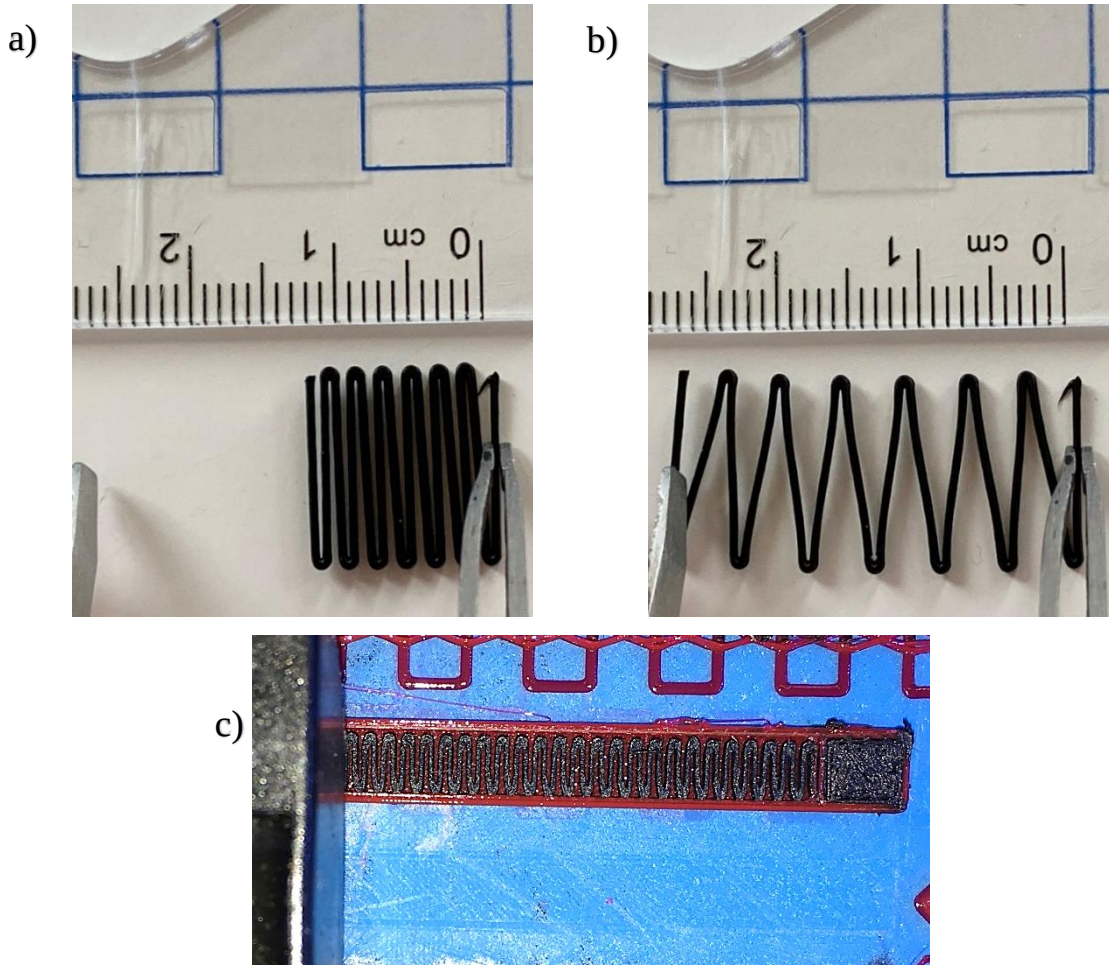

Figure 4.23: Illustration of spring-like behaviour of meander rigid GPLA at a) 0% strain, b) 100% strain and c) Image of dual extrusion 3D printing of meander conductive GPLA embedded in TPU in action.

4.9.2 Resistance response of initial strain

Based on the meander design fabricated here, we 3D printed meander traces of GPLA in stretchable TPU substrate, namely NinjaFlex and tested its electrical response. The sample was subject to 100% initial strain, while the substrate accommodates the tensile strain; the GPLA traces encapsulated acted like spring inside the substrate with little to no strain, as shown in the images in Figure 4.24a-b. Interestingly, the change in electrical resistance of the sample increased upon loading during the initial strain, as shown in Figure 4.24. Moreover, most of the resistance value recovered linearly upon unloading, as shown in Figure 4.24c. It was noticed that the electrical resistance of the sample had positive strain behaviour. The linearity of GPLA was obtained for axial strain compared to CNTTPU and CBTPU, which had a negative strain effect upon the unloading of the initial strain.

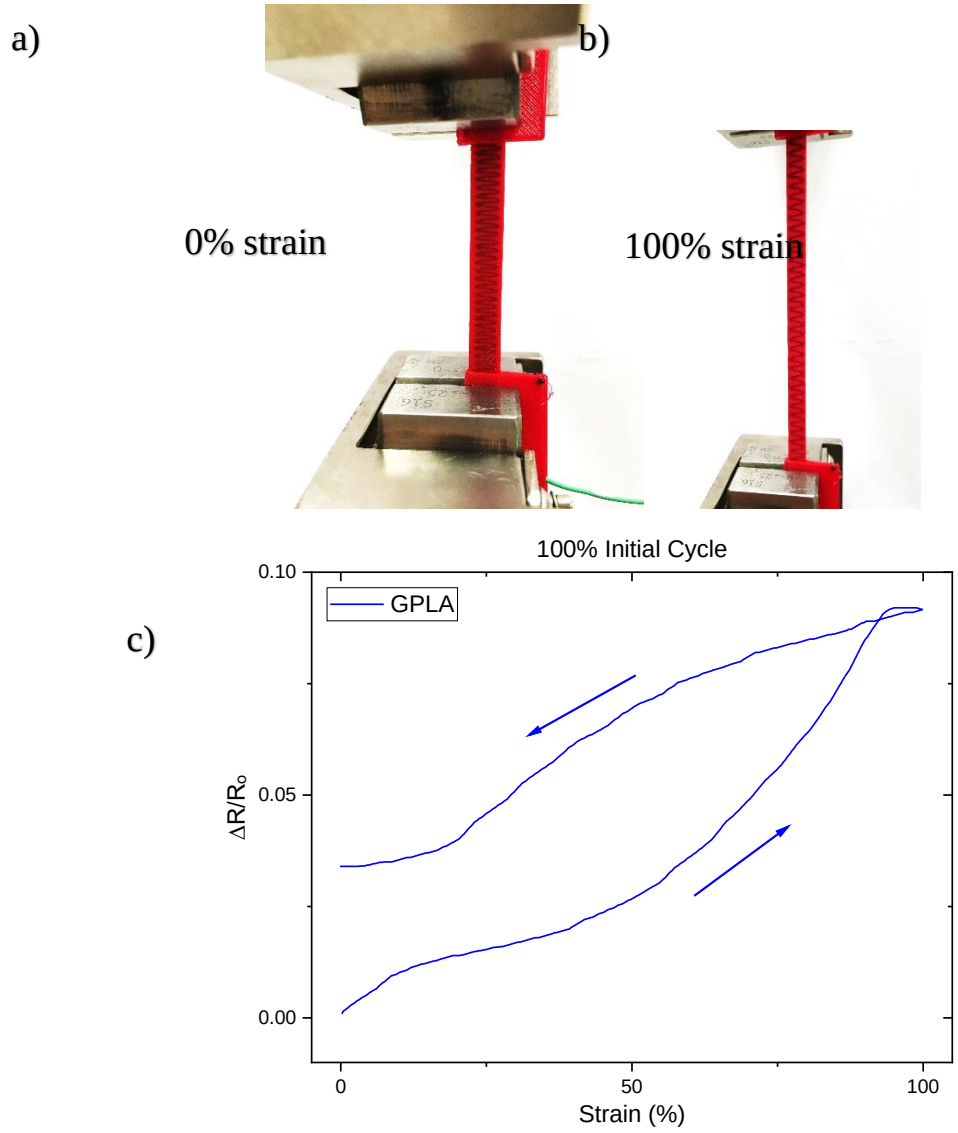

Figure 4.24: a) 3D printed meander structured sample at 0% strain, b) Sample stretched to 100% and c) Change in electrical resistance of the initial cycle of GPLA sample stretched to 100% of strain.

4.9.3 Electrical response of GPLA under cyclic strain

To further examine the 3D printed sample, cyclic strains of 10%, 30% and 50% were performed and illustrated in Figure 4.25a–c respectively, on cycles between 1st-10th cycles. The sample showed a gradual increase in the change in resistance with strain loading and a decrease with unloading, which is described as a positive strain effect. Reproducible cyclic response of change in electrical resistance can be seen in all strain amplitudes. The meander structure of GPLA in stretchable TPU was able to withstand a broad range of strain amplitudes as high as the initial strain of 100% to as low as 10% with a linear change in electrical resistance and repeatable under cyclic strain. It was suggested that the peak pre-straining of 100% strain at the first cycle resulted in the sample performing with good sensing stability at lower cyclic strains, represented with good recoverability and reproducibility.

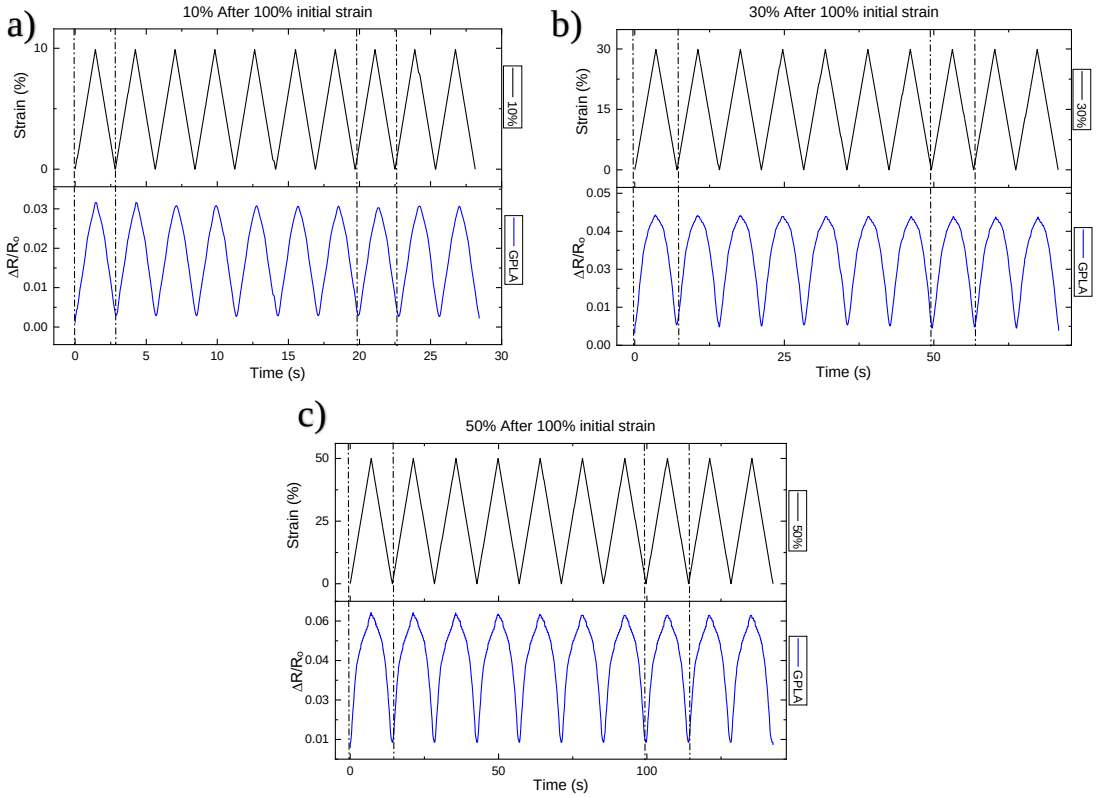

Figure 4.25: Change in electrical resistance of 10 cycles of GPLA stretched at a) 10% of cyclic strain, b) 30% of cyclic strain, and c) 50% of cyclic strain.

4.10 Electrical sensitivity and gauge factor

The gauge factor expresses the sensitivity of the samples by dividing the change in electrical resistance by the rate of change in tensile strain. The equation that calculates the gauge factor GF is expressed in Equation (2.3).

Figure 4.26 shows gauge factor values of the CBTPU, CNTTPU and GPLA at strain amplitudes of 10%, 30%, 50% and 100%. The GF values at 10%, 30% and 50% in CBTPU exhibited higher sensitivity with almost double than CNTTPU values. The highest GF value for CBTPU was 4.5 at 50% strain. In contrast, the significant destruction of carbon nanotubes in CNTTPU beyond 50% strain influenced the change in electrical resistance and led to higher sensitivity observed at 100% strain with a GF value of 6. Although positive linear behaviour was obtained in GPLA, the sensitivity was very low compared to both CBTPU and CNTTPU due to the spring-like behaviour of the sensor under applied strain. The spring-like behaviour with minimal strain on the GPLA traces upon stretching influenced the low sensitivity with the highest GF value of 0.28 at 10% strain, and the lowest was 0.09 at 100% strain.

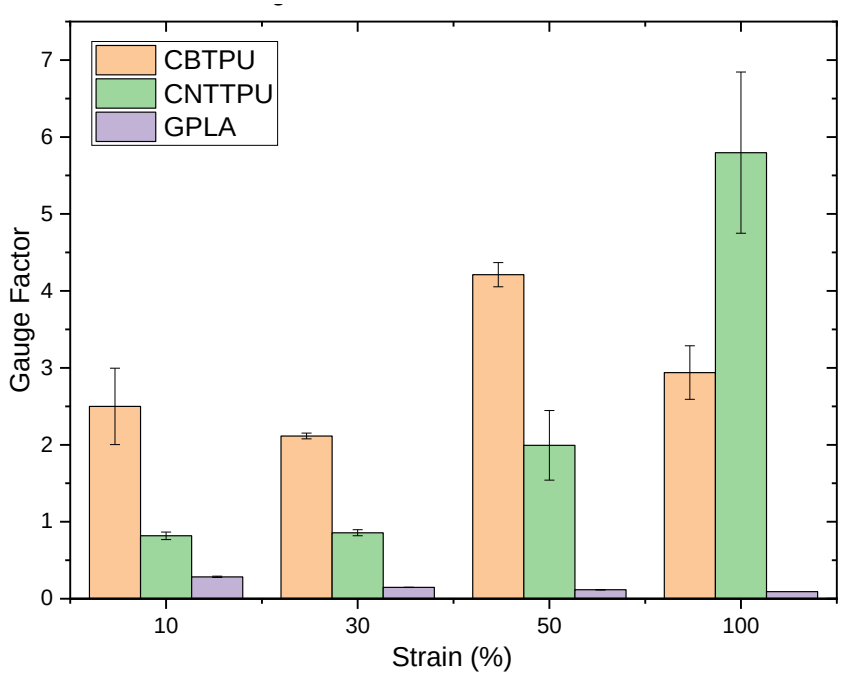

Figure 4.26: Average gauge factor GF values at various strain amplitudes between 10%-100%.

4.11 Summary

This chapter explored the feasibility of fused deposition modelling FDM 3D printing technology. The conductive materials used here were firstly processed through a filament maker to form 3D printable filaments. Carbon black, graphene and carbon nanotubes proved to be excellent conducting fillers to the polymer matrix. The mechanical performance of the materials, as well as the electrical conductivities, were tested. It was found that the type of carbon fillers greatly influenced the electrical conductivity of the filaments. It also mechanically influenced the stiffness and elasticity of the filaments.

The feasibility of multi-material 3D printing of the prepared filament was also tested. It was possible to simultaneously co-print conductive materials encapsulated within a flexible elastomer. CNTTPU samples showed high sensitivity with a gauge factor of 6 at an initial strain of 100%. However, most of the change in electrical resistance had not recovered, which led to lower GF values at lower strain amplitudes (<50%). CBTPU showed linear behaviour with a gauge factor value of 4.5 at 50% strain. Multi-material 3D printing also allowed to fabricate brittle GPLA filament in stretchable TPU substrate, which allowed for a tensile strain of up to 100% with electrical sensing capability. To our knowledge, the work presented in this chapter was the first extensive investigation to compare the strain sensing behaviour of 3 types of 3D printed conductive polymers. The 3D printed samples proved to have great repeatable and reproducible results in sensing small and large strain deformations.

Chapter 5– 3D Printing of highly sensitive multi-material composite sensors with linear electrical responses

5.1 Introduction

The rapidly growing fields of wearable soft electronics and health monitoring require more reliable, sensitive, and compliant sensory systems. Development in sensing devices relies on advances in functional materials and fabrication processes. In Chapter 4, it was possible to test the 3D printability of rigid and flexible filaments and identify the key issues found in FDM multi-material 3D printing. The digital platform and its parameters were modified to overcome the difficulties found and ensure successful 3D printing of flexible filaments. Based on the outcomes of Chapter 4, CBTPU presented higher sensitivity than all the conductive materials tested but with a negative strain effect. On the other hand, GPLA presented good cyclic behaviour with linear electrical resistance response to applied strain but suffered low sensitivity. In order to overcome the issues found in Chapter 4, a method of mixing 2 conductive pellets to fabricate highly sensitive strain sensors with a linear response is presented. CBTPU and GPLA have been chosen as the conductive pellets for this chapter. Various ratios of the 2 conductive pellets were mixed to optimise their mechanical and electrical properties. The resulting conductive mixtures were extruded to form a 3D printable filament. 3D printing utilising dual extrusion FDM was employed here to 3D print the prepared conductive composites embedded in a stretchable elastomer substrate to create highly sensitive and linear strain sensors. The set of materials and design of the multi-material strain sensors are described. The composites were characterised using SEM imaging, and the mechanical and electrical properties were further tested. The purpose was to enhance the sensors' performance to overcome non-linearity and sensitivity issues.

5.2 Composite preparation

For the sensing material, CBTPU and GPLA were combined with three weight ratios. The mass loading (wt.%) of the GPLA pellets added to CBTPU pellets is denoted as CBTPU-χGPLA, where χ represents the mass loading wt.% of GPLA to CBTPU. Prior to the filament extrusion, the pellets were dried at 70 °C overnight using a material dryer before any melt processing. Figure 5.1 shows optical images of the preparation process of the 3D printable filaments. Each material composition was melt-processed and extruded at 170 °C, using a single-screw extruder (Noztek Pro, Noztek Ltd.) to form a strand of 3D printable filament with 1.75 mm of diameter. The resulting filament measured 1.75mm (±0.04 mm) in diameter, and batches of the filaments

extruded were wound manually to filament spools as shown in Figure 5.1c to be used later for the 3D printing process. Further demonstration of the SEM images of surface morphology of the extruded composites is illustrated in Appendix A. For the substrate, the TPU filament was used as received without any modification.

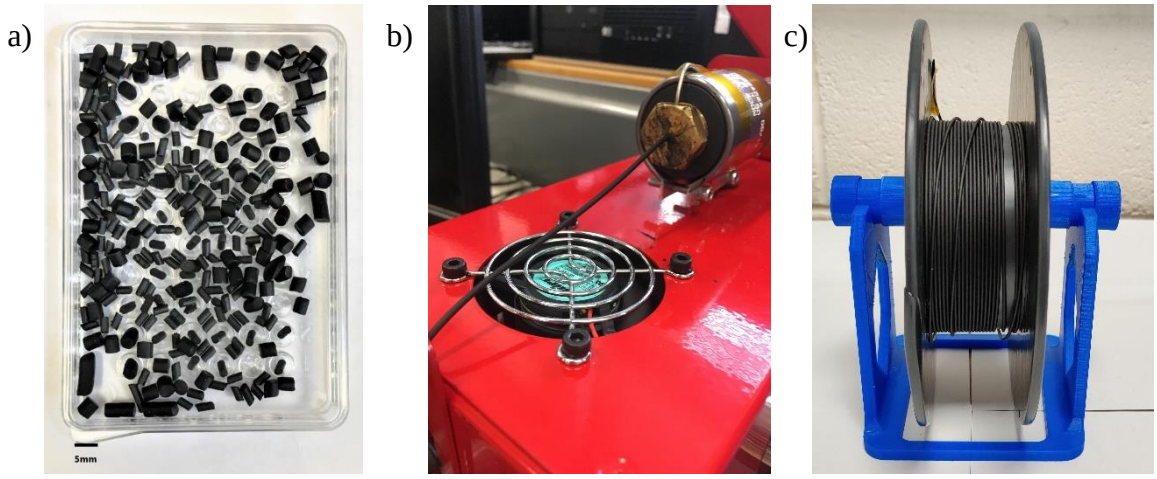

Figure 5.1: a) Composite of CBTPU and GPLA pellets, b) Pellets extruded as 3D printable filament, and c) A spool of the 3D printed filament CBTPU-50GPLA filament ready for use.

5.3 Physical properties of the filaments

5.3.1 Electrical conductivity of composites

Strands of the extruded composite filaments were prepared for measuring their electrical conductivity before the 3D printing process. 5 samples of each of the composite filaments were measured and cut to a length of 40 mm and a diameter of 1.75 mm (±0.04 mm). The samples were silver coated at both ends, as shown in Figure 5.2a, to assure the electrical connection when connected to the digital multi metre. As shown in Figure 5.2b, the addition of GPLA in the CBTPU-30GPLA filament enhanced the electrical conductivity to double that of neat CBTPU. This increase was attributed to the high electrical conductivity of the neat GPLA, which had a value of 0.11 S/m compared to the CBTPU at 0.008 S/m. CBTPU-40GPLA had an electrical conductivity of 0.025 s/m, which was slightly higher than the conductivity of CBTPU-30GPLA with a value of 0.022 S/m. CBTPU-50GPLA had the highest electrical conductivity of the 3 composite filaments reaching an electrical conductivity value of 0.03 S/m. It was found that the addition of up to 50 wt% of GPLA increased the electrical conductivity by almost 4 times the value found in the neat CBTPU.

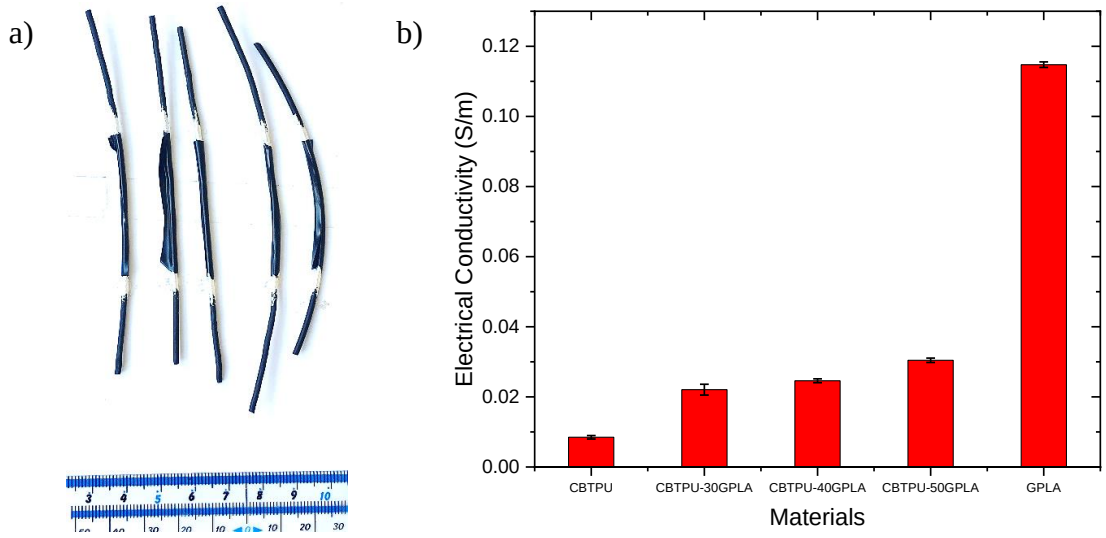

Figure 5.2: a) Strands of filament samples silver coated for electrical conductivity measurements. b) Electrical conductivity of the prepared samples.

5.3.2 Strain at break

The tensile strain testing was performed on samples of the three composites using an Instron tensile machine. Five strands of each of the 3 filaments, CBTPU-30GPLA, CBTPU-40GPLA and CBTPU-50GPLA, were prepared with lengths of 40 mm and 1.75 mm diameters (±0.04 mm). The comparison of the strain at break of the samples can be seen in Figure 5.3. CBTPU-30GPLA samples withstood considerable strain and broke at a value of over 100% of tensile strain. In comparison, CBTPU-40GPLA withstood a tensile strain of 75% with an apparent higher stress value of the tensile strain. On the other hand, CBTPU-50GPLA samples had the highest stress value breaking at a tensile strain of less than 55%.

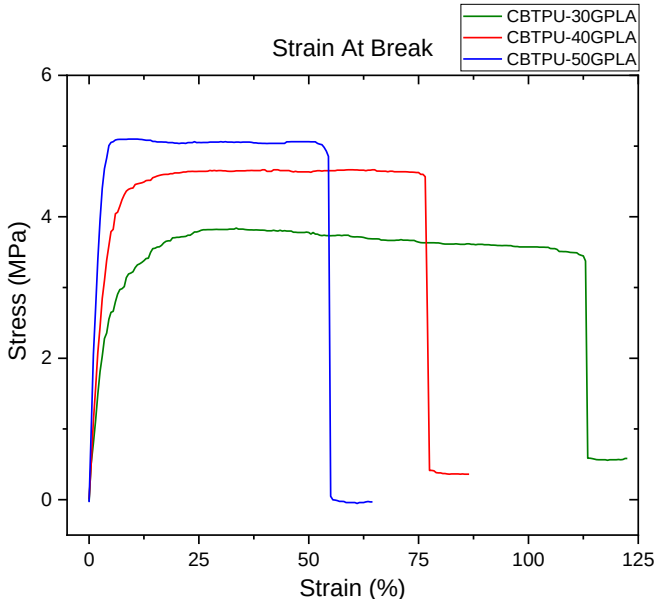

Figure 5.3: Strain at break of composite filament sample.

5.3.3 Tensile strength and Young's modulus

The tensile strength was obtained from the stress-strain curve to investigate the mechanical behaviour of the samples. As illustrated in Table 5.1 and Figure 5.5, the tensile strength value of the CBTPU-30GPLA sample was 3.64 MPa, which appeared to be the lowest tensile strength of the 3 filaments. It was noted that as the value of GPLA increases in the CBTPU-40GPLA and CBTPU-50GPLA, the tensile strength value distinctly increases to 4.78 MPa and 5.1 MPa, respectively. Furthermore, Young's modulus was calculated to investigate the materials' mechanical behaviour. It was measured by taking a secant value from the stress/strain curve in Figure 5.4 at low strain levels of < 1%, where the stress-strain curve relationship is linear. The measurement was based on the ISO 527 standard, and the measured values were summarised in Table 5.1. CBTPU-30GPLA exhibited the highest elasticity of the three filaments, with a Young's modulus value as low as 73.97 MPa. The Young's modulus value of CBTPU-40GPLA filament was 107 MPa.

On the other hand, CBTPU-50GPLA was shown to be relatively stiffer with the least elastic behaviour of the three filaments, with a Young's modulus of 184 MPa. It can be noted that the addition of GPLA has shown a significant impact on the Young's modulus of the samples. Nevertheless, these values were found to be in the elastic range of materials [48].

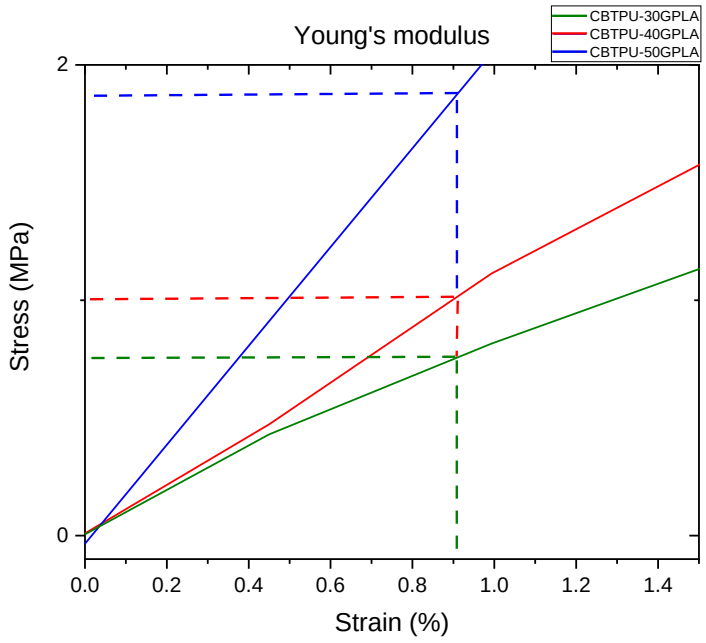

Figure 5.4: Young's modulus calculation of composite filament samples.

Table 5.1: Tensile strength and Young's modulus of composite filament samples.

	Tensile Strength (MPa)	Young's Modulus (MPa)
CBTPU-30GPLA	3.64	73.97
CBTPU-40GPLA	4.78	107
CBTPU-50GPLA	5.1	184

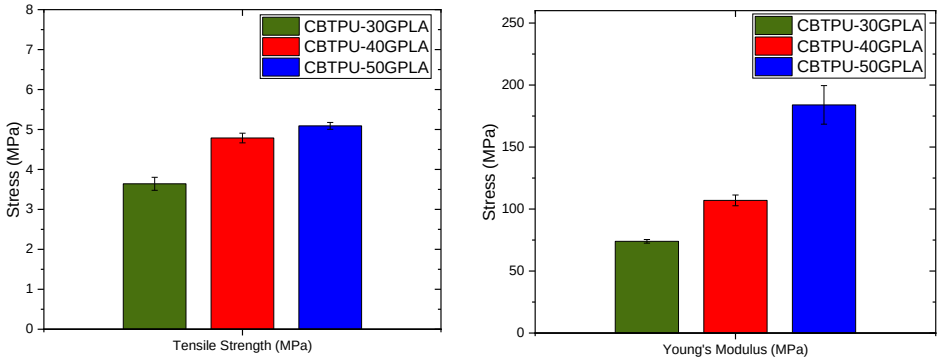

Figure 5.5: a) Average theoretical tensile strength, and b) Average theoretical Young's modulus of the samples detailed.

5.4 3D printing of strain sensors

5.4.1 Design and fabrication

The designs were prepared using CAD software called PTC Creo Parametric 3.0. Each 3D printed sample was composed of electrically conductive sensing filaments encapsulated within an elastomer substrate (i.e. embedded within an insulative TPU). For the embedded conductive filament, a straight-line design was used, measuring 36mm in length, 3.6 mm in width and 0.4 mm in thickness, as shown in Figure 4.10a. The substrate shown in Figure 4.10b had a total length of 40 mm, a width of 5 mm, and 1 mm. It was designed for the conductive material to be embedded inside. As further illustrated in Figure 4.10b, the substrate had a cavity inside that allowed the conductive model to be merged in the substrate during the simultaneous 3D printing process. The substrate was designed with apertures measuring 3 mm^2 at the 2 ends to enable electrical connection for the 3D printed samples.

The fabrication of the 3D was based on simultaneous fused deposition modelling FDM 3D printing process. Firstly, stereolithography STL files of 3D models were exported to slicer software. The STL files of the substrate and the conductive filament models were merged, and

each of the materials was assigned to an extruder. The values of the 3D printing parameters used in this work were summarised in Table 3.1. These settings were then exported to an SD card as Gcode files from which the 3D printer can be read.

The multi-material platform using the 3D printer enabled the fabrication of the samples where the right extruder was assigned for 3D printing of the conductive filaments, and the left one was for the encapsulate insulative substrate. Using the 3D slicing software, Figure 5.6a shows the merged CAD models of conductive material (black) and substrate material (red) converted into a series of discrete coordinate positions sliced layer by layer. As illustrated schematically in Figure 5.6a, the process follows the Gcode pattern generated in the software and alternates between the 2 materials to construct the 3D samples of the models. An optical image of the 3D printing process was shown in Figure 5.6b**.**

a)

b)

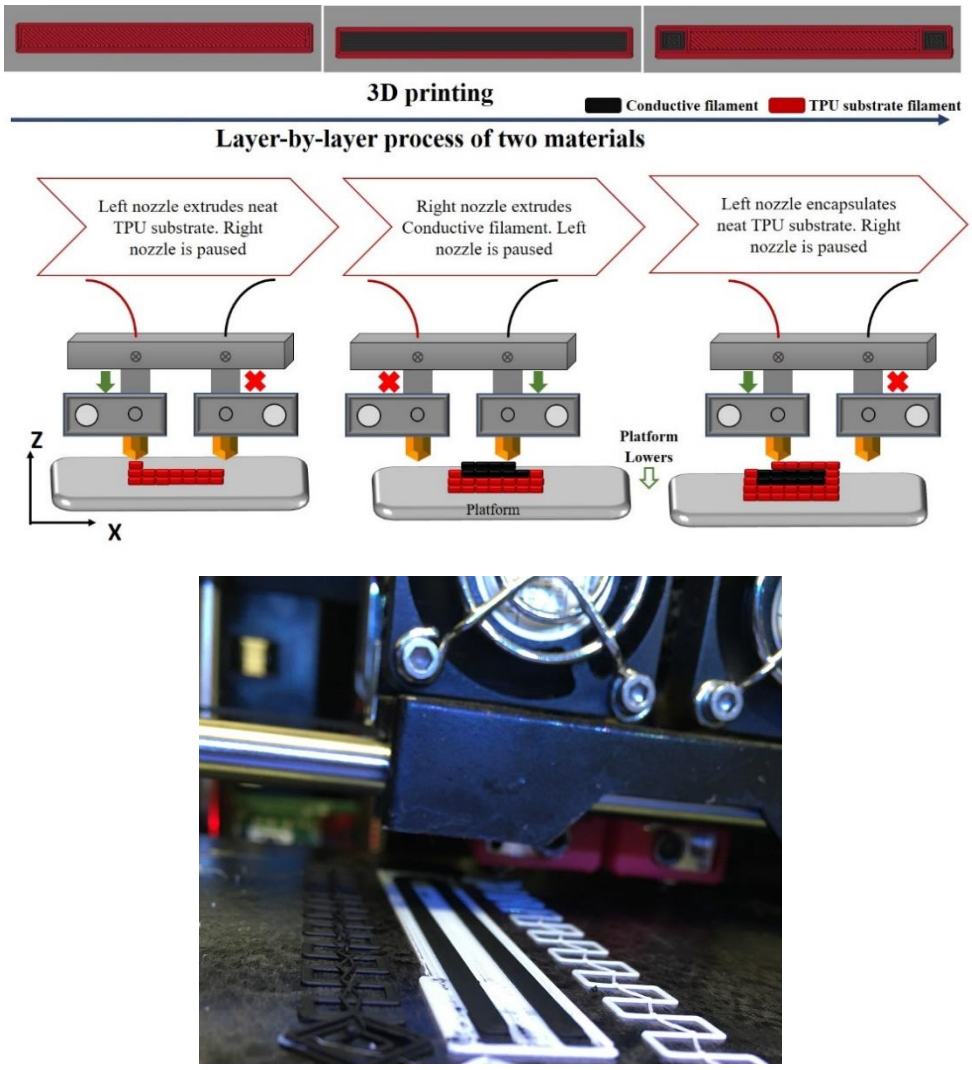

Figure 5.6: Schematic illustration of the dual extrusion 3D printing process, which deposits materials by alternating between 2 independent extruders. b) Simultaneous dual 3D printing in progress.

For the glove and robotic hand strain sensors applications, a U-shaped strain sensor was designed and illustrated schematically in Figure 5.7(a-b) of the sensing traces and the substrate, respectively. The bending of the glove and robotic hand induce a tensile strain on the 3D printed sensors, which reflects to the change in electrical resistance [15], [17], [185]. The U-shaped strain sensor was employed to facilitate the electrical wiring and measurement of the electrical signal. Figure 5.7c shows a schematic representation of the robotic hand with detailed measurements. It was worth noting that the fingers of the robotic hand had cavities to allow the u-shaped strain sensors to be merged for the simultaneous 3D printing of the robotic hand with embedded strain sensors.

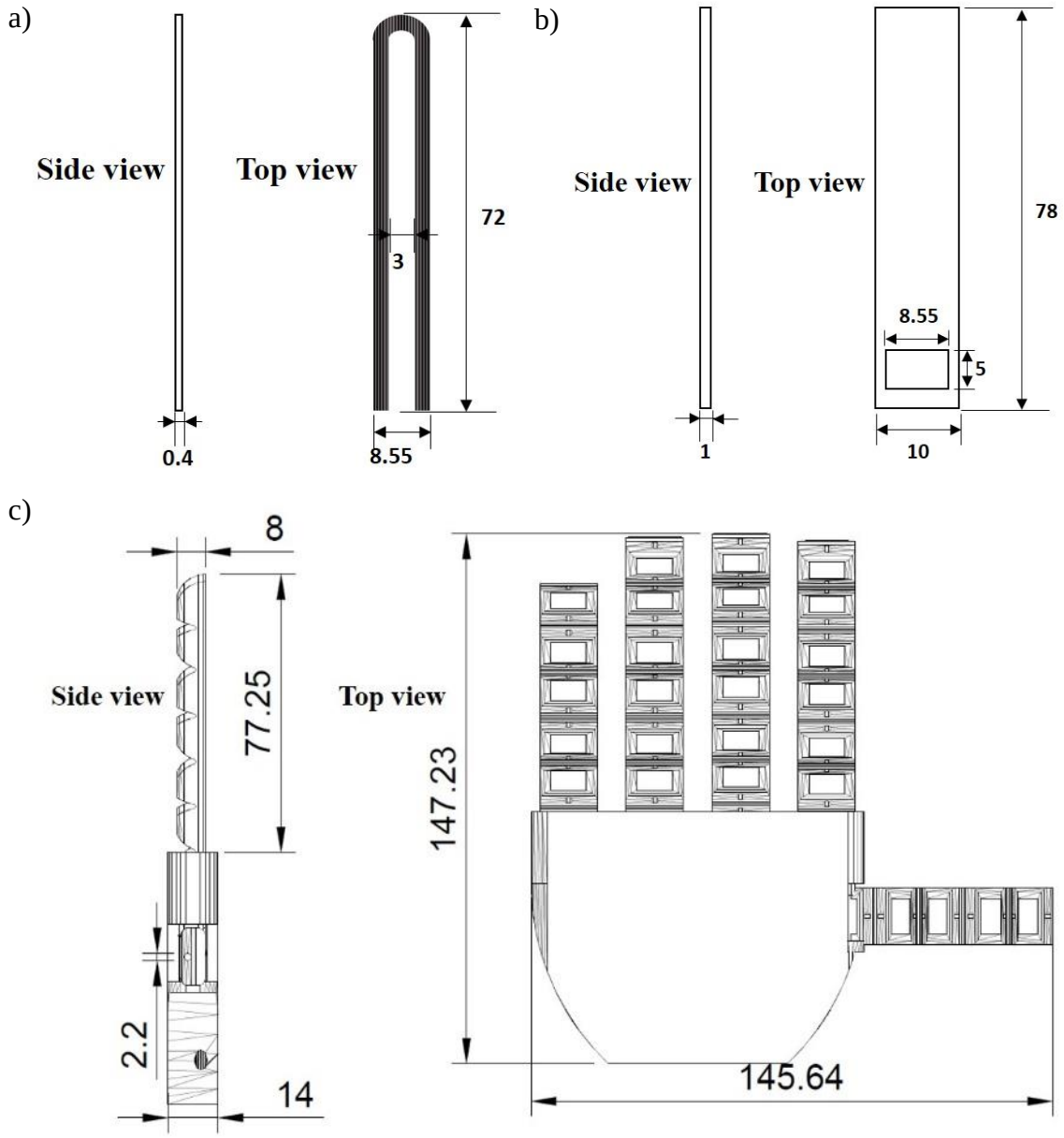

Figure 5.7: Schematic illustration of a) U-shaped 3D strain sensor model, b) 3D design of the U-shaped strain sensor's substrate, and c) 3D design of the robotic hand model (All measurements are in millimetre mm).

An exemplar sample shown in Figure 5.8a was wired with electrical wires and silver coated at the 2 ends to reduce the contact resistance to the probes for electrical testing. Figure 5.8b and Figure 5.8(c-d) showed images of the U-shaped 3D printed strain sensors and the 3D printed robotic hand with embedded strain sensors, respectively.

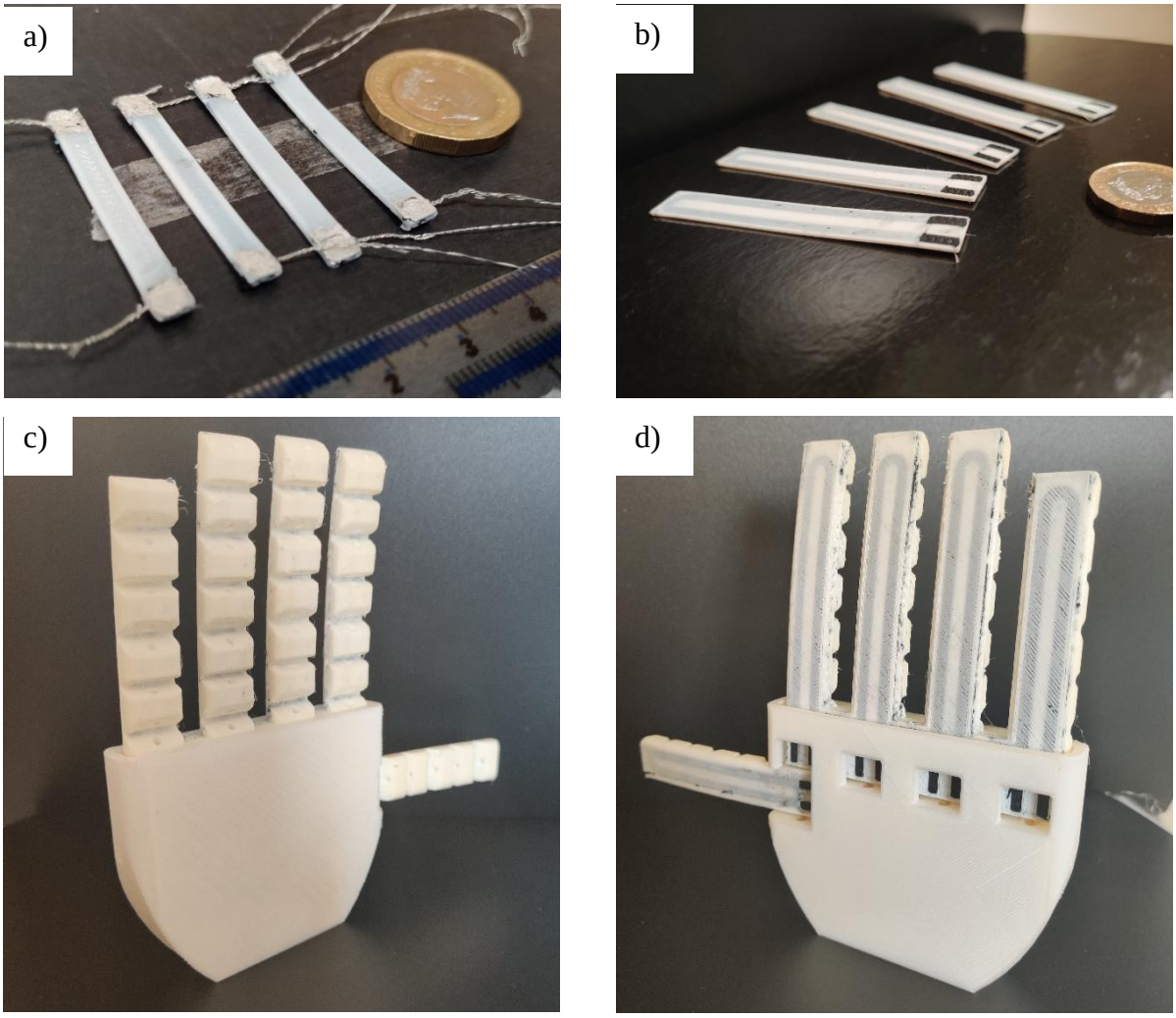

Figure 5.8: Optical images of a) 3D printed strain sensors wired and silver coated, b) U-shaped strain sensors, and (c-d) The robotic hand 3D printed.

5.4.2 Mechanical stress-strain behaviour of 3D printed samples

Tensile strain tests were conducted on the 3D multi-material printed samples. Three samples of each of the CBTPU-30GPLA, CBTPU-40GPLA and CBTPU-50GPLA filaments were prepared for the mechanical testing. The 3D printed samples were attached to the Instron tensile machine, as shown in Figure 5.9**,** with a 20mm long, 5 mm wide, and 1mm thick gauge. The tensile strength was acquired, and the stress-strain curves of a total of 9 samples were obtained. The 3D printed samples were subjected to 10 cycles of tensile strain values of 50%, 70% and 100%. The cyclic tensile pre- straining test was performed for the three types of the 3D printed

CBTPU-30GPLA, CBTPU-40GPLA and CBTPU-50GPLA to test their mechanical performance under various strain loadings. The first strain loading shows a steep increase in the stress amplitude of the applied strain. This increase is attributed to the rearrangement of the elastomer polymer chains to accommodate the applied elongation. It was also impacted by the embedded sensing materials, which increased the stress concentration on the first cycle. CBTPU-50GPLA had a steep increase in stress to the applied strain values compared to CBTPU-30GPLA, CBTPU-40GPLA from 50% to 100% of tensile strain. The increase in the concentration of stress in the first loading was also impacted by embedded composites, which have a higher elastic Young's modulus than the encapsulate substrate.

After the first cycle, the samples showed a softening effect where the curve demonstrated monotonic behaviour when loading and unloading. After that, the samples reached an equilibrium, which indicated the viability of the cyclic pre-straining to minimise the softening effect. It can be noted that the hysteresis mechanical behaviour in the cyclic curve after the first cycle increased as the tensile strain value increased from 50-100% (i.e. the linearity in loading and unloading decreases as the value of tensile strain increases). This inherent mechanical hysteresis behaviour is well known in stretchable materials [48]. As further illustrated in Figure 5.9(b-d), the samples showed a residual strain in the cyclic stress-strain with an apparent residual strain of 10%.

It was noticed that although there was slightly different behaviour in the first loading cycle, all embedded conductive materials had mechanically similar behaviour in the following cycles. However, the difference was found in the tensile strain value, where the hysteresis behaviour was more apparent in the cyclic loading-unloading curve as the strain values increased from 50-100%.

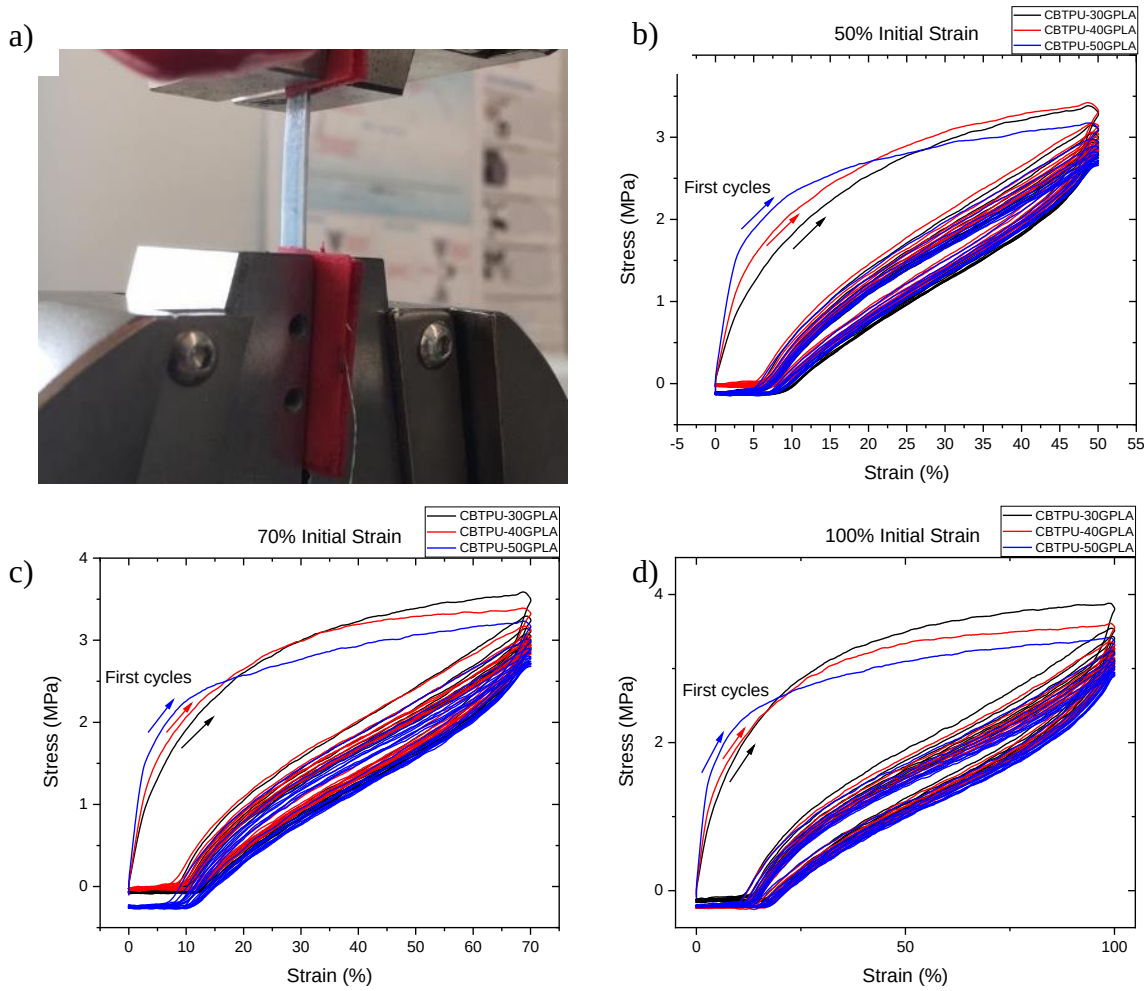

Figure 5.9: a) Optical image of the 3D printed sample clamped for mechanical testing, (b-d) Stress-strain curve of 10 cycles stretched at b) 50%, c) 70% and d) 100%. CNTTPU.

5.4.3 Electrical response of initial strain cycle

The sensing capability of the 3D printed samples was tested by measuring the change in electrical resistance to the applied strain. The samples were initially subjected to stretching of tensile strain at 1mm/s of strain rate as illustrated in the setup in Figure 5.10a. Upon loading, the results showed a monotonic change in the resistance response of the 3 embedded composites, namely CBTPU-30GPLA, CBTPU-40GPLA and CBTPU-50GPLA. The change in electrical resistance increased as a function of the applied strain due to the destruction of the conductive path networks within the sensing filaments. The 3 samples showed a distinctly different pattern of change in electrical resistance as the tensile value increases.

Upon loading 50% strain, CBTPU-30GPLA possessed low electrical resistance change, as shown in Figure 5.10b. In comparison, CBTPU-40GPLA experienced a more significant change in resistance at 50% strain than CBTPU-30GPLA. CBTPU-50GPLA showed the highest increase change in electrical resistance to the applied strain. It was noticed that at a

strain value greater than 30%, the change in electrical resistance increased rapidly to the applied strain.

The change in resistance in CBTPU-50GPLA possessed exponential behaviour at tensile strain values of 70% and 100%, as illustrated in Figure 5.10(c-d), respectively. Interestingly, CBTPU-40GPLA had also demonstrated a sharp increase in electrical resistance at strain values of 70% and 100%, as shown in Figure 5.10(c-d), respectively. On the other hand, CBTPU-30GPLA had a moderate change of electrical resistance in all strain values compared to CBTPU-40GPLA and CBTPU-50GPLA. It was worth noting that the higher the content of GPLA, the higher the change in resistance was observed. However, the change in the electrical resistance of CBTPU-50GPLA between 70-100% showed a steep exponential increase in electrical resistance. This curve of change in electrical resistance shows that the operating range for CBTPU-50GPLA reaches a tensile strain up to 50%. Upon unloading, the initial strain showed that the electrical resistance was reversible, recovering the initial electrical resistance's value considerably. This repeatable behaviour is explored further in the next section to investigate their feasibility for use as strain sensors.

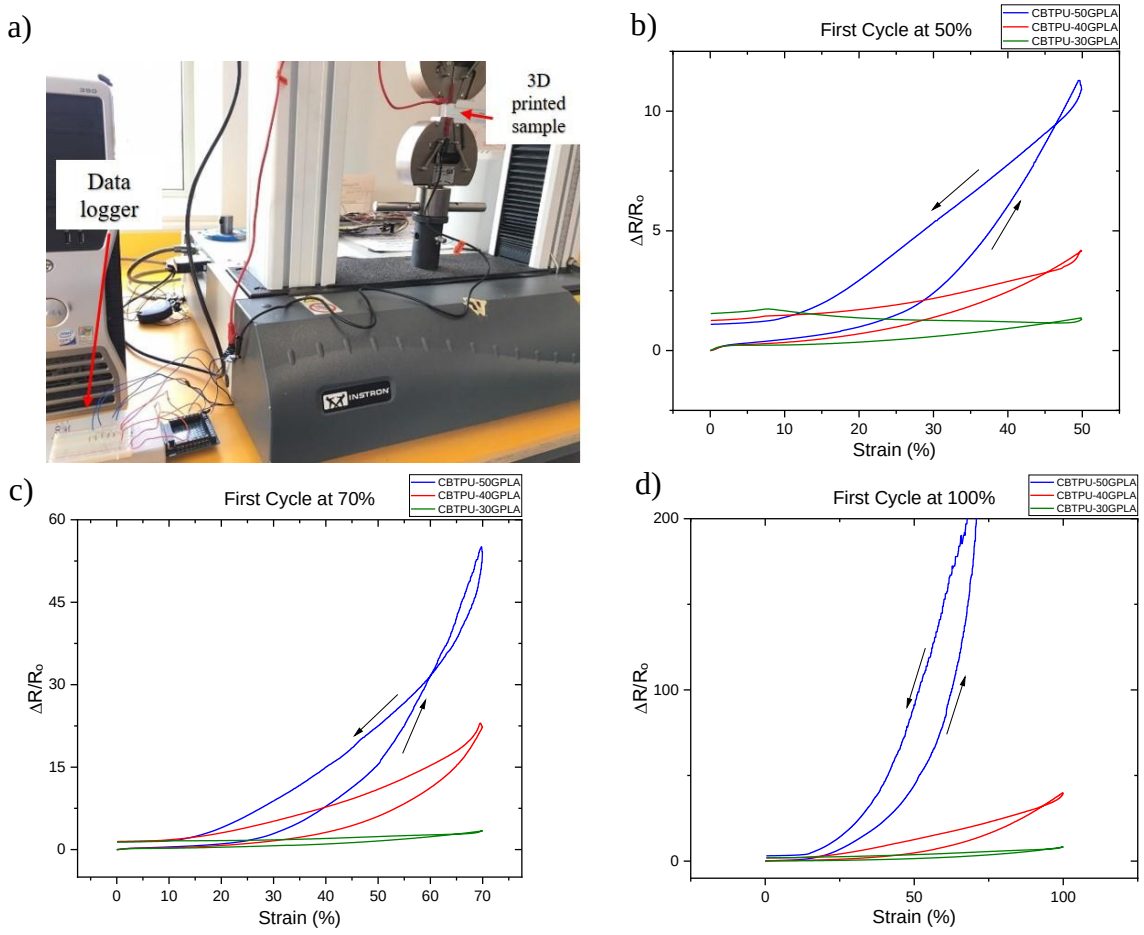

Figure 5.10: Image of data logging setup. (b-d) Change in resistance response of CBTPU-50GPLA, CBTPU-50GPLA and CBTPU-50GPLA at strain values of a) 50%, b) 70% and c) 100%.

5.5 Pre-straining of samples and their effect on materials and electrical resistance

The electromechanical behaviour of the samples was furthered explored by following cyclic pre-straining. In elastomeric stretchable materials, pre-straining is essential for regulating the elastomer matrix chains and the conductive network within the elastomer. This regulation was witnessed in the mechanical behaviour where the softening effect occurred in the first stress-strain cycles. For the use in strain sensing, pre-straining at tensile strain values of 50%, 70% and 100% was essential. Therefore, fresh samples were subject to 10 cycles of maximum strain values of 50%, 70% and 100%. At 50% cyclic strain, illustrated in Figure 5.11, the samples showed repeatable behaviour change in electrical resistance. Upon cyclic loading, the change in electrical resistance in CBTPU-30GPLA peaked at 2, which was lower than the change in CBTPU-40GPLA, which had a peak value of 4.2. CBTPU-50GPLA had the highest electrical change reaching 12.5. During the cyclic strain, CBTPU-50GPLA and CBTPU-40GPLA showed a positive change in electrical resistance where the change of resistance increased upon strain loading and decreased upon unloading. However, CBTPU-30GPLA fluctuated in response to applied strain, showing double peaks at each cycle. This fluctuation in the change of electrical resistance response is known as the negative effect where electrical resistance change is inversely proportional to applied strain [8], [42]. After the first cycle in CBTPU-30GPLA, fluctuation occurred with the change in electrical resistance increasing from 0 to 15% strain loading and then decreasing from 15% to peak 50% strain loading. Upon unloading, it continued to fluctuate with a slight decrease in electrical resistance, followed by a sharp increase in the electrical resistance.

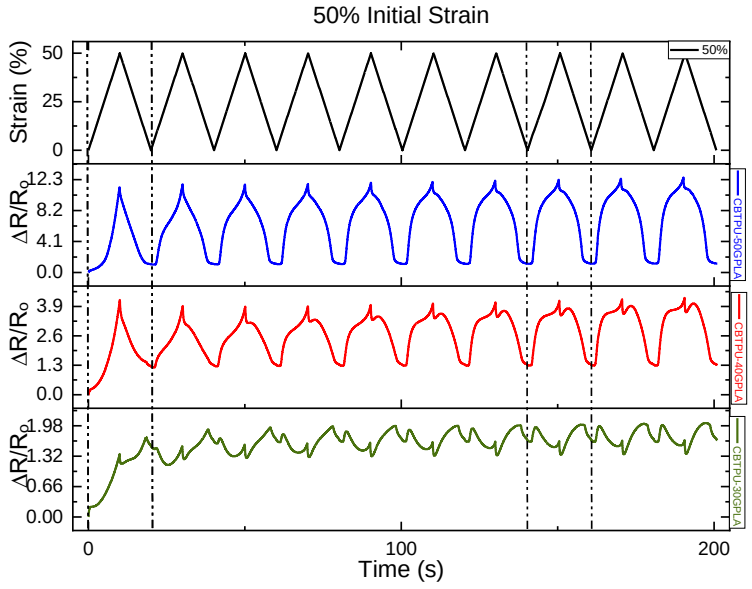

Figure 5.11: 3D printed CBTPU-50GPLA, CBTPU-50GPLA and CBTPU-50GPLA at cyclic initial strain value of 70%.

At a 70% cyclic strain, illustrated in Figure 5.12, the samples demonstrated a continuous increase in the change to the electrical resistance upon the loading and a decrease in the unloading of tensile strain. Upon cyclic loading, the change in electrical resistance in CBTPU-30GPLA reached a peak value of 3.9. CBTPU-40GPLA had a peak value of 38, which was 10 times higher than that acquired in CBTPU-30GPLA. There was apparent drifting in the CBTPU-40GPLA initiating higher values of electrical resistance upon the cyclic strain. The value of change in electrical resistance was the highest in CBTPU-50GPLA, reaching 56 with repetitive behaviour upon loading/unloading.

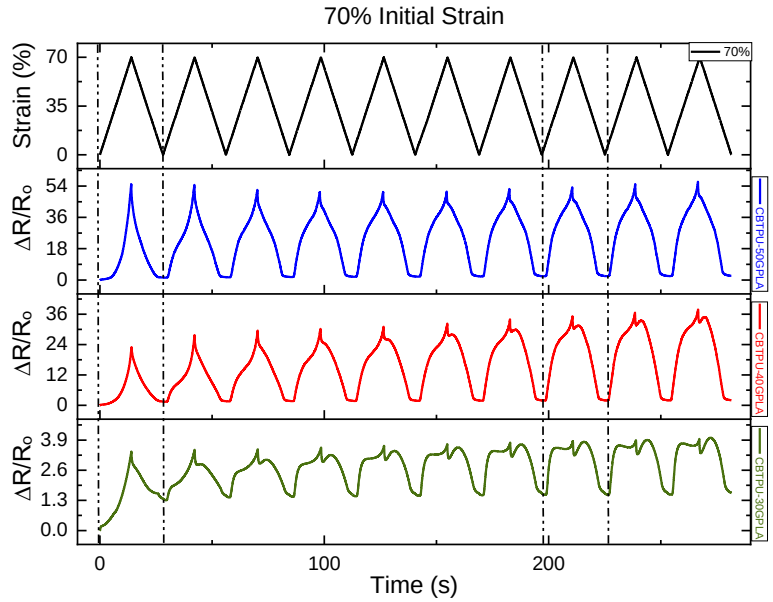

Figure 5.12: 3D printed CBTPU-50GPLA, CBTPU-50GPLA and CBTPU-50GPLA at cyclic initial strain value of 70%.

At the 100% cyclic strain, illustrated in Figure 5.13, the change in electrical resistance for the CBTPU-30GPLA reached a peak value of 15, with apparent drifting observed during the cyclic strain. The CBTPU-40GPLA peaked at 52, which was more than 3 times the change in resistance value found in the CBTPU-30GPLA. On the other hand, CBTPU-50GPLA showed an irregular change in electrical resistance, reaching a peak value of 1963, suggesting a disconnection in the conductive paths. However, CBTPU-50GPLA showed repeatable behaviour upon loading/unloading despite the electrical signal disconnecting at a peak strain value of 100%. Furthermore, the TPU substrate encapsulates exhibited the ability to withstand high stretchability mechanically and govern the reconstruction of the conductive pathways upon unloading, as evidenced by the ability of the sample to recover after each cycle.

It was noticed that the samples did not fully recover after each cycle, which was expected in stretchable materials. The non-recoverable electrical resistance was attributed to the residual strain observed in the mechanical behaviour of the samples. Another reason was that the permanent destruction of conductive paths due to tensile strain prevented the full recovery of change in electrical resistance after each cycle.

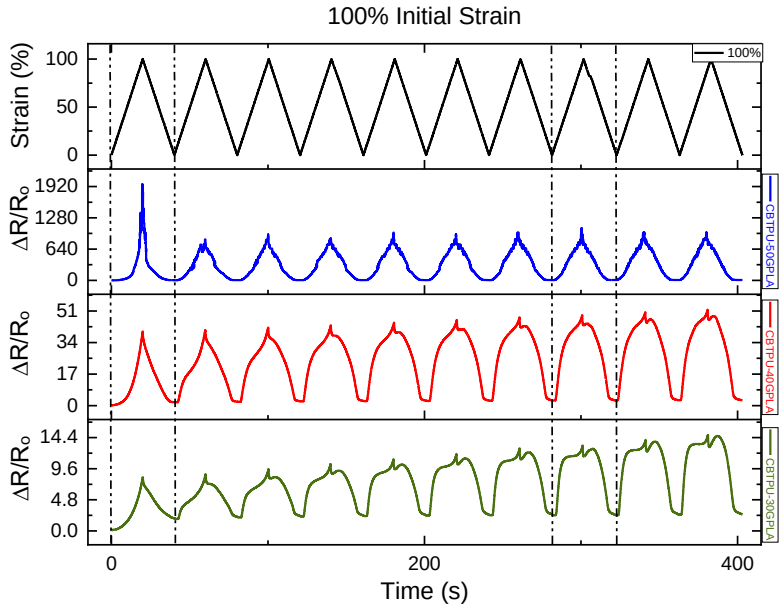

Figure 5.13: 3D printed CBTPU-50GPLA, CBTPU-50GPLA and CBTPU-50GPLA at cyclic initial strain value of 100%.

5.6 Analysis and characterisation of crack formation

The samples were characterised using an optical microscope. The substrate colour was a clear visible TPU filament to allow visualisation of the embedded conductive filaments. CBTPU-30GPLA, CBTPU-40GPLA and the CBTPU-50GPLA embedded in the substrate were black. The samples were characterised in the optical microscope while they were subjected to tensile strain. This process was carried out to investigate the distinct difference in electrical resistance behaviour in the 3 samples at strain values up to 100% tensile strain. Optical microscopic images were taken in real-time as the strain values increases. The images were further processed in software called ImageJ (See Appendix A). In the software, the images were converted into binary black and white, where black represented uncracked conductive material and white represented the cracked areas of the embedded sensing material. This software allowed us to capture the cracks, and consequently, we were able to take measurements of their effect in the sensing materials. It was possible to identify the average cracks' opening height to the longitudinal strain and registered the values in excel sheets.

At 50% strain, the sensing filaments embedded within the substrate had different responses to the applied strain. Samples with higher GPLA (>= 40 wt%) content showed apparent crack formation to the applied strain. CBTPU-50GPLA and CBTPU-40GPLA induced crack formations to the sensing material (black) embedded within the encapsulate (clear) substrate. CBTPU-50GPLA, induce a relatively high density of crack formation at a strain value of 50%. On the other hand, CBTPU-40GPLA showed low crack formation at strain value >= 50% in comparison to CBTPU-50GPLA. In contrast, CBTPU-30GPLA with the least content of GPLA had not shown any crack formation up to a strain value of 100%.

It was also found that the cracks propagated as a function to applied strain where higher strain induced a higher value of average crack openings, as shown in Figure 5.14. Also, the heights of the longitudinal strain depended on the content of GPLA within the sensing materials. The higher the addition of GPLA to CBTPU, the higher the average height of cracks in the embedded conductive material within the stretchable substrate. Looking at the graph of comparison between the CBTPU-50GPLA and CBTPU-40GPLA, we can see a distinct difference in the crack openings at tensile strain values of 50%, 70% and 100%.

This difference was attributed to the mechanical capability of CBTPU-30GPLA to withstand tensile strain >100% to break. Increasing the content of the GPLA increased the rigidity of the material and introduced crack formation to the sensing material within the stretchable substrate with GPLA content => 40 wt%. Sensors with 50 wt% GPLA content showed the highest crack formation, with crack density increasing gradually with increased tensile strain from 50-100% strain. The optical microscopic images allowed us to see which of the samples had crack formation induced. Also, we were able to see which value of tensile strain the cracks started to occur.

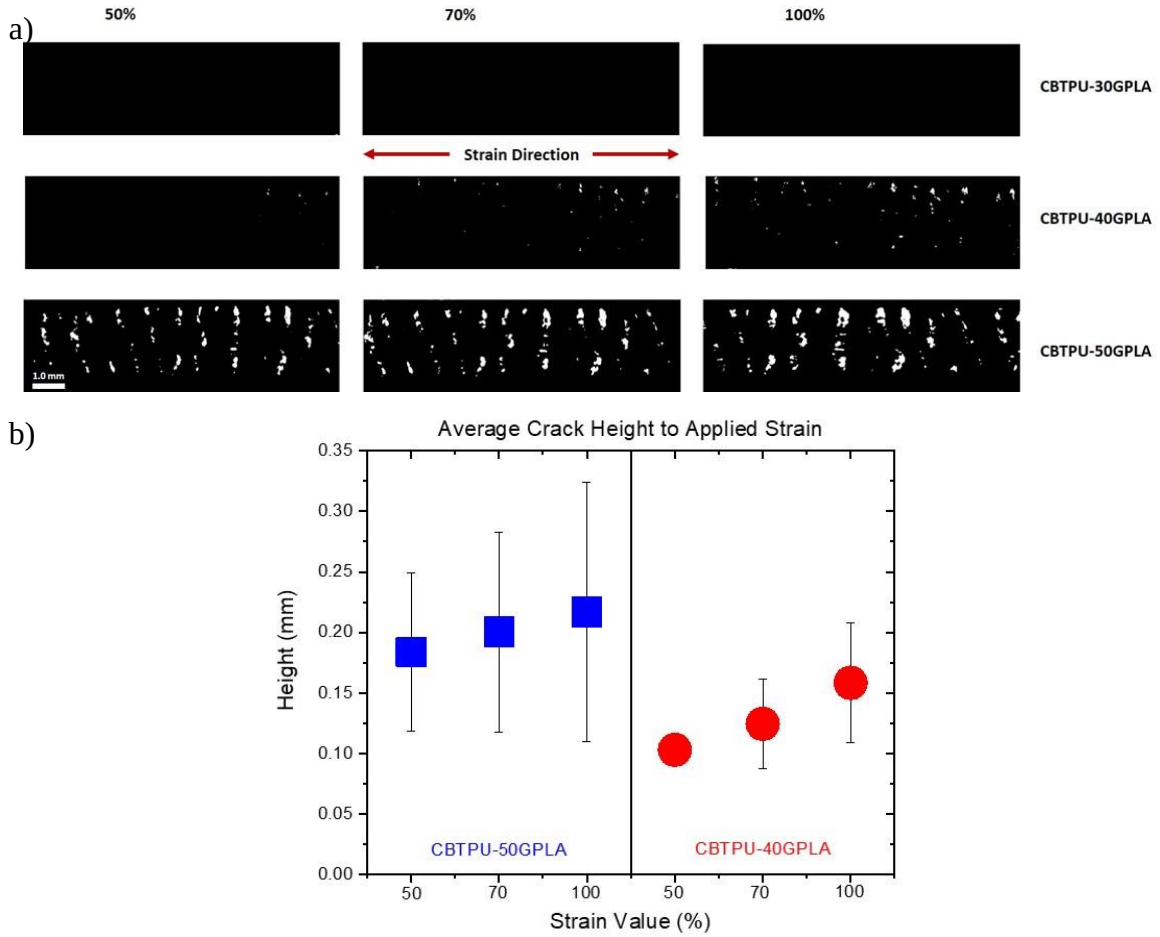

Figure 5.14: a) Crack formation of different samples at various strain values. b) Comparison of average crack height (mm) between CBTPU-50GPLA and CBTPU-40GPLA at various strain values.

5.7 Crack formation of CBTPU-50GPLA at lower strain values

We further investigated the optical microscopic images of CBTPU-50GPLA in the range between 5-50%, as illustrated in Figure 5.15. Inspection of the crack openings revealed average crack opening values increased at tensile strain values between 5-10%, as shown in Figure 5.15b. The average crack height slightly changed between 10-30%. At higher strain values, we noticed a sharp increase between 40-50%. The sharp increase could be attributed to the higher mechanical stiffness of the sensing material to accommodate the higher strain. To investigate the crack effect in the samples more thoroughly, we looked at the total area of cracks at strain values from 5-50%. In the CBTPU-50GPLA samples, Figure 5.15c shows the total area of crack formation in the sensing material, the percentage of the total crack area increases gradually as the strain value increases from 5-50%. Looking at the graph, we see a gradual increase in the total crack area as in strain value increases. At strain values from 10-30%, although there was no significant increase in crack height, there was an apparent gradual increase in the total cracks' area as the strain increases. The increase of total crack area was

attributed to the increased number of crack spots, as evidenced in the optical images. Looking at the total crack area in the range between 40-50%, we can see a distinct increase in the total crack area complementing the increase in average crack heights.

As seen in the previous section, increasing the content of the GPLA introduced a crack formation to the sensing material within the stretchable substrate with GPLA content => 40 wt%. At 40 wt% GPLA content, the sensors showed a small crack formation at a tensile strain of 50%, 70% and 100%. Sensors with 50 wt% GPLA content showed the highest crack formation, with crack density increasing gradually with increased tensile strain from 50-100% strain. The crack formation explains the higher value of change in electrical resistance as the content of GPLA increases. We also saw higher tensile strain-induced higher crack density, which led to higher electrical resistance change at a peak strain value of 100%.

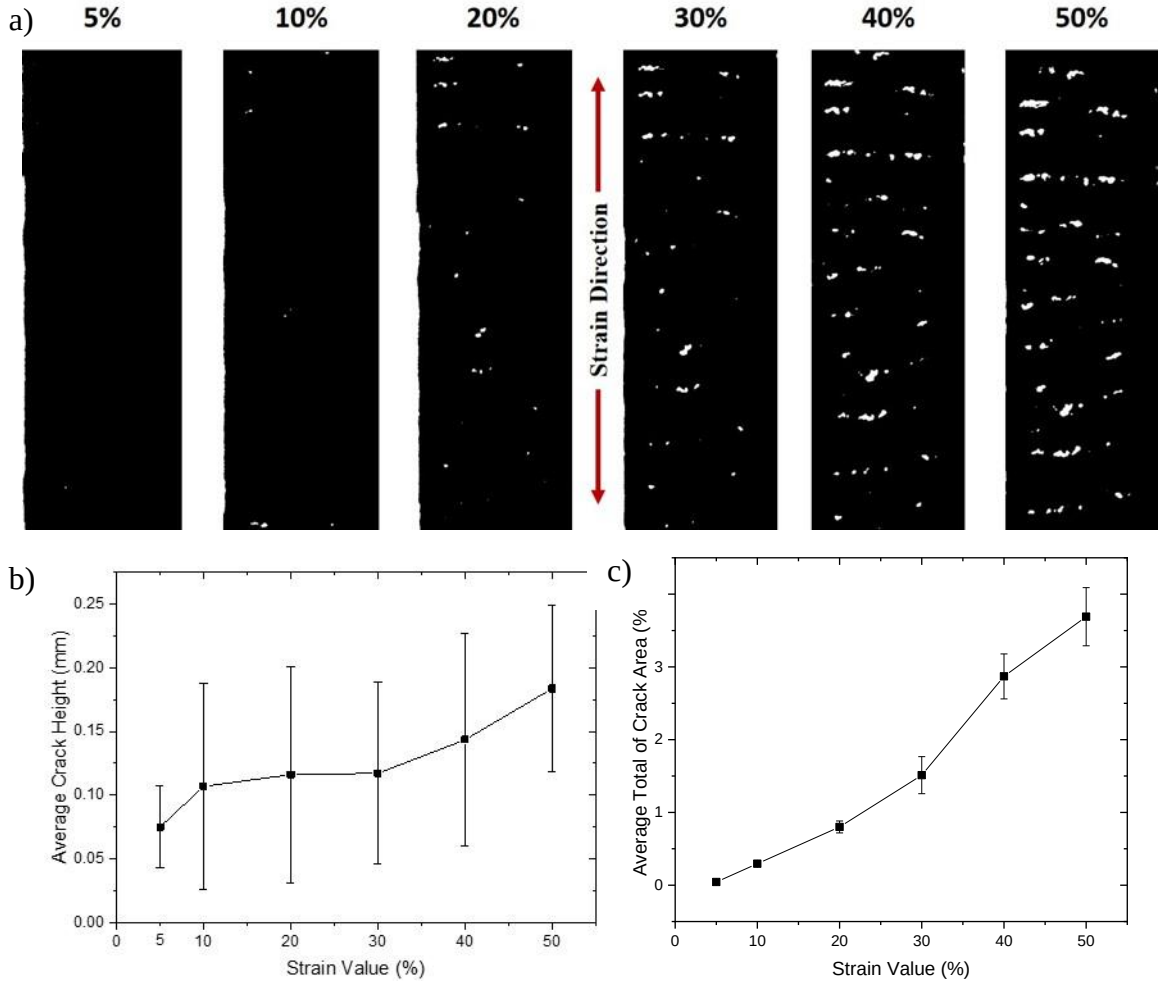

Figure 5.15: a) Crack formation of CBTPU-50GPLA at strain values between 5-50%. b) Comparison of average crack height (mm) of CBTPU-50GPLA as strain value increases from 5-50%. c) Calculation of total crack area (%) of CBTPU-50GPLA as strain value increases from 5-50%.

5.8 Electrical response of cyclic strain

The samples were further monitored under cyclic loading at relatively lower strain amplitude after the initial tensile strain cycles. The samples pre-strained to 50%, 70% and 100% were further subjected to 30% of 10 strain cycles. The change in electrical resistance was measured simultaneously as the samples were subject to cyclic strain. Cyclic testing of the 3D printed samples was performed to investigate their reversibility and reliability for strain sensing applications.

Figure 5.16a shows the change in electrical resistance of 10 cycles at 30% strain of samples with 50% pre-straining. CBTPU-50GPLA and CBTPU-40GPLA showed a gradual increase in the change to resistance with strain loading and a decrease with unloading, which is described as the positive strain effect. However, CBTPU-40GPLA showed a slight double peak effect as the strain value increased from 15%-50%. Reproducible cyclic response of change in electrical resistance can be seen in both CBTPU-50GPLA and CBTPU-40GPLA as illustrated in the 8^{th} cycle magnified in Figure 5.16b. In contrast, CBTPU-30GPLA showed a negative strain effect, where the cyclic change in electrical resistance decreased inversely to the increase in tensile strain and a further increase in the electrical resistance as the strain value decreased. CBTPU-50GPLA change in electrical resistance reached a peak value of 5.7, which was almost 4 times higher than CBTPU-40GPLA with a peak value of 1.5. CBTPU-30GPLA reached a peak value of 0.45, which was noticeably lower than that found in CBTPU-50GPLA and CBTPU-40GPLA.

The change in electrical resistance at 30% strain in samples with 70% pre-straining is illustrated in Figure 5.16(c-d). CBTPU-50GPLA and CBTPU-40GPLA also performed with good linear stability at cyclic strains reaching peak values of 14.2 and 7.4, respectively. CBTPU-30GPLA showed a positive linear increase in electrical resistance up to 15%, followed by a slight double peak effect as the strain value increased from 15%-50%, reaching a peak value of 1.2.

Figure 5.16(e-f) shows the cyclic behaviour of change in electrical resistance in samples with 30% strain and 100% pre-straining. CBTPU-50GPLA and CBTPU-40GPLA also performed with good linear stability at cyclic strains reaching peak values of 48.6 and 11.7, respectively. We noticed the value of change in electrical resistance in CBTPU-50GPLA pre-strained to 100% increased more than 3 and 8 times than those in samples pre-strained to 70% and 50%, respectively. CBTPU-30GPLA showed a positive linear increase in electrical resistance of up to 15%, followed by a minor double peak effect as the strain value increased from 15-50%, reaching a peak value of 4. All 3 samples pre-strained to 100% showed good linearity with a

moderate double peak effect observed in the CBTPU-30GPLA sample. Overall, they performed with good sensing stability at 30% cyclic strain, represented with good recoverability and reproducibility.

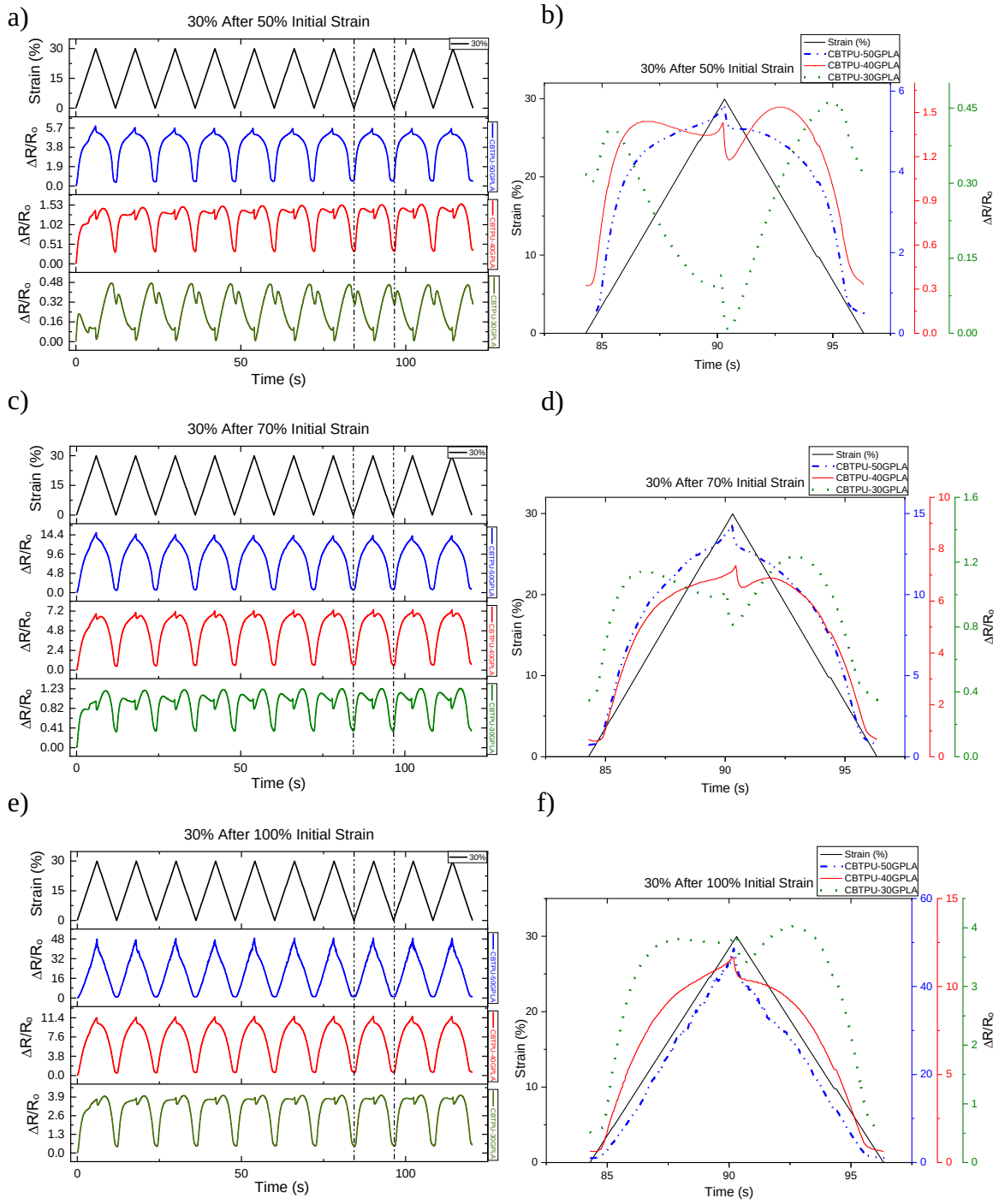

Figure 5.16: Change in electrical resistance at 30% strain under 10 cycles of samples pre-strained at a) 50% pre-strain with b) 8th cycle magnified, c) 70% pre-strain with d) 8th cycle magnified, and e) 100% pre-strain with f) 8th cycle magnified.

5.9 Gauge factor

We measured the gauge factor of the sensors at a 30% strain value. The gauge factor was calculated by dividing the change in electrical resistance divided by the change in length of the sensor caused by tensile strain. The calculation for the gauge factor GF is expressed in Equation (2.3). Figure 5.17 shows the average gauge factor calculations at 30% cyclic strain of samples pre-strained from 50%-100% strain values. CBTPU-30GPLA showed relatively low sensitivities with an average gauge factor ranging between 1.5, 4 and 13 at samples pre-strained to 50%, 70% and 100%. In contrast, CBTPU-40GPLA showed noticeably higher sensitivity with average gauge factor ranging between 5, 24 and 39 at samples pre-strained to 50%, 70% and 100%, respectively. CBTPU-50GPLA showed the highest calculated sensitivity with average gauge factors ranging between 19, 48 and 161 at samples pre-strained to 50%, 70% and 100%, respectively. Looking at the Gauge factor values shown in Figure 5.17, we can see that 2 distinct factors influenced the sensitivity of the 3D printed samples. The samples with the highest value of GPLA content had markedly higher sensitivity values, for example, CBTPU-50GPLA. Another factor was that as the higher initial strain increased, the sensitivity increased sharply. For example, the samples reached the highest gauge factor of 163 in the CBTPU-50GPLA sample with 100% initial strain. The increase in sensitivity was due to the increase in the crack formation as the strain value increases (as seen in the crack formation section 5.6).

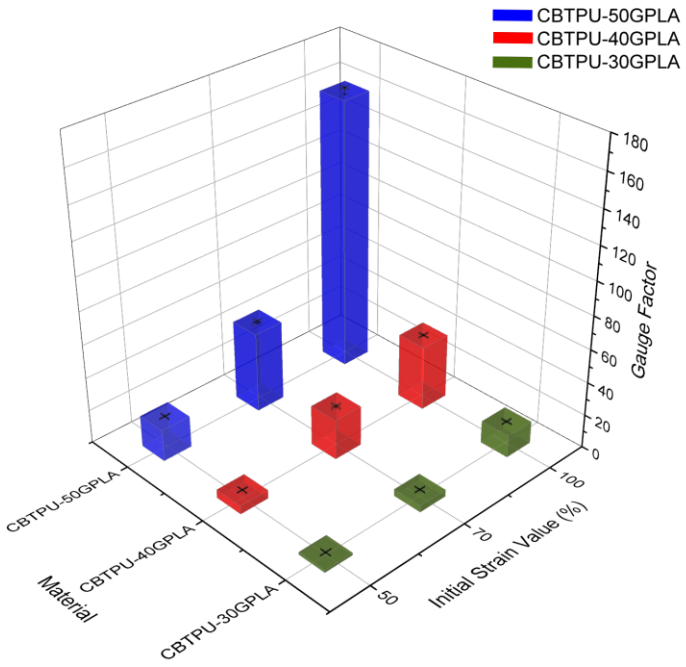

Figure 5.17: Average theoretical gauge factor GF values at 30% cyclic strain of samples with various GPLA content and pre-strained values.

5.10 Varying range and strain rate

In order to further illustrate the capability and wide range of sensitivity, Figure 5.18 shows the CBTPU-50GPLA sample at various cyclic strain values ranging from 5-50%. The sensor showed good linearity and reproducibility of change in electrical resistance.

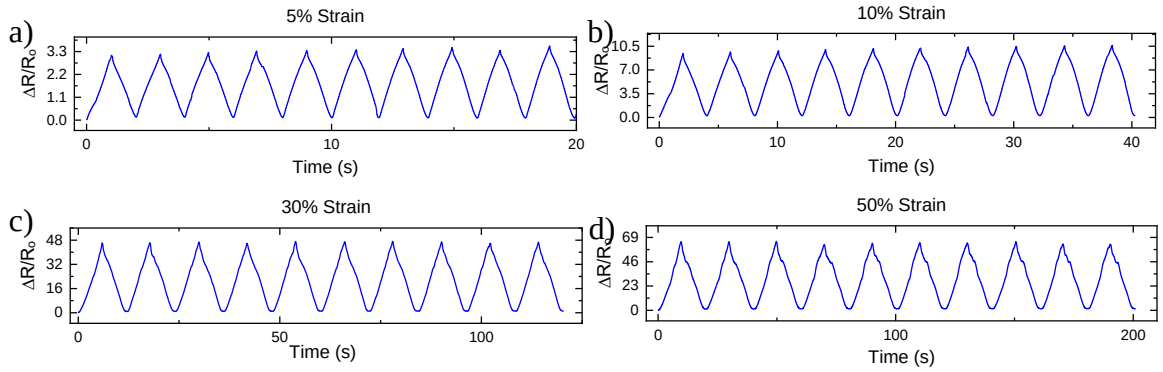

Figure 5.18: Cyclic resistance change at various strain values.

The strain sensor was also subjected to various strain rates, and the electrical response was measured. Figure 5.19 shows the sensor subjected to strain rates ranging from 0.5-4 mm/s as different applications may require various strain rates. It shows that the sensor coped with little to no effect in electrical resistance response under various strain rates. This result also shows the strain independent of stretching speed rate.

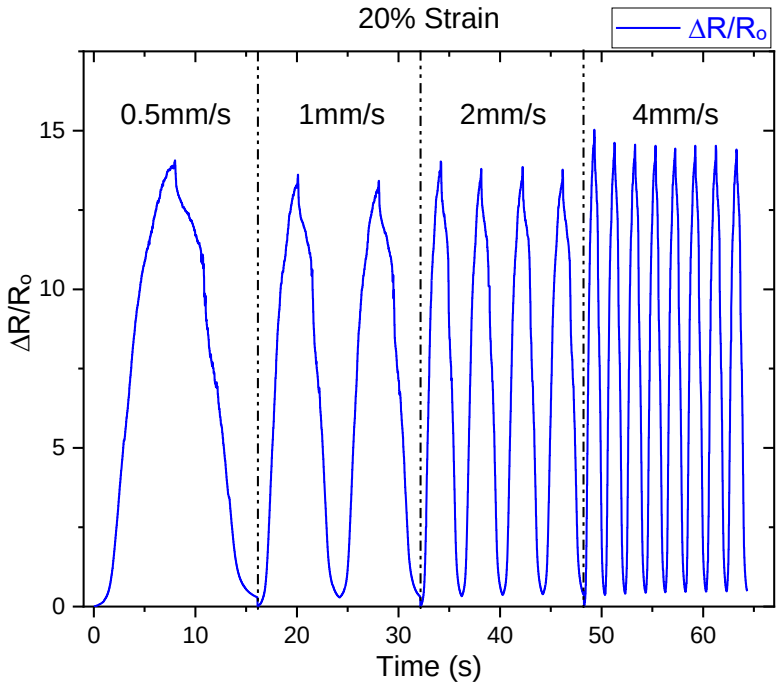

Figure 5.19: Cyclic resistance change of 20% tensile strain at various strain rates.

5.11 Reliability and stability performance

One thousand cycles were performed to test stability and reproducibility to ensure the sensor's reliability for long term use. The CBTPU-50GPLA sensor was subjected to 1000 cycles at 30% strain, as shown in Figure 5.20. The sensor possessed excellent repeatability and reproducibility, proving it to be a great candidate for vast applications in human motion detection and robotics.

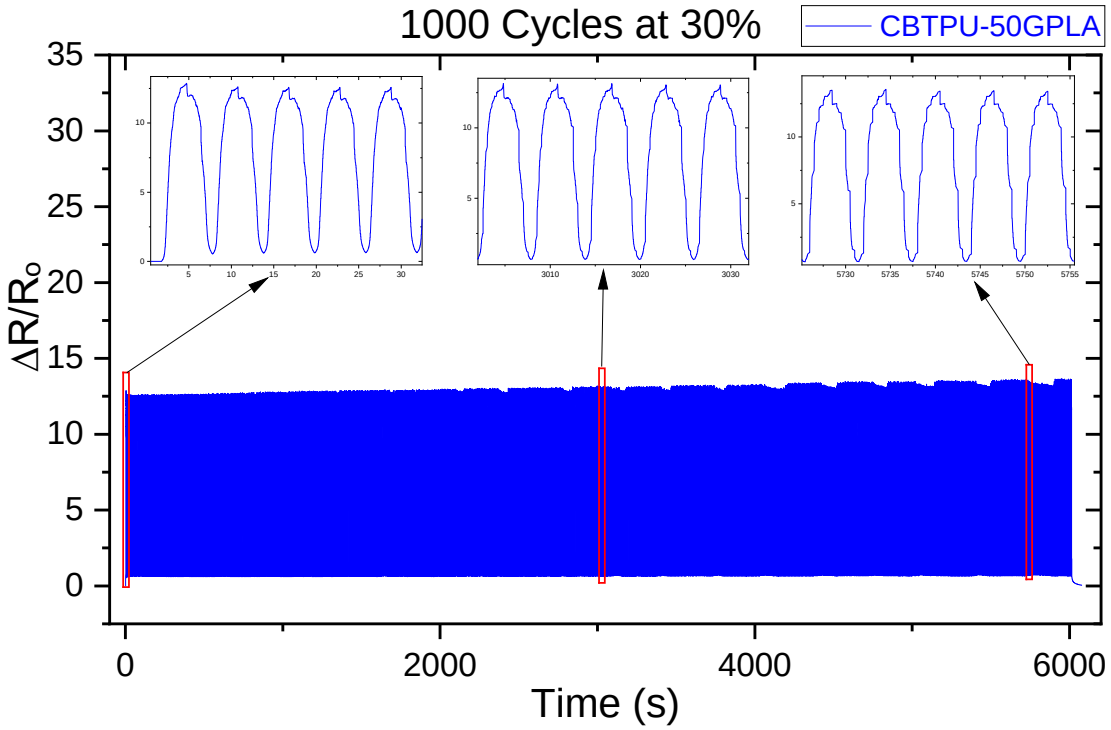

Figure 5.20: Electrical response at 1000 cycles. Insets of magnified cycles from first 5 cycles through 500-504 cycles and 950-954 cycles.

5.12 Applications of the 3D printed strain sensors

5.12.1 Hand fingers motion detection

We fabricated a number of these sensors to detect the motion of hand fingers, robotic hand fingers and detect the heartbeat pulses to demonstrate the potential of the 3D printed strain sensors. Five strain sensors were sewed to a glove by attaching one sensor for every finger, as illustrated in Figure 5.21a. The attached sensors were connected to a data logger through a PC to record the sensors in real-time. The attached sensors allowed us to register the motion of each finger in real-time by recording change in electrical resistance as fingers moved, as demonstrated in Figure 5.21b.

a)

b)

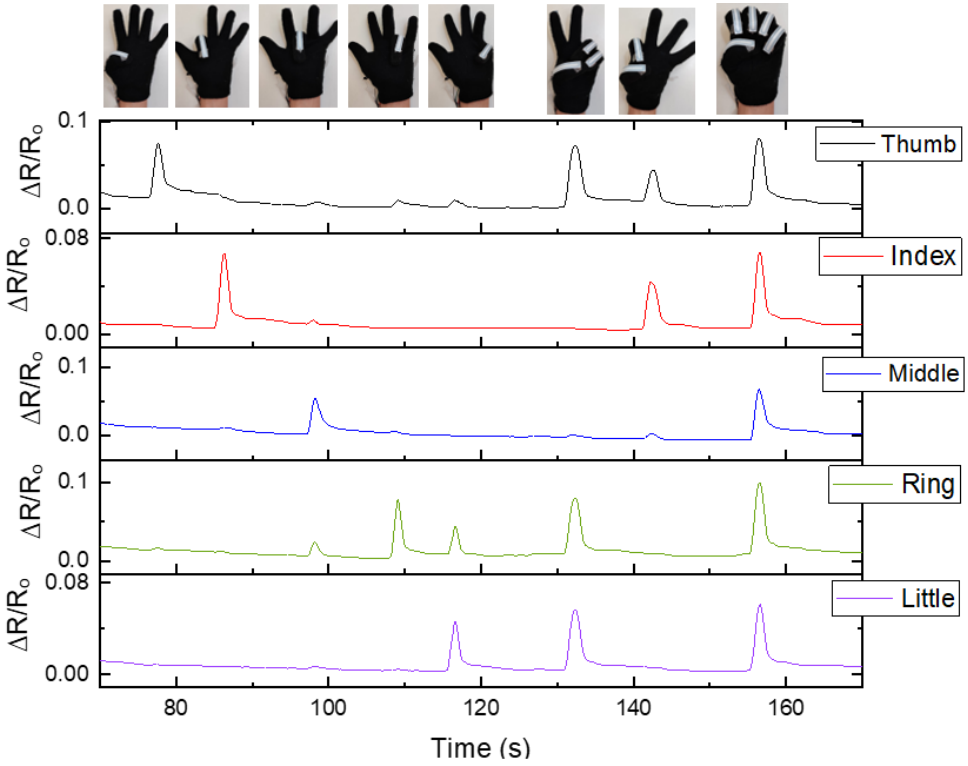

Figure 5.21: a) Optical image of the strain sensors attached to glove. b) Electrical resistance change as function of time for capturing finger motion detection to various hand gestures.

5.12.2 Robotic hand finger motion detection

A robotic hand was fabricated with 5 embedded strain sensors 3D printed simultaneously inside the robotic hand's fingers. The robotic hand fingers were attached to 5 servo motors connected to an Arduino and connected to a PC, as illustrated in Figure 5.22, allowing us to programme the motion of the fingers by writing a simple code for the servo motors. The servo motors which move the robotic fingers were assigned to the Arduino digital channels. Then, a code provided from the Arduino library was used to rotate the servo motors, which move the robotic

fingers. The motion of the fingers can be monitored and registered by recording the change in resistance of the sensors embedded in the robotic hand. These embedded sensors provided feedback function of the 3D printed robotic hand. (See Appendix B)

a)

b)

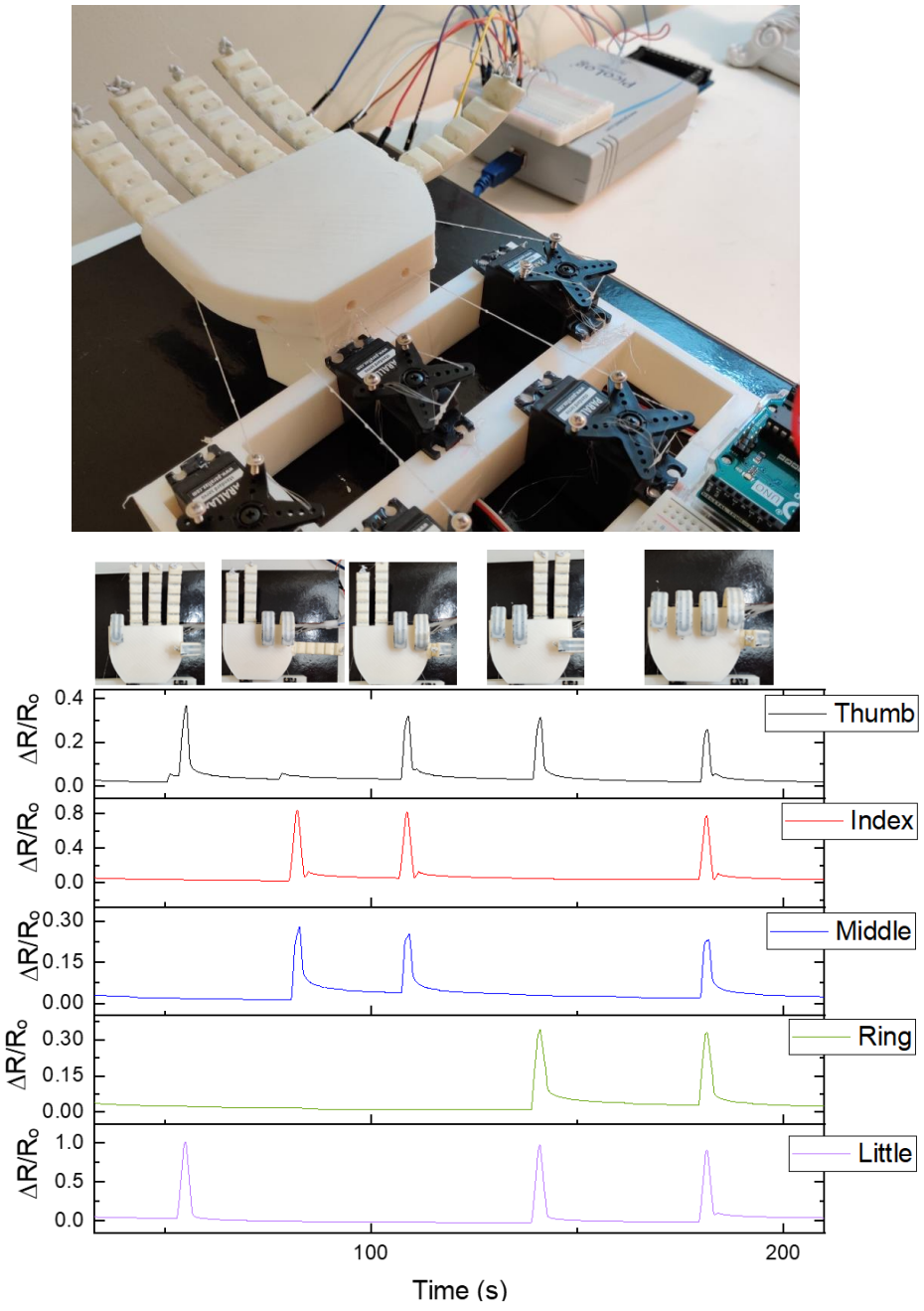

Figure 5.22: a) Optical image of the robotic hand with embedded strain sensors, b) Electrical resistance change as a function of time for the strain sensors embedded in the robotic hand.

5.12.3 Heartbeat sensing

A 3D printed strain sensor was attached to the wrist to record the physical movement of the heartbeat pulses, as shown in Figure 5.23a. Monitoring was achieved by recording the change in electrical resistance in real-time as the heartbeats, as illustrated in Figure 5.23b. The ability

to detect the physical strain caused by the heartbeat pulses on the wrist proved that these 3D printed strain sensors were able to detect very low strain values.

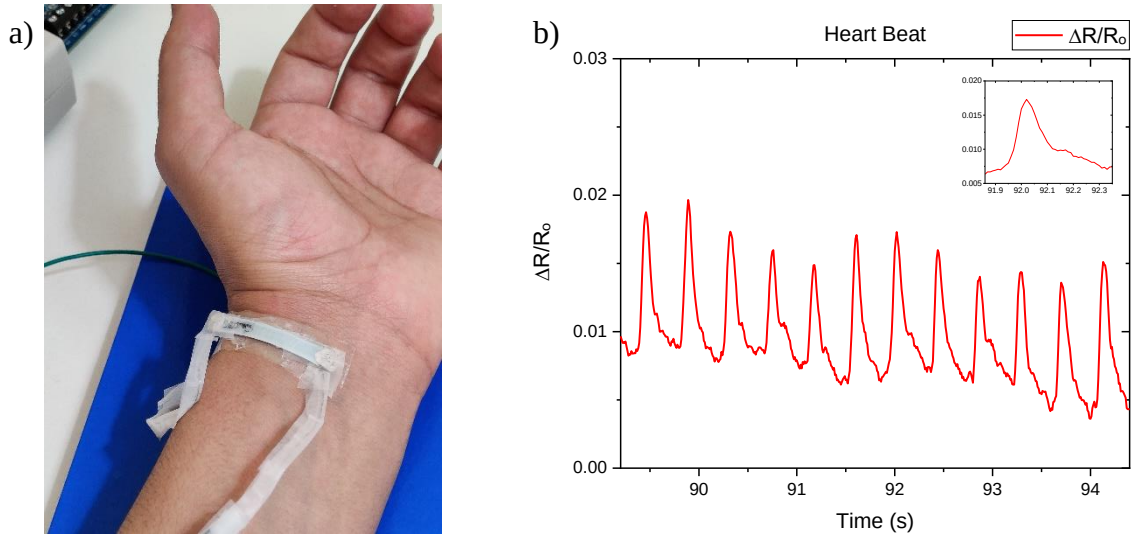

Figure 5.23: a) Optical image of strain sensor attached to the wrist, b) Heartbeat pulse detected by the strain sensor attached and Inset showing magnified image of accurate measurement of a heartbeat pulse.

5.13 Summary

The development of the sensing material composites allowed the creation of strain sensors with good recoverability and reproducibility. These samples were subjected to various strain amplitudes ranging from 5 to 100% tensile strain values. A method of mixing 2 conductive pellets to fabricate highly sensitive strain sensors with a linear response is presented. Pre-straining of the 3D printed sensors caused a crack formation, which possesses high sensitivity. The influence of pre-straining was evident in the sensitivity as higher pre-straining values resulted in higher sensitivity. The pre-straining positively impacted the 3D printed strain sensors' cyclic behaviour, and it was evident that samples with a higher GPLA content had a positive linear behaviour with higher sensitivity under cyclic strain. The results obtained combined the ability of highly stretchable 3D printed strain sensors of >50% while maintaining positive linearity. In addition, the values of gauge factors obtained reaching as high as 163 showed unprecedented sensing capabilities in comparison to previously 3D printed strain sensors summarised in Table 2.1. The sensors performed with little evidence of hysteresis at various strain values and demonstrated good stability and reproducibility in cyclic tests of up to 1000 cycles. Consequently, these sensors proved they had a comprehensive range of sensing capabilities ranging from robotic hand and finger motion detection to a heartbeat.

Chapter 6–Tuneable sensitivity by multi-material 3D printing of multi-layered resistive pressure sensors

6.1 Introduction

Tactile and pressure sensors are examples of devices that play a major role in advancing human machine interaction, wearable electronics and soft robotics. The purpose of this chapter is to extend further the capabilities of the digital platform developed in Chapter 4 and Chapter 5 by taking advantage of multi-material 3D printing in developing pressure-sensing applications. Piezoresistive pressure and tactile sensors have attracted much attention in recent years due to their inherent flexibility, stretchability, low energy consumption, and easy read-out. This chapter presents the development of 3D printed multi-layered resistive pressure sensors and their performance under compressive load. A novel method of fabricating soft compressible multi-layered pressure sensors via FDM 3D printing is presented. The set of materials and design of the pressure sensors are also described. It is followed by the illustration of the layer-by-layer fabrication process and post-processing. The chapter introduces a multi-layered pressure sensor design that takes advantage of multi-material 3D FDM printing. The mechanical and electrical performance of the 3D printed pressure sensors tests is outlined in detail. The distinctive tuneable sensitivity of the multi-layered pressure sensors is further illustrated and discussed. The proposed multi-layered sensor design is compared to a solid design of the same conductive material. We also look at how increasing the thickness of the multi-layered sensor influenced the sensitivity of the samples. The use of 3D printing allowed us to tune the sensitivity using supporting scaffold material and made it possible to increase the number of sensing layers. The design flexibility offered by 3D multi-material printing overcame the constraint of conventional fabrication techniques. Eventually, to show the capability, versatility and potential of these sensors, various applications are illustrated.

6.2 Materials preparation

For the sensing material, carbon black thermoplastic polyurethane CBTPU was chosen as it was the highest elastic material suitable for the pressure sensor. To prepare the 3D printable filament, pelletised CBTPU was extruded via a filament extruder. CBTPU pellets were dried at 70 °C overnight before any melt processing using a material dryer. After that, CBTPU was melt-processed and extruded at the recommended temperature of 170 °C, using a single-screw extruder (Noztek Pro, Noztek Ltd.) to form a strand of 3D printable filament with a 1.75 mm diameter. The average electrical resistivity of the material measures 100 Ω.m. For the

supporting material, Polyvinyl alcohol (PVA, a dissolvable material, was chosen. It was used as the supporting structure for 3D printed pressure sensors that included overhang structures. It is a water-soluble material in the form of a 3D printing filament spool and was used as received.

6.3 3D Design and fabrication of pressure sensors

6.3.1 Design

The pressure sensors were modelled using 3D CAD modelling software. The design considered the flexibility of the sensing material chosen and the accuracy of the 3D printer. As shown in the schematic illustration in Figure 6.1, the design concept consists of suspended layers measuring an area of 10 mm^2. Since the conductive material was highly flexible, we designed the layers to be 0.4 mm thick for the integrity of the structure. The layers were connected at 2 corners, measuring an area of 2 mm^2 and 0.2 mm thick. These thin interface corners make a 0.2 mm gap between each of the suspended layers. The sensors were designed with 3 different heights based on the number of layers illustrated in Figure 6.1. The heights of the sensors were 1.6 mm, 2.8 mm and 4 mm. The dimensions of the samples consider the smallest feature size for their use and practicality in various applications [150], [151]. For comparison, a solid sensor was designed to measure an area of 10 mm^2 and 1.6 mm in height.

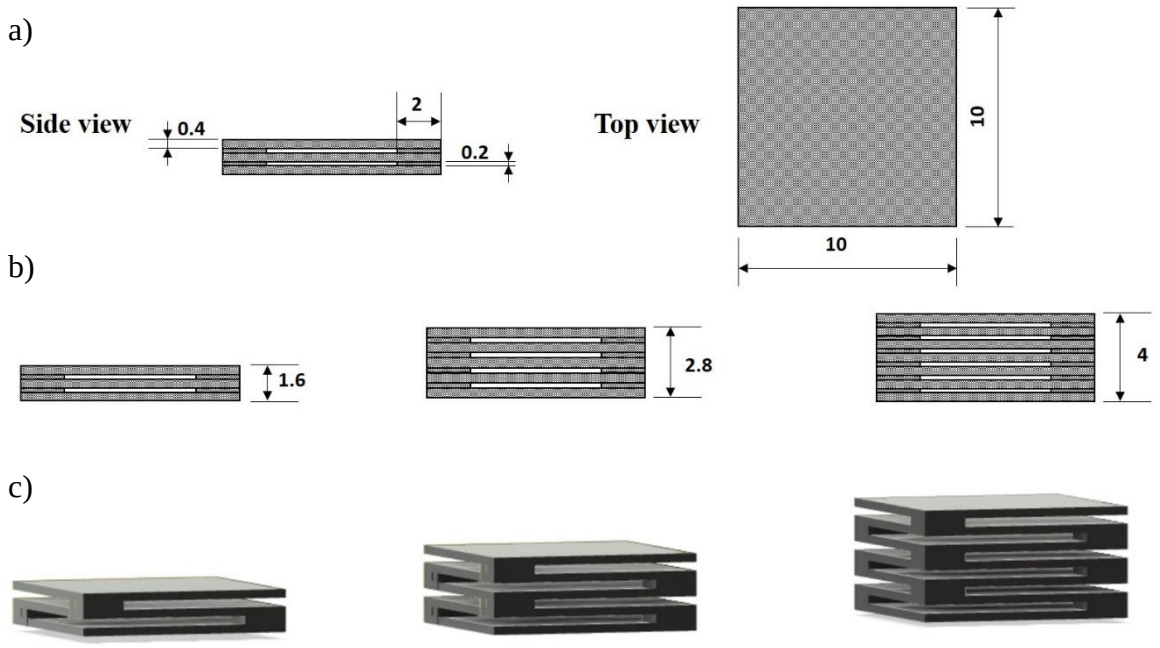

Figure 6.1: Schematic illustration of the multi-layered design of a) Side and top views showing measurements of the design, b) Side view of the models with various thicknesses, and c) 3D models of the sensors with varying thicknesses.

6.3.2 Multi-material fabrication

The fabrication of the pressure sensors takes advantage of multi-material FDM 3D printing. A 3D printer with a dual extrusion FDM system was employed to 3D print the conductive sensing filament simultaneously with the supporting material. The schematic illustration in Figure 6.2 shows the one-step fabrication of the multi-layered pressure sensors. The sensors were 3D printed layer by layer. Firstly, the 3D CAD design was imported to the printer's software to tune the printing settings and slice the model in layers. The tuned design was then exported to an SD card in a G-code format that the 3D printer understands. For each layer, the printer's platform lowers to allow for the next layer to be printed. At the start of 3D printing, 2 layers of the conductive material were printed with a layer thickness of 0.2 mm each. Then for the next layer, 2 corners were printed to connect the lower conductive layer to the subsequent upper one. In order to ensure the integrity of the design, the gaps between the suspended conductive layers were filled by the simultaneous printing of the PVA supporting material in which the printer switches to the second extruder to print the PVA. After that, the upper conductive layer is printed over the supporting PVA. This step was then repeated for the subsequent layers based on the number of layers for each sensor.

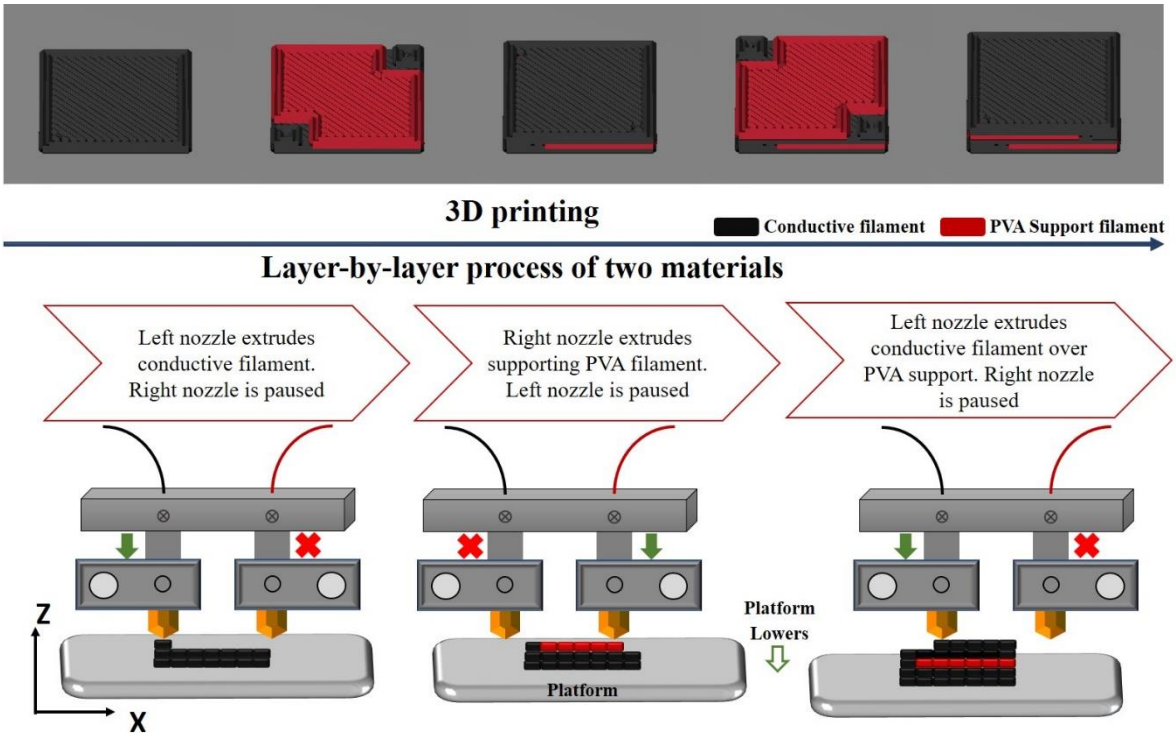

Figure 6.2: Schematic illustration of the dual extrusion 3D printing process, which deposits materials by alternating between 2 independent extruders.

Figure 6.3a shows images of the samples freshly 3D printed and ready for post-processing. Images in Figure 6.3(a-d) show the 3D printed sensors before, during, and after the removal of

the supporting material, respectively. The post-processing of a 3D printed sample was performed to remove the water-soluble PVA scaffold material. After the 3D printing was finished, the PVA scaffold material was simply removed by immersing the sample in water. The sample stayed in the water for 24 hours to allow complete removal of the PVA supporting material. After that, the sample was rinsed and dried at 70°C for an hour to ensure the removal of the remaining water. The delamination apparent in Figure 6.3d can be attributed to the immersion of the samples in water.

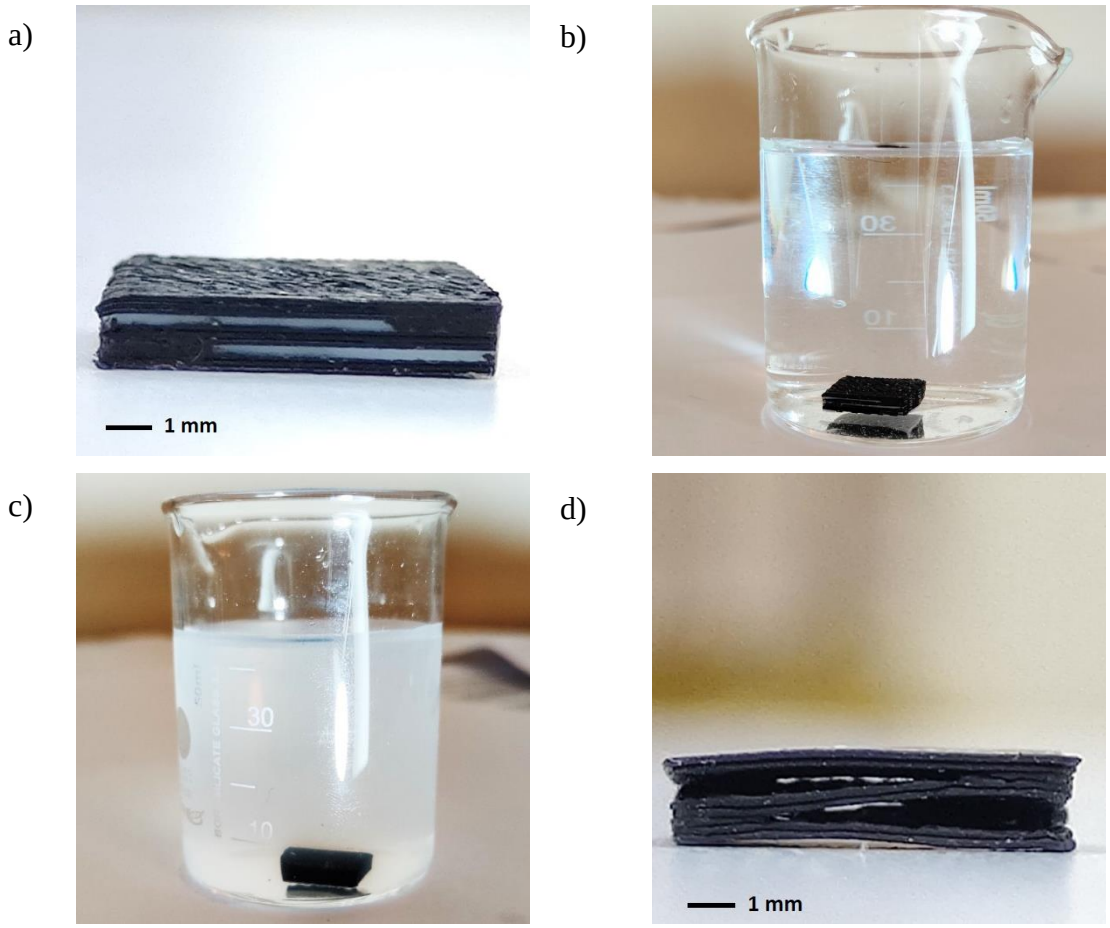

Figure 6.3: Images of the 3D printed multi-layered 1.6 mm sensor of a) The model as 3D printed without any post-processing, b) The sample immersed in water and left for 24 hours, c) Image of the soluble scaffold material dissolving in water and d) Image of the sample dried and ready for use.

For comparison purpose, a solid sample measuring 10 mm^2 and 1.6 mm thickness was printed and is shown in Figure 6.4a. The multi-layered 3D printed samples fabricated in 1.6 mm, 2.8 mm and 4 mm thicknesses were shown in Figure 6.4b, c and d, respectively. The images show visible gaps between the multi-layered samples after the removal of the support material. The structure's integrity was maintained in the samples due to the printed corners between the suspended layers, ensuring continuous electrical conduction through the samples in the vertical

(Z) direction. The 1.6mm sample had 2 gap interfaces between the conductive layers, whereas the 2.8mm and the 4mm samples had 4 and 6 gap interfaces. The gaps were introduced to alter the samples' mechanical and electrical behaviour, explored in the following sections.

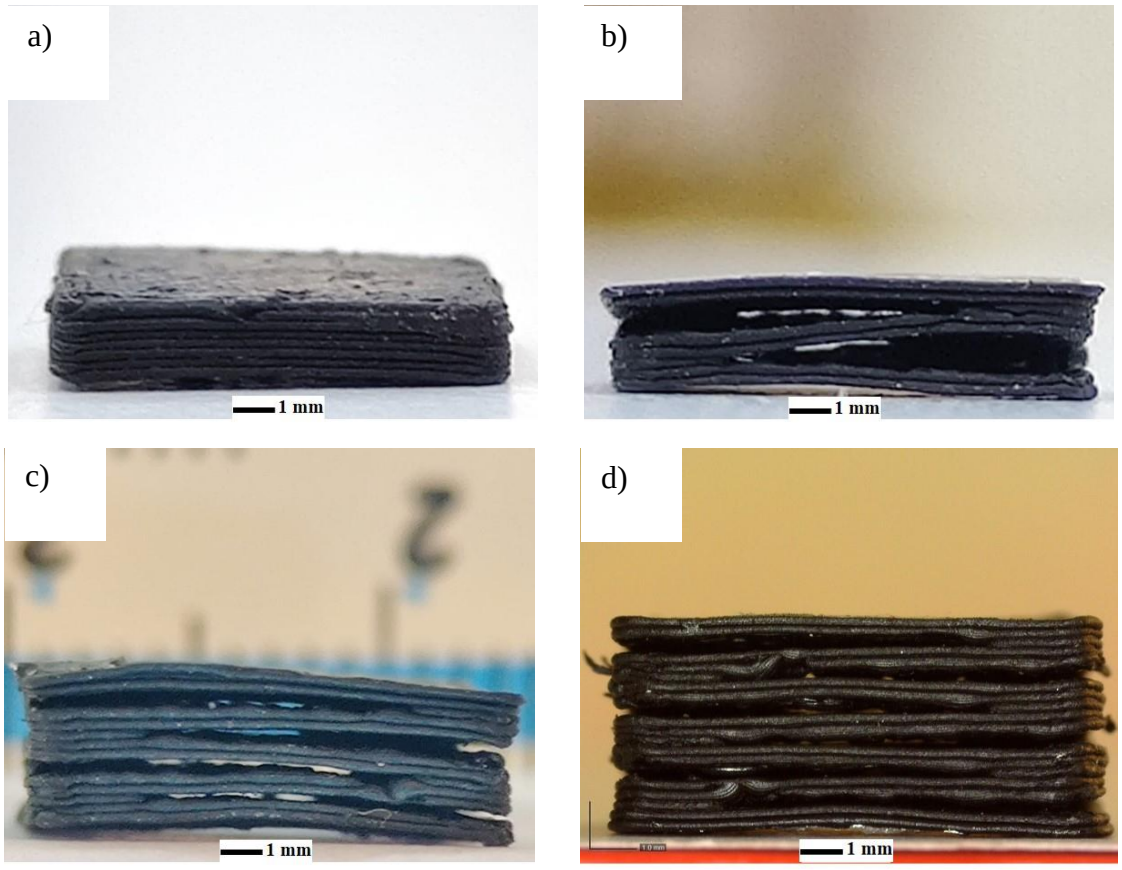

Figure 6.4: Optical images of 3D printed a) 1.6mm Solid sample, b) 1.6mm multi-layered sample, c) 2.8mm multi-layered sample, and d) 4mm multi-layered sample.

6.4 Mechanism of the 3D printed resistive pressure sensors

The working principle of the resistive pressure-sensing of the 3D printed multi-layered sensor is illustrated in Figure 6.5, which shows a schematic representation of the mechanical and electrical behaviour of the resistive pressure sensors used in this research. The represented schematic illustrates the compressive behaviour of multi-layered sensors upon pressure input. When pressure force is applied to a flexible pressure sensor, the resulting mechanical compression enhances the conductive pathways within the sensing material, leading to a decrease in electrical resistance. As the pressure increases, the applied force increases the interface area of contact between suspended layers. The higher the pressure value, the more the sensor compresses, and hence the area of contact between the suspended layers increases. This dynamic mechanical contact deformation greatly influenced the change in electrical resistance of our 3D printed sensors. The applied pressure compressed the layers, which brought the 2

ends of the samples closer together. This compression enhanced the interface contact area between the layers in our sensors. The applied pressure caused the electrical resistance to change as it is compressing the 2 ends of the samples closer together. Higher-pressure compresses the top and bottom ends of the sample closer together, which lowers electrical resistance. The mechanical change in the sensor induced change in electrical resistance measured simultaneously using a simple voltage divider circuit. The sensing mechanism is represented in an equivalent circuit illustrated in the schematic in a graph. When a mechanical force is applied to the sensor, the change of contact area between the suspended layers results in a change in the electrical resistance upon pressure force. The change in electrical resistance upon pressure is measured by Equation (2.2).

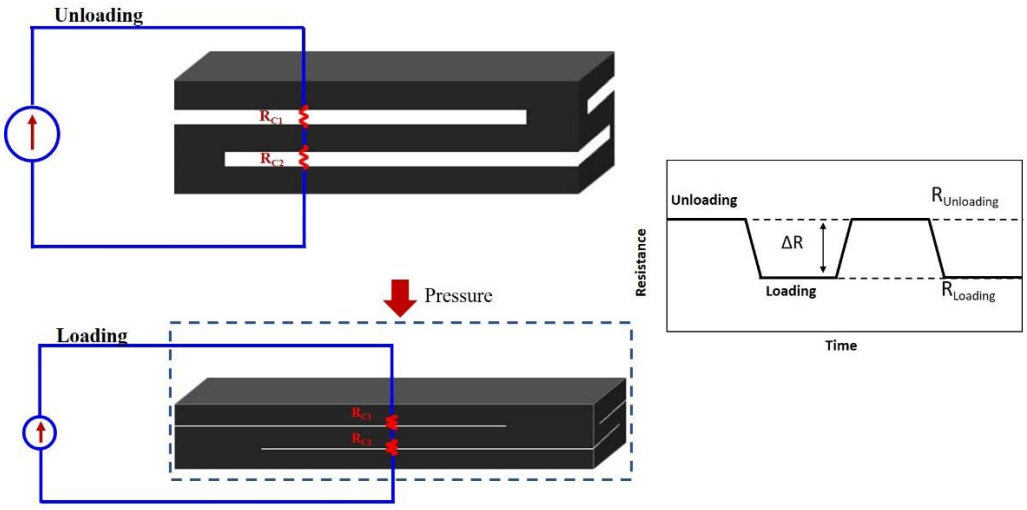

Figure 6.5: Schematic illustration of the mechanism of the multi-layered resistive pressure sensor

6.5 Mechanical results

The mechanical performance of the solid and multi-layered sensors was evaluated. The sensors were subjected to 200 kPa of compressive pressure loading to test its compressibility measured in compressive strain (%) using the Instron machine. The graph shows the resulting compressive strain of the first compressive loading at 200 kPa in Figure 6.6. When 200kPa was applied, the solid sensor's low change in strain compression decreased to 3.5% of compressive strain. On the other hand, the applied pressure greatly influenced the compression strain in the multi-layered sensor. The compressibility in the suspended multi-layered sensor was 4 times higher than that of the solid sensor. The influence of the suspended multi-layer design showed that it was compressed by 13% compressive strain in comparison to the solid sensors with 3.5% compression, both at 200kPa of maximum pressure.

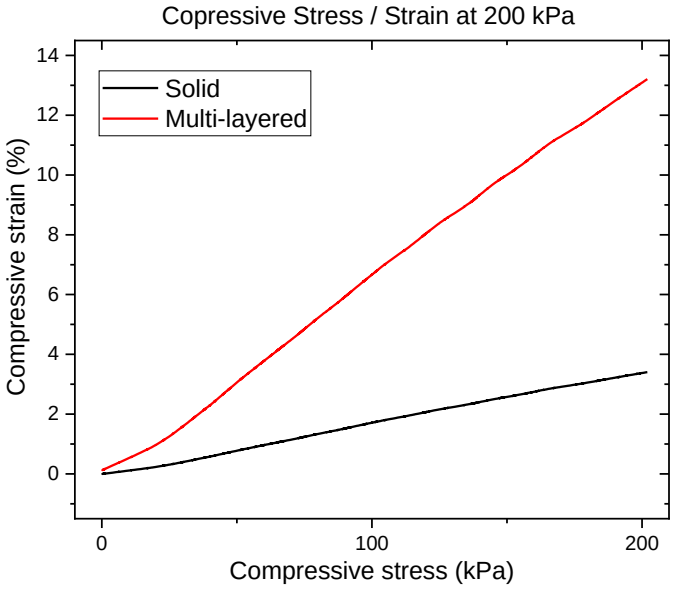

Figure 6.6: Mechanical compressive strain (%) to applied pressure (kPa).

To further investigate their mechanical behaviour, the solid and multi-layered sensors were subjected to cyclic pressure to evaluate their compressibility. Figure 6.7 shows the corresponding response of compressive strain for 10 cycles of constant 200kPa compressive pressure. The cyclic loading demonstrated repeatable mechanical behaviour of both solid and multi-layered sensors. Both sensors showed reproducible strain compressibility with an applied constant pressure of 200kPa. However, the cycles presented a distinct difference in the mechanical behaviour where high compressibility was noted in the multi-layered sensor compared to the solid sensor. With gaps between conductive layers, the multi-layered design allowed for noticeably high compressibility of the multi-layered sensor.

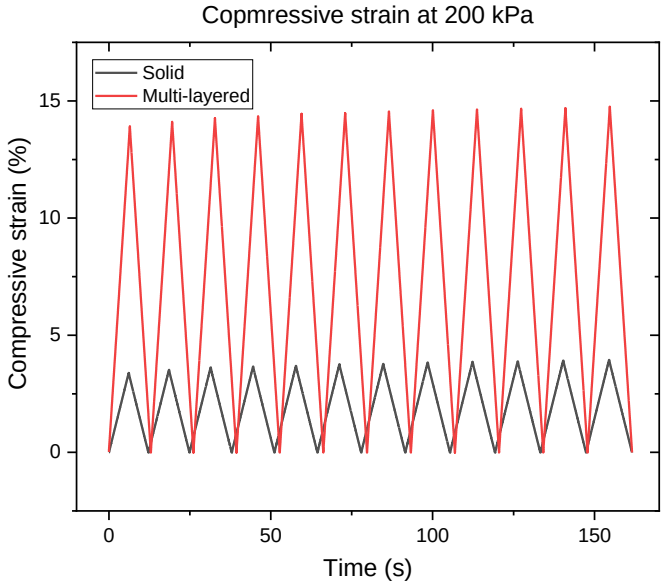

Figure 6.7: Mechanical cyclic strain response (%) to 200 kPa of applied pressure (kPa).

6.6 Optical microscopic images

An optical microscope was used to explore the mechanism of the multi-layered pressure sensor under compression further. Figure 6.8 shows optical microscopic images of the 4mm 3D printed multi-layered sensor before, during applied pressure forces between 200-1000 Pascals, and after the release of the force. The optical microscopic images show an example of how applied pressure affects the pressure sensor from 0-1000 Pa. The images also show the concept of a contact interface with a 4mm sensor under dynamic compressive pressure. The increase in pressure from 0-1000 pascal compressed the sensor's layers in which area of contact increases between the suspended layers as pressure increased. Under compression, the suspended layers were forced to pack more closely together. When the pressure was released, the sensor returned to its initial state, leading to full recovery of the sensor.

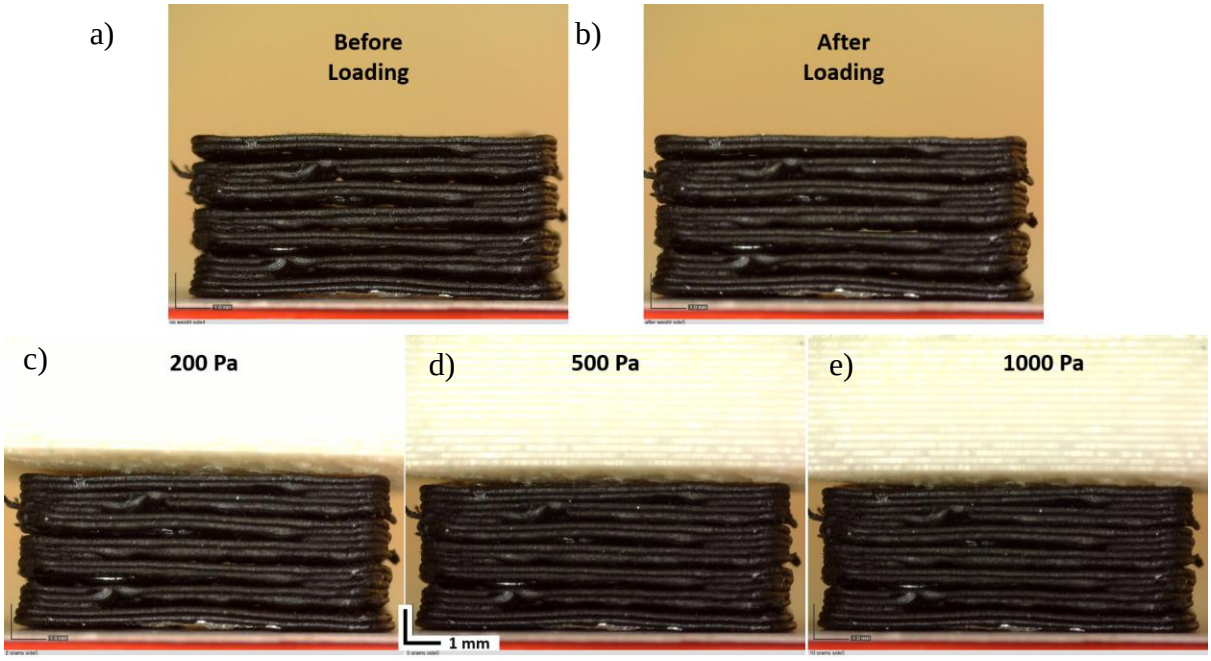

Figure 6.8: Optical microscopic images of the 3D printed sensor a) Before pressure loading, b) After pressure loading, c) Under 200 Pa, d) Under 500 Pa, and d) Under 1000 Pa of compressive pressures.

6.7 Measurement of initial electrical resistance of solid vs multi-layered samples

6.7.1 Initial electrical resistance

The samples were wired and silver coated at the top and bottom ends, as shown in Figure 6.9**,** to assure the electrical connection when connected to the digital multi metre. The average electrical resistance was measured in the 3D printed solid and multi-layered samples. The 2-

probe measurement was satisfactory for the pressure sensors due to their high electrical resistance values (well above 1 Ω), which does not require higher 3 or 4 probe electrical resistance measurements [15]. The 3D printed solid sample measured a low value of 27 Ω of initial electrical resistance. In comparison, the 3D printed multi-layered sample had markedly higher electrical resistance, reaching 77 Ω. The solid samples achieved lower electrical resistance due to the conductive material's intense content, which led to higher conductivity and a lower electrical resistance value. In comparison, the multi-layered sample exhibited markedly lower conductivity due to the suspended multi-layered structure, which had 0.2mm layer gaps between every 2 layers printed.

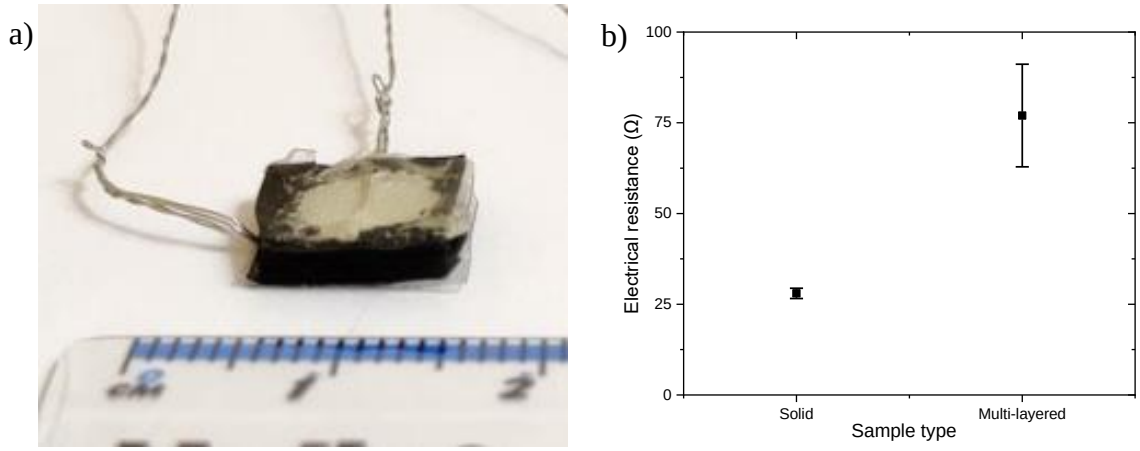

Figure 6.9: a) Optical image of a wired and silver coated 3D printed sensor and b) Initial electrical resistance values of the solid and multi-layered sensors.

6.7.2 Initial change of electrical resistance under compressive load

The change in electrical resistance was measured for solid and multi-layered samples under compressive load. Figure 6.10 shows the change in electrical resistance to compressive pressure loading. The applied pressure caused the electrical resistance to decrease as the pressure increased. A sharp change in electrical resistance was observed in suspended layers compared to moderate change in the solid sample. At 100kPa of compressive pressure, the change of electrical resistance in the multi-layered sample reached -0.634, which was 10 times higher than the solid sample with a change in the resistance value of -0.0674. At 140kPa, the multi-layered sample started to reach a plateau reaching a change in resistance of -0.7787. A lower change in resistance was evident after 140kPa, as the highest value measured at 200kPa was -0.805.

On the other hand, the solid sample demonstrated moderately linear behaviour with the highest value of change in electrical resistance, reaching -0.1778 at 200kPa. The graph shows that the electrical resistance change was very high in the multi-layered sample compared to the solid sample under a 200kPa compressive load. The multi-layered sample change in resistance value was 5 times higher than that of the solid sample at 200kPa. This difference was attributed to the fact that, under compression, the layers in the multi-layered sample were forced to pack more closely together, decreasing the electrical resistance sharply and increasing the electrical conduction pathways. The contact interface between the suspended layers was previously illustrated in the optical microscopic images in Figure 6.8. The gradual closure between suspended layers under compression increased the effective resistance change, which was noticeably distinct from the solid sample. It was also influenced by the fact that the suspended multi-layered sample had 5 times higher compression strain to applied compression force at 200kPa compared to the solid sample.

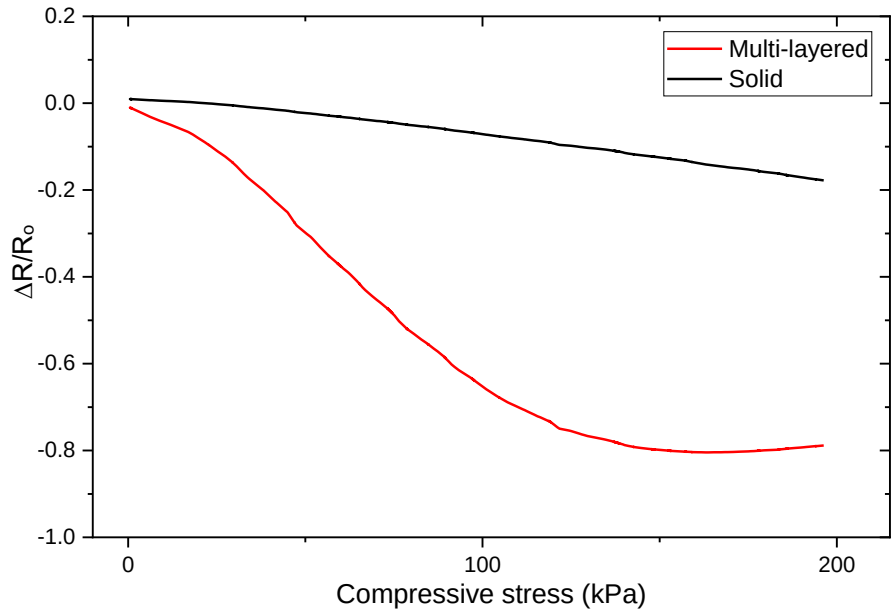

Figure 6.10: Electromechanical response of the first pressure loading of solid and multi-layered samples.

6.7.3 Change of electrical resistance under cyclic pressure

Cyclic loading was performed to compare the repeatability and reproducibility of the solid and multi-layered samples. Figure 6.11 shows the corresponding change in electrical resistance to 10 cycles of applied 200kPa compressive pressure. Both sensors showed repeatable and reproducible electrical resistance change to cyclic loading and unloading. However, the cycles showed a distinct difference in the change in electrical resistance values between the multi-layered and solid sensors. It can be noted that the multi-layered sample had a distinctly more

significant change in electrical resistance, reaching an average value of -0.77, in comparison to the solid sample with an average value of -0.18. The high compressibility of the multi-layered sample and repeatable higher change in electrical resistance suggests that it is feasible to use the 3D printed multi-layered design as a pressure sensor. A slight fluctuation was observed in the first 3 cycles of both sensors. This oscillation could be attributed to elastic deformation of the CBTPU material where the sensors experienced rearrangement of the polymer chains to accommodate the applied pressure during the first loading-unloading cycles. The overall response to cyclic pressure in the multi-layered sample showed repeatable and reproducible behaviour. This behaviour indicated it is feasible to investigate them further for use as pressure sensors.

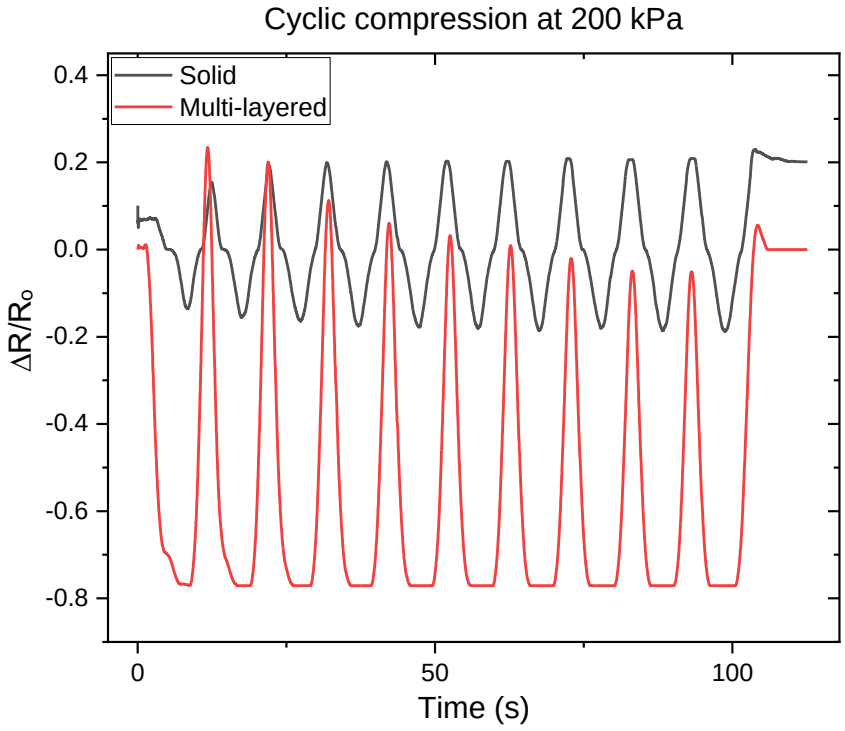

Figure 6.11: Electromechanical response of solid and multi-layered samples under cyclic pressure of 200kPa.

6.8 Influence of thickness increase on multi-layered sensors

6.8.1 Initial electrical resistance of multi-layered samples with various heights

The multi-layered design was further explored by testing the effect of varying the number of layers on the electrical resistance behaviour. As shown in Figure 6.12, 3D printed samples with total heights of 1.6 mm, 2.8 mm and 4 mm were wired and silver coated to test their electrical resistance. The values of electrical resistance measured were illustrated in Figure 6.12b. It was

noticed that increasing the height influenced the initial electrical resistance distinctively. The 1.6mm had an initial electrical resistance of 77 Ω, the 2.8mm measured 250 Ω and the 4mm measured the highest electrical resistance reaching 635 Ω. It can be noticed that the increase in electrical resistance was proportional to the number of layers. The increase in the height of the 3D printed sensor increased the measured electrical resistance. This rise was mainly influenced by the growth in the number of gaps between the suspended layers and the increase in the overall distance between the top and bottom ends, where the wire connections were attached.

a)

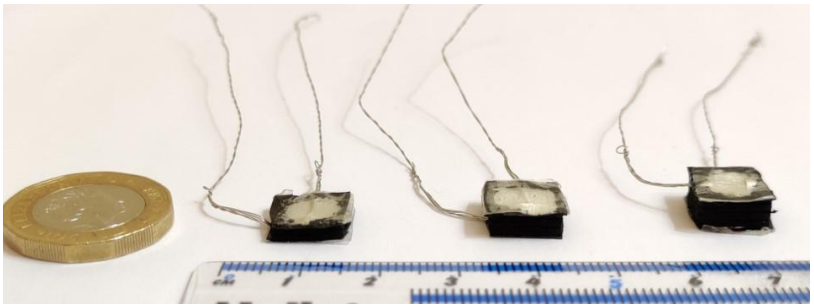

b)

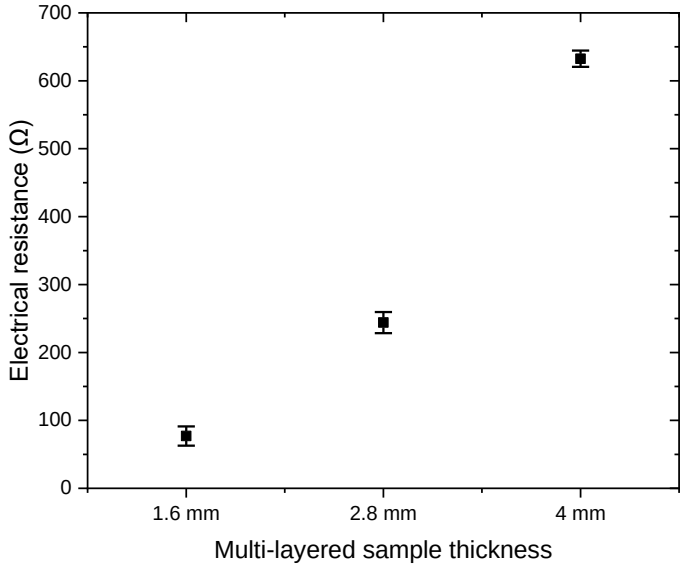

Figure 6.12: a) Optical image of the 3D printed sensors with various thicknesses wired for electrical measurement and b) Values of initial electrical resistance of the samples (Ω).

6.8.2 Measurement of electrical resistance under compressive load

6.8.2.1 Initial change of electrical resistance

The change in electrical resistance to an initial compressive load was measured in the multi-layered samples with thicknesses of 1.6 mm, 2.8 mm, and 4 mm. As shown in Figure 6.13, the samples followed a similar trend in the change of electrical resistance from the initial first loading. The thinnest sample was at 100kPa, with a thickness of 1.6mm, reaching a value of -0.634 of change in electrical resistance. With higher thickness samples, the change in electrical

resistance reached -0.774 and -0.811 in the 2.8mm and 4mm samples. A slight increase in the change of electrical resistance was observed in the first loading of the samples in Figure 6.13. This increase could be attributed to the elastic compression of the material experienced upon pressure loading, further explored under cyclic loading in the following section. At approximately 140kPa, the 3 samples' change in electrical resistance continued decreasing and reached a plateau with an apparent difference in the peak values. Under compression, the suspended layers were forced to pack more closely, decreasing the electrical resistance. The 1.6mm sample reached a value of -0.7786 at 140kPa. In contrast, the 2.8mm and 4mm samples reached higher values of -0.834 and -0.945, respectively. At 200kPa, the peak change in electrical resistance reached -0.788, -0.855 and -0.94 for the 1.6mm, 2.8mm and 4mm samples, respectively. These changes showed that increasing the number of suspended layers increased the change in electrical resistance.

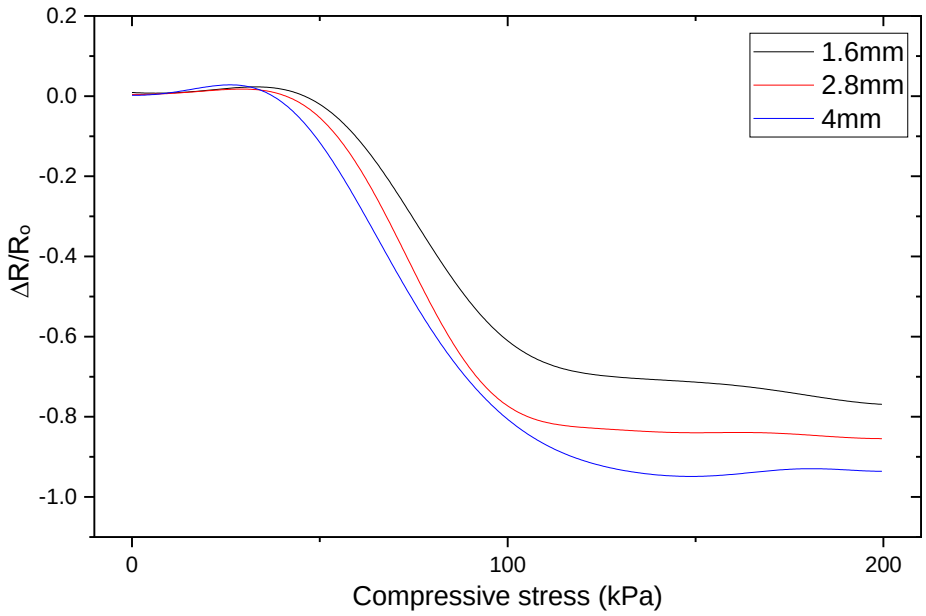

Figure 6.13: Electromechanical response of the first pressure loading of the multi-layered samples with different thicknesses.

6.8.2.2 Electrical resistance under cyclic compressive load

The change of electrical resistance was examined for the multi-layered samples under cyclic compressive loading. The 1.6mm, 2.8mm and 4mm samples were tested at various pressure values ranging from 10kPa to 200kPa to evaluate their electromechanical behaviour. After the initial loading in the previous section, the samples were first subjected to 10 cycles at a maximum 200kPa compressive pressure. This step was essential to regulate the conductive network within the 3D printed elastomer pressure sensors. At 200kPa, Figure 6.14 shows that

the average change in electrical resistance measured was -0.77 in the thinnest 1.6mm sample. The 2.8mm sample averaged a change in the resistance value of -0.86. The thicker 4mm sample registered the most significant change in electrical resistance, reaching an average value of -0.94 at peak 200kPa of applied pressure. It can be observed that the samples slightly fluctuated in the first 3 cycles, which could be attributed to softening effect experienced in elastic materials. The change in electrical resistance to cyclic pressure was stable in the following cycles. The thinner sample had a close vertical distance between the top and bottom silver coated wires which could have caused a slight fluctuation in the resistance behaviour under cyclic pressure. When the pressure was released, the sensors could recover due to their elastic properties resulting in the complete recovery of electrical resistance.

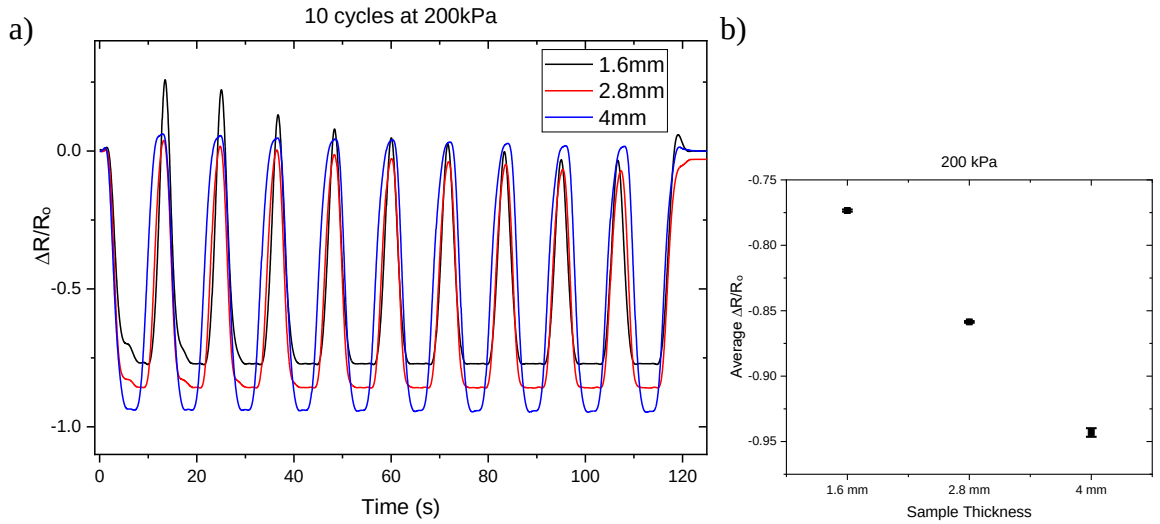

Figure 6.14: a) Electromechanical response of the multi-layered samples with different thicknesses under cyclic pressure of 200 kPa and b) Average change in resistance with an error bar.

The samples were further subjected to cyclic loading at relatively lower values after the initial compressive pressure cycles. The sensors were subjected to cyclic pressure-sensing ranging between 10-50kPa to test their reproducibility and durability; Figure 6.15 shows the change in electrical resistance of 10 cycles at 10kPa compressive pressure. The change in electrical resistance under cyclic pressure in the 1.6mm sample showed an average value of -0.163. The 2.8mm sample showed an average change of electrical resistance of -0.409, which was more than twice the one found in the thinner sample. The 4mm sample registered the biggest average change in electrical resistance, reaching a value of -0.549 at 10kPa. A slight variation in the change in electrical resistance was experienced here due to the relatively low value of 10kPa of compressive pressure.

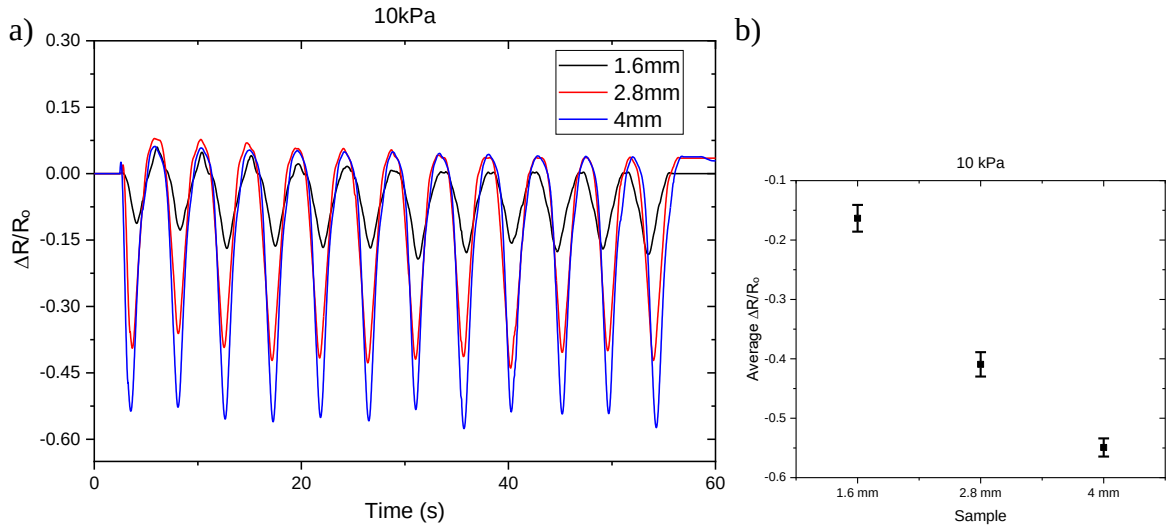

Figure 6.15: a) Electromechanical response of the multi-layered samples with different thicknesses under cyclic pressure of 10 kPa and b) Average change in resistance with an error bar.

The cyclic behaviour of the samples' change in electrical resistance at 30kPa is illustrated in Figure 6.16. The 1.6mm sample had an average change in electrical resistance of -0.419 at 30kPa of cyclic pressure. However, the 2.8mm sample showed an average change of -0.726. The 4mm sample had an average change of -0.826 which was 2 times higher than the value found in the thinnest sample at 30kPa. It can be noticed that the average change in electrical resistance of the 3 samples was more than double at 30kPa in comparison to the value registered at 10kPa. This change demonstrates the 3D printed multi-layered sensors' ability to discern the amount of mechanical pressure applied reflected in the electrical resistance response.

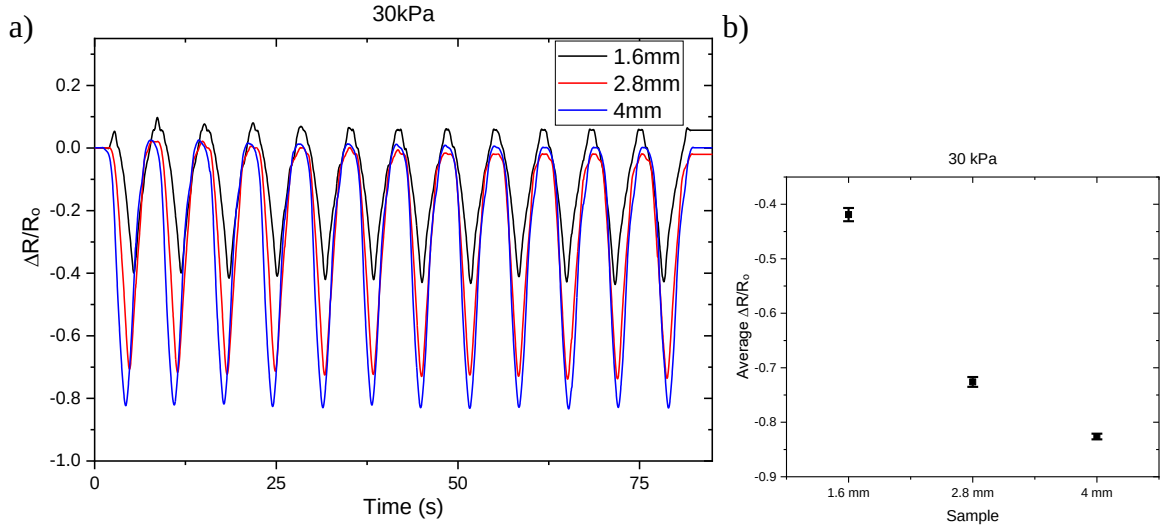

Figure 6.16: a) Electromechanical response of the multi-layered samples with different thicknesses under cyclic pressure of 30 kPa and b) Average change in resistance with an error bar.

Figure 6.17 shows the change in electrical resistance under cyclic pressure of 50kPa. The change in electrical resistance in the 1.6mm showed an average value of -0.525. The 2.8mm sample had an average change of -0.808. In contrast, the 4mm sample had an average value of -0.887, which was slightly higher than the one found in the 2.8mm sample. In all compressive pressure values, it was found that the sensors' thicknesses influenced the resulting change in electrical resistance.

Consequently, increasing the number of layers increased the initial electrical resistance. Therefore, as the initial resistance increased, the change in electrical resistance was more significant. This finding suggests that the rate of change in electrical resistance can be tuned by changing the sensor's thickness.

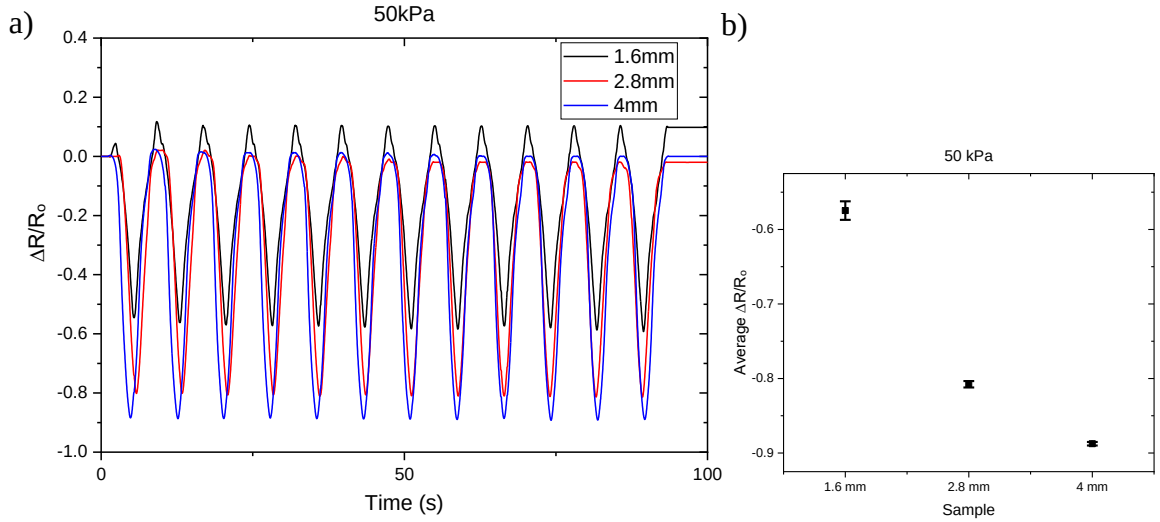

Figure 6.17: a) Electromechanical response of the multi-layered samples with different thicknesses under cyclic pressure of 50 kPa and b) Average change in resistance with an error bar.

6.8.3 Evaluation of the electromechanical response of the multi-layered sensor

To demonstrate the capability of the 3D printed multi-layered sensor, we further evaluated their electromechanical response to a broader range of applied pressures. To test its durability, we ran cyclic loading under compressive pressure ranging from as low as 10 kPa to as high as 200kPa. The 4mm sensor was chosen for testing under cyclic compressive pressures of 10, 20, 40, 100, and 200 kPa. Figure 6.18 illustrates the sensor's ability to perform at a wide range of pressures producing a distinctive change in electrical resistance based on the value of pressure (kPa). As the applied pressure increased from 10-200 kPa, the device's change in electrical resistance decreased by nearly 2-folds, from -0.56 to -0.95, exhibiting very stable pressure-sensing performance.

The sensor showed pronounced electromechanical stability, which has been attributed to the suspended multi-layered design allowing from low to high-pressure values. A negligible hysteresis was observed in the cyclic behaviour when the applied pressure was below 20kPa and no apparent hysteresis observed at higher pressure. The hysteresis can be attributed to elastic deformation of the sensor during loading-unloading. Figure 6.18b shows the corresponding compressive strain (%) to applied pressure to determine the mechanical response to this pressure. At a lower pressure 10-40kPa, the compressive strain increased sharply from 2.4% at 10kPa, 4.8 at 20kPa and 7.3% at 40kPA. However, as the pressure increased to 100 and 200 kPa, the rate of change in compressive strain increased slightly to 11% and 14.5%, respectively. The reason was that the suspended layers had already compacted closely together at lower pressure values which was also evident by the higher rate of change in electrical resistance at lower strain values.

The 3D printed sensor was further explored at very low-pressure values of 0.1, 0.3, 0.5 and 1 kPa, as shown in Figure 6.18c. The maximum change in resistance value reached 0.1kPa was 0.071. On the following pressure values of 0.3, 0.5 and 1 kPa, the change in resistance reached maximum values of 0.22, 0.38 and 0.56, respectively. The ability to perform at very low-pressure values demonstrated the sensor's ability for a more comprehensive pressure range. The change in electrical response showed slight time dependence in the sensor's response to applied pressure.

The pressure sensor's detection response and relaxation times were analysed to investigate the sensing response to applied pressure further. As illustrated in Figure 6.18d**,** the sensor exhibited a fast response time to loading and unloading with the response and relaxation times measured to 300 and 250 milliseconds (ms). It can be seen that the acquired response and relaxation times measured to 300 and 250 ms for the loading and releasing of the sensor, the estimated time.

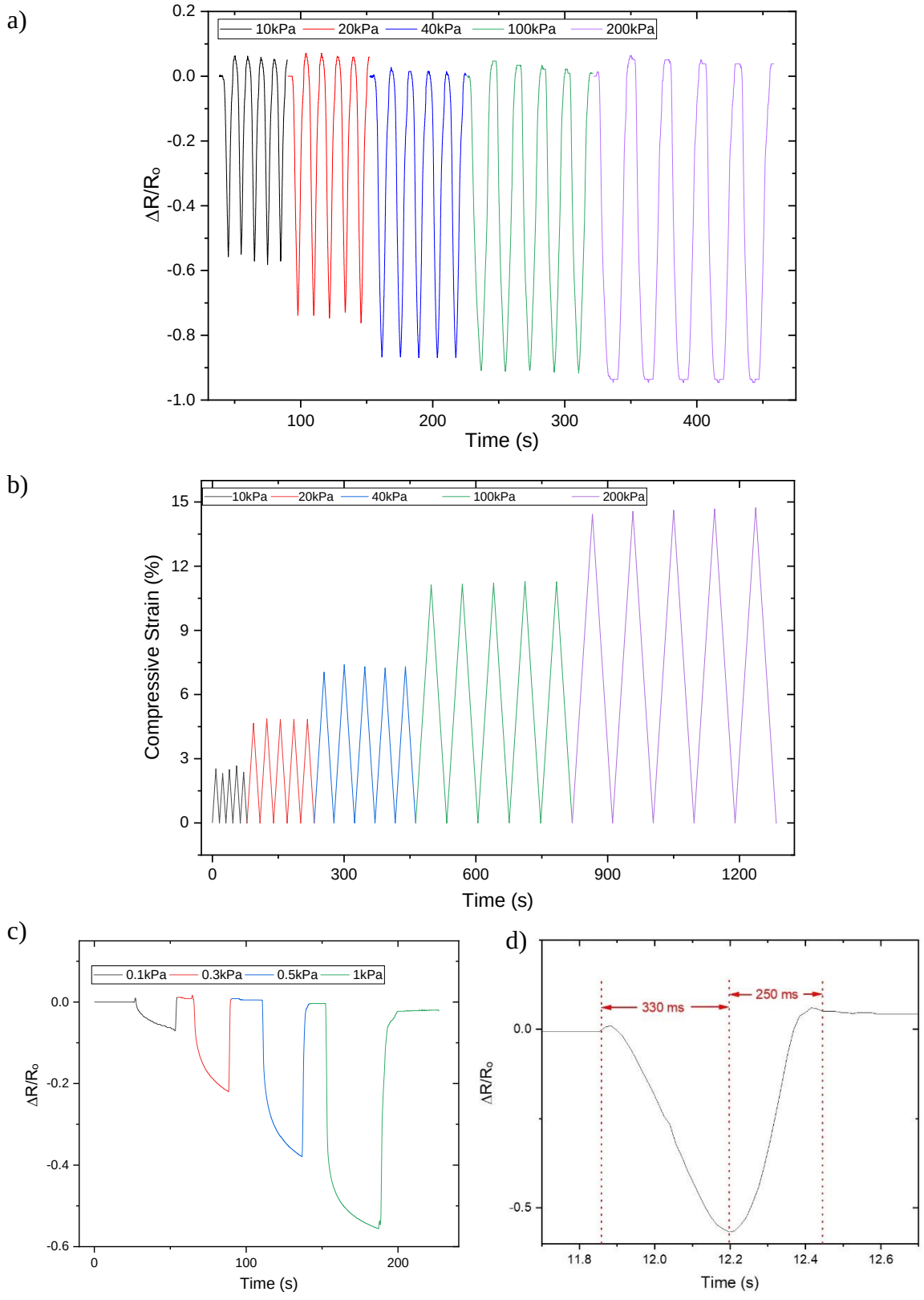

Figure 6.18: a) Corresponding change in resistance to a varying range of applied pressure (kPa) of the 4mm sample, b) Mechanical cyclic strain response (%) to varying applied pressure (kPa), c) Change of electrical resistance to low range of applied pressure (kPa) and d) Loading and relaxation response speed of the 3D printed sensor.

6.9 Pressure sensitivity and gauge factor

The sensitivity of the pressure sensors was measured to evaluate the performance of 3D printed sensors. It was calculated by dividing the change in electrical resistance value by applied pressure in kPa. The equation to calculate the sensitivity of the pressure sensors is defined in Equation (2.4).

Figure 6.19 compares the average sensitivity of the multi-layered sensors at 10, 30 and 50 kPa of compressive pressure. At 10kPa, the 4mm sensor exhibited the highest measured average sensitivity reaching 0.055 kPa^{-1}. The measured sensitivity in the 2.8mm and 1.6mm exhibited average values of 0.041 kPa^{-1} and 0.016 kPa^{-1}, respectively. These values emphasise the impact of increasing the thickness as the sensor with more layers showed higher sensitivity. It also shows that the sensitivity can be tuned by increasing the layers of the pressure sensor. At 30kPa, the sensitivity of the 4mm sharply decreased to 0.028 kPa^{-1}. The sensitivity also decreased to 0.024 kPa^{-1} and 0.014 kPa^{-1} for the 2.8mm and 1.6mm sensors. At 50kPa, the sensitivity slightly decreased reaching 0.018 kPa^{-1}, 0.016 kPa^{-1} and 0.012 kPa^{-1} for the 4mm, 2.8mm and 1.6mm sensors, respectively. The resulting sensitivity values highlighted the ability of tuneable sensitivity by tuning the number of suspended layers. The 4mm sensor demonstrated the highest sensitivity of the 3 sensors at all pressure levels. The suspended multi-layers allowed for more contact interface area between the suspended layers and therefore achieved comparable sensitivity to previous work and higher sensitivity at higher-pressure values >20kPa.

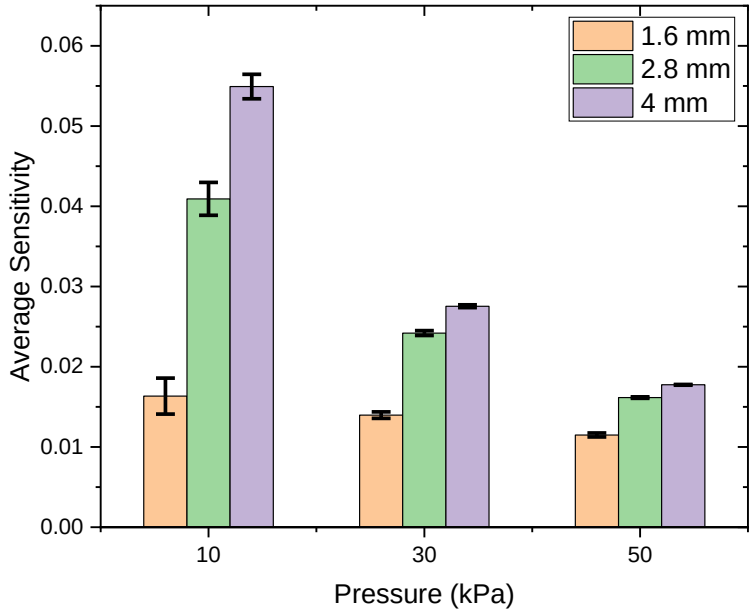

Figure 6.19: Average sensitivity of the 3D printed sensors of various thicknesses at pressure values between 10 – 50 kPa.

Table 6.1 and Figure 6.20 summarise the measured sensitivities of the 4mm sensor at very low-pressure values ranging from 0.1-1kPa to investigate the sensitivity. The sensitivity measured 0.675 kPa^{-1} at 0.1 kPa and 0.69 kPa^{-1} at 0.3 kPa. It was found that at low pressure ranges up to 0.5 kPa, the sensitivity was relatively convergent, with the highest sensitivity acquired was 0.73 kPa^{-1} at 0.5 kPa. The lowest value of all measured lower pressure values was 0.55 kPa^{-1} at 1 kPa. The resulting sensitivity values in relation to applied forces suggest these sensors can detect and differentiate various levels of deformation.

Table 6.1: Average theoretical sensitivity of the 4mm sensor at low-pressure values between 0.1 – 1 kPa.

	0.1kPa	0.3kPa	0.5kPa	1kPa
Sensitivity (kPa^{-1})	0.675	0.69	0.73	0.55

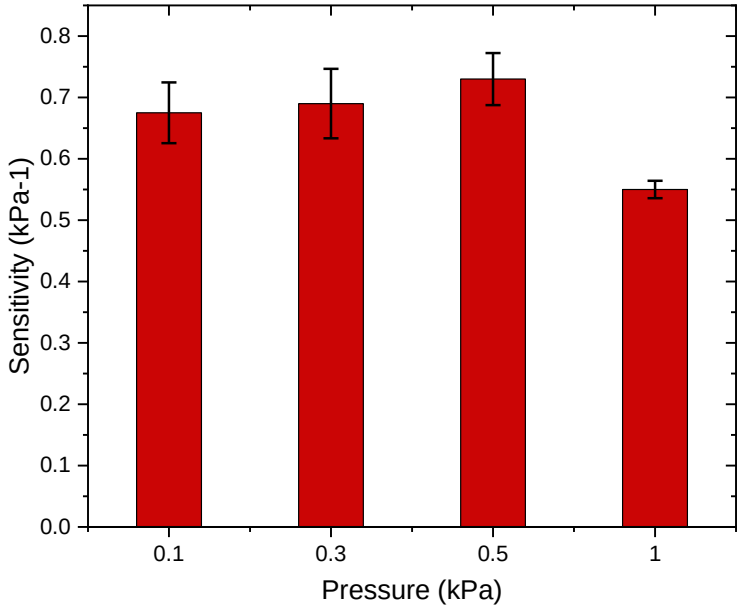

Figure 6.20: Average sensitivity of the 4mm sensor at low-pressure values between 0.1 – 1 kPa.

Another way to evaluate the sensitivity of the 3D printed sensors was by calculating the gauge factor. The gauge factor expresses the sensitivity of the samples by dividing the theoretical change in electrical resistance by the rate of change in compressive strain. The equation that calculates the gauge factor GF is expressed in Equation (2.3).

The 4mm was chosen to measure its gauge factor at a wide range of compressive pressure between 10-200 kPa. Figure 6.21 summarises the average GF values acquired to compressive pressures of 10, 20, 40, 100 and 200 kPa. The average gauge factor value measured 6.5 at 200kPa, 8 at 100kPa and 12 at 40kPa. The GF value maintained a steady increase as the pressure decreased, measuring 16 at 20kPa and reaching the highest value of 23 at 10kPa. The

GF values were influenced by the mechanical strain compressibility between the suspended layers, which resulted in a change in electrical resistance. This steady increase in GF as the pressure decreased was in good agreement with the measured sensitivity.

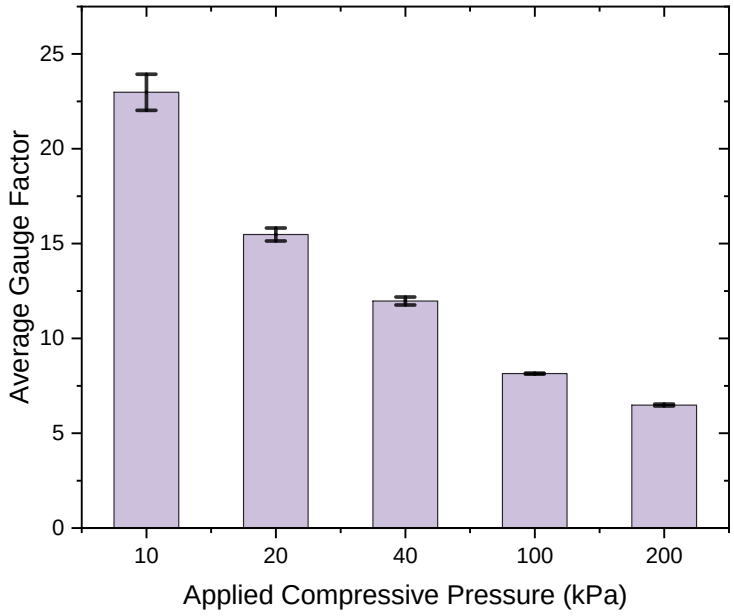

Figure 6.21: Average gauge factor of the 4mm sensor at wide pressure range values between 10 – 200 kPa.

6.10 Discussion

Most previous work on pressure sensors was either affected by the complex fabrication process or showed lower pressure sensitivity at higher-pressure ranges > 20kPa. Previously 3D printed pressure sensors suffered a low range of sensitivity or used 3D printed templates, which added more steps to the process. The low-pressure range limited their feasibility for a broader range in wearable applications requiring more pressure ranges >20kPa. Here, CBTPU was chosen as the conductive filament for the pressure sensors. The mechanical and electrical properties of the 3D printed sensors were investigated. 3D printing using dual extrusion FDM was employed here to 3D print the conductive sensing filament simultaneously with the supporting scaffold material to create highly sensitive pressure sensors. The samples were rinsed in water, and the sacrificial material dissolved, leaving suspended multi-layered pressure sensors. The purpose of the simultaneous dual printing was to enhance the sensors' performance to overcome the low sensitivity and low sensing range issues of the bulk conductive material. It is possible to perform continuous higher sensitivity at a higher-pressure range > 20kPa. The one-step FDM 3D printing process enabled tuning the sensing range and sensitivity by increasing the number of suspended layers. The mechanical and electrical tests of these sensors show their ability to perform with good stability and reproducibility. The flexible and stretchable nature of the TPU

based conductive material was a significant factor that governed the sensor's high compressibility. Moreover, the multi-layered design increased the sensor's compressibility compared to the solid sample with low compressibility, which resulted in a greater change in the electrical resistance of the multi-layered one. Creating the gaps by 3D printing of a sacrificial interface layer simultaneously between the conducting layers improved their sensitivity for the potential to use in a number of pressure-sensing applications. The simplicity of the design and fabrication enabled by FDM 3D multi-material printing enabled the creation of pressure sensors with a wide range of sensitivity. The sensors demonstrated their ability to perform with distinct electrical resistance changes based on the amount of pressure applied, ranging from pressure as low as 0.1 kPa to as high as 200kPa. More noticeably, the sensor exhibited higher sensitivity at higher-pressure values >20kP compared to recent studies.

6.11 Applications of the 3D printed pressure sensors

Due to the high sensitivity and flexibility, various applications of these 3D printed pressure sensors were demonstrated. The sensors were employed to detect different types of forces, including pressing, finger bending, lifting a cup, coins stacking and hand gesture control. The first application was attaching a 4mm sensor to an index finger and lifting an empty and filled cup. The sensor attached to the fingertip could detect the variant levels of pressure resulting from lifting an empty versus a filled cup. Figure 6.22 showed how the sensor’s change in resistance differed when lifting an empty versus a filled cup. The sensor attached to the index finger was able to acquire a higher value of change in resistance of the filled cup compared to lifting an empty cup.

The 3D printed 4mm sensor was also examined under varying pressure caused by finger pressing, as demonstrated in Figure 6.23. When the sensor was subjected to a manual force of soft and firm pressing, the resulting change in resistance varies depending on the force applied. The resulting response of change in resistance to applied forces indicates these sensors can detect and differentiate various levels of deformation.

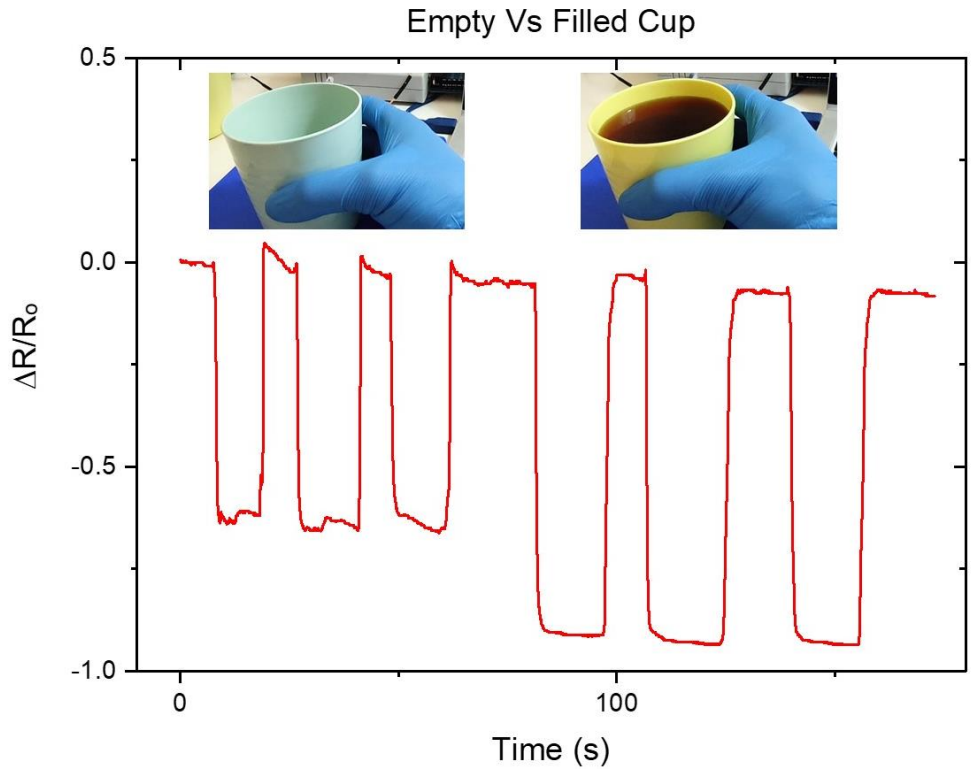

Figure 6.22: Change in resistance response to the repeatable lifting of an empty and filled cup.

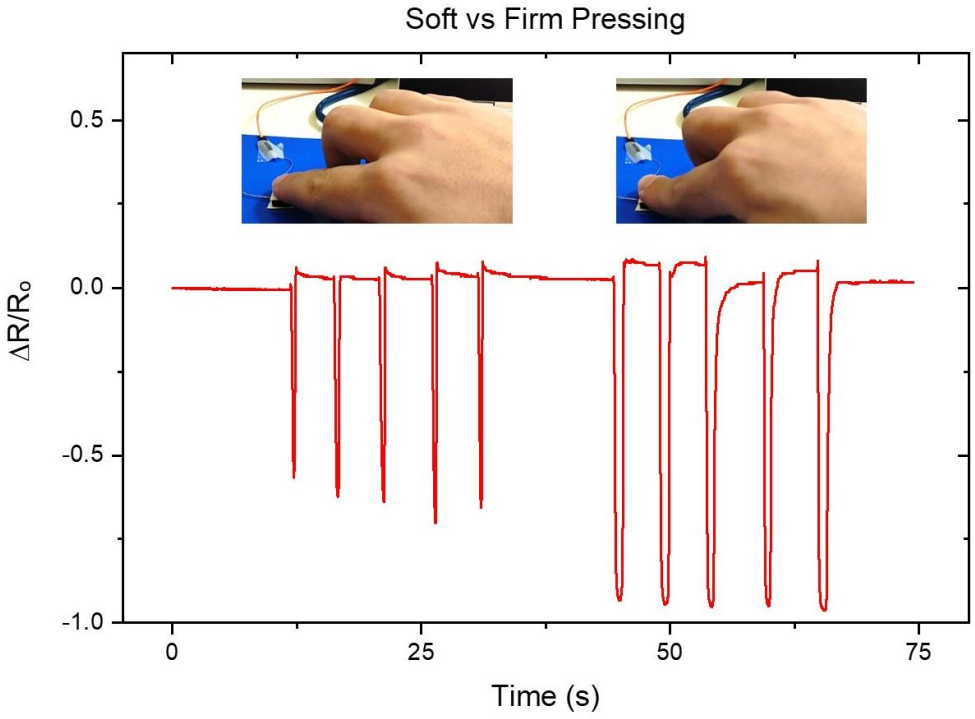

Figure 6.23: Change in resistance response to repeatable soft and firm pressing of the sensor.

Figure 6.24 shows a 2.8mm sensor attached to a finger and detected different angles of finger bending. When a sensor was attached on top of an index finger, it was able to detect the bending of the finger. It can be noticed that the more the finger bends results in a more significant

change in the electrical signal of the sensor. The change in resistance increased as the finger bent down. Such an example of finger bending shows the sensor's wide range of detection capability in which the detection was distinct from low to high bending angles. Inversely, the sensor was able to return to the initial state as the change in resistance corresponded to the release bending angle of the finger all the way back.

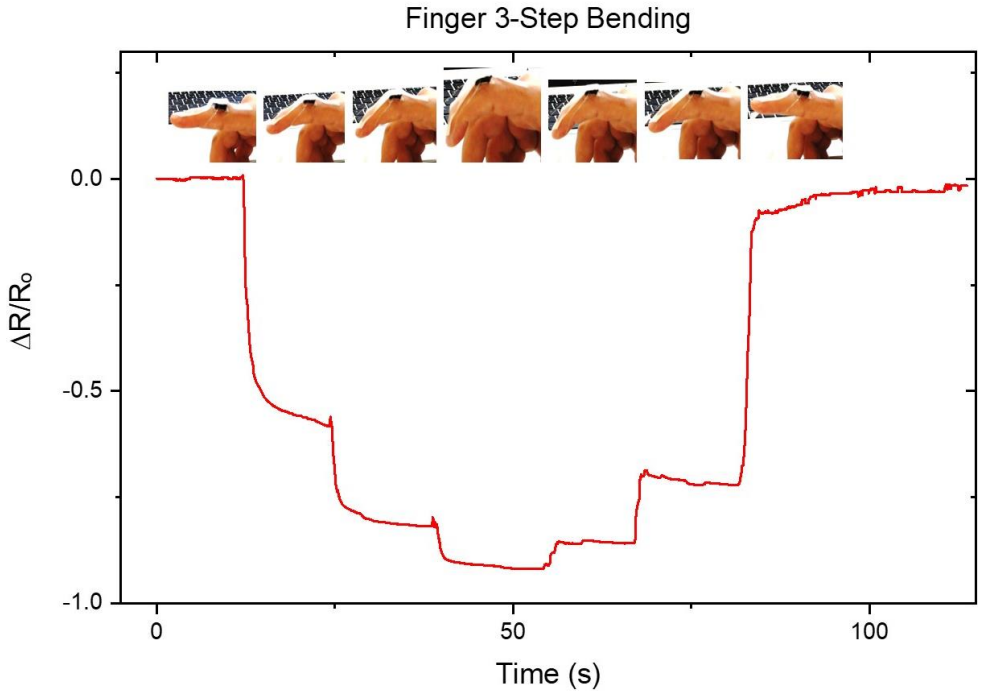

Figure 6.24: Corresponding change in electrical resistance to 3-step bending and releasing of an index finger with a 3D printed sensor attached on top.

We placed British coins by increment on top of a 2.8mm sensor to show the sensor's detection's versatility. Figure 6.25 shows the change in electrical resistance as we placed a sensor on a table and stacked British coins on top of it. The sensor was able to detect the stacking of the coins by detecting an increase in the change in electrical resistance as the number of coins was incremented on top of the sensor. The amount was stacked one by one, sequentially representing step-like measurement. The addition of more coins was detected as the value of change in resistance increased proportionally to more stacking.

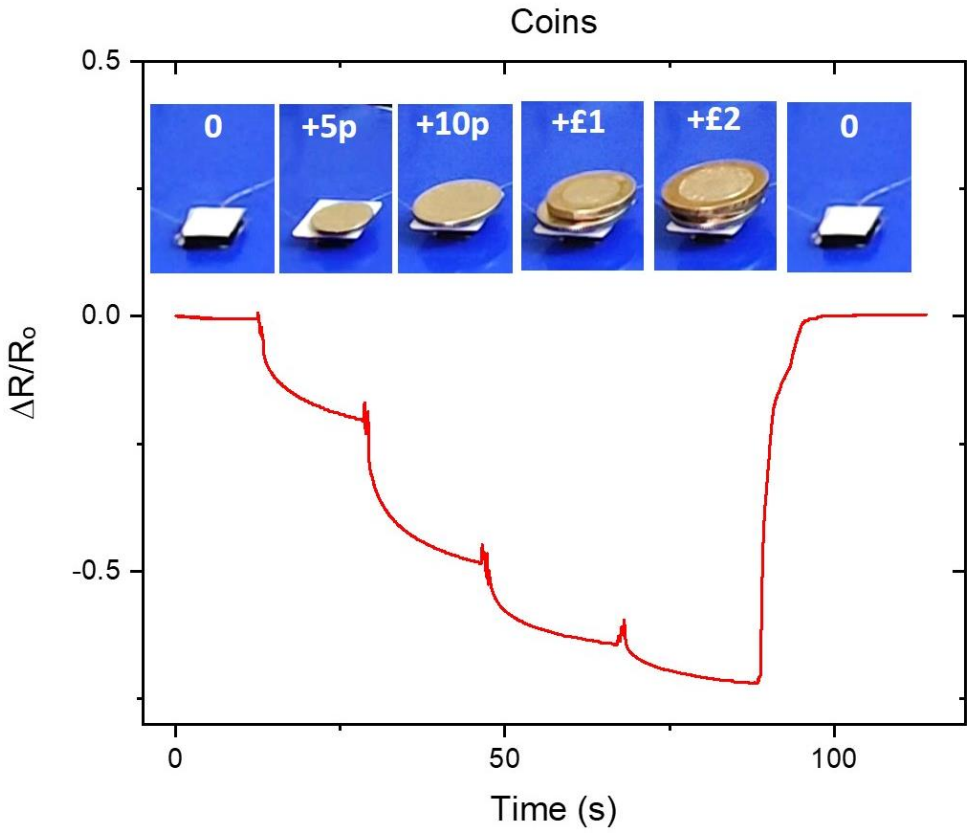

Figure 6.25: Corresponding change in resistance to the stacking of British coins on top of a 3D printed sensor.

We attached 5 of the 2.8mm sensors to a glove with one sensor for each finger to demonstrate the capability of the 3D printed sensors further. It was possible to control a robotic hand by sending the signal from the 3D printed sensors (attached to the glove) to the robotic hand's finger. The 3D printed pressure sensors were connected to the analogue pins of the Arduino Uno (see appendix B). The servo motors which move the robotic fingers were assigned to the Arduino digital channels. After that, a code provided from the Arduino library was used to rotate the servo motors to move the robotic fingers from the input of the analogue pins (the 3D printed sensors). As demonstrated in Figure 6.26, one can wear the glove, and it was possible to control the robotic by bending the fingers to control the 5 fingers of the robotic hand individually, mimicking the hand gestures. The varying change in electrical resistance altered the voltage signal sent to the fingers' motors; this varying signal caused the motor to bend the fingers. For more details on the control of the servo motors via the 3D printed pressure sensors, see appendix B.

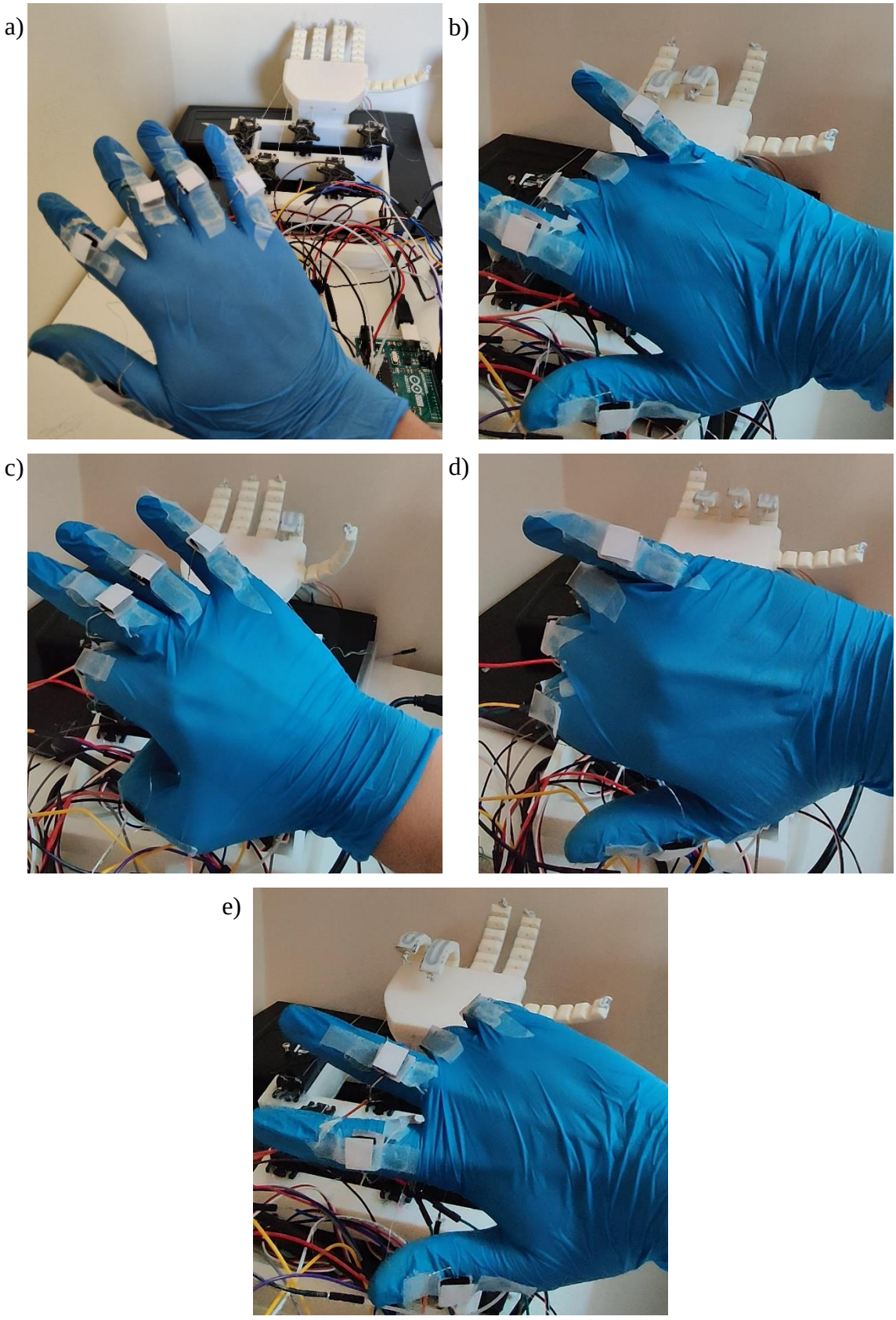

Figure 6.26: a) Image of the robotic hand and glove setup with 3D printed sensors attached to the glove, b-e) Corresponding movement of the robotic hand to bending b) Middle and ring, c) Thumb and index, d) Index, middle and ring and e) Ring and little fingers.

6.12 Summary

In conclusion, a method of fabricating soft compressible multi-layered pressure sensors via FDM 3D multi-material printing was presented. The design flexibility offered by 3D multi-material printing was suggested to overcome the constraint of conventional fabrication techniques. Simple simultaneous 3D printing of active sensing material with second sacrificial material was employed to fabricate highly sensitive and tuneable pressure sensors. Multi-material 3D printing allowed the customisation of a novel suspended multi-layered design that outperformed the solid sensor of the same conductive material. It was possible to overcome the conventional 2D fabrication process's constraints by harnessing multi-materials simultaneously in a one-step fabrication without any additional assembly.

The mechanical and electrical properties of the 3D printed sensors were evaluated. The tests showed good stability and reliable reproducibility with negligible hysteresis. Depending on the number of suspended layers printed, the sensors demonstrated the ability to work and respond rapidly to a wide range of pressures. Two factors determined the sensitivity; the first was by dividing the ratio of change in electrical resistance by compressive pressure in kPa. The second was by dividing the change in electrical resistance by the amount of compressive strain known as the gauge factor GF. The sensitivity was tuned by using supporting scaffold material to enhance the compressibility and the possibility of increasing the number of sensing layers. Here, it was possible to overcome the low sensing range by employing FDM multi-material 3D printing compared to previous works summarised in Table 2.2. The use of removable supporting scaffold via simultaneous multi-material 3D printing enhances the mechanical compressibility of the multi-layered pressure sensor by 4-folds. This enhancement consequently improves the change in electrical resistance by 5-folds in comparison to a solid one. The advantage of multi-material 3D printing is that it allows for the simple, rapid fabrication of pressure sensors without additional assembly steps. Various applications were presented and prove the feasibility and versatility of these 3D printed sensors demonstrating their capabilities and potential.

Chapter 7– Conclusions and future work

7.1 Conclusions

This project employed an additive manufacturing process that used conductive composite materials to create functional strain and pressure sensors. 3D printing has demonstrated its feasibility for the manufacturing of highly sensitive and customisable devices. It was found that extrusion-based 3D printing processes are the most popular technologies for the fabrication of soft and stretchable sensors. Extrusion-based 3D printing technologies such as FDM have paved the way towards a more effective single-step process for wearable soft electronics. It is possible to realise wearable soft electronics, human-machine interaction, biomedical and health monitoring applications due to their vast materials options, multi-material fabrication possibilities.

In the first stage, the thesis explored the feasibility of multi-material 3D printing via the FDM technique. Before 3D printing, the sensing materials were first prepared using a filament maker extruder to form strands of 3D printable filaments. After that, it was possible to simultaneously co-print conductive materials encapsulated within flexible elastomer. It was possible to overcome issues with 3D printing flexible materials by replacing the extruder assembly with one that was compatible with flexible materials. The 3D printed conductive composites were subjected to electrical and mechanical tests to evaluate the strain sensing capabilities. Experiments followed this to investigate the electromechanical behaviour under dynamic loading, allowing us to determine the hysteresis and nonlinearity issues found in conductive elastomers to be further resolved.

After that, a simple method of 3D printed conductive composites simultaneously embedded within a stretchable substrate was presented for strain sensors. The mechanical performance, as well as the electrical conductivity of the 3D printed composites, were tested. The modified conductive composites' mechanical test was essential to evaluate their stiffness, strength, and strain at break. The 3D printed strain sensors were further evaluated under dynamic loading. The samples were subjected to various strain amplitudes ranging between 5-100% tensile strain values. The electromechanical and cyclic loading of the samples showed their feasibility to be used as strain sensors. Modifying thermoplastic conductive filaments using a filament maker prior to 3D printing allowed us to obtain the highest sensitive 3D printed strain sensors with linear response. The mixture of conductive-based rigid and elastomer polymers allowed for the creation of highly stretchable, sensitive and linear strain sensors. The impact of pre-straining

on the cyclic behaviour of the samples was investigated with pre-strain values ranging between 50-100%. The influence of the pre-straining was evident in the sensitivity of the 3D printed strain sensors as higher pre-straining values resulted in higher sensitivity. It was also found that samples with higher GPLA content had positive linear behaviour with higher sensitivity under cyclic strain. The high values of gauge factors obtained showed unprecedented sensing capabilities in comparison to previously 3D printed strain sensors summarised in Table 2.1, reaching a GF value of 163. The cyclic loading and unloading of the 3D printed samples showed good sensing stability and recoverability while maintaining a positive strain effect. The approach allowed for the rapid fabrication of strain sensors for several applications, including body motion detection, embedded sensing of 3D printed robotic hand and heart pulse detection.

A method of fabricating soft compressible multi-layered pressure sensors via FDM 3D multi-material printing was also presented**.** Simultaneous 3D printing of active sensing material with second sacrificial material was later removed by simply immersing the sensor in water to form suspended multi-layered pressure sensors. The mechanical and electrical properties of these 3D printed pressure sensors were evaluated under dynamic pressure loading. The 3D printed pressure sensors mainly operated by the change of contact resistance influenced by the compressibility between the suspended layers, which could tune its sensitivity. One of the main reasons governing the tuneability was the increase of initial electrical resistance as the number of layers increased.

It was possible to overcome the constraints to the conventional 2D fabrication process by harnessing multi-materials simultaneously to a one-step fabrication without any additional assembly. Multi-material 3D printing allowed for the innovation of a customisable suspended multi-layered pressure-sensing design that outperformed the solid one. The 3D printed multi-layered pressure sensor was 4 times more compressible than the solid sensor made with the same material. The multi-layered design proved to be an effective method that showed the capability of constructing highly sensitive and tuneable pressure sensors fabricated in 3D. The tests showed good stability and reliable reproducibility with negligible hysteresis. The approach allowed for the rapid fabrication of pressure sensor for several applications, including body motion detection and human-machine interaction.

In conclusion, the development of the sensing material composites allowed for the creation of strain and pressure sensors with good recoverability and reproducibility. The 3D printed sensors were characterised using SEM and optical microscopic imaging techniques. These 3D printed sensors proved their wide range of applications ranging from robotic hand and finger

motion detection to heartbeat sensing capabilities. The design flexibility offered by 3D multi-material printing was suggested to overcome the constraint of conventional fabrication techniques. Eventually, to show the capability, versatility and potential of these sensors, various applications of 3D printed strain and pressure sensors were demonstrated.

Previously 3D printed strain and pressure sensor have limitations as summarised in Table 2.1 and Table 2.2. Achieving highly stretchable 3D printed strain sensor of up to 100% with linear response was associated with low sensitivity [13], [15], [139]. Furthermore, the sensors that achieved GF values of up to 176, suffered non-linear behaviour. For the 3D printed pressure sensors, it was found that that previous works presented high sensitivity, but the maximum sensing range presented was up to 20kPa (as illustrated in Table 2.2). Consequently, the contribution of this project was summarised as follows:

1. The combination of 3D printed highly sensitive (GF163) with high stretchability >50% and positive linear response strain sensors was achieved here by employing a simple and customisable 3D printing FDM fabrication process.
2. Pre-straining of the 3D printed strain sensors caused crack formation which possessed high sensitivity. The influence of pre-straining was evident in the sensitivity as higher pre-straining values resulted in higher sensitivity.
3. The use of removable supporting scaffold via simultaneous multi-material 3D printing with electrically conductive filament, enhanced the mechanical compressibility of the multi-layered pressure sensor by 4-folds in comparison to solid sensor.
4. The change in electrical resistance of the 3D printed multi-layered pressure sensor was improved by 5-folds in comparison to solid one.
5. The sensitivity of the multi-layered sensor was tuneable by increasing the layers which also allowed for wide range sensitivity measurements between 0.1 – 200 kPa.

7.2 Future work

Regarding the potential of continuing with this scope of research, we proposed the following recommendations to consider for future work:

- To realise an AM fabrication process that can 3D print pressure, strain and more sensory systems in one step. This process could lead to the realisation of multi-sensory systems with closed-loop feedback and allow real-time error correction of the fabricated devices. The optimisation of additive manufacturing with the incorporation of these novel sensors could allow for the futuristic rapid fabrication process.

- Work should also investigate how to complement the innovative and novel design introduced in Chapter 6 by testing more designs. It requires designing pressure sensors that can take not only square but multi-layered circular, hexagonal, rectangular and many more shapes depending on the application. Furthermore, the integration of a closed-loop feedback system enhances the reliability of these 3D printed sensors.
- Research should also investigate combining 2 extrusion-based technologies such as fused deposition modelling (FDM) and direct ink writing (DIW) in one system, allowing a novel one-step fabrication process. This process would enhance the electrical conductivity and eliminate unnecessary post-processing, such as silver coating of 3D printed samples. This innovation can be harnessed by direct ink writing DIW of silver paste using a syringe. Such a Hybrid manufacturing method would enable a diverse selection of materials to fabricate multi-material and multi-functional systems. Harnessing multi-material capabilities of simultaneous 3D printing of more than 2 materials enables the adaption of multi-sensory systems and devices to be fabricated in one step. It can be expanded by allowing the addition of multiple extrusion systems in one device.
- Investigations into developing a framework to customise the designs, materials, and processes of these 3D printed sensors to be industrial ready and fit prospective future applications should be undertaken. The realisation of manufacturing flexible materials with sensing capabilities holds excellent potential in biologically inspired systems and can facilitate the integration of innovative devices in wearable electronics, robotics, health monitoring and human-machine interaction. Combining 2 extrusion systems can facilitate the use of DIW of silver paste as an example of highly conductive material that cannot be fabricated using FDM. The development of materials with greater electrical conductivity is required for electrical connections to eliminate the sensors' need for manual wiring.
- Extending this work is motivated by the great promise that such digital manufacturing technologies can reduce material waste, increase efficiency, be more sustainable and reduce environmental impacts. The evolving developments in AM technologies could allow rapid product development, freeform fabrication, and customisation to overcome current technologies' limitations. These innovations could transfer AM technologies to the next level of a production process with novel and innovative future systems.

References

[1] T. C. Lee, R. Ramlan, N. Shahrubudin, T. C. Lee, and R. Ramlan, “An Overview on 3D Printing Technology: Technological, Materials, and Applications,” *Procedia Manuf.*, vol. 35, pp. 1286–1296, 2019.

[2] S. Gabriel and C. W. Hull, “Apparatus for Production of Three-Dimensional Objects by Stereolithography,”, US4575330A, USA, 1984.

[3] T. D. Ngo, A. Kashani, G. Imbalzano, K. T. Q. Nguyen, and D. Hui, “Additive Manufacturing (3D Printing): A Review of Materials, Methods, Applications and Challenges,” *Compos. Part B Eng.*, vol. 143, pp. 172–196, 2018.

[4] J. Lee, J. An, and C. K. Chua, “Fundamentals and Applications of 3D Printing for Novel Materials,” *Appl. Mater. Today*, vol. 7, pp. 120–133, 2017.

[5] S. H. Ahn, M. Montero, D. Odell, S. Roundy, and P. K. Wright, “Anisotropic Material Properties of Fused Deposition Modeling ABS,” *Rapid Prototyp. J.*, vol. 8, no. 4, pp. 248–257, 2002.

[6] R. Singh, R. Kumar, I. Farina, F. Colangelo, L. Feo, and F. Fraternali, “Multi-Material Additive Manufacturing of Sustainable Innovative Materials and Structures,” *Polymers* , vol. 11, no. 1. 2019.

[7] M. Amjadi, K. U. Kyung, I. Park, and M. Sitti, “Stretchable, Skin-Mountable, and Wearable Strain Sensors and Their Potential Applications: A Review,” *Adv. Funct. Mater.*, vol. 26, no. 11, pp. 1678–1698, 2016.

[8] F. Avilés, A. I. Oliva-Avilés, and M. Cen-Puc, “Piezoresistivity, Strain, and Damage Self-Sensing of Polymer Composites Filled with Carbon Nanostructures,” *Adv. Eng. Mater.*, vol. 20, no. 7, pp. 1–23, 2018.

[9] R. L. Truby and J. A. Lewis, “Printing Soft Matter in Three Dimensions,” *Nature*, vol. 540, no. 7633, pp. 371–378, 2016.

[10] S. K. Dhinesh and K. L. Senthil Kumar, “A Review on 3D Printed Sensors,” *IOP Conf. Ser. Mater. Sci. Eng.*, vol. 764, p. 12055, 2020.

[11] C. Liu, N. Huang, F. Xu, J. Tong, Z. Chen, X. Gui, Y. Fu, and C. Lao, “3D Printing Technologies for Flexible Tactile Sensors toward Wearable Electronics and Electronic Skin,” *Polymers* , vol. 10, no. 6. 2018.

[12] R. L. Truby, M. Wehner, A. K. Grosskopf, D. M. Vogt, S. G. M. Uzel, R. J. Wood, and J. A. Lewis, “Soft Somatosensitive Actuators via Embedded 3D Printing,” *Adv. Mater.*, vol. 30, no. 15, p. 1706383, Apr. 2018.

[13] J. Gooding, J. F. Mahoney, and T. D. Fields, “3D Printed Strain Gauge Geometry and Orientation for Embedded Sensing,” *58th AIAA/ASCE/AHS/ASC Structures, Structural Dynamics, and Materials Conference (p. 0350).*, 2017.

[14] K. Elgeneidy, G. Neumann, M. Jackson, and N. Lohse, “Directly Printable Flexible Strain Sensors for Bending and Contact Feedback of Soft Actuators,” vol. 5, no. February, pp. 1–14, 2018.

[15] J. T. Muth, D. M. Vogt, R. L. Truby, D. B. Kolesky, R. J. Wood, and J. A. Lewis, “Embedded 3D Printing of Strain Sensors within Highly Stretchable Elastomers,” *Adv. Mater.*, pp. 6307–6312, 2014.

[16] M. Abshirini, M. Charara, Y. Liu, M. Saha, and M. C. Altan, “3D Printing of Highly Stretchable Strain Sensors Based on Carbon Nanotube Nanocomposites,” *Adv. Eng. Mater.*, vol. 20, no. 10, p. 1800425, Oct. 2018.

[17] J. F. Christ, N. Aliheidari, P. Pötschke, and A. Ameli, “Bidirectional and Stretchable Piezoresistive Sensors Enabled by Multimaterial 3D Printing of Carbon Nanotube/Thermoplastic Polyurethane Nanocomposites,” *Polymers (Basel).*, vol. 11, no. 1, p. 11, Dec. 2018.

[18] J. F. Christ, N. Aliheidari, A. Ameli, and P. Pötschke, “3D Printed Highly Elastic Strain Sensors of Multiwalled Carbon Nanotube/Thermoplastic Polyurethane Nanocomposites,” *Mater. Des.*, vol. 131, pp. 394–401, 2017.

[19] Y. Ni, R. Ji, K. Long, T. Bu, K. Chen, and S. Zhuang, “A Review of 3D-Printed Sensors,” *Appl. Spectrosc. Rev.*, vol. 4928, 2017.

[20] B. Lu, H. Lan, and H. Liu, “Additive Manufacturing Frontier: 3D Printing Electronics,” *Opto-Electronic Adv.*, vol. 1, no. 1, p. 170004, 2018.

[21] Y. Wang, J. Hao, Z. Huang, G. Zheng, K. Daia, C. Liu, and C. Shen, “Flexible Electrically Resistive-Type Strain Sensors Based on Reduced Graphene Oxide-Decorated Electrospun Polymer Fibrous Mats for Human Motion Monitoring,” *Carbon N. Y.*, vol. 126, pp. 360–371, 2018.

[22] L. Xu, S. R. Gutbrod, A. P. Bonifas, Y. Su, M. S. Sulkin, N. Lu, H. Chung, K. Jang, Z. Liu, M. Ying, C. Lu, R. C. Webb, J. Kim, J. I. Laughner, H. Cheng, Y. Liu, A. Ameen, J. Jeong, G. Kim, Y. Huang, I. R. Efimov, and J. A. Rogers, “3D Multifunctional Integumentary Membranes for Spatiotemporal Cardiac Measurements and Stimulation across the Entire Epicardium,” *Nat. Commun.*, vol. 5, pp. 1–10, 2014.

[23] Y. Gao, H. Ota, E. W. Schaler, K. Chen, A. Zhao, W. Gao, H. M. Fahad, Y. Leng, A. Zheng, F. Xiong, C. Zhang, L. Tai, P. Zhao, R. S. Fearing, and A. Javey, “Wearable Microfluidic Diaphragm Pressure Sensor for Health and Tactile Touch Monitoring,” *Adv. Mater.*, vol. 29, no. 39, p. 1701985, Oct. 2017.

[24] C. L. Ventola, “Medical Applications for 3D Printing : Current and Projected Uses,” *P&T*, vol. 39, no. 10, pp. 704–711, 2014.

[25] H. Dodziuk, “Applications of 3D Printing in Healthcare,” *Polish Journal of Cardio-Thoracic Surgery*, vol. 13, no. 3, pp. 283–293, 2016.

[26] D. Therriault and L. L. Lebel, “Solvent-Cast Based Metal 3D Printing and Secondary Metallic Infiltration,” *J. Mater. Chem. C*, vol. 5, no. 40, 2017.

[27] R. L. Truby and J. A. Lewis, “Printing Soft Matter in Three Dimensions,” *Nature*, vol. 540, no. 7633, pp. 371–378, 2016.

[28] T. Campbell, “Could 3D Printing Change the World? Technologies, Potential, and Implications of Additive Manufacturing,” *Atlantic Council, Washington, DC, 3.* 2012.

[29] K. H. Church, N. B. Crane, P. I. Deffenbaugh, T. P. Ketterl, C. G. Neff, P. B. Nesbitt, J. T. Nussbaum, C. Perkowski, H. Tsang, J. Castro, J. Wang, and T. M. Weller, “Multimaterial and Multilayer Direct Digital Manufacturing of 3-D Structural Microwave Electronics,” *Proc. IEEE*, vol. 105, no. 4, pp. 688–701, 2017.

[30] T. Chartier, A. Badev, Y. Abouliatim, P. Lebaudy, and L. Lecamp, “Stereolithography Process : Influence of the Rheology of Silica Suspensions and of the Medium on Polymerization Kinetics – Cured Depth and Width,” *J. Eur. Ceram.*, vol. 32, pp. 1625–1634, 2012.

[31] J. Xing, M. Zheng, and X. Duan, “Two-Photon Polymerization Microfabrication of Hydrogels: An Advanced 3D Printing Technology for Tissue Engineering and Drug Delivery,” *Chem. Soc. Rev.*, vol. 44, no. May, pp. 5031–5039, 2015.

[32] Q. Mu, L. Wang, C. K.Dunn, X. Kuang, F. Duan, Z. Zhang, H. J. Qi, and T. Wang, “Digital Light Processing 3D Printing of Conductive Complex Structures,” Additive Manufacturing,” *Addit. Manuf.*, vol. 18, pp. 74–83, 2017.

[33] D. B. Vennilaa, G. Karuppusami, and P. Senthil, “Analysis of Different Infiltration Effect for Selective Laser Sintering Process through Taguchi Method Analysis of Different Infiltration Effect for Selective Laser Sintering Process,” *Aust. J. Mech. Eng.*, vol. 4846, pp. 1–7, 2016.

[34] J. O’Donnell, F. Ahmadkhanlou, H.-S. Yoon, and G. Washington, “All-Printed Smart Structures: A Viable Option?,” in *Proc.SPIE*, 2014, vol. 9057.

[35] T. D. Ngo, A. Kashani, G. Imbalzano, K. T. Q. Nguyen, and D. Hui, “Additive Manufacturing (3D Printing): A Review of Materials, Methods, Applications and Challenges,” *Compos. Part B*, vol. 143, no. February, pp. 172–196, 2018.

[36] B. Redwood, F. Schöffer, and B. Garret, "The 3D Printing Handbook : Technologies, Design and Applications," 1st ed. Amsterdam: 3D Hubs, 2018.

[37] T. J. Wallin, J. Pikul, and R. F. Shepherd, “3D Printing of Soft Robotic Systems,” *Nat. Rev. Mater.*, vol. 3, no. June, 2018.

[38] A. D. Valentine, T. A. Busbee, J. W. Boley, J. R. Raney, A. Chortos, A. Kotikian, J. D. Berrigan, M. F. Durstock, and J. A. Lewis, “Hybrid 3D Printing of Soft Electronics,” *Adv. Mater.*, vol. 1703817, pp. 1–8, 2017.

[39] J. Herzbergera, J. M. Sirrinea, C. B.Williams, and T. E. Long, “Polymer Design for 3D Printing Elastomers: Recent Advances in Structure, Properties, and Printing,” *Progress in Polymer Science* 97, 101144. 2019.

[40] A. E. Jakus, E. B. Secor, A. L. Rutz, S. W. Jordan, and M. C. Hersam, “Three-Dimensional Printing of High-Content Graphene Scaffolds for Electronic and Biomedical Applications,” *ACS nano*, no. 4, pp. 4636–4648, 2015.

[41] C. Liu, N. Huang, F. Xu , J. Tong, Z. Chen, X. Gui , Y. Fu, and C. Lao, “3D Printing Technologies for Flexible Tactile Sensors toward Wearable Electronics and Electronic Skin,” *Polymers*, pp. 1–31, 2018.

[42] A. Crist, J; Aliheidari, N; Potschke, P; Ameli, “Bidirectional and Stretchable Piezoresistive Sensors

Enabled by Multimaterial 3D Printing of Carbon Nanotube/Thermoplastic Polyurethane Nanocomposites," *Polymers (Basel).*, vol. 11, no. 1, p. 11, Dec. 2018.

[43] V. Katseli, A. Economou, and C. Kokkinos, "Single-Step Fabrication of an Integrated 3D-Printed Device for Electrochemical Sensing Applications," *Electrochem. commun.*, vol. 103, no. May, pp. 100–103, 2019.

[44] H. Kim, E. Park, S. Kim, B. Park, N. Kim, and S. Lee, "Experimental Study on Mechanical Properties of Single- and Dual-material 3D Printed Products," *Procedia Manuf.*, vol. 10, pp. 887–897, 2017.

[45] H. Gao and T. Qiang, "Fracture Surface Morphology and Impact Strength of Cellulose/PLA Composites," *Materials* , vol. 10, no. 6. 2017.

[46] M. Á. Caminero, J. M. Chacón, E. García-Plaza, P. J. Núñez, J. M. Reverte, and J. P. Becar, "Additive Manufacturing of PLA-Based Composites Using Fused Filament Fabrication: Effect of Graphene Nanoplatelet Reinforcement on Mechanical Properties, Dimensional Accuracy and Texture," *Polymers* , vol. 11, no. 5. 2019.

[47] S. R. G. Bates, I. R. Farrow, and R. S. Trask, "Compressive Behaviour of 3D Printed Thermoplastic Polyurethane Honeycombs with Graded Densities," *Mater. Des.*, vol. 162, pp. 130–142, 2019.

[48] H. J. Qi and M. C. Boyce, "Stress–Strain Behavior of Thermoplastic Polyurethanes," *Mech. Mater.*, vol. 37, no. 8, pp. 817–839, 2005.

[49] M. G. Tadesse, D. Dumitrescu, C. Loghin, Y. Chen, L. Wang, and V. Nierstrasz, "3D Printing of NinjaFlex Filament onto PEDOT:PSS-Coated Textile Fabrics for Electroluminescence Applications," *J. Electron. Mater.*, vol. 47, no. 3, pp. 2082–2092, 2018.

[50] A. Woern and J. Pearce, "Distributed Manufacturing of Flexible Products: Technical Feasibility and Economic Viability," *Technologies*, vol. 5, p. 71, Oct. 2017.

[51] K. Kim, J. Park, J. hoon Suh, M. Kim, Y. Jeong, and I. Park, "3D Printing of Multiaxial Force Sensors Using Carbon Nanotube (CNT)/Thermoplastic Polyurethane (TPU) Filaments," *Sensors Actuators, A Phys.*, vol. 263, pp. 493–500, 2017.

[52] R. Torres, Z. Cheng, R. Ramalingame, and O. Kanoun, "Electrical Characterization of Elongation Sensors Based on SBS-CTPU Filaments," in *2018 15th International Multi-Conference on Systems, Signals & Devices (SSD)*, 2018, pp. 1212–1215.

[53] N. P. Kim, "3D-Printed Conductive Carbon-Infused Thermoplastic Polyurethane," *Polymers (Basel).*, vol. 12, no. 6, p. 1224, 2020.

[54] G. Wolterink, R. Sanders, F. Muijzer, B. Van Beijnum, and G. Krijnen, "3D-Printing Soft sEMG Sensing Structures," *IEEE SENSORS Conference*, pp. 3–5, 2017.

[55] Y. Yang, S. Member, and Y. Chen, "3D Printing of Smart Materials for Robotics with Variable Stiffness and Position Feedback," *IEEE International Conference on Advanced Intelligent Mechatronics (AIM)*, 2017, pp. 418-423.

[56] K. Prashantha and F. Roger, “Multifunctional Properties of 3D Printed Poly(Lactic Acid)/Graphene Nanocomposites by Fused Deposition Modeling,” *J. Macromol. Sci. Part A Pure Appl. Chem.*, vol. 54, no. 1, pp. 24–29, 2017.

[57] C. Hu, Z. Li, Y. Wang, J. Gao, K. Dai, and G. Zheng, “Comparative Assessment of the Strain-Sensing Behaviors of Polylactic Acid Nanocomposites: Reduced Graphene Oxide or Carbon Nanotubes,” *J. Mater. Chem. C*, pp. 2318–2328, 2017.

[58] G. Postiglione, G. Natale, G. Griffini, M. Levi, and S. Turri, “Conductive 3D Microstructures by Direct 3D Printing of Polymer/Carbon Nanotube Nanocomposites via Liquid Deposition Modeling,” *Compos. Part A Appl. Sci. Manuf.*, vol. 76, pp. 110–114, 2015.

[59] C. E. Y. Erpek, G. Ozkoc, and U. Yilmazer, “Comparison of Natural Halloysite with Synthetic Carbon Nanotubes in Poly(Lactic Acid) Based Composites,” *Polym. Compos.*, vol. 38, no. 11, pp. 2337–2346, 2017.

[60] K. S. Geim, A K; Novoselov, “The Rise of Graphene,” *Nature*, pp. 183–192. 2010.

[61] B. T.-T. Chu and Sanjukta, “Graphene Science Handbook: Applications and Industrialization (Chapter 14 of volume 6),” 2015 by Taylor & Francis Group, LLC.

[62] A. V. Alaferdov, R. Savu, T. A. Rackauskas, S. Rackauskas, M. A. Canesqui, D. S. de. Lara, G. O. Setti, E. Joanni, G. M. de. Trindade, U. B. Lima, A. S. de. Souza, and S. A. Moshkalev, “Wearable, Highly Stable Strain and Bending Sensor Based on High Aspect Ratio Graphite Nanobelts,” *Nanotechnology*, vol. 27, Aug. 2016.

[63] D. Zhang, B. Chi, B. Li, Z. Gao, Y. Du, J. Guo, and J. Wei, “Fabrication of Highly Conductive Graphene Fl Exible Circuits by 3D Printing,” *Synth. Met.*, vol. 217, pp. 79–86, 2016.

[64] X. Sun, H. Sun, H. Li, and H. Peng, “Developing Polymer Composite Materials: Carbon Nanotubes or Graphene?,” *Adv. Mater.*, vol. 25, no. 37, pp. 5153–5176, 2013.

[65] S. Patton, C. Chen, J. Hu, L. Grazulis, A. Schrand, and A. Roy, “Characterization of Thermoplastic Polyurethane (TPU) and Ag-Carbon Black TPU Nanocomposite for Potential Application in Additive Manufacturing,” *Polymers (Basel).*, vol. 9, p. 6, Dec. 2016.

[66] K. Yamaguchi, J. J. C. Busfield, and A. G. Thomas, “Electrical and Mechanical Behavior of Filled Elastomers. I. The Effect of Strain,” *J. Polym. Sci. Part B Polym. Phys.*, vol. 41, no. 17, pp. 2079–2089, Sep. 2003.

[67] Y. Zheng, Y. Lia, K. Daiab, M. Liua, K. Zhoua, G. Zhenga, C. Liua, and C. Shen, “Conductive Thermoplastic Polyurethane Composites with Tunable Piezoresistivity by Modulating the Filler Dimensionality for Flexible Strain Sensors,” *Compos. Part A Appl. Sci. Manuf.*, vol. 101, pp. 41–49, 2017.

[68] J. Zhao, K. Dai, C. Liu, G. Zheng, B. Wang, C. Liu, J. Chen, and C. Shen, “A Comparison between Strain Sensing Behaviors of Carbon Black/Polypropylene and Carbon Nanotubes/Polypropylene Electrically Conductive Composites,” *Compos. Part A Appl. Sci. Manuf.*, vol. 48, pp. 129–136, 2013.

[69] H. Liu, Y. Li, H. Dai, G. Zheng, C. Liu, C. Shen, X. Yan, J. Guo, and Z. Guo,, “Electrically Conductive

Thermoplastic Elastomer Nanocomposites at Ultralow Graphene Loading Levels for Strain Sensor Applications," *J. Mater. Chem. C*, vol. 4, no. 1, pp. 157–166, 2015.

[70] C. Hohimer, N. Aliheidari, C. Mo, and A. Ameli, "Mechanical Behavior of 3D Printed Multiwalled Carbon Nanotube/Thermoplastic Polyurethane Nanocomposites," *Smart Materials, Adaptive Structures and Intelligent Systems.* vol. 58257. no. 2017.

[71] K. Gnanasekaran, T. Heijmans, S. Bennekom, H. Woldhuis, S. Wijnia, G. With, and H. Friedrich, "3D Printing of CNT- and Graphene-Based Conductive Polymer Nanocomposites by Fused Deposition Modeling," *Appl. Mater. Today*, vol. 9, pp. 21–28, Dec. 2017.

[72] G. Kaur, R. Adhikari, P. Cass, M. Bown, M. D. M. Evans, A. V. Vashia, and P. Gunatillake, "Graphene/Polyurethane Composites: Fabrication and Evaluation of Electrical Conductivity, Mechanical Properties and Cell Viability," *RSC Adv.*, vol. 5, Nov. 2015.

[73] C. S. Boland, U. Khan, G. Ryan, S. Barwich, R. Charifou, A. Harvey, C. Backes, Z. Li, M. S. Ferreira, M. E. Möbius, R. J. Young, and J. N. Coleman, "Sensitive Electromechanical Sensors Using Viscoelastic Graphene-Polymer Nanocomposites," *Science*, vol. 354, no. 6317, 2016.

[74] M. Melnykowycz, B. Koll, D. Scharf, and F. Clemens, "Comparison of Piezoresistive Monofilament Polymer Sensors," *Sensors* , vol. 14, no. 1. 2014.

[75] Z Wang, Y. Huang, J. Sun, Y. Huang, H. Hu, R. Jiang, W. Gai, G. Li, and C. Zhi, "Polyurethane/Cotton/Carbon Nanotubes Core-Spun Yarn as High Reliability Stretchable Strain Sensor for Human Motion Detection," *ACS Appl. Mater. Interfaces*, vol. 8, Aug. 2016.

[76] M. Amjadi, Y. J. Yoon, and I. Park, "Ultra-Stretchable and Skin-Mountable Strain Sensors Using Carbon Nanotubes–Ecoflex Nanocomposites," *Nanotechnology*, 26.37 375501. 2015.

[77] T. Yan, Z. Wang, and Z. J. Pan, "Flexible Strain Sensors Fabricated Using Carbon-Based Nanomaterials: A Review," *Curr. Opin. Solid State Mater. Sci.*, vol. 22, no. 6, pp. 213–228, 2018.

[78] R. Zhang, "Conductive TPU/CNT Composites for Strain Sensing," *Queen Mary, University of London*, no. July, pp. 1–201, 2009.

[79] L. Lin, S. Liu, Q. Zhang, X. Li, M. Ji, H. Deng, and Q. Fu, "Towards Tunable Sensitivity of Electrical Property to Strain for Conductive Polymer Composites Based on Thermoplastic Elastomer," *ACS Appl. Mater. Interfaces*, vol. 5, no. 12, pp. 5815–5824, 2013.

[80] C. Pang, G Lee, T. Kim, S. Kim, H. N. Kim, S. Ahn, and K. Suh, "A Flexible and Highly Sensitive Strain-Gauge Sensor Using Reversible Interlocking of Nanofibres," *Nat. Mater.*, vol. 11, no. 9, pp. 795–801, 2012.

[81] T. Yang, W. Wang, H. Zhang, X. Li, J. Shi, Y. He, Q. Zheng, Z. Li, and H. Zhu, "A Tactile Sensing System Based on Arrays of Graphene Woven Micro-Fabrics: Electromechanical Behavior and Electronic Skin Application," *ACS Nano*, vol. 9, Oct. 2015.

[82] B. U. Hwang, J. Lee, T. Trung, E. Roh, D. Kim, S. Kim, and N. Lee, "Transparent Stretchable Self-Powered Patchable Sensor Platform with Ultrasensitive Recognition of Human Activities," *ACS Nano*,

vol. 9, no. 9, pp. 8801–8810, 2015.

[83] A. Frutiger, J. T. Muth, D. M. Vogt, Y. Mengüç, A. Campo, A. D. Valentine. C. J. Walsh, and J. A. Lewis, “Capacitive Soft Strain Sensors via Multicore – Shell Fiber Printing,” *Adv. Mater.*, pp. 2440–2446, 2015.

[84] L. Pan, A. Chortos, G. Yu, Y. Wang, S. Isaacson, R. Allen, Y. Shi, R. Dauskardt, and Z. Bao, “An Ultra-Sensitive Resistive Pressure Sensor Based on Hollow-Sphere Microstructure Induced Elasticity in Conducting Polymer Film,” *Nat. Commun.*, vol. 5, no. 1, p. 3002, 2014.

[85] J. Ge, L. Sun, F. Zhang, Y. Zhang, L. Shi, H. Zhao, H. Zhu, H. Jiang, and S. Yu, “A Stretchable Electronic Fabric Artificial Skin with Pressure-, Lateral Strain-, and Flexion-Sensitive Properties,” *Adv. Mater.*, vol. 28, no. 4, pp. 722–728, Jan. 2016.

[86] F. Zhang, Y. Zang, D. Huang, C. Di, and D. Zhu, “Flexible and Self-Powered Temperature–Pressure Dual-Parameter Sensors Using Microstructure-Frame-Supported Organic Thermoelectric Materials,” *Nat. Commun.*, vol. 6, no. 1, p. 8356, 2015.

[87] A. Rinaldi, A. Proietti, A. Tamburrano, and M. S. Sarto, “Wearable Graphene-Based Sensor Array for Finger Tracking,” *IEEE SENSORS*, 2016, pp. 1–3.

[88] S. Shin, S. Ji, S. Choi, K. Pyo, B. W. An, J. Park, J. Kim, J. Kim, Ki. Lee, S. Kwon, J. Heo, B. Park, and J. Park, “Integrated Arrays of Air-Dielectric Graphene Transistors as Transparent Active-Matrix Pressure Sensors for Wide Pressure Ranges,” *Nat. Commun.*, vol. 8, no. 1, p. 14950, 2017.

[89] K. Dai, C. Liu, and Z. Guo, “Lightweight Conductive Graphene/Thermoplastic Polyurethane Foams with Ultrahigh Compressibility for Piezoresistive Sensing,” *J. Mater. Chem. C*. vol. 5, no. 1, 2017.

[90] M. Liu, X. Pu, C. Jiang, T. Liu, X. Huang, L. Chen, C. Du, J. Sun, W. Hu, and Z. L. Wang, “Large-Area All-Textile Pressure Sensors for Monitoring Human Motion and Physiological Signals,” *Adv. Mater.*, vol. 1703700, pp. 1–9, 2017.

[91] H. Zhu, X. Wang, J. Liang, H. Lv, H. Tong, L. Ma, Y. Hu, G. Zhu, T. Zhang, Z. Tie, Z. Liu, Q. Li, L. Chen, J. Liu, and Z. Jin, “Versatile Electronic Skins for Motion Detection of Joints Enabled by Aligned Few-Walled Carbon Nanotubes in Flexible Polymer Composites,” *Adv. Funct. Mater.*, vol. 27, no. 21, pp. 1–7, 2017.

[92] H. Jung, C. Park, H. Lee, S. Hong, H. Kim, and S. J. Cho, “Nano-Cracked Strain Sensor with High Sensitivity and Linearity by Controlling the Crack Arrangement,” *Sensors* , vol. 19, no. 12. 2019.

[93] X. Li, T. Yang, Y. Yang, J. Zhu, L Li, F. E. Alam, X. Li, K. Wang, H. Cheng, C. Lin, Y. Fang, and H. Zhu, “Large-Area Ultrathin Graphene Films by Single-Step Marangoni Self-Assembly for Highly Sensitive Strain Sensing Application,” *Adv. Funct. Mater.*, vol. 26, pp. 1322–1329, Mar. 2016.

[94] M. Amjadi, A. Pichitpajongkit, S. Lee, S. Ryu, and I. Park, “Highly Stretchable and Sensitive Strain Sensor Based on Silver,” *ACS Nano*, vol. 8, no. 5, pp. 5154–5163, 2014.

[95] Y. Wang, L. Wang, T. Yang, X. Li, X. Zang, M. Zhu, K. Wang, D. Wu, and H. Zhu, “Wearable and Highly Sensitive Graphene Strain Sensors for Human Motion Monitoring,” *Adv. Funct. Mater.*, vol. 24,

Aug. 2014.

[96] R. Sun, X. C. Zhang, J. Rossiter, and F. Scarpa, "A Highly Sensitive Pressure Sensor Using Conductive Composite Elastomers with Wavy Structures," *Smart Biomedical and Physiological Sensor Technology XIII*. Vol. 9863. International Society for Optics and Photonics, 2016.

[97] W. Zhong, Q. Liu, Y. Wu, Y. Wang, X. Qing, M. Li, K. Liu, W. Wang, and D. Wang, "A Nanofiber Based Artificial Electronic Skin with High Pressure Sensitivity and 3D Conformability," *Nanoscale*, vol. 8, no. 24, pp. 12105–12112, 2016.

[98] C. Lozano-Pérez, J. V Cauich-Rodríguez, and F. Avilés, "Influence of Rigid Segment and Carbon Nanotube Concentration on the Cyclic Piezoresistive and Hysteretic Behavior of Multiwall Carbon Nanotube/Segmented Polyurethane Composites," *Compos. Sci. Technol.*, vol. 128, pp. 25–32, 2016.

[99] D. S. A. De Focatiis, D. Hull, and A. Sánchez-Valencia, "Roles of Prestrain and Hysteresis on Piezoresistance in Conductive Elastomers for Strain Sensor Applications," *Plast. Rubber Compos.*, vol. 41, no. 7, pp. 301–309, Sep. 2012.

[100] R. Zhang, H. Deng, R. Valenca, J. Jin, Q. Fu, E. Bilotti, and T. Peijs, "Strain Sensing Behaviour of Elastomeric Composite Films Containing Carbon Nanotubes under Cyclic Loading," *Compos. Sci. Technol.*, vol. 74, pp. 1–5, 2013.

[101] S. Gong, Z. H. Zhu, and S. A. Meguid, "Carbon Nanotube Agglomeration Effect on Piezoresistivity of Polymer Nanocomposites," *Polymer (Guildf).*, vol. 55, no. 21, pp. 5488–5499, 2014.

[102] C. Lozano-Pérez, J. V Cauich-Rodríguez, and F. Avilés, "Influence of Rigid Segment Content on the Piezoresistive Behavior of Multiwall Carbon Nanotube/Segmented Polyurethane Composites," *J. Appl. Polym. Sci.*, vol. 134, no. 6, Feb. 2017.

[103] F. Avil, "Influence of Rigid Segment and Carbon Nanotube Concentration on the Cyclic Piezoresistive and Hysteretic Behavior of Multiwall Carbon Nanotube / Segmented Polyurethane Composites," *Compos. Sci. Technol.*, vol. 128, pp. 25–32, 2016.

[104] H. Liu, J. Gao, W. Huang, K. Dai, G. Zheng, C. Liu, C. Shen, X. Yan, J. Guo, and Z. Guo, "Electrically Conductive Strain Sensing Polyurethane Nanocomposites with Synergistic Carbon Nanotubes and Graphene Bifillers," *Nanoscale*, pp. 12977–12989, 2016.

[105] D. Focatiis, D. Hull, and A. Sánchez-Valencia, "Roles of Prestrain and Hysteresis on Piezoresistance in Conductive Elastomers for Strain Sensor Applications." *Plastics, Rubber and Composites*, 41.7. 301-309. 2012.

[106] H. Liu, Q. Li, S. Zhang, R. Yin, X. Liu, Y. He, K. Dai, C. Shan, Jiang Guo, C. Liu, C. Shen, X. Wang, N. Wang, Z. Wang, R. Wei, and Z. Guo, "Electrically Conductive Polymer Composites for Smart Flexible Strain Sensors: A Critical Review," *Journal of Materials Chemistry C*, 6(45), 12121-12141. 2018.

[107] H. Yazdani, K. Hatami, E. Khosravi, K. Harper, and B. P. Grady, "Strain-Sensitive Conductivity of Carbon Black-Filled PVC Composites Subjected to Cyclic Loading," *Carbon N. Y.*, vol. 79, pp. 393–405, 2014.

[108] K. Kim, S. Hong, H. Cho, J. Lee, Y. Suh, J. Ham, and S. H. Ko, “Highly Sensitive and Stretchable Multidimensional Strain Sensor with Prestrained Anisotropic Metal Nanowire Percolation Networks,” *Nano Lett.*, vol. 15, no. 8, pp. 5240–5247, Aug. 2015.

[109] J. Zhou, X. Xu, Y. Xin, and G. Lubineau, “Coaxial Thermoplastic Elastomer-Wrapped Carbon Nanotube Fibers for Deformable and Wearable Strain Sensors,” *Adv. Funct. Mater.*, vol. 28, no. 16, pp. 1–8, 2018.

[110] X. Li, R. Zhang, W. Yu, K. Wang, J. Wei, D. Wu, A. Cao, Z. Li, Y. Cheng, Q. Zheng, R. S. Ruoff, and H. Zhu, “Stretchable and Highly Sensitive Graphene-on-Polymer Strain Sensors,” *Sci. Rep.*, pp. 1–6, 2012.

[111] S. Chen, Y. Wei, S. Wei, Y. Lin, and L. Liu, “Ultrasensitive Cracking-Assisted Strain Sensors Based on Silver Nanowires/Graphene Hybrid Particles,” *ACS Appl. Mater. Interfaces*, vol. 8, Sep. 2016.

[112] D. Kang, P. V. Pikhitsa, Y. W. Choi, C. Lee, S. S. Shin, L. Piao, B. Park, K. Suh, T. Kim, and M. Choi, “Ultrasensitive Mechanical Crack-Based Sensor Inspired by the Spider Sensory System,” *Nature*, vol. 516, no. 7530, pp. 222–226, 2014.

[113] T. Yang, X. Li, X. Jiang, S. Lin, J. Lao, J. Shi, Z. Zhen, Z. Li and H. Zhu, “Structural Engineering of Gold Thin Films with Channel Cracks for Ultrasensitive Strain Sensing,” *Mater. Horizons*, vol. 3, no. 3, pp. 248–255, 2016.

[114] K. H. Nam, I. H. Park, and S. H. Ko, “Patterning by Controlled Cracking,” *Nature*, vol. 485, no. 7397, pp. 221–224, 2012.

[115] B. C. Kim, T. Matsuoka, C. Moraes, J. Huang, M. D. Thouless, and S. Takayama, “Guided Fracture of Films on Soft Substrates to Create Micro/Nano-Feature Arrays with Controlled Periodicity,” *Sci. Rep.*, vol. 3, pp. 1–6, 2013.

[116] X. Liao, Q. Liao, X. Yan, Q. Liang, H. Si, M. Li, H. Wu, S. Cao, and Y. Zhang, “Flexible and Highly Sensitive Strain Sensors Fabricated by Pencil Drawn for Wearable Monitor,” *Adv. Funct. Mater.*, vol. 25, no. 16, pp. 2395–2401, Apr. 2015.

[117] J. Lee, S. Kim, J. Lee, D. Yang, B. C. Park, S. Ryu, and I. Park, “Stretchable Strain Sensor based on Metal Nanoparticle Thin Film for Human Motion Detection,” *Nanoscale*, vol. 6, Aug. 2014.

[118] F. M. Guo, X. Cui, K. L. Wang, and J. Q. Wei, “Stretchable and Compressible Strain Sensors Based on Carbon Nanotube Meshes,” *Nanoscale*, vol. 8, no. 46, pp. 19352–19358, 2016.

[119] Y. Arafat, I. Dutta, and R. Panat, “Super-Stretchable Metallic Interconnects on Polymer with a Linear Strain of up to 100%,” *Appl. Phys. Lett.*, vol. 107, no. 8, p. 81906, Aug. 2015.

[120] M. Serry and M. Sakr, "Modeling and Experimental Characterization of Flexible Graphene Composite Strain Sensors," *IEEE SENSORS*, pp. 1-3 2016.

[121] B. Zhang, J. Lei, D. Qi, Z. Liu, Y. Wang, G. Xiao, J. Wu, W. Zhang, F. Huo, and X. Chen, “Stretchable Conductive Fibers Based on a Cracking Control Strategy for Wearable Electronics,” *Adv. Funct. Mater.*, vol. 28, no. 29, p. 1801683, Jul. 2018.

[122] C. Lee, K. H. Park, C. J. Han, M. S. Oh, B. You, Y. Kim, and J. W. Kim, “Crack-Induced Ag Nanowire Networks for Transparent, Stretchable, and Highly Sensitive Strain Sensors,” *Sci. Rep.*, vol. 7, no. 1, p. 7959, 2017.

[123] T. Yamada, Y. Hayamizu, Y. Yamamoto, Y. Yomogida, A. Izadi-Najafabadi, D. N. Futaba, and K. Hata, “A Stretchable Carbon Nanotube Strain Sensor for Human-Motion Detection,” *Nat. Nanotechnol.*, vol. 6, no. 5, pp. 296–301, 2011.

[124] Y. Song, J.-I. Lee, S. Pyo, Y. Eun, J. Choi, and J. Kim, “A Highly Sensitive Flexible Strain Sensor Based on the Contact Resistance Change of Carbon Nanotube Bundles,” *Nanotechnology*, vol. 27, p. 205502, Apr. 2016.

[125] Z. Tang, S. Jia, X. Shi, B. Li, and C. Zhou, “Coaxial Printing of Silicone Elastomer Composite Fibers for Stretchable and Wearable Piezoresistive Sensors,” *Polymers (Basel).*, vol. 11, no. 4, p. 666, Apr. 2019.

[126] C. Yan, J. Wang, W. Kang, M. Cui, X. Wang, C. Y. Foo, K. J. Chee, and P. S. Lee, “Highly Stretchable Piezoresistive Graphene–Nanocellulose Nanopaper for Strain Sensors,” *Adv. Mater.*, vol. 26, no. 13, pp. 2022–2027, Apr. 2014.

[127] Y. Jiang, Z. Liu, N. Matsuhisa, D. Qi, W. R. Leow, H. Yang, J. Yu, G. Chen, Y. Liu, C. Wan, Z. Liu, and X. Chen, “Auxetic Mechanical Metamaterials to Enhance Sensitivity of Stretchable Strain Sensors,” *Adv. Mater.*, vol. 30, no. 12, p. 1706589, Mar. 2018.

[128] H. Vandeparre, Q. Liu, I. Minev, Z. Suo, and S. Lacour, “Localization of Folds and Cracks in Thin Metal Films Coated on Flexible Elastomer Foams,” *Adv. Mater.*, vol. 25, Jun. 2013.

[129] Z. Chen, W. Ren, L. Gao, B. Liu, S. Pei, and H.-M. Cheng, “Three-Dimensional Flexible and Conductive Interconnected Graphene Networks Grown by Chemical Vapour Deposition,” *Nat. Mater.*, vol. 10, no. 6, pp. 424–428, 2011.

[130] N. Lu, C. Lu, S. Yang, and J. Rogers, “Highly Sensitive Skin-Mountable Strain Gauges Based Entirely on Elastomers,” *Adv. Funct. Mater.*, vol. 22, no. 19, pp. 4044–4050, Oct. 2012.

[131] H. Jeon, S. K. Hong, M. S. Kim, S. J. Cho, and G. Lim, “Omni-Purpose Stretchable Strain Sensor Based on a Highly Dense Nanocracking Structure for Whole-Body Motion Monitoring,” *ACS Appl. Mater. Interfaces*, vol. 9, no. 48, pp. 41712–41721, Dec. 2017.

[132] M. Maurizi, J. Slavič, F. Cianetti, M. Jerman, J. Valentinčič, A. Lebar, and M. Boltežar, “Dynamic Measurements Using FDM 3D-Printed Embedded Strain Sensors,” *Sensors*, vol. 19, p. 2661, Jun. 2019.

[133] A. Smith, “Design and Fabrication of FDM 3D Printed Strain Sensors,” *Lousiana Tech Uni.*, 2018.

[134] G. Andria, A. Di Nisio, A. M. L. Lanzolla, G. Percoco, and G. Stano, “Design and Characterization of Innovative 3D Printed Embedded Strain Gauges,” *IEEE 5th International Workshop on Metrology for AeroSpace (MetroAeroSpace)*, pp. 54–59. 2019.

[135] M. Maurizi, F. Cianetti, J. Slavič, G. Zucca, and M. Palmieri, “Piezoresistive Dynamic Simulations of FDM 3D-Printed Embedded Strain Sensors: A New Modal Approach,” *Procedia Struct. Integr.*, vol. 24, pp. 390–397, 2019.

[136] M. Dukic, M. Winhold, C. H. Schwalb, J. D. Adams, V. Stavrov, M. Huth, and G. E. Fantner, "Direct-Write Nanoscale Printing of Nanogranular Tunnelling Strain Sensors for Sub-Micrometre Cantilevers," *Nat. Commun.*, vol. 7, no. 1, p. 12487, 2016.

[137] J. H. Song, Y. Kim, S. Cho, W. Song, S. Moon, C. Park, S. Park, J. M. Myoung, and U. Jeong, "Surface-Embedded Stretchable Electrodes by Direct Printing and their Uses to Fabricate Ultrathin Vibration Sensors and Circuits for 3D Structures," *Adv. Mater.*, vol. 29, Oct. 2017.

[138] J. U. Lind, T. A. Busbee, A. D. Valentine, F. S. Pasqualini, H. Yuan, M. Yadid, S. J. Park, A. Kotikian, A. P. Nesmith, P. H. Campbell, J. J. Vlassak, J. A. Lewis, and Kevin K. Parker, "Instrumented Cardiac Microphysiological Devices via Multimaterial Three-Dimensional Printing," *Nat. Mater.*, vol. 16, no. 3, pp. 303–308, 2017.

[139] X. Wang, J. Li, H. Song, H. Huang, and J. Gou, "Highly Stretchable and Wearable Strain Sensor Based on Printable Carbon Nanotube Layers/Polydimethylsiloxane Composites with Adjustable Sensitivity," *ACS Appl. Mater. Interfaces*, vol. 10, no. 8, pp. 7371–7380, Feb. 2018.

[140] J. R. Mcghee, M. Sinclair, D. J. Southee, and K. G. U. Wijayantha, "Strain Sensing Characteristics of 3D-Printed Conductive Plastics," *Electron. Lett.*, vol. 54, no. 9, pp. 10–11, 2018.

[141] H. Yan, Y. Chen, Y. Deng, L. Zhang, X. Hong, W. Lau, J. Mei, D. Hui, H. Yan, and Y Liu, "Coaxial Printing Method for Directly Writing Stretchable Cable as Strain Sensor," *Appl. Phys. Lett.*, vol. 083502, no. August, pp. 1–5, 2016.

[142] X. Li, M. M. Honari, Y. Fu, A. Kumar, H. Saghlatoon, P. Mousavi, and H. J. Chung, "Self-Reinforcing Graphene Coatings on 3D Printed Elastomers for Flexible Radio Frequency Antennas and Strain Sensors," *Flex. Print. Electron.*, vol. 2, no. 3, p. 35001, 2017.

[143] M. Alsharari, B. Chen, and W. Shu, "3D Printing of Highly Stretchable and Sensitive Strain Sensors Using Graphene Based Composites †," *MDPI*, pp. 8–11, 2018.

[144] J. F. Christ, C. J. Hohimer, N. Aliheidari, A. Ameli, C. Mo, and P. Pötschke, "3D Printing of Highly Elastic Strain Sensors Using Polyurethane/Multiwall Carbon Nanotube Composites," *Proc.SPIE*, 2017, vol. 10168.

[145] S. Dul, A. Pegoretti, and L. Fambri, "Fused Filament Fabrication of Piezoresistive Carbon Nanotubes Nanocomposites for Strain Monitoring," *Frontiers in Materials* , vol. 7. p. 12, 2020.

[146] Y. Park, B. Chen, and R. J. Wood, "Design and Fabrication of Soft Artificial Skin Using Embedded Microchannels and Liquid Conductors," *IEEE Sens. J.*, vol. 12, no. 8, pp. 2711–2718, 2012.

[147] M. G. Mohammed and R. Kramer, "All-Printed Flexible and Stretchable Electronics," *Adv. Mater.*, vol. 29(19), 1604965. 2017.

[148] E. L. White, J. C. Case, and R. K. Kramer, "Multi-Mode Strain and Curvature Sensors for Soft Robotic Applications," *Sensors Actuators A Phys.*, vol. 253, pp. 188–197, 2017.

[149] P. Bifulco, D. Esposito, G. D. Gargiulo, S. Savino, V. Niola, L. Iuppariello, and M. Cesarelli, "A Stretchable, Conductive Rubber Sensor to Detect Muscle Contraction for Prosthetic Hand Control," *E-*

Health and Bioengineering Conference (EHB), 2017, pp. 173–176.

[150] S. Peng, P. Blanloeuil, S. Wu, and C. H. Wang, "Rational Design of Ultrasensitive Pressure Sensors by Tailoring Microscopic Features," *Adv. Mater. Interfaces*, vol. 5, no. 18, p. 1800403, Sep. 2018.

[151] S. Guo, K. Qiu, F. Meng, S. H. Park, and M. C. Mcalpine, "3D Printed Stretchable Tactile Sensors," *Adv. Mater.*, vol. 1701218, pp. 1–8, 2017.

[152] Z. Wang, X. Guan, H. Huang, H. Wang, W. Lin, and Z. Peng, "Full 3D Printing of Stretchable Piezoresistive Sensor with Hierarchical Porosity and Multimodulus Architecture," *Adv. Funct. Mater.*, vol. 29, no. 11, p. 1807569, Mar. 2019.

[153] B. Eijking, R. Sanders, and G. Krijnen, "Development of Whisker Inspired 3D Multi-Material Printed Flexible Tactile Sensors," *IEEE SENSORS*, 2017, pp. 1–3.

[154] M. Liu, Y. Zhao, Y. Shao, Q. Zhang, and C. Liu, "3D Printed Force Sensor with Inkjet Printed Piezoresistive Based Strain Gauge," *IEEE SENSORS*, 2018, pp. 1–4.

[155] C. Hong, Y. Zhang, and L. Borana, "Design, Fabrication and Testing of a 3D Printed FBG Pressure Sensor," *IEEE Access*, vol. 7, pp. 38577–38583, 2019.

[156] W. Dang, V. Vinciguerra, L. Lorenzelli, and R. Dahiya, "Printable Stretchable Interconnects," *Flex. Print. Electron.*, vol. 2, no. 1, p. 13003, 2017.

[157] Y. Wang, S. Gong, S. J. Wang, G. P. Simon, and W. Cheng, "Volume-Invariant Ionic Liquid Microbands as Highly Durable Wearable Biomedical Sensors," *Mater. Horizons*, vol. 3, no. 3, pp. 208–213, 2016.

[158] M. Melnykowycz, M. Tschudin, and F. Clemens, "Piezoresistive Carbon-based Hybrid Sensor for Body-Mounted Biomedical Applications," *IOP Conf. Ser. Mater. Sci. Eng.*, vol. 175, p. 12006, Feb. 2017.

[159] D. Y. Choi, Mi. H. Kim, Y. S. Oh, S. H. Jung, J. H. Jung, H. J. Sung, H. W. Lee, and H. M. Lee, "Highly Stretchable, Hysteresis-Free Ionic Liquid-Based Strain Sensor for Precise Human Motion Monitoring," *ACS Appl. Mater. Interfaces*, vol. 9, no. 2, pp. 1770–1780, Jan. 2017.

[160] K. Sim, Z. Rao, Z. Zou, F. Ershad, J. Lei, A. Thukral, J. Chen, Q. Huang, J. Xiao, and C. Yu, "Metal Oxide Semiconductor Nanomembrane – Based Soft Unnoticeable Multifunctional Electronics for Wearable Human-Machine Interfaces," *Sci. Adv.*, no. August, pp. 1–11, 2019.

[161] S.-Y. Wu, C. Yang, W. Hsu, and L. Lin, "3D-Printed Microelectronics for Integrated Circuitry and Passive Wireless Sensors," *Microsystems Nanoeng.*, vol. 1, no. 1, p. 15013, 2015.

[162] S. Gong, D. T. Lai, Y. Wang, L. W. Yap, K. J. Si, Q. Shi, N. N. Jason, T. Sridhar, H. Uddin, and W. Cheng, "Tattoolike Polyaniline Microparticle-Doped Gold Nanowire Patches as Highly Durable Wearable Sensors," *ACS Appl. Mater. Interfaces*, vol. 7, no. 35, pp. 19700–19708, 2015.

[163] K. Tian, J. Bae, S. E. Bakarich, C. Yang, R. D. Gately, G. M. Spinks, M. Panhuis, Z. Suo, and J. J. Vlassak, "3D Printing of Transparent and Conductive Heterogeneous Hydrogel–Elastomer Systems," *Adv. Mater.*, vol. 29, no. 10, p. 1604827, 2017.

[164] G. ALICI, "Softer is Harder: What Differentiates Soft Robotics from Hard Robotics?," *MRS Adv.*, vol. 3,

no. 28, pp. 1557–1568, 2018.

[165] Y. Mengüç, Y. Park, H. Pei, D. Vogt, P. M. Aubin, E. Winchell, L. Fluke, L. Stirling, R. J. Wood, and C. J. Walsh, “Wearable Soft Sensing Suit for Human Gait Measurement,” *Int. J. Rob. Res.*, vol. 33, no. 14, pp. 1748–1764, Nov. 2014.

[166] H. Wei, K. Li, W. G. Liu, H. Meng, P. X. Zhang, and C. Y. Yan, “3D Printing of Free-Standing Stretchable Electrodes with Tunable Structure and Stretchability,” *Adv. Eng. Mater.*, vol. 19, no. 11, pp. 1–6, 2017.

[167] Y. Cheng, R. Wang, J. Sun, and L. Gao, “A Stretchable and Highly Sensitive Graphene-Based Fiber for Sensing Tensile Strain, Bending, and Torsion,” *Adv. Mater.*, vol. 27, no. 45, pp. 7365–7371, Dec. 2015.

[168] S. Chen, Y. Wei, X. Yuan, Y. Lin, and L. Liu, “A Highly Stretchable Strain Sensor Based on a Graphene/Silver Nanoparticle Synergic Conductive Network and a Sandwich Structure,” *J. Mater. Chem. C*, vol. 4, no. 19, pp. 4304–4311, 2016.

[169] J.-S. Noh, “Conductive Elastomers for Stretchable Electronics, Sensors and Energy Harvesters,” *Polymers (Basel).*, vol. 8, p. 123, Apr. 2016.

[170] G. Schwartz, B. Tee, J. Mei, A. L. Appleton, D. H. Kim, H. Wang, and Z. Bao, “Flexible Polymer Transistors with High Pressure Sensitivity for Application in Electronic Skin and Health Monitoring,” *Nat. Commun.*, vol. 4, no. 1, p. 1859, 2013.

[171] NinjaTek, “NinjaFlex,” 2016. [Online]. Available: https://ninjatek.com/ninjaflex/. [Accessed: 02-Mar-2017].

[172] T. Hexpol, “Carbon Black Thermoplastic Polyurethane,” 2016. [Online]. Available: https://www.hexpoltpe.com/en/dryflex-c.htm. [Accessed: 02-Sep-2019].

[173] S. A. Nanocyl, “PLASTICYL™ TPU1001,” 2017. [Online]. Available: https://www.nanocyl.com/product/plasticyl-pp2001-2/. [Accessed: 02-Feb-2018].

[174] Blackmagic3D, “Graphene PLA,” 2016. [Online]. Available: http://www.blackmagic3d.com/Conductive-Thermoplastic-Graphene-PLA-Pellets-0-5-p/graph-pla-p.htm. [Accessed: 05-Sep-2017].

[175] eSun, “PVA,” 2017. [Online]. Available: http://www.esun3d.net/products/82.html. [Accessed: 05-Mar-2018].

[176] Noztek, “Noztek Pro Filament Extruder,” 2017. [Online]. Available: https://www.noztek.com/product/noztek-pro/. [Accessed: 15-Jul-2017].

[177] FlashForge-Corporation, “Flashforge Creator Pro 3D Printer,” 2016. [Online]. Available: https://www.flashforge.com/consumer/Creator Pro series?id=12. [Accessed: 14-Sep-2016].

[178] Diabase, “Flexion Extruder,” 2016. [Online]. Available: https://flexionextruder.com/how-it-works/. [Accessed: 05-Sep-2016].

[179] C. K. Chua, K. F. Leong, and C. S. Lim, "Rapid Prototyping: Principles and Applications," *Second. Singapore: World Scientific*, 2003.

[180] PicoTechnology, “PicoLog 1000 Series,” 2017. [Online]. Available: https://www.picotech.com/data-logger/picolog-1000-series/picolog-1000-manuals. [Accessed: 25-Mar-2017].

[181] Arduino, “Arduino software and hardware,” 2018. [Online]. Available: https://www.arduino.cc/. [Accessed: 12-Sep-2018].

[182] Dino-Lite, “Dino-Lite AD4113ZTL digital microscope,” 2018. [Online]. Available: https://www.dinolite-uk.com/index.php/microscopes. [Accessed: 20-Aug-2018].

[183] Z. Wang and X. Ye, “A Numerical Investigation on Piezoresistive Behaviour of Carbon Nanotube/Polymer Composites: Mechanism and Optimizing Principle,” *Nanotechnology*, vol. 24, no. 26, p. 265704, 2013.

[184] N. Hu, Y. Karube, C. Yan, Z. Masuda, and H. Fukunaga, “Tunneling Effect in a Polymer/Carbon Nanotube Nanocomposite Strain Sensor,” *Acta Mater.*, vol. 56, no. 13, pp. 2929–2936, 2008.

[185] K. Elgeneidy, G. Neumann, M. Jackson, and N. Lohse, “Directly Printable Flexible Strain Sensors for Bending and Contact Feedback of Soft Actuators,” *Frontiers in Robotics and AI* , vol. 5. p. 2, 2018.

[186] B. Balakrisnan, A. Nacev, J. Burke, A. Dasgupta, and E. Smela, “Design of Compliant Meanders for Applications in MEMS, Actuators, and Flexible Electronics,” *Smart Mater. Struct,* vol. 21, Jul. 2012.

[187] H. Lee, B. Seong, H. Moon, and D. Byun, “Directly Printed Stretchable Strain Sensor Based on Ring and Diamond Shaped Silver Nanowire Electrodes,” *RSC Adv.*, vol. 5, no. 36, pp. 28379–28384, 2015.

[188] H. Ragones, S. Menkin, Y. Kamir, A. Gladkikh, and T. Mukra, “Towards Smart Free Form-Factor 3D Printable Batteries,” *Sustain. Energy Fuels,* pp. 1542–1549, 2018.

[189] C. Y. Foo, H. N. Lim, M. A. Mahdi, and M. H. Wahid, “Three-Dimensional Printed Electrode and Its Novel Applications in Electronic Devices,” *Sci. Rep.*, no. November 2017, pp. 1–11, 2018.

[190] G. I. Márk and L. P. Biró, “Mechanical and Electromagnetic Properties of 3D Printed Hot Pressed Nanocarbon / Poly (Lactic) Acid Thin Films,” *J. Appl. Phys.*, vol. 064105, 2017.

[191] H. Gao, and T. Qiang, “Fracture Surface Morphology and Impact Strength of Cellulose/PLA Composites,” *Materials (basel)*, pp. 1–11, 2017.

[192] L. Sang, S. Han, Z. Li, X. Yang, and W. Hou, “Development of Short Basalt Fi Ber Reinforced Polylactide Composites and Their Feasible Evaluation for 3D Printing Applications,” *Compos. Part B*, vol. 164, no. October 2018, pp. 629–639, 2019.

Appendix A

Scanning electron microscopy SEM images

The extruded mixtures were characterised using an SEM imaging technique. SEM images were taken to show the morphology of the composite materials. Specimens used were CBTPU, GPLA, CBTPU30GPLA, CBTPU40GPLA, and CBTPU50GPLA, each was 10 mm in length and 1.75 mm in diameter. Images of different ratios of conductive CBTPU and GPLA filaments are shown in Figure 0.1. The neat CBTPU and GPLA were characterised as received, and it can be observed that the CBTPU and GPLA had distinct surface profiles. The GPLA filament had visible roughness on its surface. The surface roughness was significant in the GPLA in comparison to the smooth surface of the CBTPU and could be attributed to the manufacturing process of the purchased filament, the rigidity and brittleness of the host polylactic acid PLA matrix or the structure of 2D graphene sheets as the conductive filler.

On the other hand, CBTPU contains carbon black CB particles as the conductive filler and thermoplastic polyurethane TPU as the host matrix. The spherical structure of the CB and the inherent smooth surface of TPU could be attributed to the smooth surface profile of the neat CBTPU. The presence of surface roughness experienced here agrees with previously reported polymers infused with nanocomposites which showed roughness in their surface profile [58], [59], [71], [72]. The distinct difference in the surface profiles helped characterise the mixture of the 2 conducting polymer composites. The surface roughness impacted on the filaments with a higher content of GPLA. The addition of GPLA to CBTPU increased the material's surface roughness, as shown in Figure 0.1c-e, respectively. The higher the content of GPLA added to CBTPU, the higher the roughness observed in the surface of the filaments. Inversely, the composite with a higher value of CBTPU had a smoother surface consequently. Further analysis of the filaments evaluating their mechanical and electrical properties is carried out in the following sections [188]–[192].

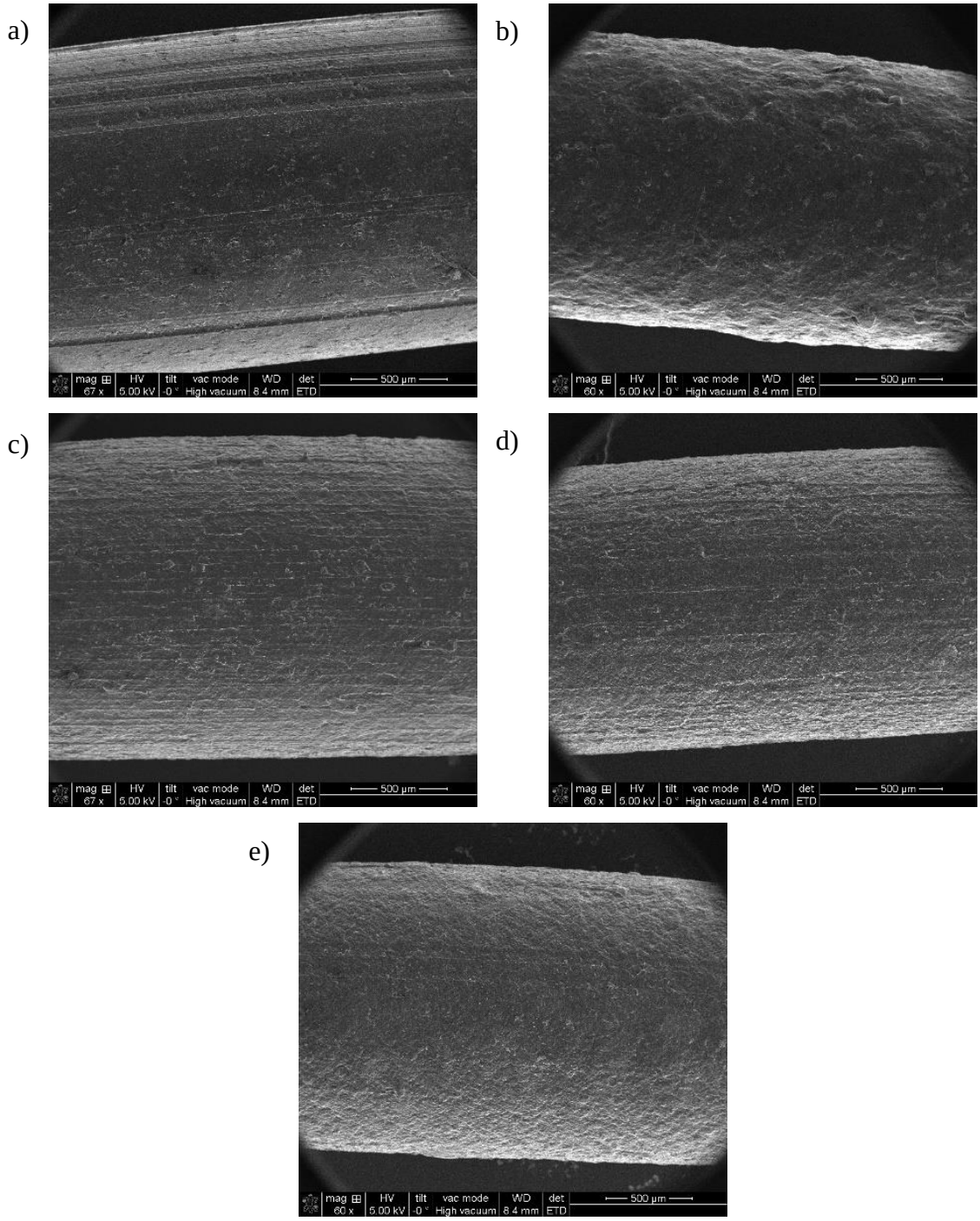

Figure 0.1: SEM images of a) CBTPU, b) GPLA, c) CBTPU-30GPLA, d) CBTPU-40GPLA and e) CBTPU-50GPLA.

Calculation of crack formation via ImageJ software

ImageJ is an intuitive software used to analyse the crack formation of the 3D printed strain sensors. This section presents the steps that were followed to characterise and analyse the crack formation in the 3D printed strain sensors. The analysis and characterisation of the cracks were

achieved by measuring the average crack openings and calculating the overall area of the cracks. The images of the 3D printed strain sensors were acquired under dynamic strain loading using an optical microscope.

Firstly, an image was exported to ImageJ software, as illustrated in Figure A. 1. The scale bar of the image exported from the optical microscope was used to set the measurement in millimetre (mm) instead of pixels (default ImageJ scale). The area of interest where the cracks formed is then cropped to be used in the following steps. The image was then converted to an 8 -bit grayscale to simplify the processing and eliminate the noise. This step converted the image from full coloured (RGB colour) to an 8-bit grayscale image.

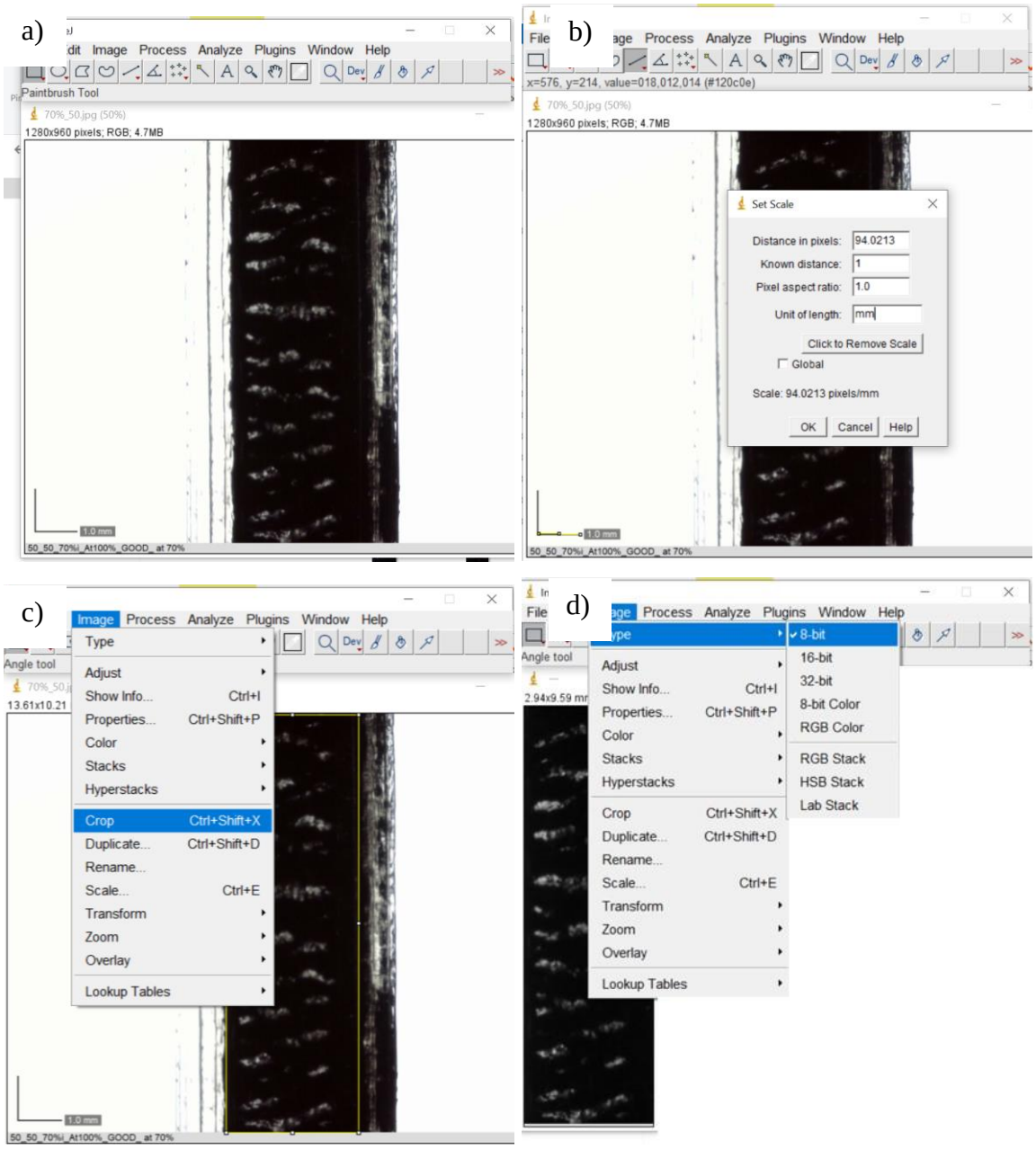

Figure A. 1: Steps of crack analysis starting with a) Importing an image to ImageJ, b) Setting the scale in mm, c) Cropping the desired image of interest and d) Converting the cropped image to an 8-bit greyscale from the imported full coloured RGB colour image.

After that, the image was further processed by adjusting the threshold, which converts the image to binary, facilitating the calculation and analysis of the cracks. Threshold (Figure A. 2) was performed to segment the particles in the binary image and eliminated the background to leave only the particles (which, in this case, the cracks). This step allowed us to determine the cracks easily. Consequently, the software then enabled us to analyse the particles, as illustrated in Figure A. 3. It was then possible to acquire the theoretical average heights in (mm) and the area of the crack formation in percentages (%).

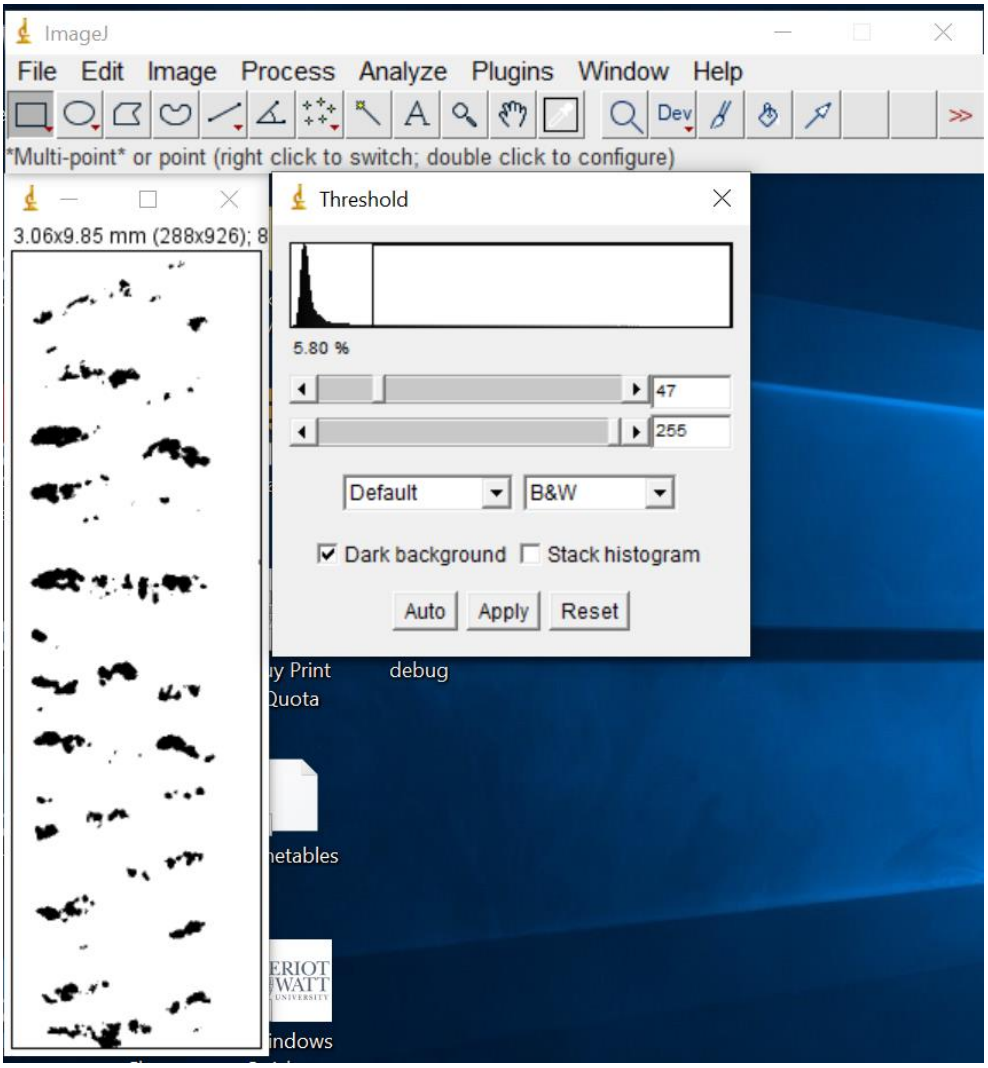

Figure A. 2: Setting the threshold of the image.

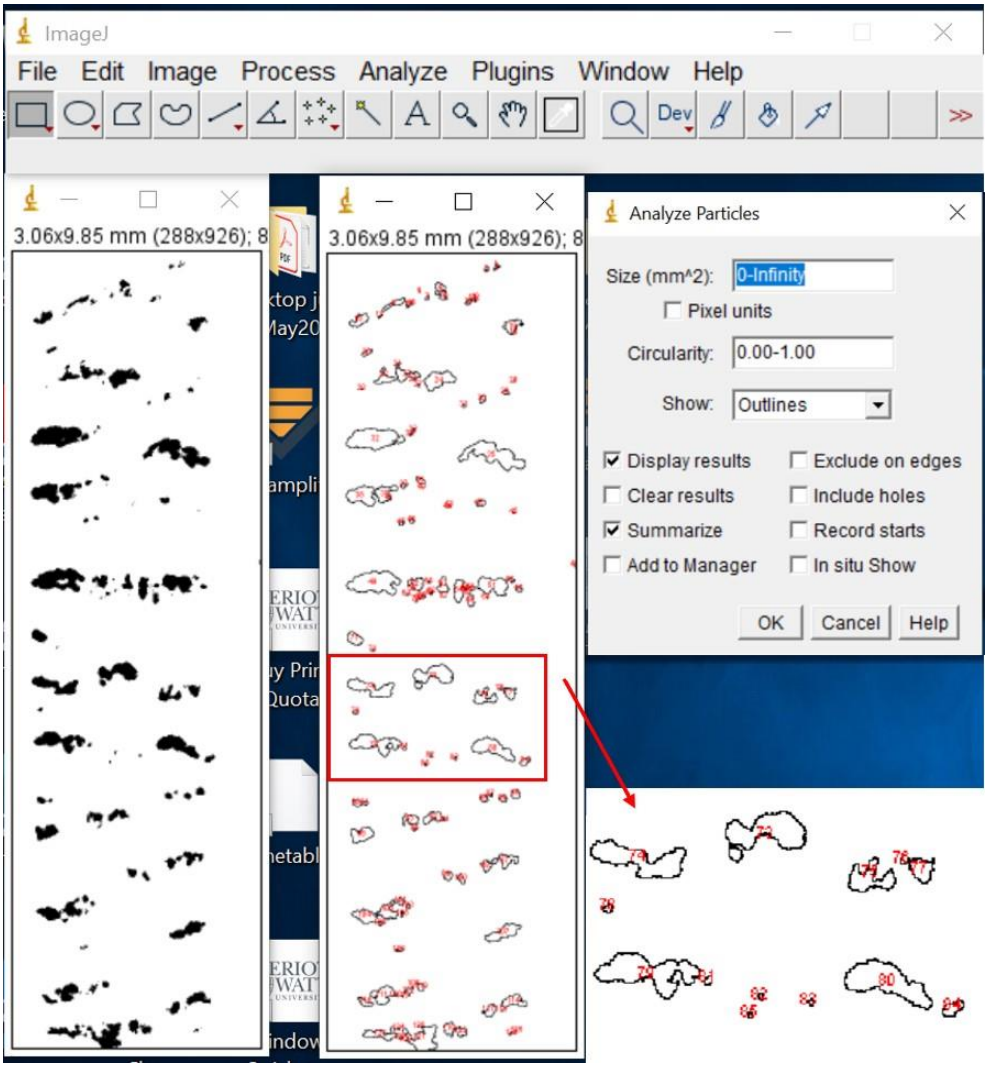

Figure A. 3: Analysing the particles (the cracks).

Figure A. 4a shows the original images of all 3D printed CBTPU-30GPLA, CBTPU-40GPLA and CBTPU-50GPLA strain sensors under dynamic loading in the ranges between 50-100%. The images were obtained from the optical microscope. Figure A. 4b shows the CBTPU-50GPLA under dynamic loading in the full range between 5-100%.

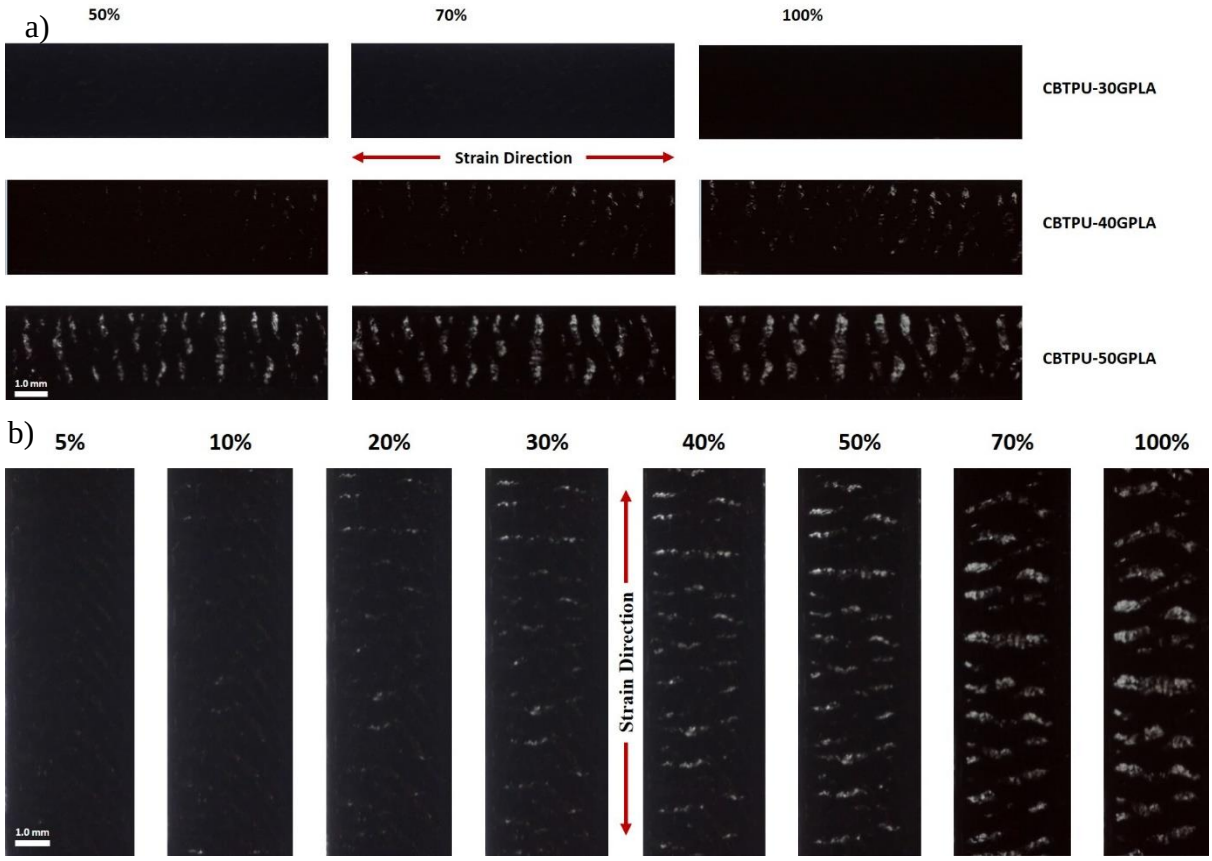

Figure A. 4: Original images acquired by the optical microscope of the 3D printed strain sensors under dynamic loading of a) All the composite samples as illustrated in the image and b) the CBTPU-50GPLA.

Appendix B

The Arduino and servo motors

Servo motors were used to provide fingers' movement of the 3D printed robotic hand. Five servo motors were used to provide individual movements of the 5 robotic fingers. The servo motors were mounted on a 3D printed stand adhered to the 3D printed robotic hand, as shown in Figure B1. The servo motors were connected mechanically to the fingers using fishing thread. Electrical wiring was employed to power the servo motors from the Arduino, as shown schematically. The servo motors were assigned to an Arduino digital channel, and a code provided from the Arduino library was used to rotate the servos to move the robotic fingers.

a)

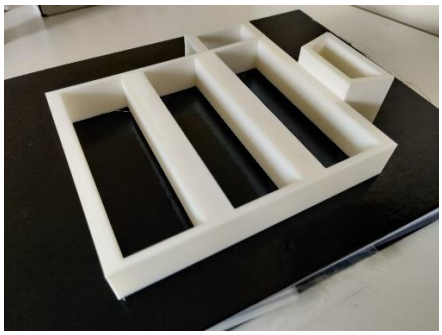

b)

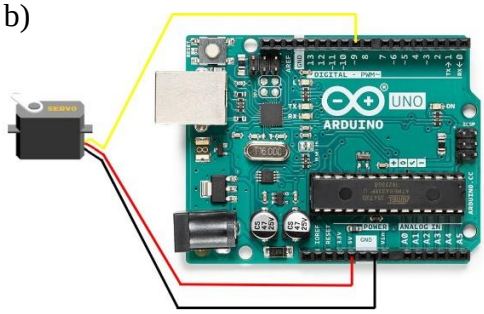

c)

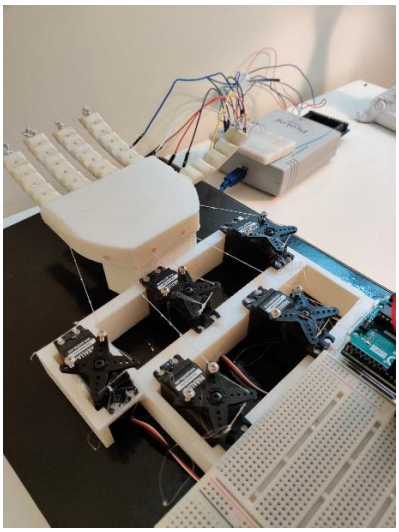

FigureB. 1: A) The 3D printed mount for servo motors, b) Schematic of servo motor connection to the Arduin for power and control, and c) optical image of the robotic hand setup.

The Arduino has a library in their associate software that includes codes that can rotate the servo motors when attached to the Arduino Uno. The code that was used to rotate the servo motors and hence bends the fingers of the 3D printed robotics is as follows:

/*

by Scott Fitzgerald

```
 http://www.arduino.cc/en/Tutorial/Sweep
*/
#include <Servo.h>
Servo myservo;  // create servo object to control a servo
int pos = 0;    // variable to store the servo position
void setup() {
  myservo.attach(9);  // attaches the servo on pin 9 to the servo object
}
void loop() {
  for (pos = 0; pos <= 180; pos += 1) { // goes from 0 degrees to 180 degrees
    // in steps of 1 degree
    myservo.write(pos);              // tell servo to go to position in variable 'pos'
    delay(15);                       // waits 15ms for the servo to reach the position
  }
  for (pos = 180; pos >= 0; pos -= 1) { // goes from 180 degrees to 0 degrees
    myservo.write(pos);              // tell servo to go to position in variable 'pos'
    delay(15);                       // waits 15ms for the servo to reach the position }
}
```

The code was modified to include all of the 5 servos as follows:

```
#include <Servo.h>
Servo myservo1;
Servo myservo2;
Servo myservo3;
Servo myservo4;
Servo myservo5;
void setup() {
```

```
  myservo1.attach(8);
  myservo1.write(10);
  myservo2.attach(9);
  myservo2.write(10);
  myservo3.attach(10);
  myservo3.write(0);
  myservo4.attach(11);
  myservo4.write(0);
  myservo5.attach(12);
  myservo5.write(10);
  delay(10000);
}
void loop() {
  myservo1.write(180);
  myservo2.write(180);
  myservo3.write(180);
  myservo4.write(180);
  myservo5.write(180);
  delay(1000);
  myservo1.write(160);
  myservo2.write(160);
  myservo3.write(170);
  myservo4.write(170);
  myservo5.write(160);
  delay(500000);
}
```

Controlling a robotic hand via our 3D printed pressure sensors

Our 3D printed sensors can act as a variable resistor. This dynamic change in electrical resistance upon mechanical pressure can be employed to control servo motors. In order to control the robotic hand via 3D printed pressure sensors, we connected the 3D printed sensors to the analogue inputs of the Arduino Uno, as illustrated schematically in Figure B2. The voltage variation of the sensors that resulted was assigned to control the movements of the servo motors of the robotic hand. We used a code provided by the Arduino library, which translates the analogue inputs (in this case, our 3D printed pressure sensors) to a digital signal that control the servo motors.

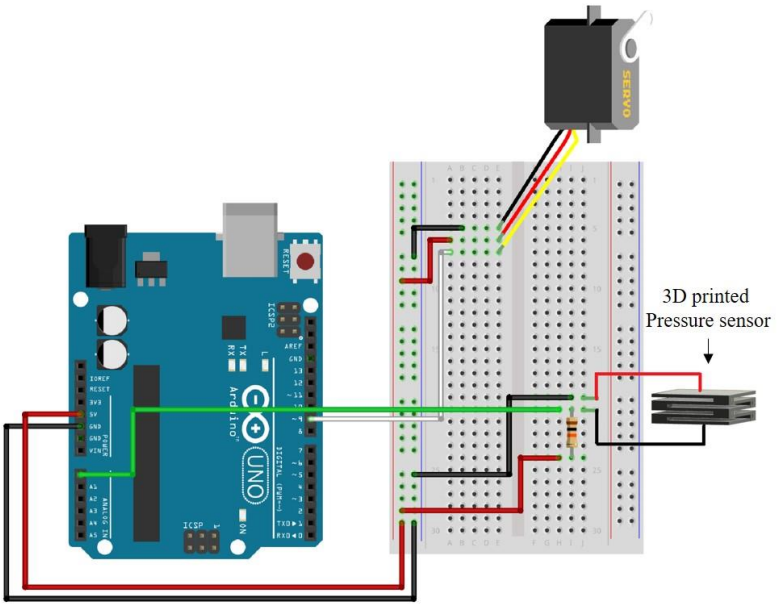

***Figure** B. 1: Schematic illustration of the setup used to control servo motors using the 3D printed pressure sensors and via the Arduino.*

The code that translates the variable change in electrical resistance to a digital signal that servo motors can read is acquired from the Arduino library. The 3D printed pressure sensors were attached to a glove worn on a human hand and used as variable resistors that input an analogue signal. This signal is then sent to the assigned servo motors in the digital pins using the Arduino code. The code that was used to rotate the servo motors and hence bends the fingers of the 3D printed robotic hand is as follows:

```
/*

 Controlling a servo position using a potentiometer (variable resistor)
```

```
 by Michal Rinott <http://people.interaction-ivrea.it/m.rinott>
 modified on 8 Nov 2013
 by Scott Fitzgerald
 http://www.arduino.cc/en/Tutorial/Knob
*/
#include <Servo.h>
Servo myservo;  // create servo object to control a servo
int potpin = 0;  // analog pin used to connect the potentiometer
int val;    // variable to read the value from the analog pin
void setup() {
  myservo.attach(9);  // attaches the servo on pin 9 to the servo object
}
void loop() {
  val = analogRead(potpin);            // reads the value of the potentiometer (value between 0 and
1023)
  val = map(val, 0, 1023, 0, 180);     // scale it to use it with the servo (value between 0 and 180)
  myservo.write(val);                  // sets the servo position according to the scaled value
  delay(15);                           // waits for the servo to get there
}
```

The code was modified to include all of the 5 servos as follows:

```
/*
 Controlling a servo position using a potentiometer (variable resistor)
 by Michal Rinott <http://people.interaction-ivrea.it/m.rinott>
 modified on 8 Nov 2013
 by Scott Fitzgerald
 http://www.arduino.cc/en/Tutorial/Knob
```

```
*/
#include <Servo.h>
Servo myservo1;  // create servo object to control a servo
Servo myservo2;
Servo myservo3;
Servo myservo4;
Servo myservo5;

int potpin1 = 0;  // analog pin used to connect the potentiometer
int val1;         // variable to read the value from the analog pin
int potpin2 = 1;  // analog pin used to connect the potentiometer
int val2;
int potpin3 = 2;  // analog pin used to connect the potentiometer
int val3;
int potpin4 = 3;  // analog pin used to connect the potentiometer
int val4;
int potpin5 = 4;  // analog pin used to connect the potentiometer
int val5;
void setup() {
  myservo1.attach(8);  // attaches the servo on pin 9 to the servo object
   myservo2.attach(9);
    myservo3.attach(10);
     myservo4.attach(11);
      myservo5.attach(12);
}
```

```
void loop() {
  val1 = analogRead(potpin1);            // reads the value of the potentiometer (value between 0 and 1023)
  val1 = map(val1, 450, 150, 0, 180);     // scale it to use it with the servo (value between 0 and 180)
  myservo1.write(val1);                  // sets the servo position according to the scaled value
   val2 = analogRead(potpin2);            // reads the value of the potentiometer (value between 0 and 1023)
  val2 = map(val2, 800, 550, 0, 180);     // scale it to use it with the servo (value between 0 and 180)
  myservo2.write(val2);
   val3 = analogRead(potpin3);            // reads the value of the potentiometer (value between 0 and 1023)
  val3 = map(val3, 850, 500, 0, 180);     // scale it to use it with the servo (value between 0 and 180)
  myservo3.write(val3);
   val4 = analogRead(potpin4);            // reads the value of the potentiometer (value between 0 and 1023)
  val4 = map(val4, 700, 200, 0, 180);     // scale it to use it with the servo (value between 0 and 180)
  myservo4.write(val4);
   val5 = analogRead(potpin5);            // reads the value of the potentiometer (value between 0 and 1023)
  val5 = map(val5, 850, 700, 0, 180);     // scale it to use it with the servo (value between 0 and 180)
  myservo5.write(val5);
  delay(15);                             // waits for the servo to get there
}
```